MODELING AND APPLICATIONS OF FERROELECTRIC BASED DEVICES

by

Atanu Kumar Saha

A Dissertation

Submitted to the Faculty of Purdue University

In Partial Fulfillment of the Requirements for the degree of

Doctor of Philosophy

School of Electrical and Computer Engineering

West Lafayette, Indiana

August 2021

THE PURDUE UNIVERSITY GRADUATE SCHOOL
STATEMENT OF COMMITTEE APPROVAL

Dr. Sumeet Gupta, Chair

School of Electrical and Computer Engineering

Dr. Kaushik Roy

School of Electrical and Computer Engineering

Dr. Peide Ye

School of Electrical and Computer Engineering

Dr. Anand Raghunathan

School of Electrical and Computer Engineering

Approved by:

Dr. Dimitrios Peroulis

To my family

ACKNOWLEDGMENTS

I would like to wholeheartedly extend my sincere gratitude to my Ph.D. advisor, Pof. Sumeet Kumar Gupta, for his excellent guidance and mentorship at every step during the entire duration of my graduate studies. Besides my advisor, I would like to thank my thesis committee members, Prof. Kaushik Roy, Prof. Peide Ye and Prof. Anand Raghunathan for their continuous guidance, collaboration, and experimental support. In addition, I want to express my gratitude to Prof. Suman Datta (University of Notre Dame) for the collaborative support. I wish to thank my fellow lab mates in the Integrated Circuits and Device Laboratory. I have had a good fortune to work with them as my colleagues.

My deepest gratitude goes to my father, Anil Saha and my mother, Swapna Saha, for their encouraging support to pursue my Ph.D. degree. I am genuinely grateful to my wife, Orthi Sikder for her support, motivation and unconditional love throughout this journey.

Finally, I would like to acknowledge Defense Advanced Research Projects Agency (DARPA), Semiconductor Research Corporation (SRC), and National Science Foundation (NSF) for providing the funding to support my Ph.D. research works.

TABLE OF CONTENTS

LIST OF FIGURES

ABSTRACT

To sustain the upcoming paradigm shift in computations technology efficiently, innovative solutions at the lowest level of the computing hierarchy (the material and device level) are essential to delivering the required functionalities beyond what is available with current CMOS platforms. Motivated by this, in this dissertation, we explore ferroelectric-based devices for steep-slope logic and energy-efficient non-volatile-memory functionalities signifying the novel device attributes, possibilities for continual dimensional scaling with the much-needed enhancement in performance.

Among various ferroelectric (FE) materials, Zr doped HfO_2 (HZO) has gained immense research attention in recent times by virtue of CMOS process compatibility and a considerable amount of ferroelectricity at room temperature. In this work, we investigate the Zr concentration-dependent crystal phase transition of $Hf_{1-x}Z_xO_2$ (HZO) and the corresponding evolution of dielectric, ferroelectric, and anti-ferroelectric characteristics. Providing the microscopic insights of strain-induced crystal phase transformations, we propose a physics-based model that shows good agreement with experimental results for 10 nm $Hf_{1-x}Z_xO_2$. Further, in a heterogeneous system, ferroelectric materials can exhibit negative capacitance (NC) behavior. Such NC effects may lead to differential amplification in local potential and can provide an enhanced charge and capacitance response for the whole system compared to their constituents. Such intriguing implications of NC phenomena have prompted the design and exploration of many ferroelectric-based electronic devices to not only achieve an improved performance but potentially also overcome some fundamental limits of standard transistors. However, the microscopic physical origin as well as the true nature of the NC effect, and direct experimental evidence remain elusive and debatable. To that end, in this work, we systematically investigate the underlying physical mechanism of the NC effect in the ferroelectric material. Based upon the fundamental physics of ferroelectric material, we investigate different assumptions, conditions, and distinct features of the quasi-static NC effect in the single-domain and multi-domain scenarios. While the quasi-static and hysteresis-free NC effect was initially propounded in the context of a single-domain scenario, we highlight that the similar effects can be observed in multi-domain FEs with soft domain-wall (DW) displacement. Furthermore, to obtain the soft-DW, the gradient energy coefficient of the FE material is required

to be higher as well as the ferroelectric thickness is required to be lower than some critical values. Otherwise, the DW becomes hard, and their displacement would lead to hysteretic NC effects. In addition to the quasi-static NC, we discuss different mechanisms that can lead to the transient NC effects. Furthermore, we provide guidelines for new experiments that can potentially provide new insights on unveiling the real origin of NC phenomena.

Utilizing such ferroelectric insulators at the gate stack of a transistor, ferroelectric-field-effect transistors (FeFETs) have been demonstrated to exhibit both non-volatile memory and steep-slope logic functionalities. To investigate such diverse attributes and to enable application drive optimization of FeFETs, we develop a phase-field simulation framework of FeFETs by self-consistently solving the time-dependent Ginzburg-Landau (TDGL) equation, Poisson's equation, and non-equilibrium Green's function (NEGF) based semiconductor charge-transport equation. Considering HZO as the FE layer, we first analyze the dependence of the multi-domain patterns on the HZO thickness (T_{FE}) and their critical role in dictating the steep-switching (both in the negative and positive capacitance regimes) and non-volatile characteristics of FeFETs. In particular, we analyze the T_{FE}-dependent formation of hard and soft domain-walls (DW). We show that, T_{FE} scaling first leads to an increase in the domain density in the hard DW-regime, followed by soft DW formation and finally polarization collapse. For hard-DWs, we describe the polarization switching mechanisms and how the domain density impacts key parameters such as coercive voltage, remanent polarization, effective permittivity and memory window. We also discuss the enhanced but positive permittivity effects in densely pattern multi-domain states in the absence of hard-DW displacement and its implication in non-hysteretic attributes of FeFETs. For soft-DWs, we present how DW-displacement can lead to effective negative capacitance in FeFETs, resulting in a steeper switching slope and superior scalability. In addition, we also develop a Preisach based circuit compatible model for FeFET (and antiferroelectric-FET) that captures the multi-domain polarization switching effects in the FE layer. Utilizing this model, we have explored the FeFET operation as multi-bit NVM as well as multi-level synapses for neuromorphic hardware.

Unlike semiconductor insulators (e.g., HZO), there are ferroelectric materials that exhibit a considerably low bandgap (< 2eV) and hence, display semiconducting properties. In this regard, non-perovskite-based 2D ferroelectric α-In_2Se_3 shows a bandgap of ~1.4eV and that suggests a

combined ferroelectricity and semiconductivity in the same material system. As part of this work, we explore the modeling and operational principle of ferroelectric semiconductor metal junction (FeSMJ) based devices in the context of non-volatile memory (NVM) application. First, we analyze the semiconducting and ferroelectric properties of the α-In_2Se_3 van der Waals (vdW) stack via experimental characterization and first-principles simulations. Then, we develop a FeSMJ device simulation framework by self-consistently solving the Landau–Ginzburg–Devonshire equation, Poisson's equation, and charge-transport equations. Our simulation results show good agreement with the experimental characteristics of α-In_2Se_3-based FeSMJ suggesting that the FeS polarization-dependent modulation of Schottky barrier heights of FeSMJ plays a key role in providing the NVM functionality. Moreover, we show that the thickness scaling of FeS leads to a reduction in read/write voltage and an increase in distinguishability. Array-level analysis of FeSMJ NVM suggests a lower read-time and read-write energy with respect to the HfO_2-based ferroelectric insulator tunnel junction (FTJ) signifying its potential for energy-efficient and high-density NVM applications.

1. INTRODUCTION

In the last few decades, computing has evolved in a fundamentally different way, not only with an extensive increase in complexity and but also being driven by data-centric applications. To cope up with the continuous increase in computational complexity and to process massive amounts of data efficiently, the computing hardware not only requires new architectures with diffused boundaries between memory and logic but also entails delivering continued performance gains and novel device functionalities. Consequently, the demand for high-performance logic and energy-efficient non-volatile memory technologies are more than ever for the continuation of the semiconductor industry to thrive in the upcoming era of beyond-von-Neumann computing.

Historically, transistor scaling following Moore's law [1] – [4] has acted as the key to enhance the integration density for coping with the computational complexity in an efficient manner. To that end, in the past few decades, the semiconductor industry has gone through extensive innovations in transistor design - scaling of transistor geometry , modification of device structures (planar to non-planar), use of new materials (such as high-*k* dielectrics) etc. As the transistor and memory features reach sub-7nm node, it is apparent that the room for further scaling is running out due to the enhancement in several detrimental effects (i.e., short channel effects, quantum effects etc.). At the same time, the fundamental limit on attainable subthreshold-swing (SS) has become a major impediment against the continuation of supply voltage (V_{DD}) scaling [4]. In conventional metal-oxide-semiconductor-FET (MOSFET), Fermi statistics of charge carriers (approximated as the Boltzmann's statistics in the sub-threshold region) impose that a minimum of 60mV change in gate voltage (V_{GS}) is required for inducing a decade change in drain current (I_D), setting the lower limit for subthreshold-swing (SS = $d\log(I_D)/dV_{GS}$) to be 60mV/decade at room temperature. Such a lower limit in SS restricts the scalability of the supply voltage (V_{DD}) without sacrificing the drive current and ON-OFF ratio. Therefore, to prolong the advancements of the electronic systems, it is imperative to explore novel material-device concepts that can go beyond this Boltzmann's limit. Towards that end, steep-slope transistors have emerged as promising candidates over the last decade [5]–[8]. One example of such beyond-Boltzmann FETs is Tunnel-FET (TFET) that utilizes band-to-band quantum tunneling to overcome the Boltzmann limit and can potentially achieve SS

lower than 60mV/decade [7]. However, the experimental demonstration of p-type TFET with a reasonable ON state current has not yet been done and remains an unsolved problem in the TFET community [8]. Therefore, there is a strong demand for innovative device solutions for steep-slope functionality.

From the architecture perspective, a surge in the computation complexity has worsened the memory bottleneck that exists in conventional von-Neumann computing architectures. As a result, significant research and development effort has been focused on memory technologies that offer high-speed and low-power read/write operations. One aspect of low power operation is to introduce non-volatility, so that the memory macro can be shut down in the stand-by state, thus saving leakage energy. Hence, over the past few decades, several non-volatile memory devices have been investigated e.g. Resistive RAM [9]–[12], NAND/NOR Flash [13]–[15], Magnetic RAM [16]–[18], Phase Change Memory [19]–[22] etc. However, each of these memory technologies exhibits its own limitations and overheads (i.e., low disgushibility and high write energy in Magnetic-RAM, high write energy in Flash, thermal drifts in PCM based memories, etc.) [23]–[26] and thus, there is a strong need to continue the exploration of new memory technologies.

Simultaneously, the next-generation data-intensive applications compel dedicated hardware with trillions of energy-efficient devices that can effectively process an enormous amount of data in real-time. However, in conventional architectures, the physical separation of computation cores (logic units) and the memory blocks leads to power-hungry and performance-limiting transfer of humungous amount of data. Thus, new techniques than can enable efficient logic-memory intrgration have been identified as one of the key enablers of future systems. In that context, new computing paradigms are being explored to overcome the limitations of the conventional computing architectures. As an example, neuromorphic computing shows an immense promise for tasks involving recognition and sensory processing [27]. Inspired by the low-power and in-memory attributes of the biological brain, the basic building blocks of such neuromimetic platforms are neurons and synapses, where the neurons are interconnected with each other in a synaptic fabric. In recent years, significant effort has been directed in developing artificial synapses and neurons using emerging devices for denser and efficient integration of neuromorphic hardware [28-36].

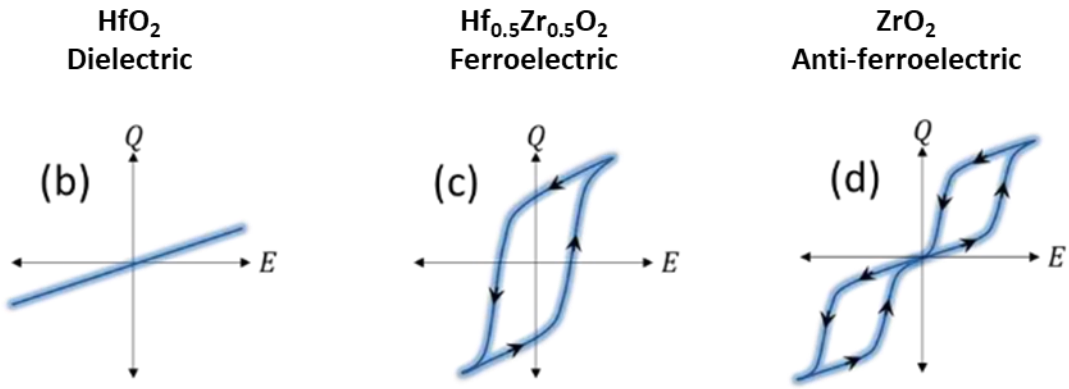

Figure 1.1. Charge (*Q*) vs E-field (*E*) characteristics of (a) dielectric (DE), (b) ferroelectric (FE) and (c) anti-ferroelectric HZO with different Zr concentration.

Meeting this multi-dimensional requirement of different computing paradigms necessitates the exploration of unique material-device concepts beyond the existing technologies. Therefore, a strong need has arisen to search for a new material-device avenue to sustain the semiconductor industry. To that end, a member of the functional material family, called 'Ferroelectric' material has been identified as one of the most promising candidates. The unique electrical properties of these materials can be utilized to design novel steep-slope logic, non-volatile memory and neuromimetic devices to meet the needs of next-generation electronics.

Ferroelectric materials exhibit spontaneous polarization, whose polarity can be altered by applying an external electric field. Further, depending on the band-gap, ferroelectric material can be broadly categorized as ferroelectric-insulator (high-bandgap) and ferroelectric-semiconductor (low-bandgap). Due to the immense possibilities of ferroelectric materials in electronic devices, ferroelectric materials compatible with silicon (Si) process technology have gained elevated research interests in recent times. Historically, as the potential candidate for ferroelectricity, Perovskite materials have been extensively investigated for several decades. However, such materials lack the possibility of CMOS process compatibility or direct integration with silicon (Si) transistors. Remarkably, one of the extensively used industry-standard CMOS process compatible high-k dielectric material HfO_2 has long been predicted to be ferroelectric under certain conditions [29]-[30]. Such ferroelectricity in HfO_2 was experimentally discovered very recently under the influence of various dopants and metal (TiN, W etc.) caping [29]. In particular, Zr doped HfO_2

($Hf_{1-x}Z_xO_2$) have been demonstrated to exhibit ferroelectricity at a broad range of temperature (-20°C to ~300°C) requiring a reasonable annealing temperature (600°C) suitable for Si process flow [29]. Unlike perovskites, the ferroelectric in HZO originates from fluorite structures when stabilized in the non-centrosymmetric and polar orthorhombic (o) phase. In addition to the o-phase, the fluorite crystal of HZO can also exhibit non-polar monoclinic (m) and tetragonal (t) phases leading to the polycrystalline nature in HZO. Interestingly, depending on the stability of different crystal phases, HZO can exhibit high-k dielectric (DE), ferroelectric (FE), anti-ferroelectric (AFE) characteristics [30]. For example, the m-phase leads to DE, o-phase yields FE and t-phase corresponds to AFE properties, and the dominant presence of a particular phase can be tuned by varying the Zr concentration in HZO. The charge (Q) vs electric-field (E) field characteristics of DE, FE and AFE are shown in Fig. 1.1. While the dielectric exhibits a linear and non-hysteretic Q-E relation, the FE and AFE exhibit a non-linear and hysteretic Q-E relation. Among them, the FE exhibits non-zero Q at E=0 and the polarity of Q (positive or negative) can be altered by applying a field larger than a critical field (known as a coercive field) yielding hysteretic Q-E attributes. As a part of the dissertation, we theoretically investigate the influence of Zr concentration in HZO and their crystal-phase dependent evolution of DE, FE and AFE properties.

Integrating HZO as the gate insulator, ferroelectric-FETs (FEFETs) have been demonstrated to exhibits a diverse set of functionalities, i.e., steep-slope logic [5]-[6], non-volatile-memory [31]-[32] and neuromimetic functionalities as well [33]-[35]. However, the role of HZO and the underlying physical mechanism for such distinct functionalities are yet to be understood for enabling the device-level and application-driven optimization of FEFET.

The FEFET that acts as a steep-slope logic transistor is generally referred to as negative-capacitance FET (NCFET) [36]. In principle, NCFETs offer a promise for SS<60mV/decade along with an enhanced ON current compared to conventional MOSFET – an attribute that has remained elusive for steep-switching technologies such as tunnel FETs (Fig. 1.3 (a)). Conceptually in an NCFET, the ferroelectric insulator in the gate stack should act as an effective negative capacitor that amplifies the applied V_{GS} at the underlying semiconductor channel yielding sub-60 mV/decade SS [36]. However, the microscopic physical origin as well as the true nature of the negative capacitance (NC) effect (both from theoretical and experimental perspectives) remain elusive and

debatable. As a part of this dissertation, we comprehensively explore the underlying physical mechanism of the NC effect in the ferroelectric material and its implication in NCFETs. While the quasi-static and hysteresis-free NC effect was initially propounded in the context of a single-domain scenario, we highlight that the NC effects can more conceivably be obtained in multi-domain ferroelectric with non-hysteretic polarization switching.

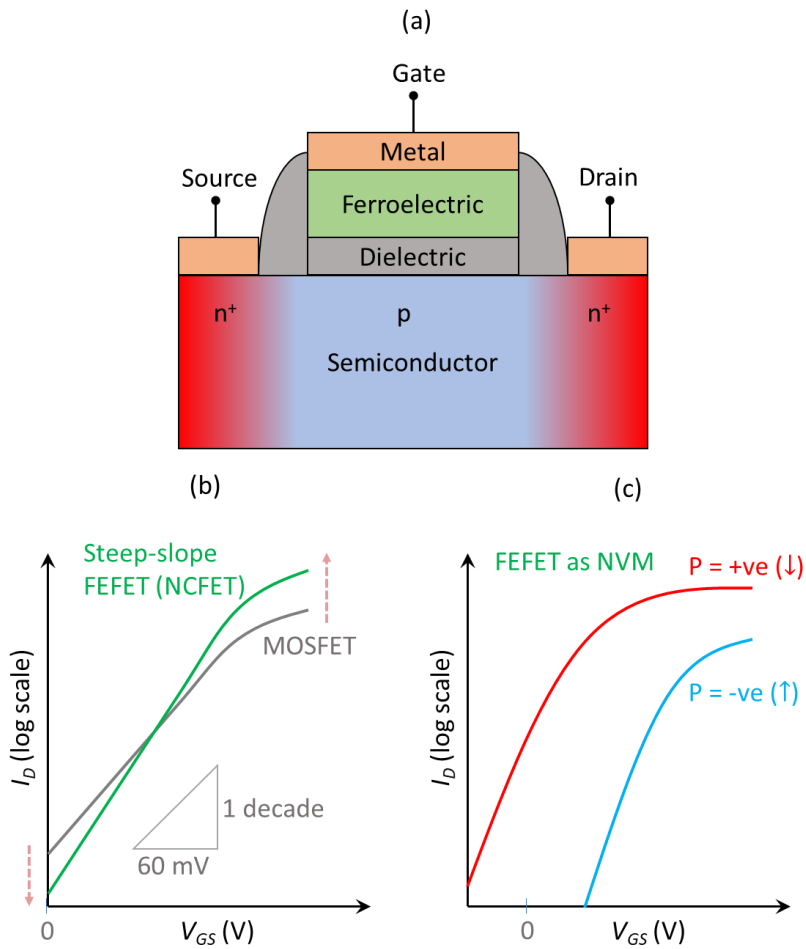

Figure 1.2. (a) Ferroelectric field-effect transistor (FEFET) structure. (a) Drain current (I_D) versus gate voltage (V_{GS}) characteristics of (b) FEFET as steep-slope negative-capacitance FET (NCFET) and (b) FEFET as non-volatile memory (NVM).

Unlike FEFET with NC functionalities that relies on the non-hysteretic polarization switching, the FEFETs that exhibit hysteretic polarization switching yield non-volatile memory functionalities. Depending on the direction (or polarity) of spontaneous polarization, an FEFET

can exhibit different threshold voltages leading to the different drain currents at the same applied gate voltage (Fig. 1.3(b)). Further, the multi-domain formation and their partial polarization switching in the ferroelectric layer leads to the stability of multiple average polarization leading to the multi-level memory functionalities. Such multi-level FEFET is a potential candidate for multi-bit/cell memory or multi-level synapses [35]. As the FEFET can act as both the steep-slope logic and non-volatile memory devices, their operational principle and underlying physics are important to understand for their application-specific optimization. In this work, we explore such FEFET optimization techniques extensively based on the phase-field simulation. In addition to that, this work also leads to the theoretical understanding of the possible origin of enhanced positive capacitance (EPC) effects in multi-domain ferroelectric materials and signifies that the EPC effect yields an enhanced FEFET performance compared to the conventional high-k MOSFETs. Furthermore, we also investigate the gate length scaling behavior of FEFETs signifying its superiority over the conventional MOSFET due to multi-domain attributes.

Similar to ferroelectric insulators, ferroelectric semiconductors (FES) also exhibit spontaneous polarization switchable via applied electric-field. The van-der-Waals stack of α-In_2Se_3 has recently been discovered as a 2D ferroelectric semiconductor material that can retain the ferroelectricity and semiconducting properties even for a monolayer thickness [37-39]. This suggests a remarkable possibility for thickness scaling. Recently, a metal-FFS-metal junction device (called FeSMJ) has been demonstrated to exhibit polarization-dependent resistance states [40]. As part of this work, we explore the non-volatile memory functionalities of α-In_2Se_3 based FeSMJ devices and analyze their array-level performances.

The major focus of this dissertation is to analyze the key physical interactions and functionalities of ferroelectric insulators (i.e., HZO) and ferroelectric-semiconductor (i.e., α-In_2Se_3) based devices for enabling the application-driven device optimization. To that end, we develope several physics-based device simulation frameworks and compact models for exploring a distinct set of concepts and for developing a synergistic understanding. Moreover, unlike the previous modeling approaches of ferroelectric based devices (that assume single-domain polarization switching [41-42], homogeneous polarization in FE layer [43], abtirary domain formation [44] and/or analytical approximations [45]), we have developed a phase-field simulation framework that solves the

Poisson's equation, time-dependent-Ginzburg-Landau equation and semiconductor charge-transport equation self-consistently. Such advanced simulation methodologies allows us to analyze electrostatic driven multi-domain formation, microscopic polarization switching via domain-nucleation and domain-wall motion, multi-domain negative chapacitance effects, enhanced positive capacitance effects and multi-domain polarization driven non-homognity in the semiconductor channel as well. The topics and key contributions of different chapters are given below.

1) In chapter – 2, we theoretically model the effect of zirconium (Zr) concentration in $Hf_{1-x}Zr_xO_2$ (HZO) and the corresponding evolution of dielectric, ferroelectric, and anti-ferroelectric properties due to the stability of different crystal phases.

2) In chapter – 3, we investigate the origin of electrostatic negative capacitance effects and enhanced positive capacitance effects in ferroelectric heterostructures and establishe key material and device properties to obtain them.

3) In chapter – 4, we analyze the transient negative capacitance effects in resistor-ferroelectric network based multi-domain Preisach and Landau-Khalatnikov (L-K) models and establish the key differences and similarities between these approaches.

4) In chapter – 5, by employing phase-field simulation, we extensively explore the multi-domain polarization switching dynamics in polycrystalline HZO (considering metal-ferroelectric-metal: MFM) providing key insights on the accumulative and domain-wall instability driven spontaneous polarization switching.

5) In chapter – 6, we analyze the multi-domain formation and polarization switching in the metal-ferroelectric-insulator-metal (MFIM) and metal-ferroelectric-insulator-semiconductor (MFIS) stack. We investigate the influence of ferroelectric and dielectric thickness scaling on different macroscopic properties (i.e., remanent polarization, coercive voltage, etc.) and the role of gradient energy coefficients on the multi-domain negative capacitance effects and enhanced positive capacitance effects in MFIM and MFIS stack.

6) In chapter – 7, we present a comprehensive phase-field simulation framework for FEFETs. Utilizing this framework, we investigate the non-volatile memory and steep-slope logic functionalities of multi-domain FEFETs and explore the application-driven optimization techniques in terms of ferroelectric thickness scaling.

7) In chapter – 8, we present a circuit-compatible compact model for multi-domain ferroelectric and anti-ferroelectric FET.
8) In chapter – 9, we present a comprehensive study on ferroelectric-semiconductor (FES) based devices (FES-metal junction: FESMJ). Our analysis includes the first-principal simulation of FES material, experimental characterization, device-level simulation and circuit/array level performance analysis.

9) In chapter – 9, we conclude this dissertation and provide an outlook and directions on the prospects of ferroelectric-based devices.

1.1 References

[1] G. E. Moore, "Cramming more components onto integrated circuits," *Electronics*, 1965.

[2] R. R. Schaller, "Moore's law: past, present, and future," *IEEE Spectrum*, 1997.

[3] M. Lundstrom, "Moore's Law Forever?," *Science*, 2003.

[4] S. Salahuddin, K. Ni, and S. Datta, "The era of hyper-scaling in electronics," *Nature Electronics*, 2018.

[5] M. Si et al., "Steep-slope hysteresis-free negative capacitance MoS2 transistors," *Nature Nanotechnology*, 2017.

[6] M. Si, C. Jiang, W. Chung, Y. Du, M. A. Alam, and P. D. Ye, "Steep-Slope WSe2 Negative Capacitance Field-Effect Transistor," *Nano Letters*, 2018.

[7] Y. Khatami and K. Banerjee, "Steep subthreshold slope n- and p-type Tunnel-FET devices for low-power and energy-efficient digital circuits," *IEEE Transactions on Electron Devices*, 2009.

[8] L. Lattanzio, L. De Michielis, and A. M. Ionescu, "The electron-hole bilayer tunnel FET," *in Solid-State Electronics*, 2012.

[9] A. Chen and M. R. Lin, "Variability of resistive switching memories and its impact on crossbar array performance," *in IEEE International Reliability Physics Symposium Proceedings*, 2011.

[10] H. S. P. Wong et al., "Metal-oxide RRAM," *in Proceedings of the IEEE*, 2012.

[11] Y. T. Li, S. B. Long, Q. Liu, H. B. Lü, S. Liu, and M. Liu, "An overview of resistive random access memory devices," *Chinese Science Bulletin*, 2011.

[12] A. Prakash, D. Jana, and S. Maikap, "TaOx-based resistive switching memories: Prospective and challenges," *Nanoscale Research Letters*, 2013.

[13] R. S. J. Shen, F. R. L. Lin, A. H. F. Chou, E. C. S. Yang, and C. C. H. Hsu, "Flash memories," *in Memory, Microprocessor, and ASIC*, 2003.

[14] A. Tal, "NAND vs. NOR flash technology," *Electronic Products (Garden City, New York)*, 2002.

[15] R. Micheloni, A. Marelli, and R. Ravasio, "NOR Flash memories," *in Error Correction Codes for Non-Volatile Memories*, 2008.

[16] S. Parkin, X. Jiang, C. Kaiser, A. Panchula, K. Roche, and M. Samant, "Magnetically engineered spintronic sensors and memory," *Proceedings of the IEEE*, 2003.

[17] K. Ando et al., "Spin-transfer torque magnetoresistive random-access memory technologies for normally off computing," *Journal of Applied Physics*, 2014.

[18] P. K. Amiri et al., "Electric-Field-Controlled Magnetoelectric RAM: Progress, Challenges, and Scaling," *IEEE Transactions on Magnetics*, 2015.

[19] R. Jeyasingh, E. C. Ahn, S. Burc Eryilmaz, S. Fong, and H. S. Philip Wong, "Phase Change Memory," *Emerging Nanoelectronic Devices*, 2015.

[20] E. Oró, A. de Gracia, A. Castell, M. M. Farid, and L. F. Cabeza, "Review on phase change materials (PCMs) for cold thermal energy storage applications," *Applied Energy*, 2012.

[21] S. Raoux, F. Xiong, M. Wuttig, and E. Pop, "Phase change materials and phase change memory," *MRS Bulletin*, 2014.

[22] S. Raoux et al., "Phase-change random access memory: A scalable technology," *IBM Journal of Research and Development*, 2008.

[23] S. Hong, O. Auciello, and D. Wouters, *Emerging non-volatile memories*, 2014.

[24] Y. Fujisaki, "Current status of nonvolatile semiconductor memory technology," *Japanese Journal of Applied Physics*, 2010.

[25] J. S. Meena, S. M. Sze, U. Chand, and T. Y. Tseng, "Overview of emerging nonvolatile memory technologies," *Nanoscale Research Letters*, 2014.

[26] S. Yu and P. Y. Chen, "Emerging Memory Technologies: Recent Trends and Prospects," *IEEE Solid-State Circuits Magazine*, 2016

[27] D. Marković, A. Mizrahi, D. Querlioz and Julie Grollier, "Physics for neuromorphic computing" *Nature Reviews Physics*, 2020.

[28] D. Hassabis, D. Kumaran, C. Summerfield, and M. Botvinick, "Neuroscience-inspired artificial intelligence," *Neuron*, 2017.

[29] J. Muller, et al., "Ferroelectricity in Simple Binary ZrO_2 and HfO_2," *Nano Letter*, 2012.

[30] R. Materlik, et al., "The origin of ferroelectricity in $Hf_{1-x}Zr_xO_2$: A computational investigation and a surface energy model," *Journal of Appied Physics*, 2015.

[31] K. Chatterjee, S. Kim, G. Karbasian, A. J. Tan, A. K. Yadav, A. I. Khan, C. Hu, and S. Salahuddin, "Self-Aligned, Gate Last, FDSOI, Ferroelectric Gate Memory Device With 5.5-nm $Hf_{0.8}Zr_{0.2}O_2$, High Endurance and Breakdown Recovery," *IEEE Electron Device Letters*, 2017.

[32] S. Dünkel et al., "A FeFET based super-low-power ultra-fast embedded NVM technology for 22nm FDSOI and beyond," *IEDM*, 2017.

[33] H. Mulaosmanovic, E. Chicca, M. Bertele, T. Mikolajickac, and S. Slesazecka, "Mimicking biological neurons with a nanoscale ferroelectric transistor," *Nanoscale*, 2018.

[34] H. Mulaosmanovic, J. Ocker, S. Müller, M. Noack, J. Müller, P. Polakowski, T. Mikolajick, and S. Slesazeck, "Novel ferroelectric FET based synapse for neuromorphic systems," *IEEE Symposium on VLSI Technology*, 2017.

[35] M. Jerry, P. Chen, J. Zhang, P. Sharma, K. Ni, S. Yu, and S. Datta, "Ferroelectric FET analog synapse for acceleration of deep neural network training," *IEDM*, 2017.

[36] S. Salahuddin, and S. Datta, "Use of negative capacitance to provide voltage amplification for low power nanoscale devices," *Nano Letters*, 2008.

[37] W. Ding, J. Jhu, Z. Wang, Y. Gao, D. Xiao, Y. Gu, Z. Zhang, and W. Zhu, "Prediction of intrinsic two-dimensional ferroelectrics in In_2Se_3 and other III_2-VI_3 van der Waals materials," *Nature Communications*, 2017.

[38] C. Zheng et al., "Room temperature in-plane ferroelectricity in van der Waals In_2Se_3," *Science Advances*, 2018.

[39] M. Si, A. K. Saha, S. Gao, G. Qiu, J. Qin, Y. Duan, J. Jian, C. Niu, H. Wang, W. Wu, S. K. Gupta, and P. D. Ye, "A ferroelectric semiconductor field-effect transistor," *Nature Electronics*, 2019.

[40] M. Si, Y. Luo, W. Chung, H. Bae, D. Zheng, J. Li, J. Qin, G. Qiu, S. Yu, and P. D. Ye, "A Novel Scalable Energy-Efficient Synaptic Device: Crossbar Ferroelectric Semiconductor Junction," *IEDM*, 2019.

[41] A. I. Khan, C. W. Yeung, C. Hu, S. Salahuddin, "Ferroelectric negative capacitance MOSFET: Capacitance tuning & antiferroelectric operation", *IEDM*, 2011.

[42] A. Aziz, S. Ghosh, S. Datta and S. K. Gupta, "Physics-Based Circuit-Compatible SPICE Model for Ferroelectric Transistors," *IEEE Electron Device Letters*, 2016.

[43] H. Ota, T. Ikegami, J. Hattori, K. Fukuda, S. Migita, A. Toriumi, "Fully coupled 3-D device simulation of negative capacitance FinFETs for sub 10 nm integration", *IEDM*, 2016.

[44] S. Deng et al., "A Comprehensive Model for Ferroelectric FET Capturing the Key Behaviors: Scalability, Variation, Stochasticity, and Accumulation," *IEEE Symposium on VLSI Technology*, 2020.

[45] K. Ni, M. Jerry, J. A. Smith and S. Datta, "A Circuit Compatible Accurate Compact Model for Ferroelectric-FETs," *IEEE Symposium on VLSI Technology*, 2018.

2. MICROSCOPIC CRYSTAL PHASE INSPIRED MODELING OF ZR CONCENTRATION EFFECTS IN HZO THIN FILMS

2.1 Introduction

In this chapter, we theoretically and experimentally investigate the Zr concentration dependent crystal phase transition of $Hf_{1-x}Z_xO_2$ (HZO) and the corresponding evolution of dielectric (DE), ferroelectric (FE) and anti-ferroelectric (AFE) characteristics. Providing the microscopic insights of strain induced crystal phase transformations, we propose a physics based model that shows good agreement with our experimental results for 10nm $Hf_{1-x}Z_xO_2$ (with x=0 through 1). Utilizing our model, we analyze HZO-FET operation as a non-volatile memory device for different x.

FE materials compatible for Si-CMOS process have attracted a great deal of attention in recent times. In this regard, doped HfO_2 seems promising by virtue of thickness scalability and seamless integration with standard CMOS process flow. In particular, Zr doped HfO_2 (HZO) shows considerable amount of ferroelectricity at room temperature and requires a low annealing temperature (600°C) [1]. Most interestingly, being a member of fluorite crystal family, depending on the stability of different crystal phases, HZO can show high-k dielectric (DE), ferroelectric (FE), anti-ferroelectric (AFE) characteristics. Such versatility in HZO characteristics needs to be understood and modeled properly for the device level optimization of HZO-FET to achieve the desired functionality. To that effect, we theoretically and experimentally investigate the role of Zr concentration in HZO and analyze the HZO-FET characteristics in the context of memory applications.

2.2 Fluorite Crystal Phases & DE/FE/AFE Characteristics

In principle, fluorite structures can exhibit three major crystal phases, (i) monoclinic (m), (ii) orthorhombic (o) and tetragonal (t) (Fig. 2.1(a)-(c)). Depending on the crystallization process and external stimuli (dopant concentration, strain, temperature etc.), stability of one phase can dominate over others. The electrical characteristics (charge (Q) vs electric field (E-field)) are strongly coupled with their crystal shape. Considering the film thickness along the z-axis, $Q=\varepsilon_r E+P_Z$; where, εr is the background permittivity (contribution from edge/face atoms), E is the

applied field along z-axis and P_Z is the polarization along z-axis (contribution from internal O-lattice). In the m-phase, the spontaneous displacements of polarized O-atoms are compensated internally within each of the two sub-lattices, yielding DE behavior (Fig. 2.1(d)). However, in the o-phase, spontaneous displacement of O-atoms in both the sub-lattices are parallel to z-axis (↑↑/↓↓) leading to non-zero spontaneous P_Z (at E=0) (Fig. 2.1(e)). In contrast, in the t-phase, the O-displacements in the sub-lattices are in anti-parallel (↑↓) and the spontaneous P_Z=0 (at E=0) (Fig. 2.1(f)); However, ↑↓ to ↑↑/↓↓ configuration in the t-phase can be achieved by applying E-field (E>/<0), thus, resulting in AFE characteristics.

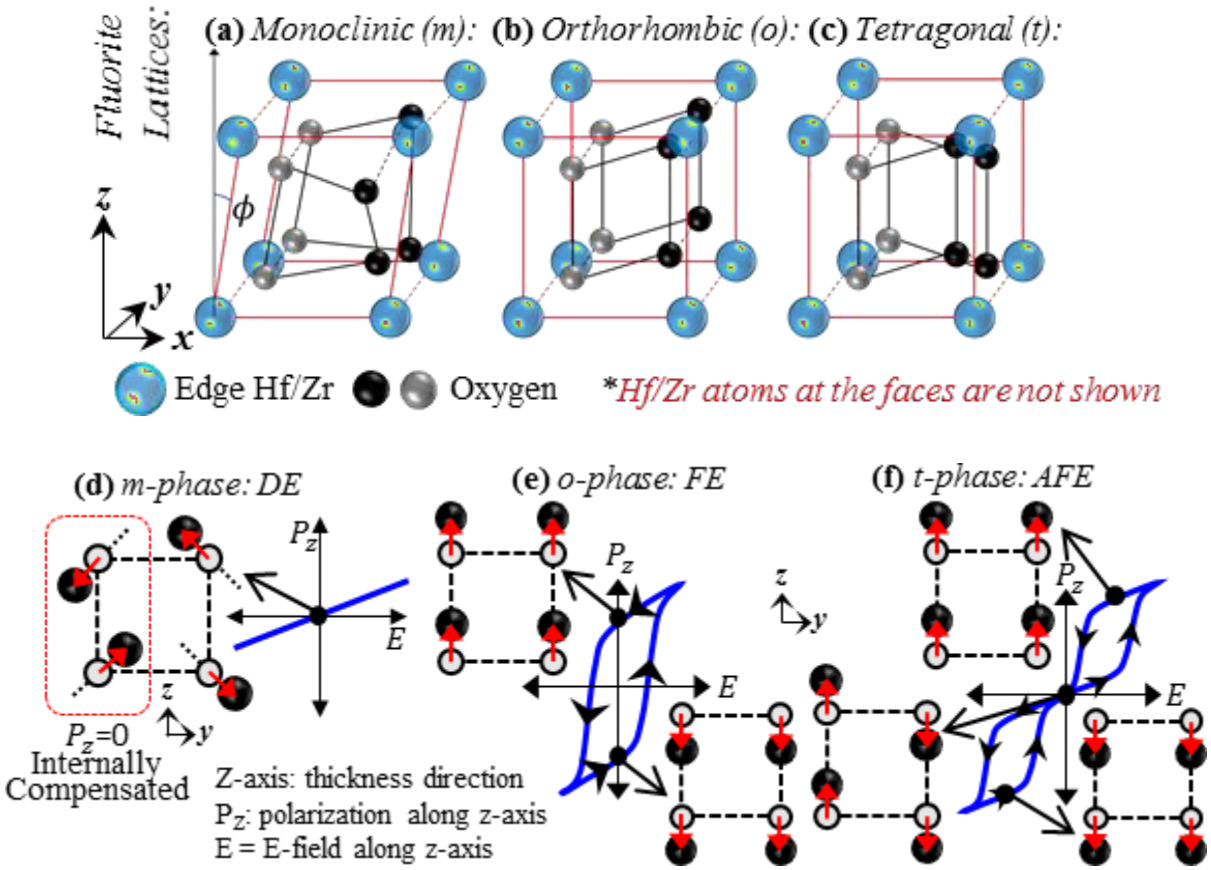

Figure 2.1. Crystal phases of $Hf_{1-x}Zr_xO_2$: (a) monoclinic, (b) orthorhombic and (c) tetragonal. Internal oxygen (O) lattice (O-lattice) configuration and the corresponding polarization (PZ) vs electric-field (E) characteristics: (d) DE in m-phase, (e) FE in o-phase and (f) AFE in t-phase. Here, red arrows are polarization (P) vectors.

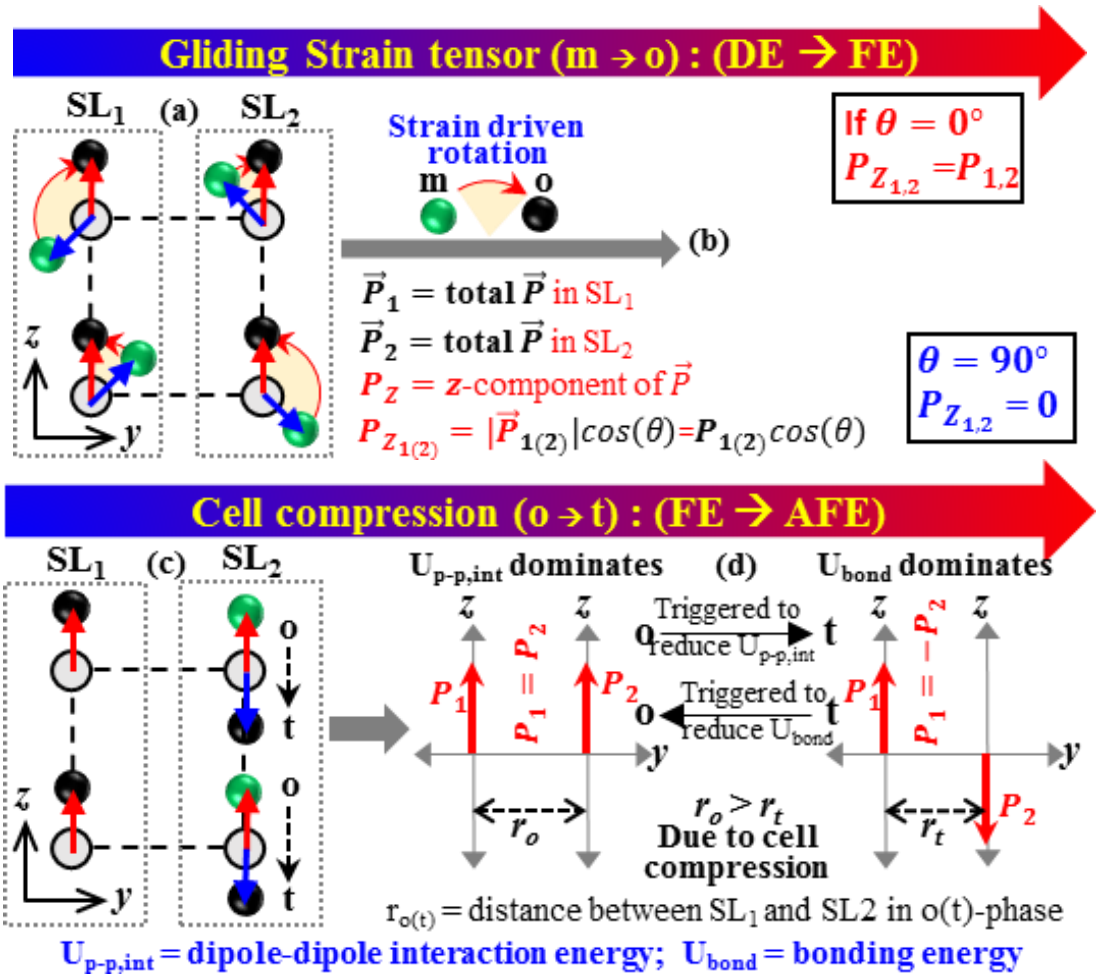

Figure 2.2. (a) Trajectory of atomic displacement in internal O-lattice during m-phase (DE) to t-phase (FE) transformation due to gliding strain tensor (change in ϕ-Fig. 1(a)) and (b) corresponding change in P vector. (c) o-phase (FE) to t-phase (AFE) transformation due to cell compression and (d) corresponding (↑↓) state

In intrinsic HfO_2 and ZrO_2, the most stable phases are m-phase and t-phase, respectively at room temperature (in absence of external stimuli). However, stabilization of o-phases can be induced in HZO by straining the film by metal capping or/and by varying Zr/[Hf+Zr] ratio (x). Technically, metal capping can provide a global strain across the sample area and Zr doping can induce strain in the internal O-lattices. With the increase in Zr concentration, HZO undergoes m-phase to t-phase transition. By taking the corresponding strain effects into account, m-phase (DE) to o-phase (FE) transformation can be understood as an effect of increasing gliding strain tensor. The corresponding O-atoms' displacement trajectories are shown in Fig. 2.2(a). We model such

phenomena (Fig. 2.2(b)) by considering an effective polarization vector ($\vec{P}_{1(2)}$) in each sub-lattice ($SL_{1(2)}$) and its traversal from y-axis (θ=90) to z-axis (θ=0). Therefore, z-component of total polarization, $P=(P_1+P_2)\cos(\theta)$. By increasing Zr concentration further, internal O-lattice undergoes cell compression [4] that reduces the distance between two SLs. Note that, there are two opposite forces that act between two SLs: (i) due to o-o covalent bonds and (ii) due to dipole-dipole interaction. As both the SLs are spontaneously polarized in o-phase (↑↑/↓↓), cell compression leads to an increase in dipole-dipole interaction energy ($U_{P\text{-}P,int}$). Given a condition, if $U_{P\text{-}P,int}$ is energetically unfavorable compared to bond stretching energy (U_{bond}), then the o-phase (↑↑, FE) transforms to t-phase (↑↓, AFE) with a decrease in $U_{P\text{-}P,int}$ and an increase in U_{bond}.

Physics based $Hf_{1-x}Zr_xO_2$ Model

Total energy of the system (inner O-lattice),

$$U = U_{free}(P_1) + U_{free}(P_2) + U_{bond}(P_1,P_2) + U_{p\text{-}p,int}(P_1,P_2) + U_{elec}(P_1,P_2)$$

Free energy of $SL_{1(2)}$, $U_{free}(P_{1(2)}) = \frac{1}{2}\alpha P_{1(2)}^2 + \frac{1}{4}\beta P_{1(2)}^4 + \frac{1}{6}\gamma P_{1(2)}^6$

$U_{bond}(P_1,P_2) = \frac{1}{2}g(r)(P_1 - P_2)^2$; $U_{p\text{-}p,int}(P_1,P_2) = \frac{1}{2}k(r)(P_1P_2)$

Electrostatic energy, $U_{elec} = -E(P_1+P_2)\cos(\theta)$;

$E = V/T_{HZO}$; V = applied voltage; T_{HZO} = HZO thickness.

$dU/dP = -\rho(dP/dt)$; ρ = kinetic coefficient, t = time.

Charge, $Q = \epsilon_r E + (P_1+P_2)\cos(\theta)$; ϵ_r = background permittivity.

Dipole-dipole interaction coefficient, $k(r)=k_1+k_0/(r-r_0)^3$; $k_0=0.22 \times 10^{-22}\,Jm^4/C^2$

Bonding energy coefficient, $g(r)=g_0(r-r_1)^2$; $g_0=0.9 \times 10^{31}\,J/m/C^2$

r = is internal oxygen SL_1 to SL_2 distance

Parameters

$\alpha = 1.5 \times 10^9 m/F$

$\beta = 1.1 \times 10^{10} m^5/F/C^2$

$\gamma = 30 \times 10^{11} m^9/F/C^4$

$\cos\theta(x) = 1.9x+0.05$ (x<0.5)

$= 1$ (x>=0.5)

$r(x) = (-0.2x+2.7)$Å

$r_0=2.63$Å, $k_1=-10^9 Jm/C^2$

$r_1=2.33$Å

Figure 2.3. Model equations for of $Hf_{1-x}Zr_xO_2$ and parameters used in the simulation

2.3 Physics Based Zr concentration dependent HZO model:

To model the Zr concentration dependent (strain induced) evolution of different crystal phases and the corresponding Q-E characteristics, we employ Landau-Ginzburg model for each of the internal O-sub-lattices, where the total energy of the system (U) is the composition of free energy of the two SLs (U_{free}), electrostatic energy (U_{elec}), U_{bond} and $U_{P\text{-}P,int}$. We consider the physics based formulation of U_{bond} and $U_{P\text{-}P,int}$, where, $U_{bond} \propto (1/2)g(r)(P_1-P_2)^2$ and $U_{P\text{-}P,int} \propto (1/2)k(r)(P_1P_2)$; r=distance between two SLs, g(r) = bonding energy coefficients ($\propto(r-r_1)2$), k(r)=dipole interaction

energy coefficients ($\propto 1/(r-r_0)^3$). The corresponding equations are shown in Fig. 2.3. Simulated U vs (P_1, P_2) characteristics for different g(r) and k(r) are shown in Fig. 2.4 that show the evolution of o-phase (↑↑) to t-phase (↑↓) as k(r) begins to dominate over g(r) with increasing *x*.

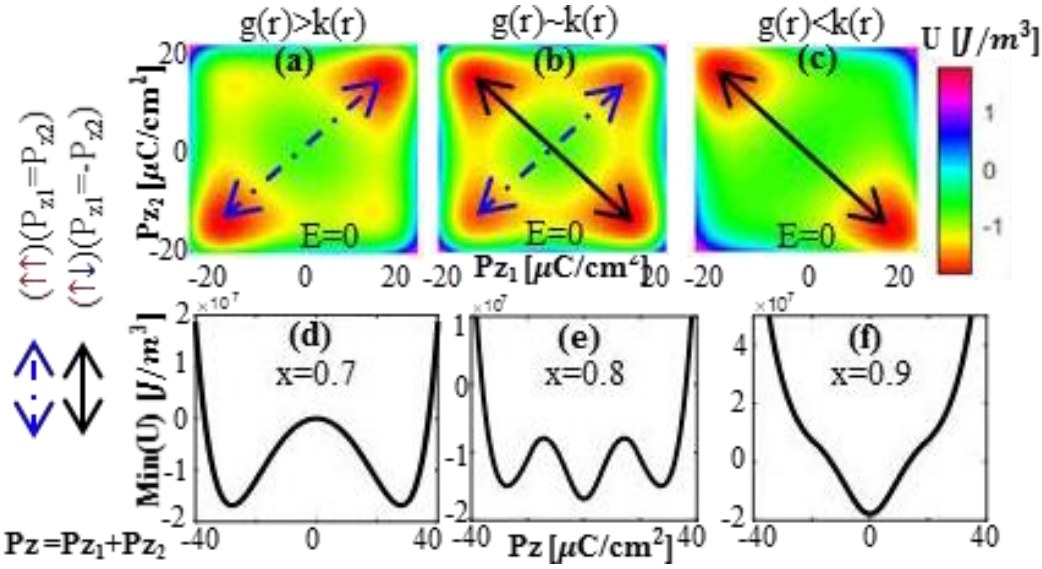

Figure 2.4. *U* vs *Pz* (Pz1, Pz2) map for (a) g(r)>k(r), (b) g(r)~*k*(*r*) and (c) g(r)<k(r). (e-f) Corresponding min(U) vs Pz showing the evolution of FE to AFE energy landscape with increasing k(r).

2.4 Experimental Measurements and Model Validation:

To experimentally analyze the effect of x on HZO characteristics, we fabricate 10nm $Hf_{1-x}Zr_xO_2$ film (ALD grown) for x=0.0 to 1.0 in steps of 0.1. The concentrations of Hf and Zr are controlled by cycling Hf *x* times, and Zr *1-x* times to obtain a laminate with the desired concentration. The top/bottom W electrodes are 100nm thick. (See the process flow in Fig. 2.5(a)). Fig. 2.5(b) shows the measured and simulated Q-E characteristics, which are in good agreement with each other. With the increase in x, ($0<x<0.6$), HZO undergoes m-phase to o-phase transition.Such transition can be understood either as the gradual transition of m-phase to o-phase in each lattice or as the increase in sample area corresponds to o-phase over the m-phase area. However, in our model, both the phenomena are mathematically equivalent. In addition, we observe the highest remnant charge window (ΔQ_R) at x~0.5 to 0.6 based on our model (Fig. 2.6(a)). Further addition in Zr (increase in x>0.6), triggers the transition from o-phase to t-phase, giving rise to AFE

characteristics, leading to a decrease in ΔQ_R. We emphasize that, at the high polarization (↑↑)state, the p-p-interaction is very dominant, therefore, further increase in strain (increase in x or decrease in r) favors the AFE state (↑↓). Similarly, the decrease in voltage hysteresis window (ΔV_H)with the increase in x (Fig. 2.6(b)) can be understood as the cause of decrease in potential barrierwith the increasing p-p interaction.

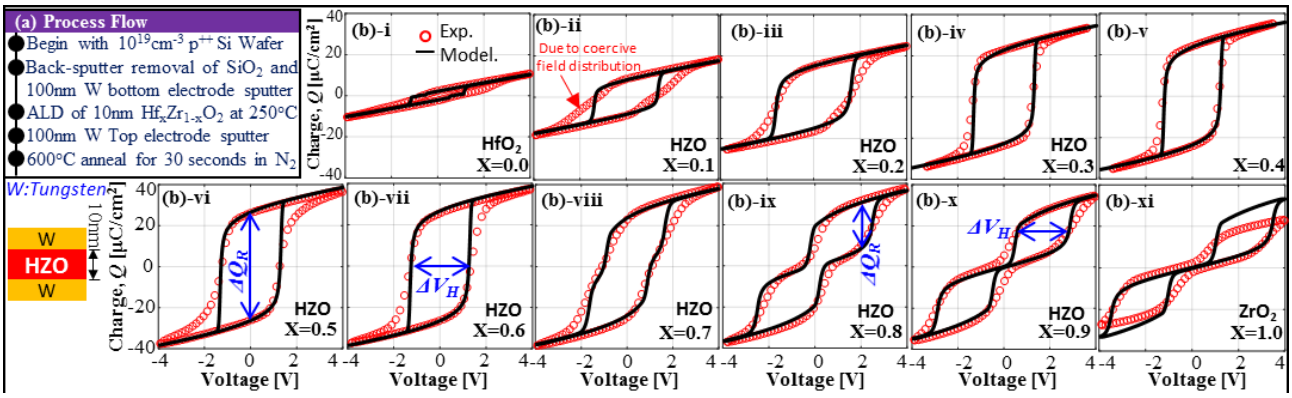

Figure 2.5. (a) Process flow of the HZO film. (b) Measured (red o) and simulated (black -) charge vs E-field (Q-E) characteristics of $Hf_{1-x}Zr_xO_2$ for different x.

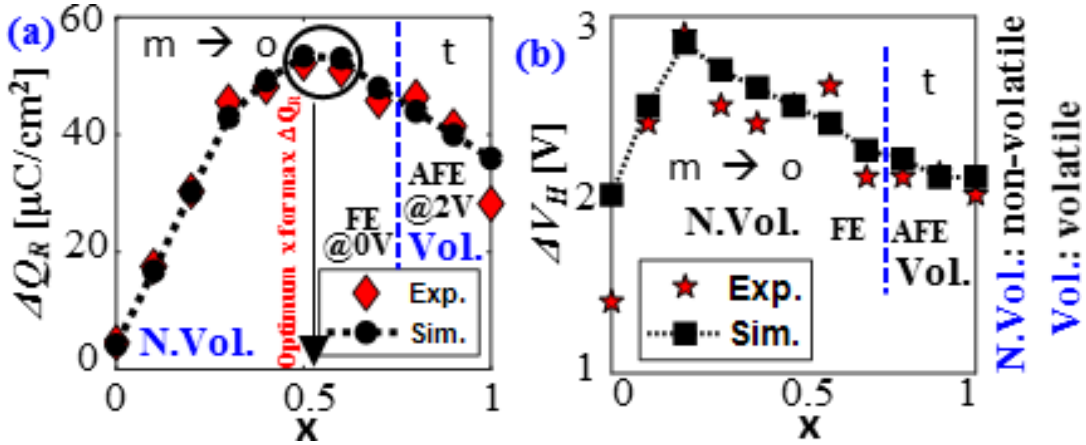

Figure 2.6. (a) Remnant charge window (ΔQ_R) and (b) hysteresis window (ΔV_H) in HZO for different x.

2.5 Summary

In summary, we propose a model for Q-V characteristics of $Hf_{1-x}Zr_xO_2$ based on theoretical and experimental analysis of Zr concentration dependent crystal phase change and the corresponding evolution of DE-FE-AFE phases. Utilizing our model, we analyze the HZO-FET operation as a non-volatile memory device. The model can also be used to analyze other applications of HZO and HZO-FETs to optimize the Zr concentration for performance enhancement.

2.6 References

[1] J. Müller, T. S. Böscke, U. Schröder, S. Mueller, D. Bräuhau, U. Böttger, L. Frey, and T. Mikolajick, "Ferroelectricity in Simple Binary ZrO_2 and HfO_2," *Nano Letters*, 2012.

[2] R. Materlik, C. Künneth, and A. Kersch, "The origin of ferroelectricity in $Hf_{1-x}Zr_xO_2$: A computational investigation and a surface energy model," *Journal of Applied Physics*, 2015.

[3] E. D. Grimley, T. Schenk, T. Mikolajick, U. Schroeder, and J. M. LeBeau, "Atomic Structure of Domain and Interphase Boundaries in Ferroelectric HfO2," *Advanced Material Interfaces*, 2018

[4] S. Clima, SRC. McMitchell, K. Florent, L. Nyns, M. Popovici, N. Ronchi, L. Di. Piazza, J. Houdt, and G. Pourtois, "First-Principles Perspective on Poling Mechanisms and ferroelectric/ Antiferroelectric Behavior of $Hf_{1-x}Zr_xO_2$ for FEFET Applications," *IEDM*, 2018.

3. NEGATIVE CAPACITANCE EFFECTS IN FERROELECTRIC BASED HETEROGENOUS SYSTEMS

3.1 Introduction

In a heterogeneous system, ferroelectric material can exhibit negative capacitance (NC) behavior given that the overall capacitance of the system remains positive. Such NC effects may lead to differential amplification in local potential and can provide an enhanced charge and capacitance response for the whole system compared to their constituents. Such intriguing implications of NC phenomena have prompted the design and exploration of many ferroelectric-based electronic devices to not only achieve an improved performance but potentially also overcome some fundamental limits of standard transistors. However, the microscopic physical origin as well as the true nature of the NC effect, and direct experimental evidence remain elusive and debatable. To that end, in this chapter, we provide a comprehensive theoretical perspective on the current understanding of the underlying physical mechanism of the NC effect in the ferroelectric material. Based upon the fundamental physics of ferroelectric material, we discuss different assumptions, conditions, and distinct features of the quasi-static NC effect in the single-domain and multi-domain scenarios. While the quasi-static and hysteresis-free NC effect was initially propounded in the context of a single-domain scenario, we highlight that the similar effects can be observed in multi-domain FE with soft domain-wall (DW) displacement. Further, to obtain the soft-DW, the gradient energy coefficient of the FE material is required to be higher as well as the FE thickness is required to be lower than some critical values. If those requirements are not met, then the DW becomes hard and their displacement would lead to hysteretic NC effects, which are adiabatically irreversible. In addition to the quasi-static NC, we discuss different mechanisms that can potentially lead to the transient NC effects. Furthermore, we discuss different existing experimental results by correlating their distinct features with different types of NC attributes and provide guidelines for new experiments that can potentially provide new insights on unveiling the real origin of NC phenomena.

3.2 Historical background of Negative Capacitance

The notion of negative capacitance (NC) in ferroelectric (FE) based devices has been intriguing many physicists, scientists and engineers for several decades [1]-[26]; not only because of the rich underlying physical mechanisms and theoretical explanations associated with such unconventional effects but also due to its potentially groundbreaking implications in the design of low power, steep switching and aggressively voltage-scalable transistors [6], [17]. The nature of the negative capacitance effects in ferroelectrics has been a subject of intense debate [13]-[17]. In particular, different schools of thought have formed in response to the question of whether or not the capacitance in ferroelectrics can be intrinsically negative [13]-[17]. On one hand, there have been strong proponents of the idea that ferroelectrics can access their intrinsic negative capacitance paths under certain conditions [6]. On the other hand, there have been several explanations that indicate that the negative capacitance observed in experiments is either an effective parameter or is the result of transient phenomena [14]-[17]. Irrespective of which notion turns out to be true, there is a convergence amongst the researchers that this effect needs a systematic investigation to explore its possible applications in the design of future electronic systems.

In order to introduce the concept of NC in more detail and to provide a proper perspective into the nature of NC effects, let us start from the fundamentals. For a capacitor based on linear dielectrics (i.e. metal-insulator-metal or MIM configuration), its capacitance (C) is a measure of how much static charge (Q) it can store when a voltage (V) is applied between the metal electrodes and is defined as $C=Q/V$. From there, the stored electrical energy in a capacitor can be obtained as $U=Q^2/(2C)$. To be electrostatically and thermodynamically stable, the capacitance of a system is required to be positive. To understand this, let us hypothetically consider a system exhibiting negative capacitance. In this case, the energy of the system can be represented as the $U = - Q^2/(2|C|)$. This implies that an increase in Q would lead to a decrease in its energy. If such a capacitor is short-circuited, then it would keep building charges spontaneously in the metal plates to minimize its energy. This implies that the system can change its internal energy without any external work, which is a violation of the first law of thermodynamics. Therefore, the electrostatic capacitance of a system must be a positive quantity to ensure thermodynamic stability.

In a more general scenario, when the capacitor is non-linear, the definition of the differential capacitance (C) is more appropriate, which relates the differential change in Q (dQ) with respect to the differential change in V (dV) as C=dQ/dV. While having a stable negative capacitance (dQ/dV<0) of the system is not physical, an unstable negative capacitance region is indeed theoretically possible if that region is bounded by a positive capacitance (dQ/dV>0) region. Hence, it is no surprise that the appearance of spontaneous charge (or polarization) in the ferroelectric material contains the signature of an unstable negative capacitance region, while the finiteness of the spontaneous charges signifies a positive capacitance region. Based on a similar rationale, the possibility of capacitance being negative for ferroelectric (FE) materials was first anticipated by R. Landauer in 1976 [1].

While the requirement that the capacitance must be positive for any system as a whole is universal, the capacitance of a *part* of the system being negative does not immediately violate any physical laws. In 2000, A. M. Bratkovsky and A. P. Levanuuk theoretically predicted that the effective capacitance of a multi-domain FE can be negative in the presence of the interfacial dead layer [4]. In this pioneering work, they show that, while the total capacitance of the system (FE layer + dead layer) remains positive, the domain-wall displacement leads to an effective negative capacitance in the FE layer [4]. Later on, in 2006, the same authors experimentally demonstrated this effect for a BTO/SRO/STO system by subtracting the estimated potential drop across the dead layer and revealing the 'real' hysteresis loop in the FE layer signifying the presence of effective negative capacitance (NC) [5].

In 2008, S. Salahuddin and S. Datta proposed an intriguing concept for overcoming the fundamental limit in the sub-threshold swing of a conventional transistor [7]. They suggested that the presence of a negative capacitor in the gate stack of a transistor can provide an amplified internal potential, which can potentially lead to a lower than 60mV/decade sub-threshold swing in the transistor characteristics at room temperature. In addition, the authors envisioned the utilization of the FE layer as the possible source of NC and proposed the 'capacitance matching' theory for obtaining a hysteresis-free operation with maximum amplification of the internal potential [7].

While the NC effect in FE and its potential application in designing steep switching transistors (NCFETs) looked intriguing, the thrust in this area took a major surge with the discovery of ferroelectricity in HfO_2-based materials [29]-[32], which are highly CMOS compatible (compared to conventional perovskite FE). This not only led to the possibilities of practical realization of steep-slope transistors [33]-[39] but has also ushered in the proposal for other FE based devices that utilize the intricate polarization switching dynamics [40] of the FE materials for memory [41]-[42] and non-Boolean applications [43]-[46]. Interestingly, the underlying physics of the NC effect is strongly correlated with the fundamental mechanism of polarization switching in the ferroelectrics. Hence, the NC phenomenon has sparked an immense interest leading to a large body of work aimed to understand the NC effects in FE based devices and its dependence on the material and device parameters.

In this subsequent sections, we provide an overview of the current theoretical understanding of the possible origins of NC effects in ferroelectrics and present a perspective on the strengths and limitations of various explanations. We also discuss the relevant experimental works and provide an outlook for what is needed to further understand these intriguing phenomena.

3.3 Fundamentals of Ferroelectric Capacitor

Microscopically, the ferroelectricity originates from the non-centrosymmetric crystal structure where the spontaneous displacement of atoms (and the corresponding electron gas and ion core) leads to a non-zero spontaneous polarization (P). Therefore, the total spontaneous P in a FE material should be considered as the combination of ionic and electronic polarization. In the simplest scenario, where the spontaneous displacement of atoms is uniaxial (uniaxial FE), the consideration of crystal symmetry provides two possible spontaneous P states depending on the direction of atomic displacement (Fig. 3.1(a-b)). Let us assume that the direction of spontaneous displacement is the ±z-axis (P_Z=P) and the corresponding P states are -P and +P (Fig. 3.1(a-b)). These -P and +P states correspond to the minimum of the free energy of a FE unit cell (Fig. 3.1(c)). Now, the bi-stability in spontaneous P and the corresponding two minima in its free energy leads to the formation of a double-well-shaped free energy landscape (Fig. 3.1(c)), which can be represented as Landau's free energy equation (eqn. 3.1) as shown below.

$$f_{free} = \frac{1}{2}\alpha P^2 + \frac{1}{4}\beta P^4 + \frac{1}{6}\gamma P^6 \qquad (3.1)$$

Here, α, β, and γ are Landau coefficients, where, α is negative and γ must be positive. Such a double-well energy landscape suggests that any reduction in P magnitude from its spontaneous value should lead to an increase in free energy, where P=0 corresponds to the energy maxima (Fig. 3.1(c)). Here, the P=0 state corresponds to a zero atomic displacement along the z-axis, however, may or may not have a finite displacement along the in-plane directions (Fig. 3.1(d-f)). It is important to note that, even though the Landau free energy polynomial was originally proposed for a macroscopic polarization, such representation holds true even for a microscopic scenario (i.e. single FE unit cell) as shown in several first-principle studies [47]-[48]. In addition to the free energy, the presence of an out-of-plane electric field (*E*) in the FE layer also leads to an energy component called electrostatic energy. The electrostatic energy density (f_{elec}) can be written as, $f_{elec} = -E.P$. Further, the presence of spatial variation in P also leads to an additional energy component, known as gradient energy. This is because, the magnitude of P in each FE unit cell is correlated to its strain and thus, the spatial variation in P (dP/dx, dP/dy and dP/dz) leads to another energy component that depends on the elastic coupling between the unit cells. This gradient energy density (f_{grad}) can be written as the following equation (eqn. 3.2).

$$f_{grad} = g_{11}(\partial \mathrm{P}/\,\partial \mathrm{x})^2 + g_{11}(\partial \mathrm{P}/\,\partial \mathrm{y})^2 + g_{44}(\partial \mathrm{P}/\,\partial \mathrm{z})^2 \qquad (3.2)$$

Therefore, the total energy density (f_{total}) in an FE layer can be written as[26-27],

$$f_{total} = f_{free} + f_{elec} + f_{grad} = \frac{1}{2}\alpha P^2 + \frac{1}{4}\beta P^4 + \frac{1}{6}\gamma P^6 - E.P + g_z\left(\frac{\partial \mathrm{P}}{\partial \mathrm{z}}\right)^2 + g_x\left(\frac{\partial \mathrm{P}}{\partial \mathrm{x}}\right)^2 + g_y\left(\frac{\partial \mathrm{P}}{\partial \mathrm{y}}\right)^2 \qquad (3.3)$$

Here, g_i is the gradient coefficients along the i = x, y and z directions. Now, according to Landau-Ginzburg-Devonshire (LGD) theory, the time (t) dependent Ginzburg Landau (TDGL) equation (in Euler-Lagrange form) can be written as [26]-[27],

$$E - \frac{1}{\Gamma} \times \frac{\partial P(r)}{\partial t} = \alpha P(r) + \beta P(r)^3 + \gamma P(r)^5 - g_{11}\frac{\partial^2 P(r)}{\partial z^2} - g_{44}\frac{\partial^2 P(r)}{\partial x^2} - g_{44}\frac{\partial^2 P(r)}{\partial y^2} \quad (3.4)$$

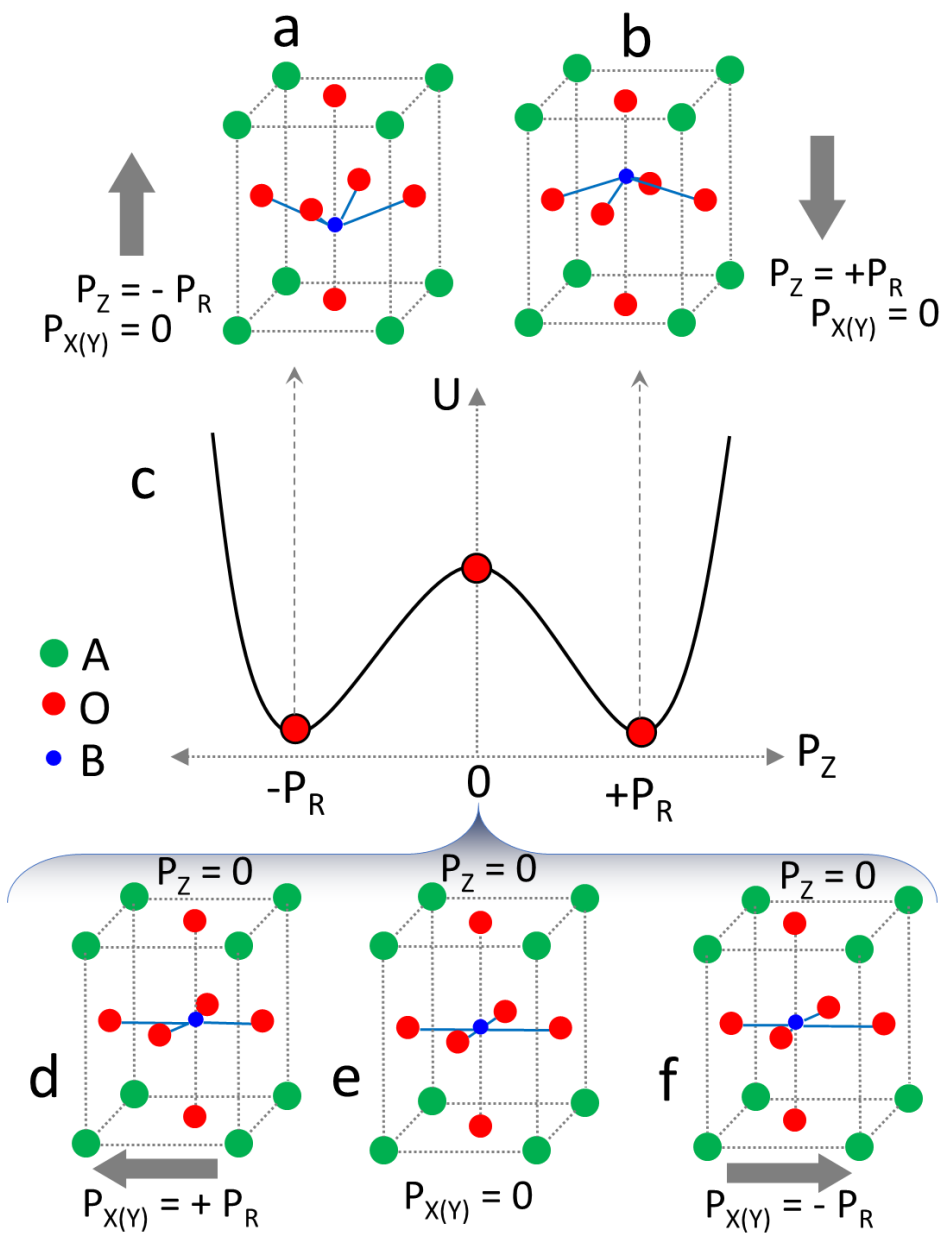

Figure 3.1. Ferroelectric ABO_3 tetragonal unit cells (i.e. $PbTiO_3$) showing spontaneous atomic displacement that correspond to (a) up polarization ($P = P_Z = -P_R$) and down polarization ($P = P_Z = + P_R$). Free energy ($U=\int f_{free} dV$) landscape with respect to polarization (P). (d-f) Different atomic configurations in a tetragonal unit cell that corresponds to $P_Z = 0$.

Here, Γ is the viscosity coefficient and $r \equiv (x, y, z)$. Note that, eqn. 4 is derived for a uniaxial FE, in which the P direction is restricted only along the z-axis. However, if the FE is multi-axial so that the P can be directed in all the x, y and z directions, then all the P components (as vectors) along with their cross-coupled terms is required to be considered. While such considerations are indeed required for multi-axial FE, to keep the discussion of this paper uncomplicated, we only consider uniaxial FE. In addition, the FE properties also depend on the mechanical strain in the film. If such strain is homogenous along the film thickness, then the strain contribution can be incorporated within the Landau coefficients. We embraced such assumptions and thus the Landau coefficients in eqn. 3.4 are strain-dependent.

Further, it is important to note that the total interface charge density, Q (or out-of-plane displacement field, D) of the FE layer incorporates both the contribution from spontaneous P as well as the background out-of-plane linear permittivity ($\epsilon_{r,z}$). Therefore, $Q = \epsilon_0 \epsilon_z^{FE} E + P(E)$. At the same time, the presence of P variation causes the long-range Coulomb interaction leading to the in-plane electric fields in the FE layer. The associated energy with the in-plane electric field further depends on the in-plane background permittivity (ϵ_x^{FE} and ϵ_y^{FE}). Therefore, to account for the associated energy with in-plane and out-of-plane electric fields in the background permittivity of the FE layer, eqn. 3.4 is needed to be solved self-consistently with Poisson's equation (eqn. 3.5) as shown below.

$$-\epsilon_0 \left[\frac{\partial}{\partial x}\left(\epsilon_x^{FE} \frac{\partial \phi(r)}{\partial x} \right) + \frac{\partial}{\partial y}\left(\epsilon_y^{FE} \frac{\partial \phi(r)}{\partial x} \right) + \frac{\partial}{\partial z}\left(\epsilon_z \frac{\partial \phi(r)}{\partial z} \right) \right] = \frac{\partial P(r)}{\partial z} \qquad (3.5)$$

It is important to note that the P direction in FE can be altered (between -P and +P) by applying an electric field higher than the coercive field ($\pm E_C$). In this paper, we refer to such a change in the P direction as P switching. However, an applied electric field, less than the P switching field, can also change the P magnitude (without changing its direction), and we use the term 'magnitude response' to refer to this aspect. Now, based on these discussed set of equation (eqn. 3.1-3.5), let us discuss the possible mechanism of achieving NC effects in FE materials.

3.4 Quasi-Static Negative Capacitance in Ferroelectric Heterostructures:

To stabilize a negative capacitor, a positive capacitor is required to be connected in series, so that the total capacitance of the system remains positive. To explain this, let us consider a heterogenous capacitive system comprising of a linear dielectric (DE) layer and an FE layer sandwiched between two metal electrodes. Such a system is also called metal-ferroelectric-insulator-metal (MFIM) stack (Fig. 3.2(a)). Let us assume the individual (or separately measured) capacitance of the DE and FE layer are C_{DE} and C_{FE}, respectively. If these individual capacitances remain unchanged in the MFIM stack, then the total capacitance of this system can be calculated as $1/(1/C_{DE}+1/C_{FE})$. However, if the *effective* capacitance of the FE layer ($C_{FE,EFF} < 0$) is negative then the actual (measured) capacitance of the system, $C_{FE\text{-}DE} > 1/(1/C_{DE}+1/C_{FE})$, as well as $C_{FE\text{-}DE} > C_{DE}$. Such an effect is known as capacitance enhancement effect[7] and can be regarded as the signature of the negative capacitance (NC) effect of the FE layer. On the other hand, if $C_{FE\text{-}DE} > 1/(1/C_{DE}+1/C_{FE})$, but $C_{FE\text{-}DE} < C_{DE}$, that would imply the effective capacitance of the FE layer is higher than its standalone value ($C_{FE,EFF} > C_{FE}$) but not negative. Therefore, depending on the extent of enhancement, $C_{FE\text{-}DE} > 1/(1/C_{DE}+1/C_{FE})$ can be observed either (1) due to an enhanced effective FE capacitance ($C_{FE,EFF} > C_{FE}$) , or (2) due to the negative effective FE capacitance ($C_{FE,EFF} < 0$). While the latter effect is the so-called NC effect in FE, the former effect can also play an important role in FE based device operation (discussed later), and sometimes can be confused with the NC effect, if not analyzed properly.

Now, let us discuss the NC effect in FE in an MFIM stack. Depending on whether the FE layer is in a single-domain (SD) state or multi-domain (MD) state, the implication of the NC effect and the corresponding conditions to stabilize them are quite distinct. Therefore, in the next subsection, we first discuss the stabilization of the NC effect in SD FE.

3.4.1 Negative Capacitance Effect in Single-Domain FE:

To impose the condition that the FE layer is in a single-domain (SD) state, let us assume that the gradient energy coefficient is infinite ($g_{11}=g_{44}\rightarrow \infty$). That implies a non-zero spatial variation in P would lead to infinite gradient energy. Therefore, to minimize the energy, the P in the FE layer is restricted to be homogeneous ($dP/dx=dP/dz=dP/dz=0$). In this hypothetical SD FE, the average

polarization in FE is equal to its microscopic P and the free energy (U) landscape is as same as the microscopic free energy landscape (f_{free}) with respect to P. Similarly, by imposing dP/dx=dP/dz=dP/dz=0 is eqn. 4, the P versus E relation can be written as, E - (1/Γ) (∂P/∂t) = $\alpha P + \beta P^3 + \gamma P^5$.

Now, considering a static scenario (dP/dt=0), one can immediately see the presence of a region in its P-E characteristics that exhibit $dP/dV_{FE}<0$ as well as $dQ/dV_{FE}<0$ region (see Fig. 3.2(b)). Such NC region (sometimes, referred to as the intrinsic negative capacitance region of FE [7], [12]) is indeed unstable in a standalone MFM capacitor and therefore the corresponding charge response would be hysteretic. However, the NC region can potentially be stabilized in an MFIM stack (Fig. 3.2(a)). The Q versus applied voltage (V_A) response of such MFIM stack can be understood from the load line picture (shown in Fig. 3.2(c)) by considering the Q-V_{FE} response of an FE layer with a thickness of T_{FE} and Q-V_{DE} response of the DE layer. That suggests, if C_{DE} > min-$|dQ/dV_{FE}|\times T_{FE}$, then the NC region is unstable, and the corresponding Q-V_A characteristics of the MFIM stack exhibits hysteresis (Fig. 3.2(d)). However, the NC region can, in principle, be stabilized, if the DE capacitance C_{DE} < min-$|dQ/dV_{FE}|\times T_{FE}$, and for that the corresponding Q-V_A characteristics become non-hysteretic [7] (Fig. 3.2(g-i)). In this case, the total capacitance of the MFIM stack, $C_{FE\text{-}DE}$ > C_{DE} since $C_{FE,EFF}$ < 0 (Fig. 3.2(j)). Consequently, the differential change in FE-DE interface potential (V_{INT}) with respect to applied voltage (V_A) shows an amplified characteristic, $dV_{int}/dV_A = [1+C_{FE,EFF}/C_{DE}]^{-1} > 1$ (Fig. 3.2(k)).

Now, to get a physical perspective of this phenomena, let us consider the implication of depolarization electric field in FE. In an FE material with finite thickness, the spontaneous P induced bound charge appears at its interface. If these bound charges are not compensated, then it should exert an electric-field which is opposite to the direction of P and hence called depolarization field. Such depolarization field causes an increase in electrostatic energy in the FE layer called depolarization energy. However, in a metal-FE-metal (MFM) configuration with ideal metal electrodes, the metal can provide the compensating charge for the spontaneous P induced bound charge without any additional energy. Therefore, in an ideal scenario, the spontaneous P state (that corresponds to the minimum of the free energy) is stabilized in an MFM configuration and the P

switching are hysteretic. However, in the MFIM stack, due to the presence of the DE layer in between the FE and metal layer, the P-induced bound charge cannot be compensated immediately at its interface. Rather, the bound charge will produce an electric field in the DE layer and that electric field will eventually get compensated in the metal-DE interface. However, the electric field in the DE layer gives rise to a potential drop across the DE thickness. Considering the short-circuited scenario (or applied voltage, V_A=0V), an equal and opposite potential should appear across the FE thickness ($V_{FE} = -V_{DE}$) and that will lead to a depolarization field in the FE layer. In such a scenario, the depolarization field will lead to non-zero depolarization energy (-E.P). That would further lead to a reduction in the P magnitude leading to an increase in free energy and a decrease in depolarization energy so that the total energy of the system is minimized. In short, in the SD scenario, the depolarization field leads to an increase in free energy by homogeneously reducing the P magnitude (Fig. 3.2(c)). However, if the DE layer is sufficiently thick (small C_{DE}), the depolarization field can be so high that the system prefers to climb the entire free energy barrier, fully suppressing the spontaneous P (P=0). In this scenario, the minimum energy configuration of the system is obtained by maximizing the free energy of the FE layer so that the depolarization energy of the FE and electrostatic energy of the DE layers is minimized. Therefore, at V_A = 0 V, Q = 0 (as P = 0), V_{FE} = 0 (zero depolarization energy in FE) and V_{DE} = 0 (zero electrostatic energy in the DE). In other words, a significant amount of energy remains stored in the FE layer for obtaining the minimum energy configuration of the system.

Now, if a non-zero voltage is applied across the MFIM stack ($|V_A|>0$), it should lead to an increase in the charge density (Q) of the metal plates as well as the P magnitude of the FE layer. This results in a positive capacitance of the whole stack ($dQ/dV_A>0$) as well as the positive susceptibility of the FE layer with respect to the external voltage ($dP/dV_A>0$). Interestingly, an increase in P magnitude (from P = 0) implies a decrease in its free energy because of the double-well shaped free energy landscape of FE (Fig. 2(g)). At the same time, the depolarization energy (-E.P) increases. However, within a certain region, the decrease in free energy is more compared to the increase in depolarization energy and thus, the total FE energy decreases with the increase in P magnitude. Therefore, the total energy in the DE layer is equal to the energy supplied by the external voltage source plus the decreased energy in the FE layer. In other words, the transfer of the energy from the FE layer to the DE layer leads to enhanced energy of the DE beyond the energy

supplied from the source. As a result, for the same V_A, the DE layer in MFIM can experience a higher displacement field compared to the situation when it is a stand-alone entity. A higher displacement field in the DE layer translates to a higher V_{DE} ($>V_A$) and that further leads to the differential amplification of V_{INT} ($dV_{INT}/dV_A > 1$). Similarly, the charge response (dQ/dV_A), which is the capacitance of the whole stack, increases beyond the value of the capacitance of the DE layer ($C_{FE\text{-}DE} > C_{DE}$). Such capacitance enhancement as well as the amplification of V_{INT}, which are the features of NC effect in FE, should take place within a specific operational region within which $d^2U/dQ^2 < 0$, so that total FE energy can decrease (decrease in free energy dominates over the increase in depolarization energy) with the change in Q.

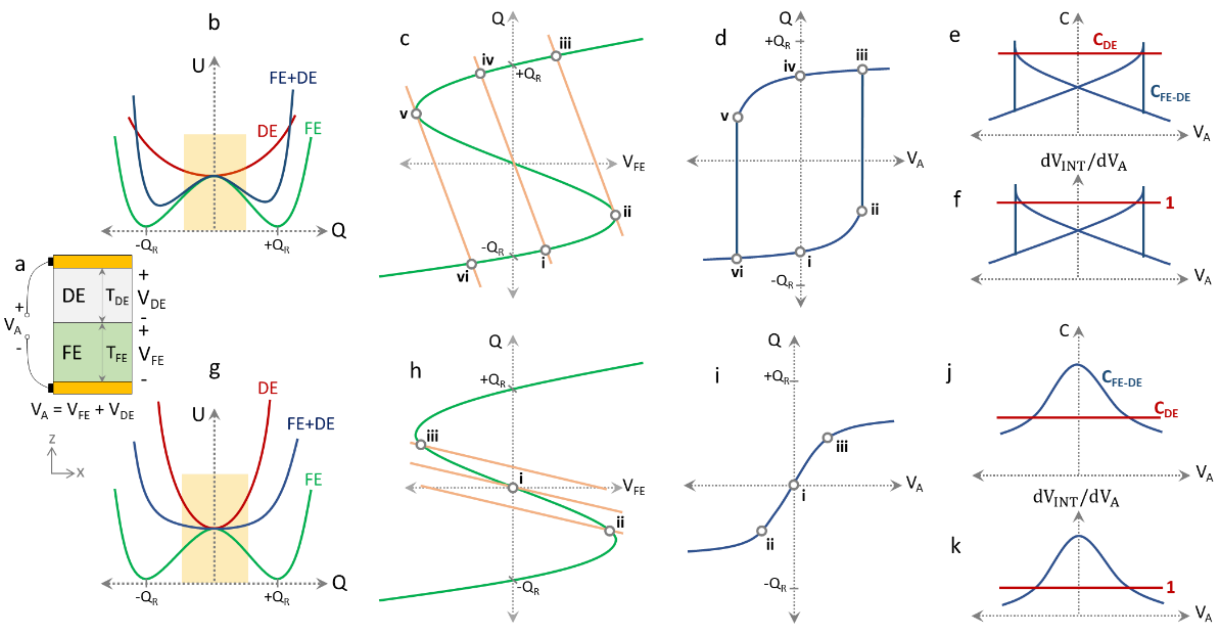

Figure 3.2. (a) Metal-ferroelectric-dielectric-metal (MFIM) or ferroelectric (FE) – dielectric (DE) stack. Here, the FE layer is assumed to be in a single-domain state. Considering a low DE thickness ($C_{DE} > \text{min-}|dQ/dV_{FE}|\times T_{FE}$) (b) Energy landscape of FE, DE and FE-DE stack, corresponding (c) Q-V_{FE} and load-line conditions, (d) Q-V_A characteristics, (e) C-V_A characteristics and (f) dV_{INT}/dV_A characteristics. Considering a higher DE thickness ($C_{DE} < \text{min-}|dQ/dV_{FE}|\times T_{FE}$) (g) Energy landscape of FE, DE and FE-DE stack, corresponding (h) Q-V_{FE} and load-line conditions, (i) Q-V_A characteristics, (j) C-V_A characteristics and (k) dV_{INT}/dV_A characteristics.

Now, the condition for non-hysteretic operation can be understood from the perspective of the transfer of energy between FE and DE. For hysteresis free operation, this energy transfer is required to be adiabatic. Such condition is satisfied, if for a differential change in Q (dQ), the decrease in FE energy (dU) is less than the required energy of the DE layer to induce a similar charge. The differential change in energy of a capacitor can be written as, $dU = Q\times (1/C)\times dQ$. From that, we can obtain the condition for obtaining non-hysteretic and quasi-static NC effect for FE in an MFIM stack to be $1/|C_{FE,EFF}| < 1/C_{DE}$ or $C_{DE} < |C_{FE\text{-}EFF}|$.

So far, our discussion was based on the assumption that the polarization in the FE layer is homogenous across its thickness and area. However, in reality, the polarization can spatially vary both along with its thickness and in-plane directions because the gradient energy coefficient is indeed finite. Moreover, in the presence of the depolarization field, the formation of a multi-domain state in the FE layer is a likely possibility [2]-[5], [49], [50] and such a multi-domain structure has a very important implication from the perspective of negative capacitance [2]-[5]. To analyze that, next, we discuss the multi-domain formation in the MFIM stack and the corresponding NC effect in the multi-domain FE layer.

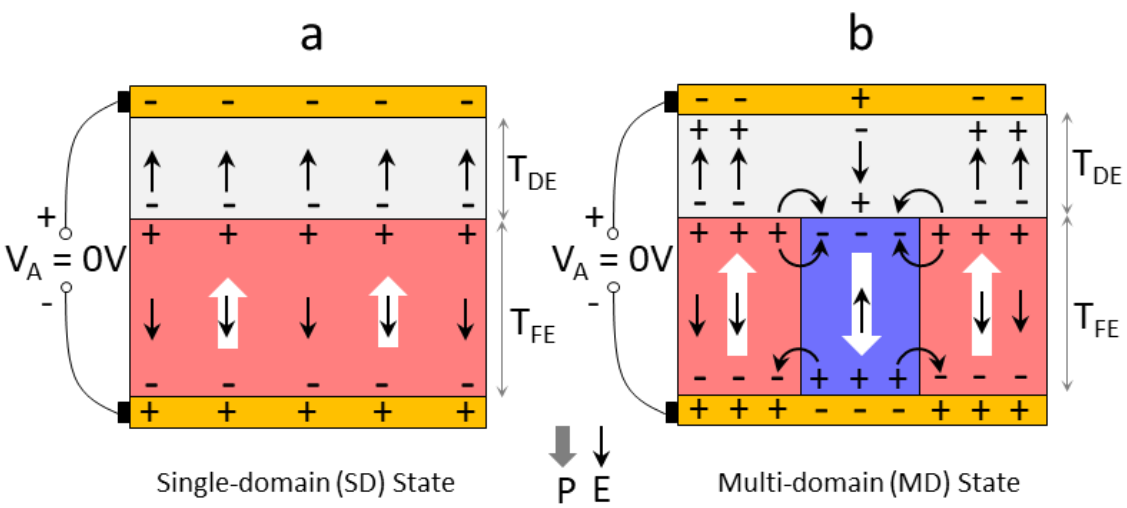

Figure 3.3. MFIM stack with the FE layer in (a) single-domain (SD) state and (b) multi-domain (MD) state. In SD state, minimum energy is obtained at cost of a significant increase in free energy by suppressing the local P magnitude. In MD state, minimum energy is obtained in a cost of domain-wall (DW) energy where the average P decrease rather than local P.

3.4.2 Negative Capacitance Effect in Multi-Domain FE:

Recall that in MFIM stack with single-domain FE, the partial compensation of depolarization energy takes place by reducing the P magnitude and thus at the cost of the free energy (Fig. 3.3(a)). However, for finite gradient energy coefficient (g), the ferroelectric has one more option to decrease the overall energy i.e. break into multiple domains with opposite P directions. Indeed, in such a multi-domain (MD) state of the ferroelectric, the depolarization energy, as well as the increase in free energy, can be significantly suppressed (Fig. 3.3(b)). In this scenario, the P-induced bound charges at the FE-DE interface not only give rise to out-of-plane electric fields but also produce in-plane electric fields, called stray fields (Fig. 3.3(b)). As the bound charges are partially getting compensated by the interfacial stray-field, it further reduces the constraint for the out-of-plane electric field in the FE and DE layer, leading to a lower depolarization field compared to the single-domain state. Consequently, this reduces the requirement for the increase of the local P magnitude which reduces the free energy compared to the single-domain state. In other words, the MD state can suppress depolarization energy as well as free energy.

However, this suppression of free energy and depolarization energy takes place at the cost of some additional energy associated with the formation of domain-wall (the boundary between the domains with opposite P directions). One component of domain-wall (DW) energy is the electrostatic energy associated with the interfacial stray field and the other component is the gradient energy linked with the variation in P at the DW. As the formation of the MD state occurs as an interplay among competing energy components to obtain the minimum energy of the whole system, it is no wonder that the configuration of the MD state is strongly dependent on the DW energy. In [27], it has been shown that, depending on the DW energy, the types of DW can be either ‘hard’ or ‘soft’. Here, the term ‘hard’ implies that the change in P direction is abrupt at the DW and thus the physical thickness of the DW is atomically thin (Fig. 3.4 (b-c)). In contrast, in ‘soft’ DW, the change in P direction takes place by gradually changing its magnitude over the length scale of several unit cells (Fig. 3.4(d-e)). In an FE with a certain thickness, the DW can be hard for small ‘g’ and soft for a larger ‘g’. The nature of the DW (hard or soft) plays an important role in the P switching characteristics of the FE layer. Before going to the discussion of P switching, it is noteworthy that in MD state, Q, U, V_{FE} and V_{DE} represent the average quantities. This is

because of the spatial varying P in MD state, which further leads to non-homogeneous potential, electric-field and energy density profiles in the FE and DE layer.

Note that the DW energy (total of this gradient energy and the electrostatic energy) gives rise to higher local energy near the DW compared to the rest of the film. In hard-DW, this local DW energy density is lower than the maximum of the free energy barrier. Interestingly, in the MD state with hard-DW, Q = 0 state can be obtained with multiple equal size domains with opposite P directions. Consequently, the average energy density (U) increases (due to the DW energy), but remains significantly lower compared to the SD scenario (Fig. 3.5 (a)). This is because in the SD state, Q = 0 can only be achieved by maximizing the free energy (local P=0). While in MD state, the P is not required to be locally zero and can eventually remain close to its spontaneous value for which free energy is low.

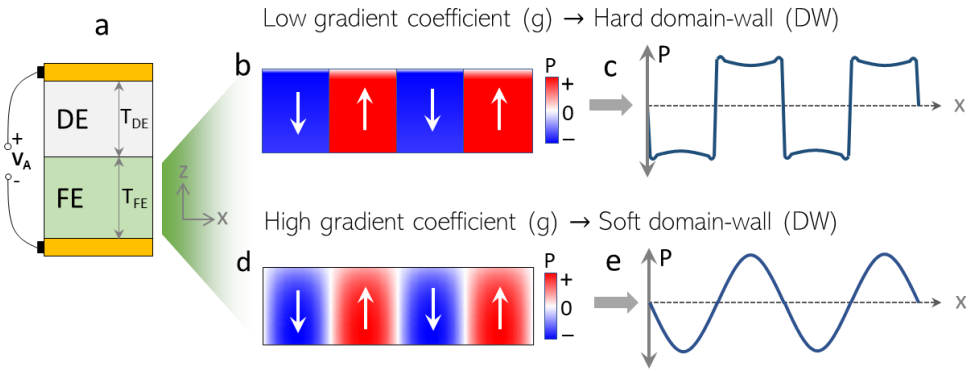

Figure 3.4. (a) MFIM stack. (b) Multi-domain polarization configuration (b) with hard-DW where (c) the change in P direction occurs abruptly and (d) with soft-DW where (e) the change in P direction takes place with a gradual change in P magnitude.

Further, within the limit of MD state with hard-DW, Q = 0 can be obtained with different domain periods (Fig. 5(a)). As the average energy density (U) depends on the DW energy which further depends on the number on DWs, the maximum U that corresponds to Q = 0 is not unique (Fig. 3.5(a)). Moreover, the domain period even depends on the physical thickness of the DE layer (i.e. the domain pattern becomes denser with the increase in DE and decrease in FE thickness). As a result, the average energy landscape (U-Q) of MD FE with hard-DW in the MFIM stack is not unique (Fig. 3.5(a)), which is a very distinct feature of the MD state compared to the SD state.

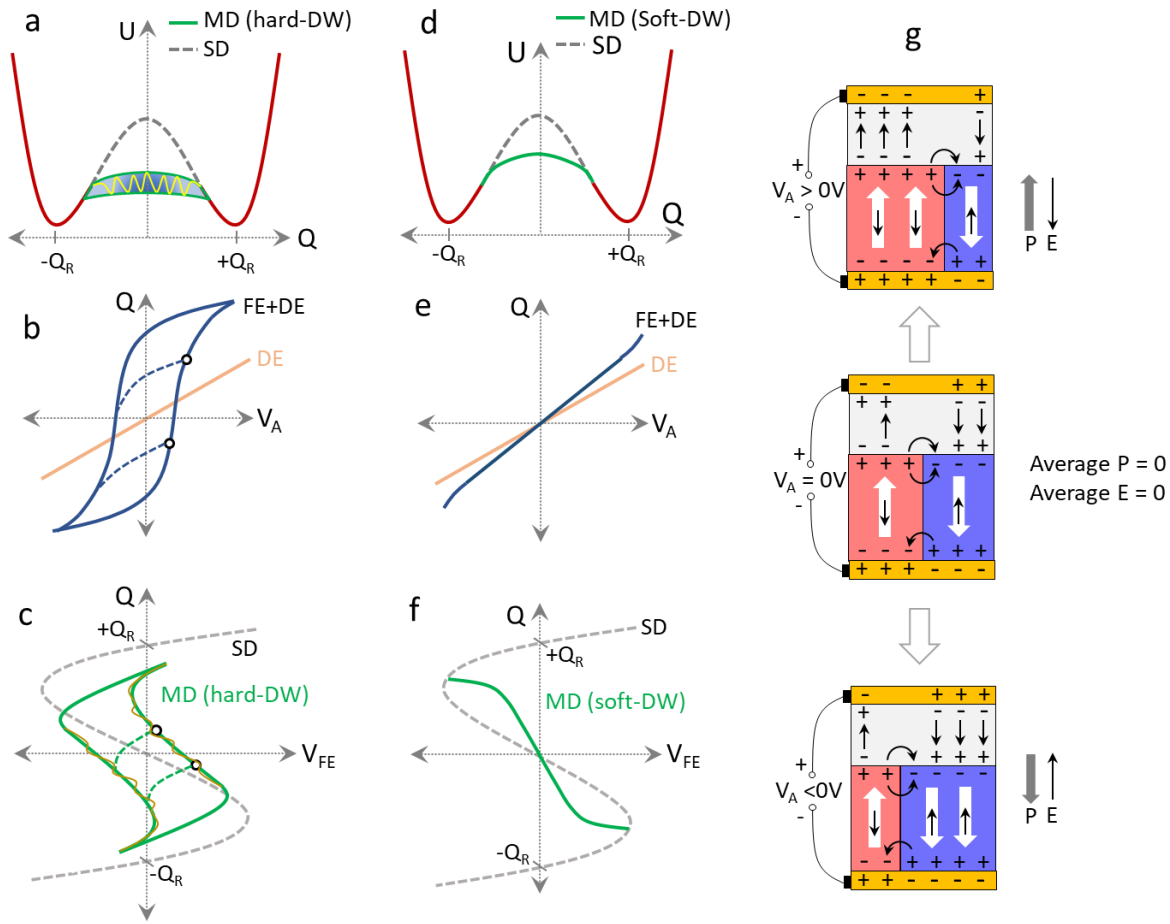

Figure 3.5. Considering multi-domain FE with hard-DW (low DW energy) in MFIM stack: (a) energy landscape of FE where the shaded regions signify the possibilities of different multi-domain configurations with different average energy (U) for the same average charge density (Q) where U=(1/A)$\int (f_{free} + f_{grad})dV$ and A is the in-plane surface area of the FE film. The yellow line displays the presence of local minima and barriers associated with hard-DW displacement for achieving different average Q. Corresponding (b) Q-V_A characteristics and (c) Q-V_{FE} characteristics for a certain FE and DE thickness signifying partial polarization switching (minor loops – as different MD states with different Q can be stabilized at the same V_A) and hysteretic NC effect in FE. Here the zigzag nature of the P switching path corresponds to the yellow line in (a). Considering multi-domain FE with soft-DW (high DW energy) in MFIM stack: (a) energy landscape of FE which is unique for a certain FE thickness signifying a unique MD configuration. Corresponding (b) Q-V_A characteristics and Q-V_{FE} characteristics display non-hysteretic NC behavior. (g) Polarization and electric field profile in MFIM stack for different V_A illustrating a generic scenario of DW displacement base P switching in FE and the macroscopic mechanism of NC effect as an outcome of increasing average P with an increasing depolarization field (opposite to the P direction).

Since the local DW energy density in hard-DW is lower than the maximum of the free energy barrier, therefore, an additional energy is required to initiate the DW displacement. In other words, to obtain P-switching for DW displacement, a voltage greater than a critical voltage must be applied to surpass the free energy barrier. As a result, the P-switching characteristics in MD FE with hard-DW displacement is hysteretic (Fig. 3.5(b)). This implies that once the DW is displaced due to a certain V_A larger than a positive critical value, a reverse DW displacement will not occur just by reducing the V_A to zero. For that, the V_A is required to be lower than another negative critical value. Further, the DW displacement takes place in a discrete fashion (lattice by lattice) and each of these displacements corresponds to the overcoming of a local energy barrier. Such local barriers, as well as local minima, manifest in the average energy landscape of FE (Fig. 3.5(a)-yellow line). Note that, different MD configurations with different average Q states corresponding to these local minimums can be stabilized at $V_A = 0V$. Therefore, Q-V_A characteristics with hard-DW scenario are hysteretic and show a signature of partial P switching with different remanent charges (Fig. 3.5(b)).

Now let us turn our attention to MD FE with soft-DW. Note that the local DW energy density in the soft-DW is higher compared to the hard-DW due to higher 'g' in the former. In fact, if the nature of DW is substantially soft, the local energy density in the DW becomes comparable to the maximum of the free energy density. In this case, an infinitesimally small differential increase in V_A would lead to the DW displacement. Further, when the V_A returns to zero, the DW displacement would seamlessly take place in the reverse direction and the FE will return to its equilibrium domain configuration. Therefore, the soft-DW displacement leads to adiabatically reversible P-switching. Moreover, the P configuration in MD FE with soft-DW is unique and that leads to a unique average energy landscape (Fig. 3.5(d)). As a result, the P switching as well as the corresponding Q-V_A characteristics are non-hysteretic (Fig. 3.5(e)).

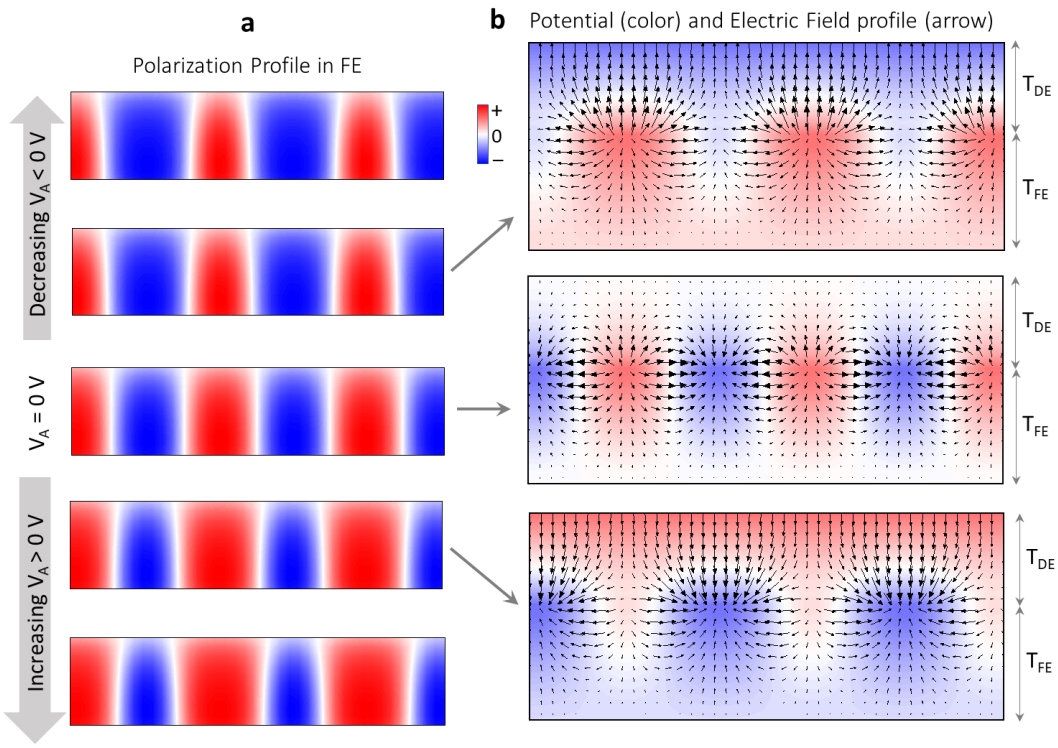

Figure 3.6. Self-consistent simulation results of eqn. 3.4 and eqn. 3.5 for an MFIM stack that includes MD FE with soft-DW. (a) Polarization profile signifying soft-DW displacement-based P switching and corresponding (b) potential profile and electric field profile in the FE and DE layers. The potential profile signifies non-homogeneous interface potential. The electric field profiles display the redistribution of the interfacial stray field due to DW displacement.

It is remarkable that the DW displacement-based P switching in FE leads to an effective NC path in the Q-V_{FE} characteristics in the MFIM stack, irrespective of the type of DW in FE. To understand that, first note that the electric-field in the FE layer is depolarizing due to the presence of the DE layer. This implies that in each of the domains, the local electric field is opposite to its P direction. Macroscopically, the DW displacement causes a change in average polarization which further leads to an increase in the depolarizing field (Fig. 3.5(g)). Such depolarization field dominates the total field in the FE layer. As the increase in average polarization takes place simultaneously with the increase in depolarization field (which is opposite to the polarization direction), the effective capacitance of the FE layer becomes negative [4], [20], [26], [27]. Note that such a description of the FE NC effect does not require the concept of local P to be zero or the local free energy to be maximum. Moreover, the displacement of a hard DW implies a sharp

change in the P direction (due to lattice by lattice P switching). Therefore, the local P switching is not adiabatic and thus observed NC effect in Q-V_{FE} characteristics exhibits hysteresis. However, in the case of soft-DW displacement, the change in local P direction takes place by gradually changing its magnitude. Therefore, the local P switching for soft-DW displacement is adiabatic, which leads to the non-hysteretic NC effect. To get a clearer picture of the NC effect under soft-DW displacement, in addition to the macroscopic features (increasing average P with increasing depolarization field), it is important to capture the microscopic phenomena (Fig. 3.6). Microscopically, the soft-DW displacements (i) redistribute the interfacial stray fields and (ii) decrease the DW energy resulting in a negative net contribution to the total FE energy [23], [27]. This leads to a local effective negative capacitance within the FE layer [13], [23], [25], [27] primarily near the FE-DE interface (due to stray field redistribution, see Fig. 3.6(b)) and the DW (due to decrease in DW energy).

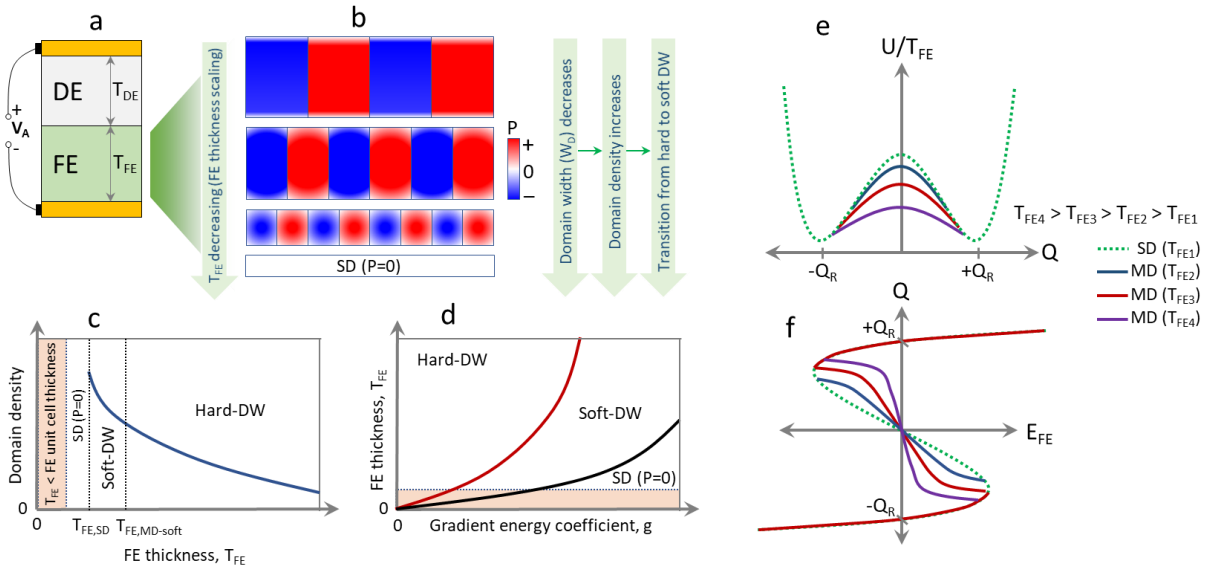

Figure 3.7. (a) MFIM stack, (b) MD polarization configuration signifies that the domain density increases and the type of DW make a transition from hard to soft with the decrease in FE thickness. (c) Dependency between the domain density and FE thickness signifying that stability of (i) MD state with hard-DW for T_{FE}>$T_{FE,MD\text{-}soft}$ (ii) MD state with soft DW for $T_{FE,SD} < T_{FE} < T_{FE,MD\text{-}soft}$ and (iii) SD state for $T_{FE,SD} > T_{FE}$. (d) The conditions for MD states with hard/soft-DW and SD states for different g and T_{FE}. Here, the shaded region corresponds to FE thickness less than a unit cell, which is not physically realizable. (e) The energy density per unit FE thickness (U/T_{FE}) for different T_{FE}. (f) Q-E_{FE} (E_{FE}=V_{FE}/T_{FE}) characteristics for different T_{FE} suggesting that the NC effect enhances with the decrease in FE thickness.

Further, it is important to note that, even though the effective NC path (negative dQ/V_{FE} region) of MD FE with soft-DW is non-hysteretic, it is quite different from the SD NC path (Fig. 3.5(f)). In fact, the MD NC effect is lower compared to SD FE (Fig. 3.5(f)). This is because the average energy in the MD state is lower compared to the SD state (Fig. 5(d)). Thus, the reduction in energy (dU) for the same change in charge density (dQ) will be higher in SD FE compared to MD FE. Therefore, $1/|C_{FE,EFF}^{SD}| > 1/|C_{FE,EFF}^{MD}|$ (Note: a higher NC effect implies a larger $1/|C_{FE,EFF}^{SD}|$). Moreover, it is noteworthy that the MD NC path depends on the permittivity of the DE layer because of the dependency of electrostatic DW energy (due to stray field) on the in-plane permittivity of the DE layer. It has been shown that the FE NC effect enhances for the lower in-plane permittivity of the DE layer. This provides an interesting distinction between the MD NC and SD NC phenomena. However, within the soft-DW limit, the MD NC path should not depend on the physical thickness of the DE layer as long as the DE thickness is sufficient enough to accommodate the interfacial stray fields.

Now, let us discuss the capacitance enhancement effect in the MFIM stack for MD NC. As the NC effect with soft-DW is non-hysteretic, a conventional C-V measurement will inevitably reveal an enhanced capacitance of the MFIM stack compared to its DE counterpart ($C_{FE\text{-}DE} > C_{DE}$). However, due to the involvement of hysteresis associated with the hard-DW displacement, the situation becomes somewhat non-trivial as the NC effect is not seamlessly reversible. In a small signal C-V measurement, if the peak-to-peak value of the applied small-signal voltage (V_{PP}) is not sufficient to surpass the local barrier to induce the DW displacement, then the NC effect may not be observed. However, if the V_{PP} is sufficiently high to induce the DW displacement, then it may be possible to observe NC effect and hence, the C-V measurement should signify $C_{FE\text{-}DE} > C_{DE}$.

Now, recall that the internal potential (V_{INT}) is homogenous for SD FE which exhibits a differential amplification ($dV_{INT}/dV_A>0$) due to the SD NC effect. However, in the case of MD FE, V_{INT} is non-homogenous, and it spatially varies by following the polarization profile in the FE layer [26], [27]. Moreover, V_{INT} exhibits spatially local maxima and minima corresponding to +P and -P domains, respectively. Nevertheless, the MD NC effect provides a differential amplification to the

average V_{INT}, but the extent of amplification is spatially non-homogeneous [27]. This is another important distinction between the SD NC and MD NC effects.

3.4.3 Correlation between FE thickness and NC Effect:

So far, we have discussed the possibilities of different types of NC effect (SD-NC, MD-NC with soft and hard-DW) in FE depending on the value of gradient coefficients signifying the importance of having a higher 'g' for obtaining non-hysteretic NC effect via SD-NC or MD-NC with soft-DW. However, since 'g' is a material parameter, it may be challenging to tune it with device optimization to meet the design requirements. (This needs further investigation, e.g. by analyzing the effect of strain via metal contacts on g, which might provide a design knob to control g, albeit only to a certain extent). Therefore, a relevant question to ask is if the nature of the DWs can be controlled by a device design parameter. To that end, the utilization of an interesting correlation between the physical thickness and the MD state in the FE layer has been proposed in [27]-[28]. According to the Landau-Kittle formula ($W \propto \sqrt{T_{FE}}$) [49]-[50], the domain width (W) in an isolated FE slab (in MD state with 180° DW) is proportional to the square-root of the FE thickness (T_{FE}). Therefore, with the decrease in physical thickness, the domain pattern in the FE layer becomes denser (Fig. 3.7(a-b)). Based on a more extensive simulation for FE-DE stack a similar correlation was obtained in [26]-[28] (Fig. 3.7(c)). With the scaling of FE thickness, as the domain pattern becomes denser, the type of DW makes a transition from hard to soft type [27]-[28] and by scaling T_{FE} further the SD state can potentially be stabilized (Fig. 3.7(b-d)). However, such critical T_{FE} for the (i) hard-DW to soft-DW transition ($T_{FE,MD\text{-}soft}$) and as well as MD state to SD state transition ($T_{FE,SD}$) depends on the value of gradient coefficient (g). In [27], we show that the smaller 'g' leads to a decrease in critical T_{FE} ($T_{FE,SD}$ and $T_{FE,MD\text{-}soft}$) as shown in Fig. 3.7(d). If 'g' is so small that the critical T_{FE} becomes smaller than the thickness of an FE unit cell, then the FE layer may not be physically realizable. Therefore, for obtaining the non-hysteretic NC effect in FE, while FE thickness scaling is the key; however, at the same time, choosing an FE material with a considerably high gradient-coefficient (g) is an important design consideration. We will come back to this aspect in section-6 and section-7.

Provided that 'g' is sufficiently large for achieving the MD state with soft-DW at a physically realizable T_{FE}, there further exists an interesting correlation between the effective permittivity (eff-ϵ_z^{FE} = T_{FE}×(dQ/dV_{FE})) of the FE layer and the FE thickness. In [27], we show that the MD NC effect enhances (1/eff-ϵ_z^{FE} increases) and moves towards the SD NC path with the decrease in T_{FE} (Fig. 3.7(f)). This is because, as the domain density in FE increases with T_{FE} scaling, the contribution of DW energy in the total FE energy increases. Therefore, the energy landscape of MD FE makes a gradual transition towards the energy landscape of SD FE with the decrease in T_{FE} (Fig. 3.7(e)). As a result, the MD NC effect changes towards the SD NC effect with T_{FE} scaling. It is important to note that the DW displacement is essential to obtain the NC effect in MD FE. However, there is another interesting phenomenon specific to hard-DW and in the absence of their displacement, which may be mistaken for non-hysteretic NC effect and therefore, is important to discuss here. This phenomenon occurs if the applied voltage is not sufficient to switch the P direction (so, no DW displacement). In this case, the Q-V_A characteristics reflect the response of background permittivity of FE and the change in P magnitude (but not the direction) to the applied voltage and therefore, are non-hysteretic. At the same time, the effective permittivity of the FE layer shows an enhancement compared to its intrinsic value [28]. However, this permittivity enhancement cannot be due to the NC effect (as no P switching occurs), but rather is an electrostatic-driven phenomenon due to the MD state. In other words, the FE permittivity can enhance in absence of DW displacement but remains positive which we will now discuss.

3.5 Enhanced but Positive Effective Permittivity of FE in MD state:

Let us consider an MFIM stack in which the FE layer is in MD state with hard-DW and applied voltage (V_A) is insignificant to induce a change in P direction (no DW displacement) (Fig. 3.8(b)). In such a scenario, the magnitude response of the local P with respect to the applied electric field and the associated redistribution of in-plane fringing fields in the FE layer (near the DW) is important to consider. In [28], we show that an applied voltage induced change in P magnitude leads to conversion from in-plane to the out-of-plane electric field (Fig. 3.8(b-e)). Such transformation of the electric-field direction leads to an additional charge in the FE-DE interface. In other words, the stored electrostatic energy in the form of an in-plane electric field in MD FE gets transformed to and hence, provides a boost to the energy associated with the out-of-plane

displacement field (Fig. 3.8(b-e)). This leads to an increase in the charges on the metal electrode (those due to initial out-of-plane fields plus those by virtue of the transformed fields) and hence, provides an enhancement in the effective permittivity of the FE layer.

Further, this positive effective permittivity of FE (ϵ_z^{FE}>0) is a function of its physical thickness (Fig. 3.8(g)). This is because, (i) the in-plane stray fields (transformed to the out of plane fields on the application of voltage) and therefore, the associated additional charge at the FE-DE interface, appears near the DW and (ii) the domain density, as well as the DW density, increases with the decrease in FE thickness (as discussed before). Therefore, the density of this additional charge increases with T_{FE} scaling. Consequently, the ϵ_z^{FE} increases with the decrease in T_{FE} (Fig. 3.8(g)). Also, it is noteworthy that this enhancement in the effective permittivity of MD FE [28] is beyond the scope of the previous analytical equations[4,8,26] that capture the contribution of DW displacement. This is because in that formulation the magnitude response of P was neglected and the DW contribution was calculated based on their non-zero displacement. On the contrary, in [28], the enhanced effective permittivity is captured by self-consistently considering the finite magnitude response P along with the T_{FE}-dependent MD configurations.

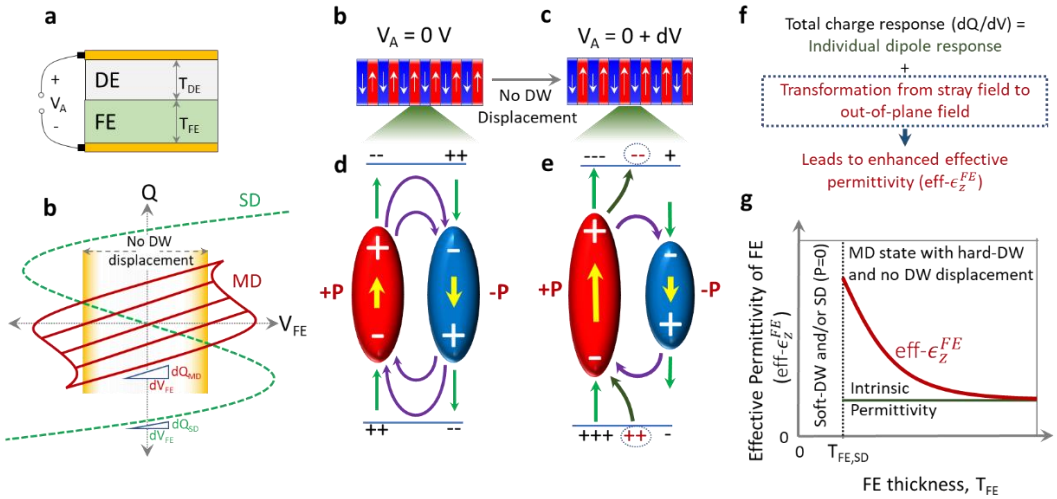

Figure 3.8. (a) MFIM stack. (b) Q-V_{FE} characteristics signifying a region within which no DW displacement takes place and the corresponding effective permittivity is higher than its intrinsic value. (b-d) A two dipole model describing the enhancement in effective permittivity of FE due to the (f) transformation of the in-plane electric field to an out-of-plane electric field component. (g) Dependency between effective FE permittivity and T_{FE}. Note that, if T_{FE} < $T_{FE,SD}$ then the DW becomes soft and thus small differential voltage would lead to DW displacement leading to NC effect and therefore, eff-ϵ_Z^{FE} becomes negative.

So far, we have discussed various possible mechanisms for the quasi-static NC effect where the FE NC region is stabilized in MFIM stack, which further leads to quasi-static enhancement in capacitance. Now, to complete the picture, let us briefly turn our attention to yet another phenomenon which leads to the NC behavior in FE due to the transient effects.

3.6 Transient negative capacitance effect:

The transient NC effect was first demonstrated by Khan et al. in a series-connected network of a resistor (R) and FE capacitor[12] as shown in Fig. 3.9(a). They showed that when a positive voltage pulse was applied in an R-FE network (Fig. x(b)), in the way of charging the FE capacitor (dQ>0), the voltage drop across the FE capacitor decreases ($dV_{FE}<0$) for a short time period (Fig. 3.9(b)). According to the single-domain LK model, the FE capacitor can be modeled as a series-connected constant resistor (R_{FE}) and a capacitor (C_{FE}) (Fig. 3.9(c)), where the C_{FE} exhibit an intrinsic NC region (Fig. 3.9(d)). In ref-12, the authors argued that the observed decreasing FE voltage while charging the FE capacitor ($dQ/dV_{FE}<0$) can be understood as the signature of the intrinsic SD NC path of the FE layer. However, alternate explanations exist in literature[14,17,18]. The work in ref-19 showed that such $dQ/dV_{FE}<0$ can be described by the intrinsic delay associated with the P switching in the FE. In this work, the FE capacitor has been considered as a positive non-linear capacitor ($C_{FE}>0$, which is described by Miller model[19]) connected in series with a resistor ($R_{FE} = \tau/C_{FE}$) that captures the delay (τ) associated with the domain nucleation and their subsequent growth. When the voltage pulse is applied at the R-FE network, the initial C_{FE} is small and R_{FE} is large. Thus, V_{FE} becomes larger than V_{CFE} due to the potential drop across R_{FE} (Fig. 3.9(e)), which can be regarded as 'voltage overshoot'. Near the coercive voltage, when P switching initiates, C_{FE} experiences a substantial increase yielding a large decrease in R_{FE}. As a result, the potential drop across R_{FE} decreases leading to an overall decrease in V_{FE} (Fig. 3.9(e)-snapback). As a result, a larger current is obtained by enhancing the potential drop across the external resistor ($V_R=V_A-V_{FE}$) to support the charging of large C_{FE}. In such a situation, V_{CFE} is still increasing and hence, $C_{FE} = dQ/dV_{CFE} > 0$. Hence, during the charging/discharging of the FE capacitor, a negative dQ/dV_{FE} may appear as an artifact of V_{FE} overshoot and its subsequent snap-back[19]. Further, this paper[19] compares different trends by considering both the SD NC and apparent NC and provides guidelines to reveal the true origin of the transient NC effect. Similarly, the transient NC phenomenon has

been analyzed in ref-14,17 based on the traditional domain switching model of the Kolmogorov–Avrami–Ishibashi (KAI) formalism, which explains the P switching in FE based on the nucleation and growth of reverse domains. According to their analysis[17], the decreasing voltage could be described by the mismatch between the influx of charge flow and its consumption by the reverse domain formation in the FE capacitor.

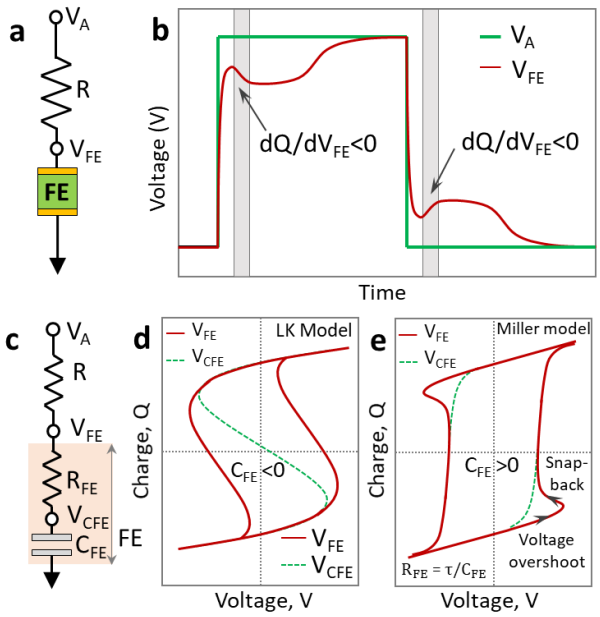

Figure 3.9. (a) Schematic of a series-connected resistor (R) and ferroelectric (FE) capacitor network. (b) Transient response of the voltage across the FE layer (V_{FE}) upon the application of voltage pulses (V_A) across the R-FE network signifying a region with $dQ/dV_{FE} < 0$ in the charging/discharging response of the FE capacitor. Here, $dQ/dV_{FE} < 0$ represents the transient NC effect. (c) Representative schematic model of R-FE network, where the FE capacitor comprises a series-connected resistive element (R_{FE}) and capacitive element (C_{FE}). Q-V_{FE} and Q-V_{CFE} characteristics based on (d) Landau-Khalatnikov model suggesting that the negative dQ/dV_{FE} originates from intrinsically negative C_{FE} and (e) Miller model suggesting that negative dQ/dV_{FE} may originate even with a positive C_{FE}.

It is noteworthy that the quasi-static and transient NC effects, although related, may involve different physical mechanisms and therefore, the observation of one may not directly prove the existence of the other. As the focus of this paper is the quasi-static NC effect (which is directly related to NC-based device applications), we now discuss some of the experimental results on the NC effect and their correlation with the different types of mechanisms we have discussed so far.

3.7 Experimental Evidence of NC Effect:

The capacitance enhancement in FE–DE heterostructures, as a signature of NC effect in FE, has been first demonstrated by Khan et al. using $PbZr_{0.2}Ti_{0.8}O_3$ as the FE and $SrTiO_3$ as the DE layer [9]. Beyond a critical temperature, the authors show that $C_{FE\text{-}DE} > C_{DE}$, which can be considered as an indication of negative effective C_{FE} in the heterostructure [9]. Later, in 2014, W. Gao et al. demonstrated a similar effect [11] in FE-DE superlattice systems with $LaAlO_3$ as the DE material and $Ba_{0.8}Sr_{0.2}TiO_3$ as the FE materials. In both of the works [9], [11], the SD picture of the NC effect has been implicitly adopted to justify the experimentally observed phenomena. However, due to the absence of completely non-hysteretic C-V characteristics, the MD NC with hard-DW displacement can be regarded as a more reasonable mechanism. In 2016, P. Zubko et al. demonstrated a similar capacitance enhancement effect [13] in an FE-DE superlattice ($Pb_{0.5}Sr_{0.5}TiO_3$-$SrRuO_3$) system for a wide range of temperatures and for the first time, such effect has been attributed to the MD NC effects in FE [13]. Further, in 2019, more extensive experimental measurements on $PbTiO_3/SrTiO_3$ superlattice, Yadav et al. mapped out the local effective permittivity of the FE layer signifying the presence of local negative effective permittivity near the FE-DE interface and DW [25]. Therefore, the presence of MD NC in Perovskite FE can be regarded as a well-demonstrated concept. However, further investigation is required to justify whether the DWs are soft or not. To that effect, an experimental demonstration of non-hysteretic Q-V characteristics is yet to be demonstrated.

Recently, the NC effect in fluorite FE has been investigated by Hoffman et al. by considering an FE-DE heterostructure with $Hf_{0.5}Zr_{0.5}O_2$ as the FE and Ta_2O_5 as the DE layers [51]. Based on the applied voltage-pulse modulated charging of the FE-DE stack, the authors traced out an 'S'-shaped Q-V_{FE} characteristics of the FE layer. In this work [51], the author assumed that the depolarization field in the FE layer, which would appear due to the presence of the DE layer, is suppressed because of the presence of polarization compensating trap charges at the FE-DE interface. Based on this assumption, they argued that the FE layer is stabilized in the SD state rather than creating MD states. Therefore, according to the author, the experimentally observed 'S'-shaped Q-V_{FE} characteristics is a direct representation of the SD NC path which was also argued to be non-hysteretic. However, based on the same experimental data, Kittl et al. have shown that the actual

trajectories of these Q-V characteristics exhibit hysteretic characteristics when both charging and discharging paths are considered [52]. As we have already discussed that the hysteretic NC path is a feature of P-switching in MD FE with hard-DW, therefore, the experimental result in [51] is neither a validation of hysteresis free SD NC path, nor a representation of the true nature of the Landau's double-well free-energy landscape in FE HfO_2. While the presence of quasi-static NC effect (with or without hysteresis) is an indication of having a double-well energy landscape, a direct experimental evidence of SD NC effect is yet to be demonstrated.

Further, as both the MD NC with soft-DW and SD NC is expected to be hysteresis free and exhibit similar macroscopic NC attributes, therefore, a direct experimental demonstration of SD NC requires to be focused on their microscopic distinction with MD NC. One of the possible mechanisms could be STEM imaging of the atomic configuration (similar to [25]) in the FE layer to discard the presence of domain-walls or multi-domain states. Such an approach is certainly applicable for perovskite FE material because of their detectable DW [25] either by visualizing the different orientations in atomic displacement in different domains or by identifying the misfit strain near the DW. Note that in perovskites (ABO_3 crystals), both B and O atoms are spontaneously displaced, and the position of B atoms are generally detectable in STEM image. However, for FE HfO_2 where oxygens are the only atoms that are spontaneously displaced, access to similar features is challenging. This is because of the negligible misfit strain near the DW and the very limited detectability of the position of oxygen atoms for their small atomic size. As a result, microscopic evidence of SD NC in HfO_2 needs further experimental investigation. However, such challenges can possibly be overcome by considering the polarization-strain correlation in FE materials. Note the unit cell size of FE HfO_2 can be determined from the STEM image and from there the change in cell size (strain) in response to applied voltage can also be detectable. In FE material, out-of-plain strain (ε_{33}) is proportional to the square of its out-of-plane polarization (P). Therefore, a typical MFM capacitor exhibits a hysteretic butterfly-shaped strain-voltage relationship (Fig. 3.10(b)) by following the hysteretic polarization-voltage characteristics (Fig. 3.10(a)).

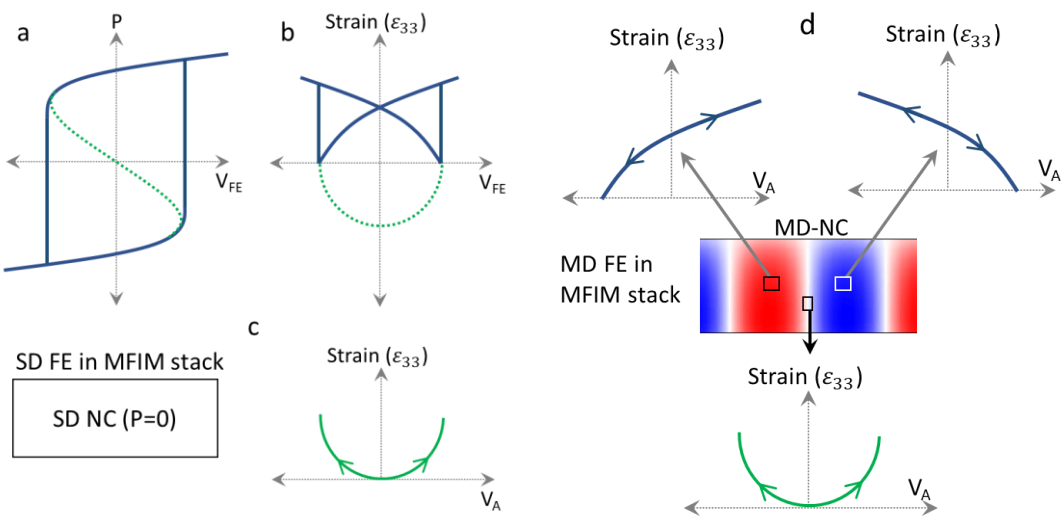

Figure 3.10. (a) polarization versus voltage characteristics of the MFM capacitor showing hysteretic characteristics (blue line). The green line represents the unstable NC region. Corresponding (b) FE strain (ε_{33}) versus applied voltage characteristics of the MFM capacitor (blue line). The U-shaped dashed line corresponds to the S-shaped region in (a), which is unstable in the MFM capacitor. However, if the S-shaped region in P-V_{FE} characteristics is stabilized in MFIM, then the U shaped characteristics can also be obtained for ε_{33}-V_A characteristics. (c) In case of the SD NC effect, such U-shaped strain characteristics can be observed in the entire FE layer. (b) For the MD NC effect, the strain in the domains will follow the different branches of the butterfly curve and the DW will follow the U-shaped curve.

However, if an FE unit cell is stabilized at the P=0 of the S-shaped path (in Fig. 3.10(a)) then the corresponding strain of that FE unit cell would follow the U-shaped curve (in Fig. 3.10(b)). Now, in the MFIM stack, if the FE layer is in the SD NC state then at V_A=0 V, the polarization is stabilized homogeneously at P=0. Therefore, a small change in V_A, irrespective of increase or decrease (from V_A=0), would lead to an increase in strain (due to U shaped FE strain characteristic) homogeneously across the entire FE layer (Fig. 3.10(c)). On the other hand, if the FE layer is in MD state, then the strain characteristic of the +P and -P domains will follow the two different branches of the butterfly curve as shown in Fig. 3.10(d). However, in MD state, the local P=0 can be stabilized at the soft-DW and therefore, the U shape strain characteristics can only be observed at the DW (Fig. 3.10(d)). Therefore, depending on whether the U-shaped strain characteristics are observed throughout or only in a portion of the FE layer in the MFIM stack such an experiment can potentially reveal the true nature of the NC effect.

3.8 Material Perspective of Quasi-static NC effect:

As we have discussed that the stabilization of the NC effect in FE is strongly correlated to its elastic properties, therefore, it will be important to analyze this aspect from the perspective of different types of FE materials (i.e. Perovskites and Fluorite). The elastic coupling between neighboring unit cells can be determined from the dispersion of the polar phonon bands. For $PbTiO_3$, the curvature of these polar phonon bands is quite significant, which suggests a strong elastic coupling among the neighboring unit cells. Such strong elastic coupling further implies a high gradient energy coefficient (g) and thus the DW energy should be significantly large. This holds true for almost all the perovskite FE (i.e. PZT, BFO, etc.). Recall that the high DW energy is favorable for obtaining a non-hysteretic NC effect. Therefore, perovskite FE materials may be suitable for obtaining hysteresis free NC effects (either MD-NC with soft-DW or SD-NC).

In contrast, Lee et al. show that the polar phonon dispersion in fluorite FE (i.e. doped HfO_2) is significantly small [53]. Such a flat phonon band indicates a very low elastic interaction between fluorite unit cells. This is because of the presence of non-polar half-cell between the consecutive polar half-cells. As a result, the gradient coefficient (g) in the fluorite FE is expected to be very low so that the DW energy is negligible. For orthorhombic HfO_2, it was shown that the DW energy is eventually negative [53], which implies an anti-parallel configuration with 180° DW is more stable compared to a parallel configuration. Where this negative DW energy originates because of the (i) energy lowering due to the local compensation of P-induced bound charge and (ii) insignificant DW energy. Considering this negligible DW energy, the MD formation in FE HfO_2 is expected to be more prominent (for suppressing the depolarization field in an FE-DE stack) and even an MD state with domain-width of a unit cell is not unlikely. Similarly, due to this negligible DW energy, achieving soft-DW as well as SD state in FE HfO_2 is not very trivial. Therefore, for hysteresis free NC operation in FE HfO_2, aggressive scaling of the FE thickness is essential. For example, it has been speculated that the MD-NC with soft-DW can be achieved in Zr doped HfO_2 below the physical thickness of 1.5 nm [28].

In short, the perovskite FE materials are more likely to provide quasi-static and hysteresis-free NC effect compared to the fluorite FE materials (i.e. doped HfO_2). On the other hand, from the

perspective of CMOS process compatibility, the fluorite FE is a better choice compared to the perovskite FE. Therefore, material level optimizations, possibly by strain engineering and appropriate dopant selection, are required to harness hysteresis free NC effect in the fluorite FE family. At the same time, exploration of other FE materials (i.e. multi-ferroics, 2D ferroelectrics) featuring high elastic coupling as well as CMOS compatibility can lead to new opportunities for the future possibilities of the FE NC effects in integrated electronic devices.

3.9 Implication of Different NC Mechanisms in FEFETs:

While in this article, we mainly focus on NC phenomena in MFIM stack, evaluating its implication in the gate stack of FEFETs requires a similar analysis for a metal-ferroelectric-insulator-semiconductor (MFIS) stack. Such analysis has been conducted in [27] by considering MD NC with soft-DW. It has been shown that similar to the MFIM stack, the MD NC effect leads to charge and capacitance enhancement as well as internal voltage amplification in the MFIS stack [27]. However, in the MD scenario, the non-homogenous internal potential leads to a significantly non-homogenous potential profile at the semiconductor surface, which is quite distinctive compared to the SD NC effect. A quantitative analysis on the implication of such potential non-homogeneity in the electronic transport of FEFET has not yet been investigated. Nevertheless, to complete the discussion on NC attributes, next, we provide a qualitative perspective on the implication of different mechanisms of NC effect on the FEFET characteristics.

In conventional Metal-Oxide-Semiconductor FET (MOSFET), only a fractional change in applied gate voltage (V_{GS}) appears as the change in semiconductor surface potential (Ψ) due to a voltage drop across the positive gate dielectric capacitance and therefore, $d\Psi/dV_{GS} < 1$. Consequently, in the drain current (I_D) versus gate voltage (V_{GS}) characteristics of MOSFET, the attainable sub-threshold swing ($SS = dV_{GS}/d\log_{10}(I_D)$) is always higher than 60 mV/decade at room temperature (300 K). However, we discussed that the FE layer in the gate stack of FEFET (equivalent to MFIS stack) can act as an effective negative capacitor under certain conditions. Such negative capacitance effects can provide differential amplification of the interface potential ($d\Psi/dV_{GS}>1$), which can potentially lead to steep-slope behavior ($SS < 60$ mV/decade) in the I_D-V_{GS} characteristics of FEFET [7], [18], as predicted by the SD NC effect or as expected from the MD

soft-DW induced NC effect [26]-[27] (see Fig. 3.11(a)). In addition to the steep-slope characteristics, FEFET also exhibits several unique features directly correlated with the NC phenomena in FE. One of such features is negative output conductance (NOC) which is also known as negative differential resistance (NDR) observed in the I_D-V_{DS} characteristics of FEFETs in their ON state [18]. While in conventional MOSFETs, the output conductance is positive, FEFETs can exhibit negative output conductance due to the effective NC effect of the FE layer in the gate stack. A similar effect is negative drain-induced barrier lowering (N-DIBL) [18], which is associated with the drain voltage-dependence of NC effect in the OFF state of the FEFET. To explain these V_{DS} dependent effects, let us first explain the impact of V_{DS} on I_D. An increase in V_{DS} leads to two primary effects: (i) it increases the lateral electric field in the semiconductor channel which tends to increase the I_D and (ii) it alters the source barrier and the electric fields in the gate oxide. The latter effect can also be thought of as capacitive coupling between the drain and gate oxide capacitances. In the case of conventional MOSFETs, the gate oxide capacitance is positive and hence, the increase in V_{DS} leads to an increase in surface potential. In the typical I_D-V_{DS} characteristics, the former effect leads to a linear increase in I_D that saturates at a certain V_{DS}. However, the saturation current ($I_{D,SAT}$) keeps increasing due to the latter effect as the surface potential increases with the increase in V_{DS}. Therefore, the output conductance ($g_{DS} = dI_{D,SAT}/dV_{DS}$) of conventional MOSFET is always a positive quantity. However, in FEFET, if the FE layer acts as an effective negative capacitor, then the increase in V_{DS} can potentially lead to a decrease in average potential at the interface of the ferroelectric and dielectric in the gate stack (V_{IS}). This is because as V_{DS} increases, the drain capacitance tends to reduce the electric displacement in the dielectric and the ferroelectric layers. (Note, this effect, in general, is more on the drain side, but also penetrates on the source side due to electrostatic coupling and domain interactions, as discussed later). In response to the decrease in electric displacement, the electric fields in the FE must increase since the FE capacitance is negative. For a fixed gate voltage, this is possible when V_{IS} reduces. To sum up, if $C_{FE}<0$, increase in V_{DS} can have two opposing effect of I_D due to increase in lateral electric field (which tends to increase I_D) and V_{IS} reduction (which tends to reduce I_D). Therefore, the I_D-V_{DS} curve of FEFET can exhibit a region where I_D decreases with the increase in V_{DS} when V_{IS} reduction dominates. This occurs when V_{DS} is sufficiently high that the effect of the lateral electric field diminishes. This reduction in I_D with V_{DS} yields negative output conductance (NOC) or negative differential resistance (NDR) [18], [54] in the output

characteristics of FEFETs (see Fig. 3.11(b)). Similarly, when the FEFET is OFF, similar effect occurs, which leads to negative DIBL (N-DIBL) [18], [54] as shown in Fig. 3.11(c). In other words, when V_{DS} increases, the drain electric field lines reduce the polarization and electric displacement in the FE layer. This reduces V_{IS} and pulls up the source barrier leading to N-DIBL. While the above description provides a macroscopic understanding of the NC phenomena responsible for reduced SS, NOC (or NDR) and N-DIBL in FEFETs, the microscopic nature of the NC effect plays an important role and is thus required to be understood properly.

Recall our earlier discussion that the nature of the NC effect in FE depends on the value of its gradient energy coefficient, g. Also, for certain FE thickness, there exists a lower limit for g above which the FE layer can potentially exhibit SD NC effect. Note that the SD NC effect in MFIM/MFIS stack implies a homogenous polarization profile along the lateral dimensions. However, the non-homogeneous potential distribution in the FE layer of the FEFETs (due to the source and drain regions) leads to a non-uniform electric-field in the FE layer along the gate length direction[18]. This leads to a mild non-homogeneity in polarization, even in the SD NC regime with finite g. Considering such polarization non-homogeneity in the SD NC regime, it has been shown that the NC attributes of FEFET enhance with the increase in g. In other words, the NC related FEFET properties, i.e., reduction in SS, N-DIBL and NOC are maximum when $g=\infty$ (homogenous polarization profile) and decreases with the decrease in g. This suggests that the domain interactions in the FE layer play a key role in transmitting the effect of V_{DS} from the part of the FE layer in proximity to the drain to that closer to the source. As a result, larger domain coupling (g) in FE offers lower SS, higher N-DIBL and higher NOC in FEFET characteristics [18].

Now, recall that if g is lower than a critical value, then the formation of the MD state takes place in the FE layer. In such a scenario, depending on the value of g, the nature of the FE DW can be either soft or hard (as discussed earlier). Similar to the SD NC effect, the MD NC effect with soft DW should also provide SS<60mV/decade, negative-DIBL and NOC in FEFET characteristics. However, such attributes are expected to be less prominent for MD NC compared to the SD NC due to the reduced NC effect in the former case [27]. Further, considering the correlation between the MD NC effect with soft-DW and g (MD NC effect decreases with the decrease in g), it can also be expected that the reduction in SS, negative-DIBL and NOC should decrease with the

decrease in *g*. Note that, both of the SD NC effect and MD NC effect with soft-DW are non-hysteretic and hence, the SS, DIBL and output-conductance characteristics of FEFET should be hysteresis free with respect to the V_{GS} and V_{DS} sweep directions. It is noteworthy that the FEFETs featuring non-hysteretic steep-slope behavior are also familiar as negative capacitance FET (NCFET) and are suitable candidate for low power logic devices due to the possibilities of aggressive voltage scaling without sacrificing the drive current.

However, if the FE layer is in MD state with hard DW (low *g*), then the process of polarization switching (i.e., DW displacement) is non-adiabatic and that leads to hysteretic NC effect. Hence, SS<60mV/decade can be observed but exhibits hysteresis in the SS versus V_{GS} characteristics. Due to the presence of hysteresis in the I_D-V_{GS} characteristics, such devices are suitable candidates for non-volatile memory operations [28] (Fig. 3.11(d)). In addition, by modulating the amplitude of applied V_{GS}, different extent of partial polarization switching in FE can be obtained yielding different I_D at the same static bias conditions in FEFET. Based on this working principle, hysteretic FEFETs with MD FE have been investigated as the potential candidate as multi-level synapses for neuromorphic hardware [45]. Now, let us discuss the implication of hard-DW displacement in the I_D-V_{DS} characteristics. For a certain V_{GS}, if the drain voltage V_{DS} increases beyond a critical point (typically $V_{DS}>V_{GS}$), then partial polarization switching (+P to -P) takes place near the drain side of the FE layer. This leads to a decrease in channel potential and hence, an increase in barrier height for electron transport near the drain side of the channel, which decreases the drain current. Therefore, a decreasing I_D with increasing V_{DS} (or NOC) can be observed in FEFET during the forward V_{DS} sweep given that the maximum V_{DS} is sufficient to cause the polarization switching in the FE layer (Fig. 3.11(e)). However, during the reverse V_{DS} sweep (when V_{DS} returns to 0V), the polarization configuration of the FE layer is retained (due to the hard nature of the DW). As a result, I_D-V_{DS} characteristics follow a different reverse path compared to its forward path. Moreover, due to the absence of polarization switching, NOC would not be observed in reverse V_{DS} sweep (Fig. 3.11(e)). Concisely, in FEFET exhibiting hard-DW displacement, the I_D-V_{DS} characteristics are hysteretic and the NOC should typically be observed only in the forward V_{DS} sweep as shown in earlier works both theoretically [28] and experimentally [55]. Note that, the NOC mechanism for MD NC with hard-DW displacement (due to polarization switching induced drain side barrier enhancement) is quite distinct compared to the NOC mechanism we discussed

for SD NC scenario where the effect of drain side polarization change influences the source side polarization due to finite domain-coupling and thus, modulates the energy barrier near the source side of the channel.

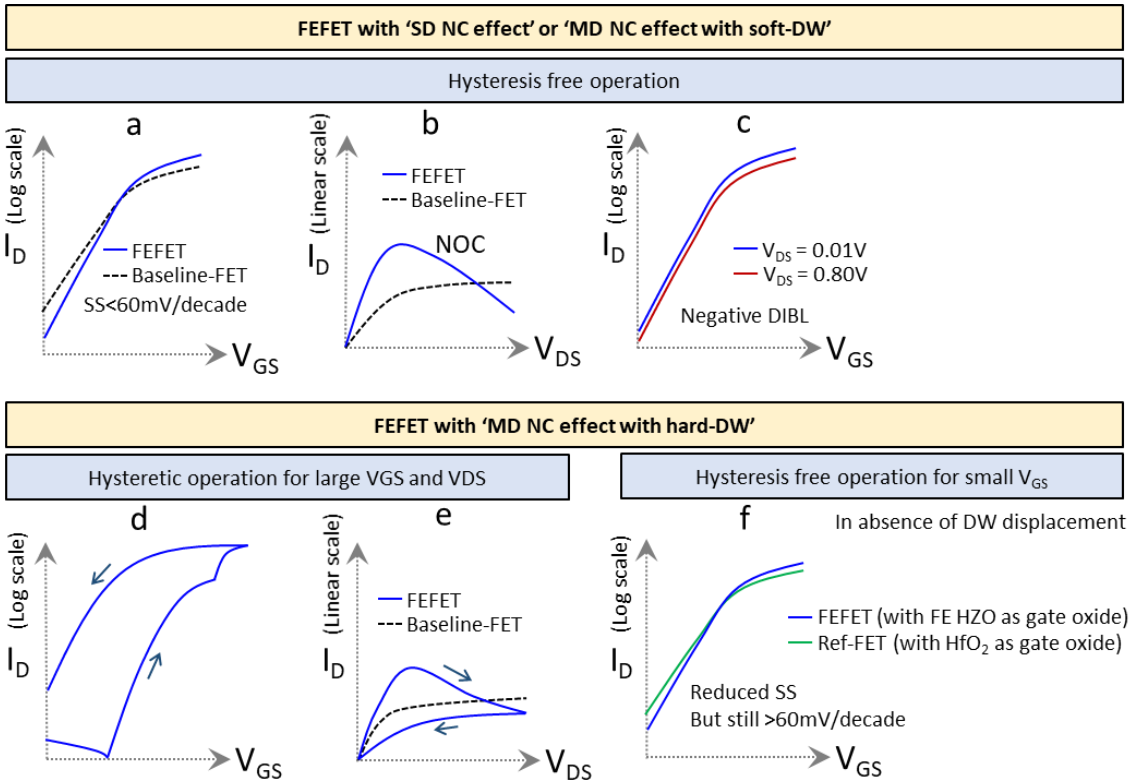

Figure 3.11. (a-c) FEFET characteristics with the FE layer exhibiting SD NC effect or MD NC effect with soft-DW displacement signifying (a) steep-slope (SS<60mV/decade), (b) negative output conductance (NOC), and (c) negative-DIBL characteristics. In this case the device operation in non-hysteretic. (d-e) FEFET characteristics with the FE layer exhibiting MD NC effect with hard-DW displacement signifying (d) hysteretic I_D-V_{GS} and (e) hysteretic I_D-V_{DS} characteristics. (f) In the MD FE with hard-DW, if the applied V_{GS} is not sufficient to cause polarization switching (i.e., DW displacement), then hysteresis free I_D-V_{GS} characteristics can be obtained suggesting enhanced permittivity or high-k operation of FEFET.

In the above discussion of FEFET employing MD FE with hard-DW, we assume that the applied V_{GS} and V_{DS} is sufficient to cause hard-DW displacement and that further yields the negative effective permittivity of the FE layer. However, if the applied V_{GS} and V_{DS} are not sufficient to cause the DW displacement, then the device characteristics should be hysteresis free. Further, in the absence of DW displacement, the effective permittivity of the MD FE with dense domain

patterns is positive but is higher than its intrinsic value [28]. Consequently, the FEEET with MD FE in absence of DW displacement should display all the attributes of a FET with a high-k gate dielectric. That implies FEFET with HZO as FE layer with a thickness that corresponds to MD state with hard-DW should exhibit reduced SS (but still greater than 60mV/decade) and reduced short channel effect (lower output conductance and lower DIBL) compared to a FET in which the FE layer is replaced with HfO_2 layer having same physical thickness (see Fig. 11(e)). Such device is also suitable for low power logic devices as discussed in [28].

To complete the discussion, recall that g in perovskite materials is expected to be sufficiently large for obtaining hysteresis free NC and hence, FEFETs employing perovskite FE with a properly optimized thickness are more likely (compared to fluorite FE) to exhibit non-hysteretic steep-slope, NOC and N-DIBL characteristics.

3.10 Summary:

We discussed the possible mechanisms of the origin of negative capacitance behavior of ferroelectric material in MFIM heterostructure, based on Landau-Ginzburg-Devonshire formalism. By discussing the implication of elastic coupling between ferroelectric unit cells, we examined the implication of the negative capacitance effect in the single-domain and multi-domain scenarios. While single-domain NC or intrinsic NC effect may take place for significantly large gradient energy coefficient, the multi-domain NC effect is more probable for the realistic values of gradient coefficient, especially for fluorite structures. In MD FE, even though the nature of the NC effect can be quasi-static, the presence of hysteresis further depends on the nature of DW. The MD NC effect due to hard-DW displacement exhibits hysteretic characteristics, while for soft-DW displacement, a hysteresis-free NC effect can be obtained. Moreover, we discussed different features of the MD NC effect, in particular, the dependency of the effective negative permittivity of the FE layer on its physical thickness as well as the properties of the underlying dielectric materials. Due to such dependency, the MD NC effect should not be believed as an intrinsic effect, rather can be considered as an effective phenomenon. Moreover, we discuss the possible mechanism for obtaining the MD state with soft-DW by FE thickness scaling. In addition, we emphasize that, under certain scenarios, the effective permittivity of the FE layer may not be

negative but can exhibit a higher effective permittivity compared to its intrinsic value. Such phenomena occur in the absence of DW displacement in MD FE with hard-DW due to the electrostatic interaction between domains. In addition, we review the relevant experimental demonstration of the FE NC effect and discussed their correlation with different types of NC mechanisms. Finally, we provide a brief perspective on the perovskite and fluorite based FE materials from the viewpoint of hysteresis free NC effect and their possible applications in electronic devices.

3.11 References:

[1] R. Landauer, "Can capacitance be negative?" *Collective Phenomena,* 1976.

[2] A. K. Jonscher, "The physical origin of negative capacitance," *Journal of the Chemical Society, Faraday Transactions,* 1986.

[3] A. Kopal, P. Mokrý, J. Fousek, and T. Bahník, "Displacements of 180° domain walls in electroded ferroelectric single crystals: The effect of surface layers on restoring force," *Ferroelectrics,* 1999.

[4] A. M. Bratkovsky, and A. P. Levanyuk, "Very large dielectric response of thin ferroelectric films with the dead layers," *Physical Review B,* 2001.

[5] A. M. Bratkovsky, and A. P. Levanyuk, "Depolarizing field and "real" hysteresis loops in nanometer-scale ferroelectric films," *Applied Physics Letters,* 2006

[6] I. Ponomareva, L. Bellaiche, and R. Resta, "Dielectric anomalies in ferroelectric nanostructures," *Physical Review Letters,* 2007.

[7] S. Salahuddin, and S. Datta, "Use of negative capacitance to provide voltage amplification for low power nanoscale devices," *Nano Letters,* 2008.

[8] A. Cano, and D. Jiménez, "Multidomain ferroelectricity as a limiting factor for voltage amplification in ferroelectric field-effect transistors," *Applied Physics Letters,* 2010.

[9] A. I. Khan, D. Bhowmik, P. Yu, S. J. Kim, X. Pan, R. Ramesh, and S Salahuddin, "Experimental evidence of ferroelectric negative capacitance in nanoscale heterostructures," *Applied Physics Letters,* 2011.

[10] D. J. R. Appleby, N. K. Ponon, K. S. K. Kwa, B. Zou, P. K. Petrov, T. Wang, N. M. Alford, and A. O'Neill, "Experimental observation of negative capacitance in ferroelectrics at room temperature," *Nano Letters*, 2014.

[11] W. Gao, A. Khan, X. Marti, C. Nelson, C. Serrao, J. Ravichandran, R. Ramesh, and S. Salahuddin, "Room-temperature negative capacitance in a ferroelectric-dielectric superlattice heterostructure," *Nano Letters*, 2014

[12] A. I. Khan, K. Chatterjee, B. Wang, S. Drapcho, L. You, C. Serrao, S. R. Bakaul, R. Ramesh & S. Salahuddin, "Negative capacitance in a ferroelectric capacitor," *Nature Materials*, 2015

[13] P. Zubko, J. C. Wojdeł, M. Hadjimichael, S. Fernandez-Pena, A. Sené, I. Luk'yanchuk, J.-M. Triscone, and J. Íñiguez, "Negative capacitance in multidomain ferroelectric superlattices," *Nature*, 2016.

[14] S. J. Song, Y. J. Kim, M. H. Park, Y. H. Lee, H. J. Kim, T. Moon, K. D. Kim, J.-H. Choi, Z. Chen, A. Jian, and C. S. Hwang, "Alternative interpretations for decreasing voltage with increasing charge in ferroelectric capacitors," *Scientific Reports*, 2016.

[15] Y. J. Kim, M. H. Park, Y. H. Lee, H. J. Kim, W. Jeon, T. Moon, K. D. Kim, D. S. Jeong, H. Yamada, and C. S. Hwang, "Frustration of negative capacitance in Al2O3/BaTiO3 bilayer structure," *Scientific Reports*, 2016.

[16] Y. J. Kim, H. Yamada, T. Moon, Y. J. Kwon, C. H. An, H. J. Kim, K. D. Kim, Y. H. Lee, S. D. Hyun, M.n H. Park, and C. S. Hwang, "Time-dependent negative capacitance effects in Al2O3/BaTiO3 bilayers," *Nano Letters*, 2016.

[17] Y. J. Kim, H.W. Park, S. D. Hyun, H. J. Kim, K. D. Kim, Y. H. Lee, T. Moon, Y. B. Lee, M. H. Park, and C. S. Hwang, "Voltage drop in a ferroelectric single layer capacitor by retarded domain nucleation," *Nano Letters*, 2017.

[18] A. K. Saha, P. Sharma, I. Dabo, S. Datta, and S. Gupta, "Ferroelectric transistor model based on self-consistent solution of 2d poisson's, non-equilibrium green's function and multi-domain landau khalatnikov equations," *IEDM*, 2017.

[19] A. K. Saha, S. Datta, S., and S. K. Gupta, "Negative capacitance" in resistor-ferroelectric and ferroelectric-dielectric networks: apparent or intrinsic?," *Journal of Applied Physics* 2018.

[20] I. Luk'yanchuk, A. Sené, and V. M. Vinokur, "Electrodynamics of ferroelectric films with negative capacitance," Phys. Rev. B, 2018.

[21] M. Hoffmann, A. I. Khan, C. Serrao, Z. Lu, S. Salahuddin, M. Pešić, S. Slesazeck, U. Schroeder, and T. Mikolajick, "Ferroelectric negative capacitance domain dynamics," J. Appl. Phys. 2018.

[22] M. Hoffmann, M. Pesic, S. Slesazeck, U. Schroeder, T. Mikolajick, "On the stabilization of ferroelectric negative capacitance in nanoscale devices," *Nanoscale*, 2018.

[23] J. Íñiguez, P. Zubko, I. Luk'yanchuk, and A. Cano, "Ferroelectric negative capacitance," Nature Rev. Mat. 2019.

[24] I. Luk'yanchuk, Y. Tikhonov, A. Sené, A. Razumnaya, and V. M. Vinokur, "Harnessing ferroelectric domains for negative capacitance," Commun. Phys. 2019.

[25] A. K. Yadav, K. X. Nguyen, Z. Hong, P. García-Fernández, P. Aguado-Puente, C. T. Nelson, S. Das, B. Prasad, D. Kwon, S. Cheema, A. I. Khan, C. Hu, J. Íñiguez, J. Junquera, L.-Q. Chen, D. A. Muller, R. Ramesh, and S. Salahuddin, "Spatially resolved steady-state negative capacitance," *Nature*, 2019.

[26] H. W. Park, J. Roh, Y. B. Lee, and C. S. Hwang, "Modeling of negative capacitance in ferroelectric thin films. Adv. Mater. 2019.

[27] A. K. Saha, and S. K. Gupta, "Multi-Domain Negative Capacitance Effects in Metal-Ferroelectric-Insulator-Semiconductor/Metal Stacks: A Phase-field Simulation Based Study," Scientific Reports 2020.

[28] A. K. Saha, M. Si, K. Ni, S. Datta, P. D. Ye, and S. K. Gupta, "Ferroelectric Thickness Dependent Domain Interactions in FEFETs for Memory and Logic: A Phase-field Model based Analysis," IEDM, 2020.

[29] J. Müller, T. S. Böscke, U. Schröder, S. Mueller, D. Bräuhaus, U. Böttger, L. Frey, and T. Mikolajick, "Ferroelectricity in simple binary ZrO2 and HfO2," Nano Lett. 2012.

[30] S. Mueller, J. Mueller, A. Singh, S. Riedel, J. Sundqvist, U. Schroeder, T. Mikolajick, "Incipient ferroelectricity in Al-doped HfO2 thin films," *Advanced Materials*, 2012.

[31] M. H. Park, Y. H. Lee, H. J. Kim, Y. J. Kim, T. Moon, K. D. Kim, J. Müller, A. Kersch, U. Schroeder, T. Mikolajick, C. S. Hwang, "Ferroelectricity and antiferroelectricity of doped thin HfO2-based films," *Advanced Materials*, 2015.

[32] A. K. Saha, B. Grisafe, S. Datta, S. K. Gupta, "Microscopic Crystal Phase Inspired Modeling of Zr Concentration Effects in Hf1-xZrxO2Thin Films," 2019 Symposium on VLSI Technology, T226-T227 (2019). DOI: 10.23919/VLSIT.2019.8776533

[33] E. Ko, H. Lee, Y. Goh, S. Jeon, C. Shin, "Sub-60-mV/decade negative capacitance FinFET with sub-10-nm hafnium-based ferroelectric capacitor. IEEE J. Electron Devices Soc. 5, 10–13 (2017). DOI: 10.1109/JEDS.2017.2731401

[34] F. A. McGuire†, Y.-C. Lin, K. Price, G. B. Rayner, S. Khandelwal, S. Salahuddin, and A. D. Franklin, "Sustained sub-60 mV/decade switching via the negative capacitance effect in MoS_2 transistors," Nano Lett. 17, 4801–4806 (2017). DOI: 10.1021/acs.nanolett.7b01584

[35] M. Si, C.-J. Su, C. Jiang, N. J. Conrad, H. Zhou, K. D. Maize, G. Qiu, C.-T. Wu, A. Shakouri, M. A. Alam, P. D. Ye, "Steep-slope hysteresis-free negative capacitance MoS2 transistors," Nature Nanotechnology 13, 24-28, (2018). DOI: 10.1038/s41565-017-0010-1

[36] H. Zhou, D. Kwon, A. B. Sachid, Y. Liao, K. Chatterjee, A. J. Tan, A. K. Yadav, C. Hu and S. Salahuddin, "Negative Capacitance, n-Channel, Si FinFETs: Bi-directional Sub-60 mV/dec, Negative DIBL, Negative Differential Resistance and Improved Short Channel Effect," IEEE Symposium on VLSI Technology, (2018). DOI: 10.1109/VLSIT.2018.8510691.

[37] M. Si, C. Jiang, W. Chung, Y. Du, M. A. Alam, and P. D. Ye, "Steep-slope WSe2 negative capacitance field-effect transistor," Nanoletters 18, 3682–3687 (2018). DOI: 10.1021/acs.nanolett.8b00816

[38] D. Kwon, K. Chatterjee, A. J. Tan, A. K. Yadav, H. Zhou, A. B. Sachid, R. D. Reis, C. Hu, S. Salahuddin, "Improved subthreshold swing and short channel effect in FDSOI n-channel negative capacitance field effect transistors," IEEE Electron Device Lett. 39, 300–303 (2018). DOI: 10.1109/LED.2017.2787063

[39] K. Ni, A. Saha, W. Chakraborty, H. Ye, B. Grisafe, J. Smith, G. B. Rayner, S. Gupta, S. Datta, "Equivalent Oxide Thickness (EOT) Scaling With Hafnium Zirconium Oxide High-κ Dielectric Near Morphotropic Phase Boundary," IEEE International Electron Devices Meeting (IEDM), 7.4. 1-7.4. 4 (2019). DOI: 10.1109/IEDM19573.2019.8993495

[40] A. K. Saha, K. Ni, S. Dutta, S. Datta, and S. Gupta, “Phase field modeling of domain dynamics and polarization accumulation in ferroelectric HZO,” Appl. Phys. Lett., 114, 20903 (2019). DOI: 10.1063/1.5092707

[41] K. Chatterjee, S. Kim, G. Karbasian, A. J. Tan, A. K. Yadav, A. I. Khan, C. Hu, and S. Salahuddin, “Self-Aligned, Gate Last, FDSOI, Ferroelectric Gate Memory Device With 5.5-nm Hf0.8Zr0.2O2, High Endurance and Breakdown Recovery,” IEEE Electron Device Lett. 38, 1379-1382, (2017). DOI: 10.1109/LED.2017.2748992

[42] S. Dünkel, M. Trentzsch, R. Richter, P. Moll, C. Fuchs, O. Gehring, M. Majer, S. Wittek, B. Müller, T. Melde, H. Mulaosmanovic, Stefan Slesazeck, S. Müller, J. Ocker, M. Noack, D-A Löhr, P. Polakowski, J. Müller, T. Mikolajick, J. Höntschel, B. Rice, J. Pellerin, and S. Beyer, “A FeFET based super-low-power ultra-fast embedded NVM technology for 22nm FDSOI and beyond”, IEEE International Electron Device Meeting (2017). DOI: 10.1109/IEDM.2017.8268425

[43] H. Mulaosmanovic, E. Chicca, M. Bertele, T. Mikolajickac, and S. Slesazecka, “Mimicking biological neurons with a nanoscale ferroelectric transistor,” Nanoscale, vol. 10, no. 46, pp. 21755-21763, Nov. 2018. DOI: 10.1039/C8NR07135G

[44] H. Mulaosmanovic, J. Ocker, S. Müller, M. Noack, J. Müller, P. Polakowski, T. Mikolajick, and S. Slesazeck, “Novel ferroelectric FET based synapse for neuromorphic systems,” in Proc. IEEE VLSI Technol., pp. T176-T177, Jun. 2017. DOI: 10.23919/VLSIT.2017.7998165

[45] M. Jerry, P. Chen, J. Zhang, P. Sharma, K. Ni, S. Yu, and S. Datta, “Ferroelectric FET analog synapse for acceleration of deep neural network training,” IEEE International Electron Device Meeting (IEDM), 6.2.1-6.2.4 (2017). DOI: 10.1109/IEDM.2017.8268338.

[46] K. Ni, B. Grisafe, W. Chakraborty, A. K. Saha, S. Dutta, M. Jerry, J. A. Smith, S. Gupta, and S. Datta, “In-Memory Computing Primitive for Sensor Data Fusion in 28 nm HKMG FeFET Technology,” in IEDM Tech. Dig., pp. 16.1.1-16.1.4, Dec. 2018. DOI: 10.1109/IEDM.2018.8614527

[47] Y. Zhang, J. Sun, J. P. Perdew, and X. Wu, “Comparative first-principles studies of prototypical ferroelectric materials by LDA, GGA, and SCAN meta-GGA,” Phys. Rev. B 96, 035143 (2017). DOI: 10.1103/PhysRevB.96.035143

[48] W. Dinga, Y. Zhanga, L. Taob, Q. Yanga, and Y. Zhoua, “The atomic-scale domain wall structure and motion in HfO2-based ferroelectrics: A first-principle study,” Acta Materialia 196, 556-564 (2020). DOI: 10.1016/j.actamat.2020.07.012.

[49] L. Landau, and E. Lifshits, “On the theory of the dispersion of magnetic permeability in ferromagnetic bodies,” Phys. Zeitsch. Sow. 8, 153–169 (1935).

[50] C. Kittel, “Theory of the structure of ferromagnetic domains in films and small particles,” Phys. Rev. 70, 965–971 (1946). DOI: 10.1103/PhysRev.70.965

[51] M. Hoffmann, F. P. G. Fengler, M. Herzig, T. Mittmann, B. Max, U. Schroeder, R. Negrea, P. Lucian, S. Slesazeck, and T. Mikolajick, “Unveiling the double-well energy landscape in a ferroelectric layer,” Nature 565, 464–467 (2019). DOI: 10.1038/s41586-018-0854-z

[52] J. Kittl, M. Houssa, V. V. Afanasiev, and J. Locquet, “Comment on "Unveiling the double-well energy landscape in a ferroelectric layer," arXiv: 2003.00426, Mesoscale and Nanoscale Physics, (2020).

[53] H.-J. Lee, M. Lee, K. Lee, J. Jo, H. Yang, Y. Kim, S. C. Chae, U. Waghmare, and J. H. Lee, “Scale-free ferroelectricity induced by flat phonon bands in HfO2,” Science 369, 6509 (2020).

[54] S. Gupta, M. Steiner, A. Aziz, V. Narayanan, S. Datta and S. K. Gupta, “Device-Circuit Analysis of Ferroelectric FETs for Low-Power Logic,” IEEE Trans. on Electron Devices, 64, 3092-3100 (2017). DOI: 10.1109/TED.2017.2717929.

[55] M. Jerry, J. A. Smith, K. Ni, A. Saha, S. Gupta and S. Datta, "Insights on the DC Characterization of Ferroelectric Field-Effect-Transistors," in 76th Device Research Conference (DRC), pp. 1-2 (2018). DOI: 10.1109/DRC.2018.8442191.

4. TRANSIENT NEGATIVE CAPACITANCE EFFECTS IN RESISTOR-FERROELETRIC NETWORK

4.1 Introduction

In this chapter, we describe and analytically substantiate an alternate explanation for the negative capacitance (NC) effect in ferroelectrics (FE). We show that the NC effect previously demonstrated in resistance-ferroelectric (R-FE) networks does not *necessarily* validate the existence of "S" shaped relation between polarization and voltage (according to Landau theory). In fact, the NC effect can be explained without invoking the "S"-shaped behavior of FE. We employ an analytical model for FE (Miller model) in which the steady state polarization strictly increases with the voltage across the FE and show that despite the inherent positive FE capacitance, reduction in FE voltage with the increase in its charge is possible in a R-FE network as well as in a ferroelectric-dielectric (FE-DE) stack. This can be attributed to a large increase in FE capacitance near the coercive voltage coupled with the polarization lag with respect to the electric field. Under certain conditions, these two factors yield transient NC effect. We analytically derive conditions for NC effect in R-FE and FE-DE networks. We couple our analysis with extensive simulations to explain the evolution of NC effect. We also compare the trends predicted by the aforementioned Miller model with Landau-Khalatnikov (L-K) model (static negative capacitance due to "S"-shape behavior) and highlight the differences between the two approaches. First, with an increase in external resistance in the R-FE network, NC effect shows a non-monotonic behavior according to Miller model but increases according to L-K model. Second, with the increase in ramp-rate of applied voltage in the FE-DE stack, NC effect increases according to Miller model but decreases according to L-K model. These results unveil a possible way to experimentally validate the actual reason of NC effect in FE.

The idea of NC effect comes from Landau's phenomenological thermodynamic model [6] where the steady-state relation between polarization (P) and voltage (V) has a negative dP/dV region. It is notable that, in a standalone-FE (SFE), such characteristics have never been observed in experiments [7-9] due to the instability of this region. However, in [5], it has been claimed that by putting a dielectric (DE) capacitor in series of an FE capacitor, it is possible to stabilize the

operation of FE in this NC region. Later on, direct findings of NC effect have been claimed in a resistor-ferroelectric (R-FE) network [10] and indirect findings of NC effects have been reported in a ferroelectric-dielectric (FE-DE) stack [11,12]. It has been suggested that these extrinsic components (R and DE) enable the traversal or stabilization of negative dP/dV_{FE} path of Landau theory. Efforts have already been made to find an alternate explanation of NC effect in an R-FE network by Song et al. [13]. The paper discussed two different models of an FE capacitor: model-1: time varying positive capacitor ($C_{FE}(t)$) and constant resistor (R_{FE}) in series and model-2: time varyingresistor ($R_{FE}(t)$) and constant positive capacitor (C_{FE}) in series. Although their simulation results show NC effect in an R-FE network, the assumption of time dependent components limits the FEmodels to be applicable for only step input voltages. Because the paper did not provide any physical reasoning for their claimed time-variant nature of C_{FE}, its utility for inputs other than step inputs (e.g., ramp inputs) or modifications required to treat generic inputs remain unclear. Moreover, modeling FE as a constant positive capacitor (considering model-2) may not be appropriate as it is well known that ferroelectric is a variable capacitor [14]. At the same time, it would be more appropriate/conventional to express C_{FE} as voltage dependent term rather than time dependent (model-1). Interestingly, treating CFE as voltage variant while RFE is assumed to be constant, NC effect can no longer be observed (discussed later).

In this chapter, we discuss an alternate explanation of NC effect in FE which, like Ref. [13], is based on modeling FE as a series combination of R_{FE} and positive C_{FE}. However, in contrast to Ref. [13], neither R_{FE} nor C_{FE} is explicitly time dependent; rather both of them depend on voltage or polarization. This enables us to perform an extensive mathematical and simulation based analysis of NC effect and explain the phenomena physically in a much more comprehensive manner for the R-FE network and FE-DE stack. We also discuss the trends for the NC effect with respect to various material, device, and circuit parameters, which is important for developing the understanding of NC effect.

In our subsequent discussion on NC effect, we utilize two models of FE, namely, Landau-Khalatnikov (L-K) model [5,6] and modified version of Miller's analytical model [17]. These models are discussed in the next section.

To begin with, let us define the total charge in the ferroelectric (Q) as $Q = A_{FE} \times (\epsilon_0 \times V_{FE}/T_{FE} + P)$. Here, ϵ_0 is the electric permittivity of vacuum, V_{FE} is the applied voltage, A_{FE} is the FE area, T_{FE} is the FE thickness, and P is the polarization. The relation between P and V_{FE} has been modeled using several approaches. Two of which we will discuss below: (i) Landau-Khalatnikov (L-K) model and (ii) Preisach based Miller model.

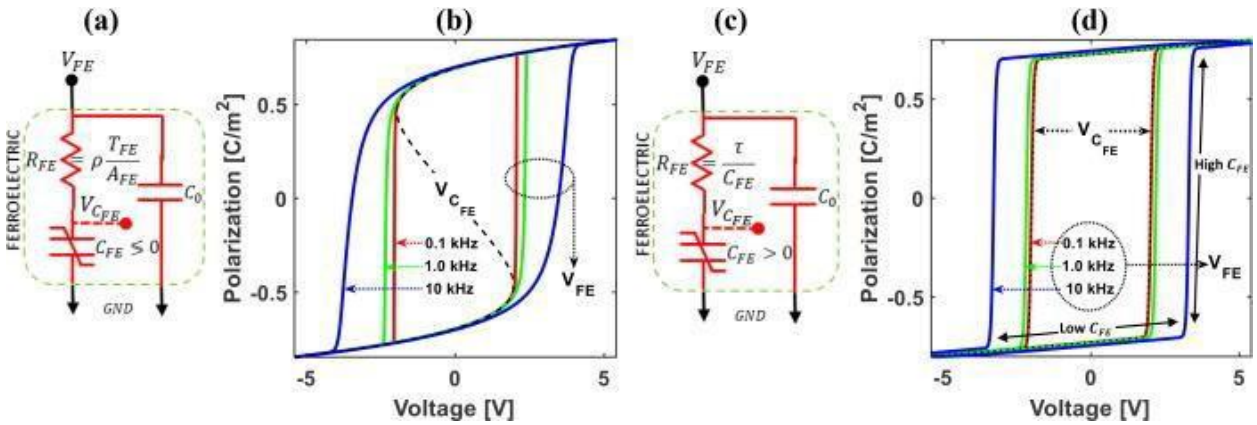

Figure 4.1. (a) Equivalent circuit model of FE capacitor according to L-K model, (b) P–V_{FE}(solid line) and P−V_{CFE} (dashed line) curve of FE according to L-K model for different frequencies, (c) equivalent circuit model of FE capacitor according to Miller model (P_S = 0.73 C/m^2, P_R = 0.72 C/m^2, V_C = 2 V, V_P = 5.4 V, η = 0.1, σ = 10 and τ = 2 μs), (d) P–V_{FE} (solid line) and P−V_{CFE} (dashed line) curve of FE according to Miller model (α = –8.8 × 10^7 m/F,β = 1 × 10^5 m^5/F/C^2 and γ = 3.8 × 10^8 m^9/F/C^4) for different frequencies. Here, $C_0 = \epsilon_0 \times T_{FE}/A_{FE}$and T_{FE} = 50 nm.

The single domain Landau-Khalatnikov model (L-K model) is a dynamic extension of Landau's symmetry based phenomenological thermodynamic phase transition model (first applied to the case of ferroelectrics by Devonshire) [1-5]. According to L-K model, the P–V_{FE} relation can be expressed through following equation:

$$V_{FE} - \left(\rho \frac{T_{FE}}{A_{FE}}\right) \times \left(A_{FE} \frac{dP}{dt}\right) = T_{FE}(\alpha P + \beta P^3 + \gamma P^5) \tag{4.1}$$

where α, β, and γ are called Landau coefficients and ρ is the kinetic coefficient representing the polarization lag with respect to the applied external voltage. The value of α is negative for all

known FE materials below Curie temperature (T_C), which leads to hysteretic characteristics of ferroelectrics. In Eq. (2.1), the term $\rho(T_{FE}/A_{FE}) \times A_{FE}(dP/dt)$ can be represented as a resistive voltage drop across an intrinsic resistor, $R_{FE} = \rho(T_{FE}/A_{FE})$, where $A_{FE}(dP/dt)$ is the displacement current (I) due to polarization switching. Hence, FE can be modeled as a series combination of capacitor (C_{FE}) and a resistor (R_{FE}) [see Fig. 4-1(a)]. Clearly, we can write the relation between voltage drop across C_{FE} (V_{CFE}) and polarization (P) as follows:

$$V_{C_{FE}} = T_{FE}(\alpha P + \beta P^3 + \gamma P^5) \tag{4.2}$$

The $P-V_{CFE}$ curve using Eq. (2.2) has been plotted in Fig. 4-1(a) (dashed line) showingthat $C_{FE}=A_{FE}(dP/dV_{CFE})$ is negative for a certain range of polarization. $P–V_{FE}$ curves for applied voltage of different frequencies are also plotted in Fig. 4-1(b). At high frequency (high dV_{FE}/dt), current ($A_{FE}(dP/dt)$) is larger, causing higher voltage drop across R_{FE} ($V_{RFE}=V_{FE}-V_{CFE}$). Hence, hysteresis increases with an increase in frequency. Note that the L-K model is a macroscopic version of multi-domain Ginzburg-Landau model based on certain assumptions, which we discuss in the subsequent chapters.

Now, we will discuss the Miller model of FE [6-7], which is an analytical version of multi-domain hysteretic Preisach model. Like the L-K model, the Miller model can be represented as a series combination of R_{FE} and C_{FE}. However, unlike the L-K model, the Miller model assumes strictly positive C_{FE} and the $P-V_{CFE}$ relation can be expressed through the following equations:

$$P = P_S\left[tanh\left[w \times \left(V_{C_{FE}} \pm VC\right)\right] + \eta\frac{V_{CFE}}{V_P}\right] \tag{4.3}$$
$$w = \sigma\frac{1}{2V_C}log\left[\frac{P_S + P_R}{P_S - P_R}\right]$$

Here, P_S is the saturation polarization, P_R is the remnant polarization, V_C is the coercive voltage, and V_P is the peak value of V_{CFE}. In the equation, we included η and σ as the fitting parameters to capture, respectively, the effects of V_C distribution in FE domains and non-ferroic linear response

of P. In Eq. (2.3a), negative sign is used if dV_{CFE}/dt is positive and vice versa. The relation between V_{FE} and V_{CFE} is expressed by the following equation:

$$\frac{dV_{C_{FE}}}{dt} = \frac{1}{\tau}[V_{FE} - V_{C_{FE}}] \tag{4.4}$$

where τ is the lag between V_{FE} and P (typically attributed as the delay caused by nucleation and domain-wall propagation). In the equivalent circuit of the Miller model [Fig. 4-1(c)] $R_{FE} = \tau/C_{FE}$ and $C_{FE}=A_{FE}(dP/dV_{CFE})$, where P is given by Eq. (2.3). From the P−VCFE curve shown in Fig. 4-1(d), we can see that C_{FE} is always positive. Considering $\tau = 2\ \mu$s, P–V_{FE} curves for different frequencies have also been shown in Fig. 4- 1(d) showing increase in hysteresis with the increase in frequency. It is noteworthy that the Millermodel of FE shows a sharp increase in the slope of $P-V_{CFE}$ characteristics (or C_{FE}) near coercive voltage (V_C). This implies that dC_{FE}/dV_{CFE} is quite large near coercive voltage. It is also noteworthy that depending on the peak value of the applied voltage, FE can be fully or partially poled and that leads to major or minor P–V_{FE} loops, respectively. It is notable that $d|C_{FE}|/dV_{CFE}$ ismaximum in major loop and deceases as poling reduces. Such characteristics of major-minor looping can be captured using the Miller model, which we discuss in the later chapter. Now, with the understanding of these two models, let us summarize the key differences as follows:

(i) According to the L-K model, C_{FE} is intrinsically negative for a certain range of polarization, whereas in the Miller model, C_{FE} is always positive.

(ii) According to the Miller model, time constant (τ) is the fundamental parameter, employedto nucleation and domain-wall propagation delay. Assumption of this delay $\tau = R_{FE}C_{FE}$ monotonically dependent on polarization makes R_{FE} strongly dependent on C_{FE}. On the other hand, in the L-K model, R_{FE} is the fundamental parameter. However, it cannot be directly related to C_{FE} through a time constant parameter, as negative C_{FE} would lead to negative R_{FE}, which is non-physical. In general, R_{FE} and τ can be a function of the electric field or polarization. However, in several studies based on the L-K model, it is common to treat R_{FE} as independent of electric field. Similarly, in [14], [17], and [22] based on the Miller model, τ is treated as
constant.

Though Q is the experimentally measured parameter, in most of the works, it has been treated as the P. Incorporating the term ($\epsilon_0 E_{FE} A_{FE}$) in our simulations, we foundthat neglecting this term does not provide any significant change in the results and conclusions. However, inclusion of this term unnecessarily complicates the mathematical analysis and takes thefocus away from the messages that we intend to convey. Hence, we include this term in our simulation but ignore in our mathematical analysis (chapter 5). It is important to understandthat V_{FE} and current (or charge, $Q=P\times A_{FE}$) are the experimentally measured variables, and the negative capacitance is observed when $dP/dV_{FE} < 0$. It is also noteworthy that V_{CFE} is not directly measurable in experiments and is a model parameter that helps in understanding the ferroelectric behavior. C_{FE} can be thought of as the "steady state" capacitance of the ferroelectric, i.e., when theferroelectric current is negligible (which implies $V_{RFE}\approx 0$ or $V_{FE}\approx V_{CFE}$). If the ferroelectric currentis substantial (which occurs when the rate of change in applied voltages is larger than the inverse of the inherent time constant associated with R_{FE} and C_{FE}), C_{FE} is different from the measured capacitance. Hence, as we will show later, it may be possible to measure negative dP/dV_{FE} even though C_{FE} is positive (for the Miller model). As a corollary, negative measured dP/dV_{FE} may notnecessarily imply negative C_{FE} (as predicted by L-K model).

4.2 Negative Capacitance Effect in Resistor-Ferroelectric (R-FE) Network

Direct observation of NC effect has been first demonstrated in an R-FE network [Fig. 5.1(a)] by Khan *et al.*[10]. Figures 5.1(b) and 5.1(c) show the experimental [10] transient result and P–V_{FE} curve, respectively, for alternating step voltage pulses in the R-FE network. After applying positive stepinput in the R-FE network, V_{FE} increases until point (a), then decreases until point (b), and again increases until reaching a steady state value [Fig. 5.1(b)]. Within points (a) and (b), as V_{FE} is decreasing with the increment of P, dP/dV_{FE} is negative, which can be attributed as NC effect. In Ref. [10], such an effect has been attributed to the traversal of negative dP/dV_{CFE} path of the Landau theory and modeled the experiment using the L-K model. We show the simulation results for a step input in an R-FE network in Figs. 5.2(a)–5.2(b) and 5.2(c)–5.2(d), respectively, for the L-K model and Miller model. From Figs. 5.2(c) and 5.2(d), it is quite interesting that the NC effect in an R-FE network can also be obtained using the Miller model of FE in response to a step-input.

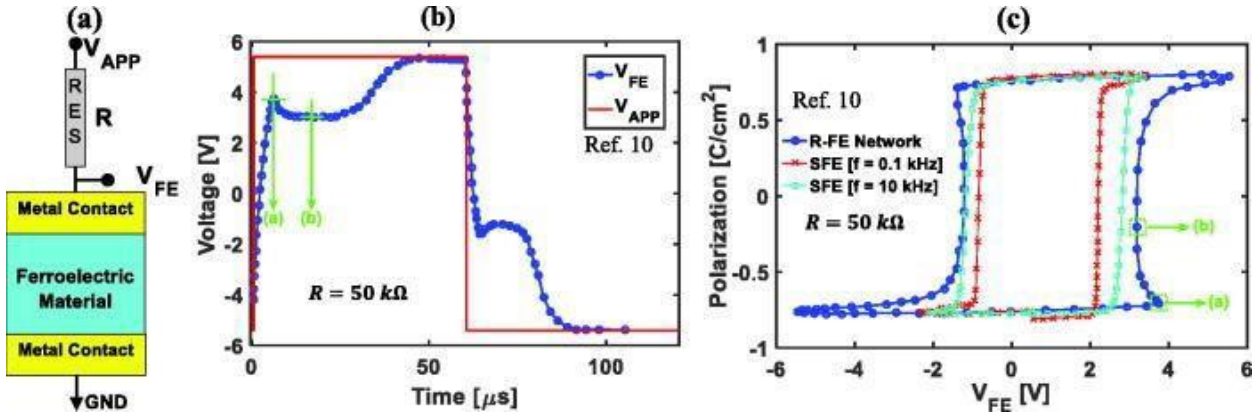

Figure 4.2. (a) Experimental[10] setup of R-FE network, (b) transient response of V_{FE}, and (c) P–V_{FE} curve of FE in an R-FE network under step-voltage as input and P–V_{FE} curve of a standalone-FE (SFE) under triangular-voltage as input. (This figure has been generated from the results presented in Ref. 10.)

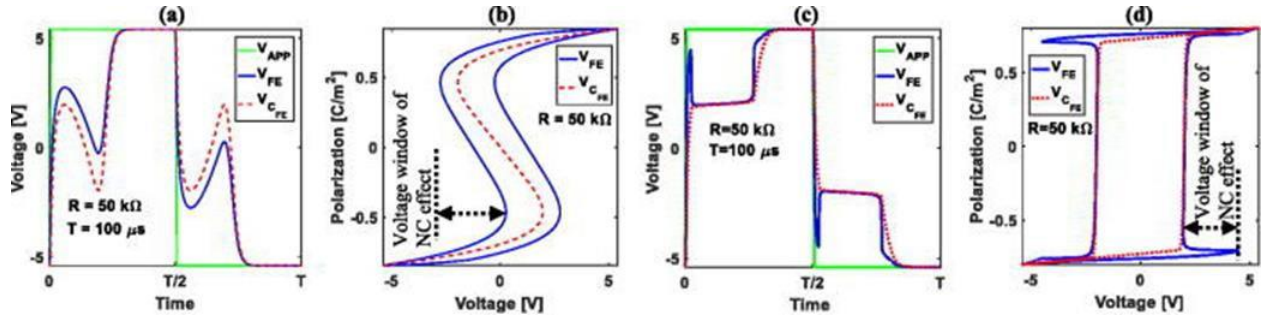

Figure 4.3. Transient response of V_{FE} and V_{CFE}, (b) P–V_{FE} and $P-V_{CFE}$ curve of FE considering L-K model in an R-FE network under step input. (c) Transient response of V_{FE} and V_{CFE}, (d) P–V_{FE} and $P-V_{CFE}$ curve of FE considering Miller model in an R-FE network under step input.

To explain the results, let us consider the equivalent circuit of the R-FE network considering the Miller model [see Fig. 5.3(a)]. Here, V_{APP} is the input applied voltage; $V_R = V_{APP} - V_{FE}$ is the voltage across R; and V_{RFE} is the voltage across R_{FE}. It is trivial to say that, in an R-C network, current (I) decreases gradually from an initial high value in response to a positive step input. The initial value of C_{FE} is low. Therefore, the initial value of R_{FE} ($=\tau/C_{FE}$) is high and so is the V_{RFE}. When V_{CFE} approaches V_C, the value of C_{FE} suddenly increases and hence the value of R_{FE} decreases. Such a change in C_{FE} demands higher I in the R-FE network, where $I = C_{FE}(dV_{CFE}/dt) = V_R/R = (V_{APP}-V_{FE})/R$. To meet this demand, V_R must increase. At the same time, dV_{CFE}/dt decreases to partially counterbalance the effect of sudden increase in C_{FE} on current.Note, since

current is positive, dV_{CFE}/dt is positive, i.e., VCFE strictly increases with time. The same, however, can be said about V_{RFE}. V_{RFE} ($=I \times R_{FE}$) may increase or decrease since increase in I is accompanied by reduction in R_{FE}. Immediately after V_{FE} reaches V_C, V_{RFE} increases due to a large current increase. However, after some time, especially if τ is sufficiently large, the impact of R_{FE} ($=\tau/C_{FE}$) reduction begins to manifest its effects leading to a decrease in V_{RFE}. Consequently, ferroelectric voltage ($V_{FE}=V_{CFE}+V_{RFE}$) can decrease if reduction in V_{RFE} is greater than the increase in V_{CFE}. Under these conditions, dV_{FE}/dt becomes negative, while $dP/dt = I/A_{FE}$ is positive, which implies the NC effect. By plotting the polarization and V_{FE}, we can describe the process of NC effect with the following two features: (i) "Voltage overshoot" is observed in the $P-V_{FE}$ curve when compared to the steady state response ($P-V_{CFE}$ curve). This means $V_{FE}>V_{CFE}$ nearthe coercive voltage which is due to an increase in V_{RFE} immediately after V_{FE} reaches $\sim|V_C|$, as described before. Physically, this reflects the lag in polarization with respect to V_{FE}. (ii) Voltage overshoot is followed by "voltage snap-back," which describes the decrease in V_{FE} with increasing P. Physically, this represents the relaxation of $P-V_{FE}$ towards the steady state response. Based on the explanation above, it can be deduced that both voltage overshoot and snap-back (and therefore, the observation of NC effect) is highly dependent on the abrupt change in C_{FE} at the vicinity of coercive voltage as well as the value of τ.

As both the Miller and L-K models can explain the NC effect in an R-FE network, it is importantto analyze the conditions under which the NC effect can be observed and investigate the differences between the two approaches.

4.3 Condition for NC Effect in R-FE Network

In this section, we will mathematically analyze the conditions for NC effect in an R-FE network. Unless otherwise stated, in this discussion, we assume that the peak value of V_{APP} is sufficiently high, so that FE is fully polled and therefore traverses through the major path. Now, recalling theequivalent circuit of an R-FE network for both the models (shown in Fig. 4.3), we can write the following equation by considering current continuity:

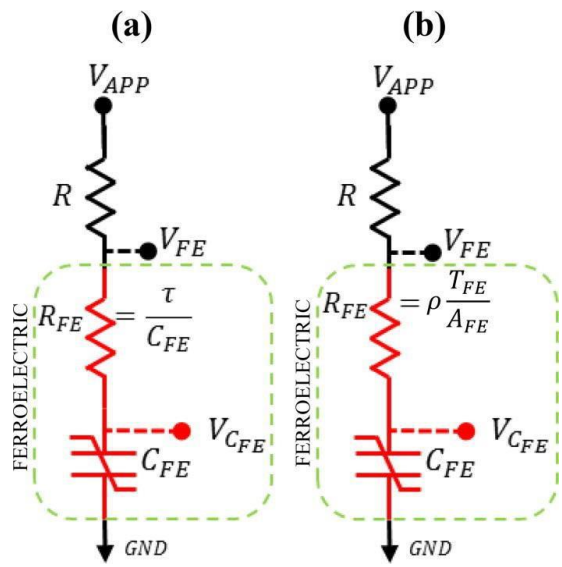

Figure 4.4. Equivalent circuit model of R-FE network according to (a) Miller model and (b) L-K model.

$$\frac{V_{APP} - V_{FE}}{R} = \frac{V_{APP} - V_{C_{FE}}}{R + R_{FE}} \tag{4.5}$$

Now, starting from this equation we will derive the condition of NC effect.

4.3.1 General condition

First, we will discuss the generic condition for the NC effect without imposing any restriction on input types and parameters, i.e., τ and ρ.

(A) Miller model of FE

For the Miller model, replacing R_{FE} with τ/C_{FE} in Eq. (4.5), and taking derivative with respect topolarization (P), we obtain –

$$\frac{dV_{FE}}{dP} = \frac{A_{FE}R}{R_{C_{FE}} + \tau}\left[\left[1 - \frac{dV_{APP}}{dV_{C_{FE}}}\right] + \frac{V_{APP} - V_{C_{FE}}}{R_{C_{FE}} + \tau}\left[\frac{d\tau}{dV_{C_{FE}}} - \frac{\tau}{C_{FE}}\frac{d_{C_{FE}}}{dV_{C_{FE}}}\right] + \frac{R_{C_{FE}} + \tau}{R_{C_{FE}}}\frac{dV_{APP}}{dV_{C_{FE}}}\right] \tag{4.6}$$

For the NC effect, dV_{FE}/dP must be negative. Using this condition in Eq. (4.6) and applying some mathematical rules for differentiation, we can write the following equation as the condition for NC effect in the R-FE network:

$$\left|\frac{dC_{FE}}{dV_{C_{FE}}}\right| > \frac{C_{FE}}{|V_{APP}-V_{C_{FE}}|}\left[1 \pm \frac{|V_{APP}-V_{C_{FE}}|}{R_{C_{FE}}+\tau} \times \frac{d\tau}{dV_{C_{FE}}} + \frac{\tau}{R_{C_{FE}}}\frac{dV_{APP}}{dV_{C_{FE}}}\right]\left[1+\frac{RC_{FE}}{\tau}\right] \quad (4.7)$$

Here, "+" sign corresponds to increase in $V_{APP}(t)$ and "–" sign corresponds to decrease in $V_{APP}(t)$ with respect to time (t). It is notable that Eq. (3.2) is valid only for $\tau \neq 0$. This is because if $\tau = 0$, then from Eq. (3.2) we can see that $dV_{FE}/dP = A_{FE}/C_{FE}$. This implies that no NC effect can be observed for $\tau = 0$. For $\tau \neq 0$, Eq. (3.3) shows that NC effect in the R-FE circuit can be observed if the left hand side is greater than the right hand side. In other words, the inherent steady state $P-V_{CFE}$ response of an FE must show an increase in its slope near the coercive field. Moreover, this increase must be greater than a value, which depends on FE parameters, R and V_{APP}. We will discuss these factors subsequently. In summary, for the NC effect considering the Miller model, there must be a finite polarization lag with respect to an applied voltage ($\tau \neq 0$) and (b) the slopeof $P-V_{CFE}$ characteristics ($|dC_{FE}/dV_{CFE}|$) must increase near the coercive voltage and this increase must be sufficiently large.

(B) L-K model of FE

For the L-K model, replacing R_{FE} with $\rho(T_{FE}/A_{FE})$ in Eq. (4.5) and taking derivative with respect to polarization (P), we obtain-

$$\frac{dV_{FE}}{dP} = \frac{\frac{A_{FE}R}{C_{FE}}}{R+\rho\left(\frac{T_{FE}}{A_{FE}}\right)}\left[\left[1-\frac{dV_{APP}}{dV_{C_{FE}}}\right] + \frac{\left(V_{APP}-V_{C_{FE}}\right)\left(\frac{T_{FE}}{A_{FE}}\right)}{R+\rho\left(\frac{T_{FE}}{A_{FE}}\right)}\left[\frac{d\rho}{dV_{C_{FE}}}\right] + \frac{R+\rho\left(\frac{T_{FE}}{A_{FE}}\right)}{R}\frac{dV_{APP}}{dV_{C_{FE}}}\right] \quad (4.8)$$

Now, using the same condition we applied to derive Eq. (4.8), we can write the following equation for the L-K model from Eq. (4.7) as the conditionof NC effect:

$$\frac{R/C_{FE}}{R+\rho\left(\frac{T_{FE}}{A_{FE}}\right)}\left[1+\frac{\frac{T_{FE}}{A_{FE}}}{\frac{R}{\rho}}\frac{dV_{APP}}{dV_{C_{FE}}}\pm\frac{\left|V_{APP}-V_{C_{FE}}\right|\left(\frac{T_{FE}}{A_{FE}}\right)}{R+\rho\left(\frac{T_{FE}}{A_{FE}}\right)}\left[\frac{d\rho}{dV_{C_{FE}}}\right]\right]<0 \tag{4.9}$$

Equation (3.4) can be satisfied in the following scenarios:

- If $\frac{d\rho}{dV_{C_{FE}}} \geq 0$, C_{FE} must be negative.
- If $\frac{d\rho}{dV_{C_{FE}}} < 0$, then either (a) C_{FE} must be positive and $\frac{d\rho}{d|VCFE|} > \frac{\left[\left(\frac{A_{FE}}{T_{FE}}\right)+\left(\frac{\rho\left(\frac{T_{FE}}{A_{FE}}\right)}{R}\right)\left(\frac{dV_{APP}}{dV_{C_{FE}}}\right)\right]\left[\left(R+\rho\left(\frac{T_{FE}}{A_{FE}}\right)\right)\right]}{[(V_{APP}-V_{C_{FE}})]}$ or (b) C_{FE} must be negative and $\frac{d\rho}{d|VCFE|} < \frac{\left[\left(\frac{A_{FE}}{T_{FE}}\right)+\left(\frac{\rho\left(\frac{T_{FE}}{A_{FE}}\right)}{R}\right)\left(\frac{dV_{APP}}{dV_{C_{FE}}}\right)\right]\left[\left(R+\rho\left(\frac{T_{FE}}{A_{FE}}\right)\right)\right]}{[(V_{APP}-V_{C_{FE}})]}$.

Since, according to the L-K model, C_{FE} can take both positive and negative values, Eq. (4.9) is always satisfied for some range of polarization, leading to NC effect, irrespective of the sign and magnitude of $d\rho/d|V_{CFE}|$.

The above discussion points to an important difference between the explanations of NC effect based on these two models. For the Miller model, the condition of NC effect in an R-FE network is dependent on the FE and circuit parameters; therefore, NC effect would only be observed undercertain scenarios (which are discussed subsequently). On the other hand, for the L-K model, the condition for NC effect in the R-FE network is always satisfied, which implies that no matter whatthe FE and circuit parameters are, NC effect is always expected to be observed in principle. However, if the left hand side of Eq. (4.9) (though negative) is very small in magnitude, the NC effect may be too small to be observed in experiments. In addition, the presence of depolarizationfield in FE with very low thickness may reduce or even completely eliminate the FE hysteresis and the negative dP/dV_{CFE} path. This may also suppress the NC

effect. Such effects have been discussed in Ref. [23] showing that the negative curvature of energy landscape of FE (which implies NC) may vanish for $T_{FE} < 3$ nm. In this work, we do not consider the explicit inclusion ofdepolarization field to maintain focus on the trends that we want to discuss. However, it may be noted that the effect of depolarization field is implicitly included in the parameters for the FE models obtained from calibration with the experiments as the experimental data already account for the depolarization fields that may be present in the sample.

We now discuss the differences between these two explanations with respect to different parameters for two different types of input signals, viz., step input and ramp input.

4.3.2 Step input with constant τ and ρ

(A) Miller model of FE:

For a step input, $dV_{APP}/dt = 0$ and $dV_{APP}/dV_{CFE}=0$ for $t > 0$. To ease the understanding of the trends let us assume τ = constant, i.e., $d\tau/dV_{CFE}=0$. We will briefly discuss the case when these parameters are not constant later. Now, imposing these conditions in Eqs. (3.2) and (3.3) we can write the following equations:

$$\frac{dV_{FE}}{dP} = \frac{A_{FE}R}{R_{C_{FE}} + \tau}\left[1 - \frac{V_{APP} - V_{C_{FE}}}{R_{C_{FE}} + \tau}\frac{\tau}{C_{FE}}\frac{dC_{FE}}{dV_{C_{FE}}}\right] \tag{4.10}$$

$$\left|\frac{dC_{FE}}{dV_{C_{FE}}}\right| > \frac{C_{FE}}{\left|V_{APP} - V_{C_{FE}}\right|}\left[1 + \frac{RC_{FE}}{\tau}\right] \tag{4.11}$$

Here, Eq. (4.10) is the condition of NC effect for step input. It is obvious that if the right hand sideof the equation becomes lower in magnitude or the left hand side increases, the condition for the NC effect will be easier to meet. This translates to NC effect that occurs for a larger polarization range, as we will show subsequently. Therefore, according to Eq. (4.10), the NC effect will occur within a larger polarization range if $|dC_{FE}/dV_{CFE}|$ increases, R decreases and/or τ increases. A graphical representation of Eq. (4.11) is shown in Figs. 4.4(a) and 5.4(b),

respectively, for differentvalues of R and τ. In the figure, solid line represents the left hand side of Eq. (4.10) as a function ofpolarization and the dashed line represents the right hand side. So, the NC effect should occur within the range of P where dashed lines fall below the solid line. From Fig. 4.4, it can be observedthat the polarization range of NC effect increases with the decrease in R and increase in τ.

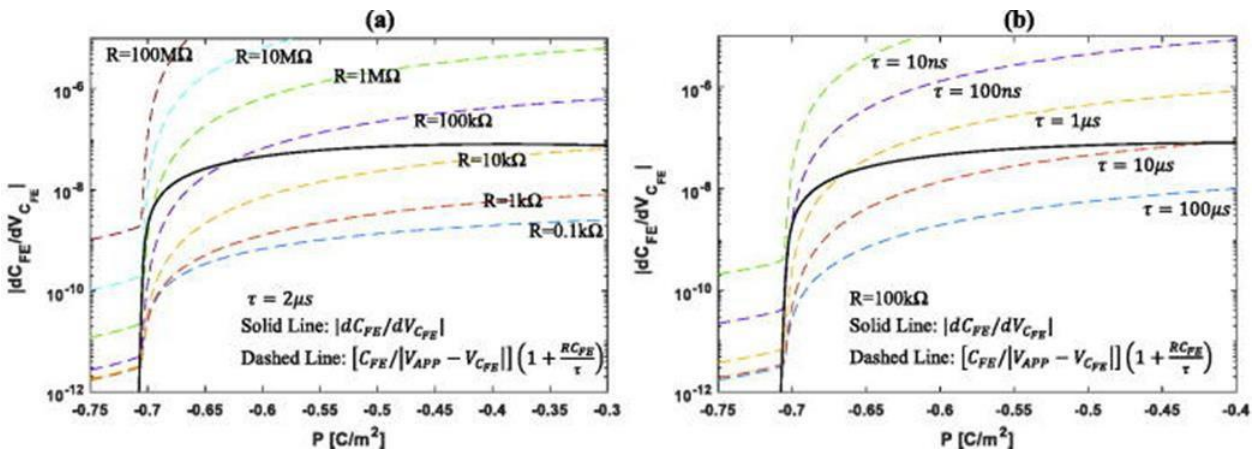

Figure 4.5. Graphical representation of Eq. (4.11) with respect to P for (a) different values of R, and (b) different values of τ.

Now we will discuss the impact of *R* on the voltage window of NC effect. To begin with, let us re- write Eq. (3.6) as $dV_{FE}/dP = X \times Y$, where $X = A_{FE}R/(RC_{FE} + \tau)$ and $Y=[1-[(V_{APP}-V_{CFE})/(R_{CFE}+\tau)]*[\tau/C_{FE}][dC_{FE}/dV_{CFE}]]$. Note that X is always positive and in the NC regime, Y is negative that gives rise to negative dV_{FE}/dP. At the same time, the term *X* increases and *Y* decreases in magnitude with the increase in *R*. Now, at first we will consider a very low value of *R*, so that $RC_{FE} \ll \tau$. In this case, if *R* increases, then the increase in *X* dominates over decrease in *Y*, making dV_{FE}/dP more negative (or $dP/dV_{FE} \approx \Delta P/\Delta V_{FE}$ less negative). That implies, within the same ΔP, ΔV_{FE} is more negative. Therefore, the voltage window of NC effect increases with the increase in *R*. Now, let us consider a very high value of *R* so that $RC_{FE} \gg \tau$. For this case, with theincrease in *R*, the decrease in *Y* dominates over increase in *X*, making dV_{FE}/dP less negative (or dP/dV_{FE} more negative). That implies the decrease in the voltage window of NC effect with the increase in *R*. This discussion signifies the non-monotonic dependence of the voltage windowof NC effect on the value of external resistor.

Simulated $P–V_{FE}$ and $P-V_{CFE}$ curves of FE (considering Miller model) in an R-FE network alongwith the transient result for different values of R are shown in Fig. 4.5. From Figs. 4.5(a)–4.5(f) we can see that the polarization range of NC effect decreases monotonically with the increasein external resistance (R), which is consistent with the result in Fig. 4.4(a). On the other hand, thevoltage window of NC effect increases from R = 0.1 kΩ to R = 10 kΩ and then decreases with further increase in R. In fact, the NC effect vanishes for a very high value of R, as we can see from Figs. 4.5(f) and 4.5(l) for R = 10 MΩ. To explain this phenomenon, recall that the NC effect is theoutcome of two-steps process: (i) V_{FE} overshoot: due to lag between P and V_{FE} and then (ii) V_{FE} snap-back: due to increase in C_{FE} and decrease in R_{FE}. For low valuesof R (R < 10 kΩ), V_{FE} overshoot remains almost independent of R (as $RC_{FE} \ll \tau$). If R is extremelysmall [Fig. 4.5(a)], low voltage drop across R results in most of the applied voltage to appear across the FE layer. That leads to very small NC effect. As R increases, the demand in high current(due to increase in C_{FE} near V_C) must be met with the higher increase in V_R ($=I \times R$).As $V_{APP}=V_R+V_{CFE}+V_{RFE}$, an increase in V_R must be supported by larger reduction in V_{RFE}. Hence, V_{FE} snap back increases with the increase in R. Therefore, the voltage window of NC effectincreases with the increase in R. Now, let us consider the range of R with higher values (R >10 kΩ).It is easy to understand that I decreases with the increase in R. Hence, the voltage-drop across R_{FE} ($V_{RFE}=R_{FE}\times I$) decreases, which reduces the V_{FE} overshoot. In other words, increase in R reduces the rate of change of V_{FE} because of which the polarization lag decreases. As the overshoot decreases, the voltage window of NC effect reduces with the increase in R. It is important to note that this non-monotonic dependence on R is a function of τ. In other words, the value of R for which the voltage window of NC effect becomes maximum also depends on the value of τ.

Similarly, for a constant R, the NC effect decreases with decreasing τ. In this case, the decrease inNC effect can be attributed to the decrease in overshoot ($V_{RFE}=I\times R_{FE}$), which is caused by decrease in R_{FE} ($=\tau/C_{FE}$) with the decrease in τ. Physically, decreasing τ reduces the polarization lag, thereby reducing the NC effect.

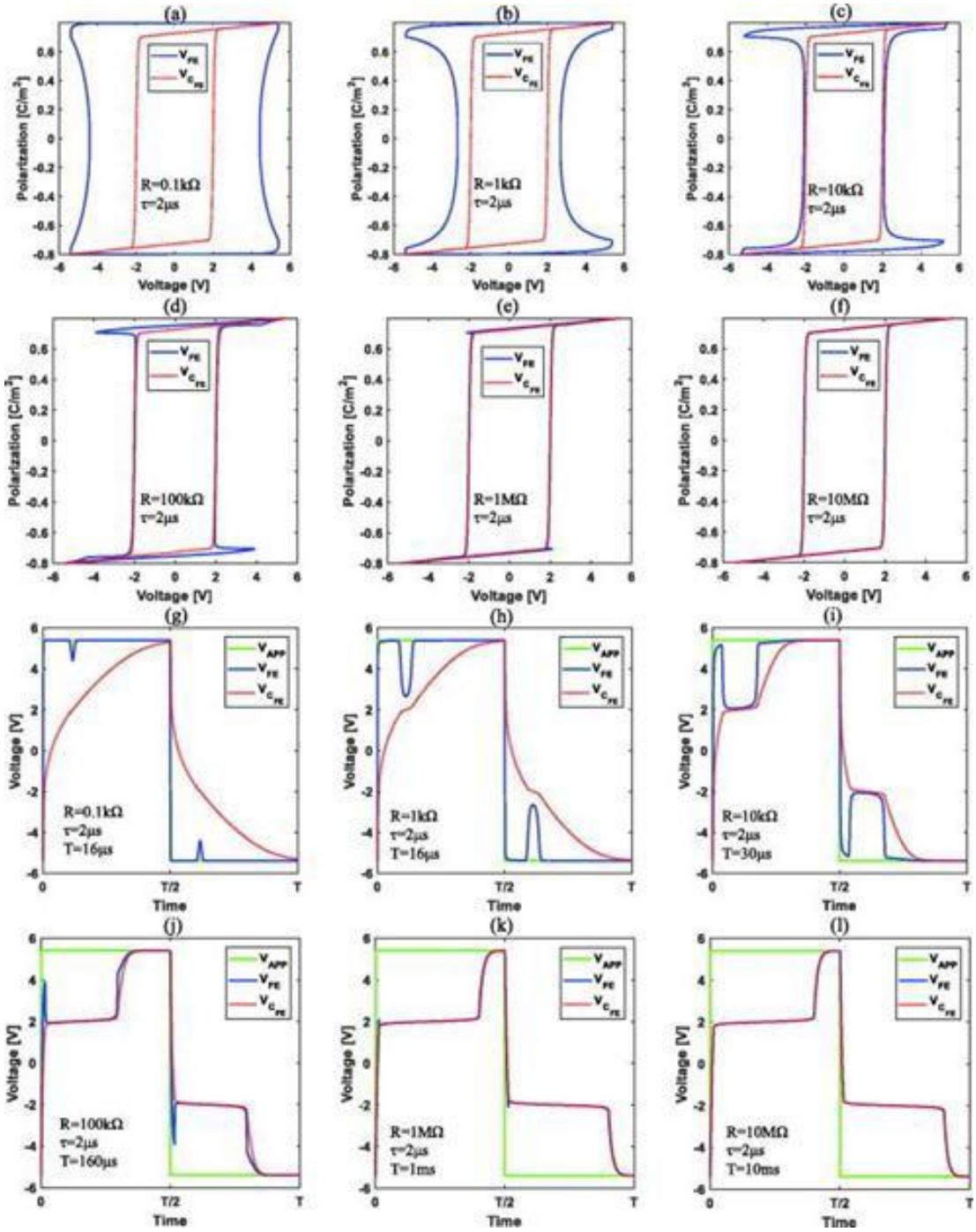

Figure 4.6. Considering Miller model (a)–(f) P–V_{FE} and $P-V_{CFE}$ loop of FE in a R-FE network under step input for R = 0.1 kΩ, 1 kΩ, 10 kΩ, 100 kΩ, 1 MΩ, 10 MΩ. (g)–(l) V_{FE} and V_{CFE} transients of FE in a R-FE network under step input for R = 0.1 kΩ, 1 kΩ, 10 kΩ, 100 kΩ, 1 MΩ, 10 MΩ.

(B) L-K model of FE

Considering step-input (dV_{APP}/dt = 0 and dV_{APP}/dV_{CFE}=0 for t > 0) and ρ = constant ($d\rho/dt$ = 0 and $d\rho/dV_{CFE}$=0), we can write the following equation from Eqs. (3.4) and (3.5):

$$\frac{dV_{FE}}{dP} = \frac{A_{FE}}{C_{FE}}\left[\frac{R}{R+\rho\left(\frac{T_{FE}}{A_{FE}}\right)}\right]$$

$$\frac{1}{C_{FE}}\left[\frac{R}{R+\rho\left(\frac{T_{FE}}{A_{FE}}\right)}\right] < 0 \qquad (4.12), (4.13)$$

According to Eq. (3.9), the NC effect can occur if and only if C_{FE} is negative. It is important to note that, considering a negative value of C_{FE}, the left hand side of Eq. (4.9) will be more negativewith an increase in R and decrease in ρ, which implies that the condition of NC effect is easier to meet with an increased value of R and a decreased value of ρ. Considering a positive step input, the graphical representations of Eq. (4.9) are shown in Figs. 4.6(a) and 4.6(b) for different valuesof R and ρ, respectively, to justify our previous statement. In the figure, the dashed line representsthe left hand side of Eq. (4.9) and the solid line represents the right hand side. So, the NC effect should occur within the range of polarization where dashed lines fall below the solid line. From Figs. 4.6(a) and 4.6(b), it is interesting to note that the polarization range, within which NC effectexists, does not depend on the value of R and ρ. This is because, according to L-K model, NC effect is directly attributed to negative C_{FE} [Eq. (4.9)] and the range of polarization for which $C_{FE}$is negative is only dependent on Landau coefficients.

Simulated P–V_{FE} and $P-V_{CFE}$ curves of FE in an R-FE network along with the transient result for different values of R are shown in Fig. 4.6. From Figs. 4.6(a)–4.6(f), it is evident that the voltage window of NC effect increases with the increase in external resistance (R). This is because, with the increase in R [while keeping $R_{FE} = \rho(T_{FE}/A_{FE})$ constant], the voltage drop across R (V_R) increases and that across R_{FE} (V_{RFE}) decreases (considering voltage division in two resistors). As V_{RFE} decreases, V_{FE} goes closer to V_{CFE} (because $V_{FE}=V_{CFE}+V_{RFE}$). This

means the $P–V_{FE}$ path of FE is more likely to follow the Landau path ($P-V_{CFE}$), which has the maximum NC effect, as can be observed in Figs. 4.7(a)–5.7(f). This argument can also be validated through Eq. (3.8), which can be re-written as $dV_{FE}/dP = A_{FE}/[C_{FE}(1 + R_{FE}/R)]$. The equation implies that with the increase in R, the magnitude of the negative dV_{FE}/dP increases, which means the voltage windowof NC effect increases for the same polarization range. In fact, for $R \gg R_{FE}$, $dV_{FE}/dP \approx A_{FE}/C_{FE}$ which leads to maximum NC effect. Similar trends are observed for decreasing ρ or R_{FE} (not shown), i.e., the NC voltage window increases with decrease in ρ.

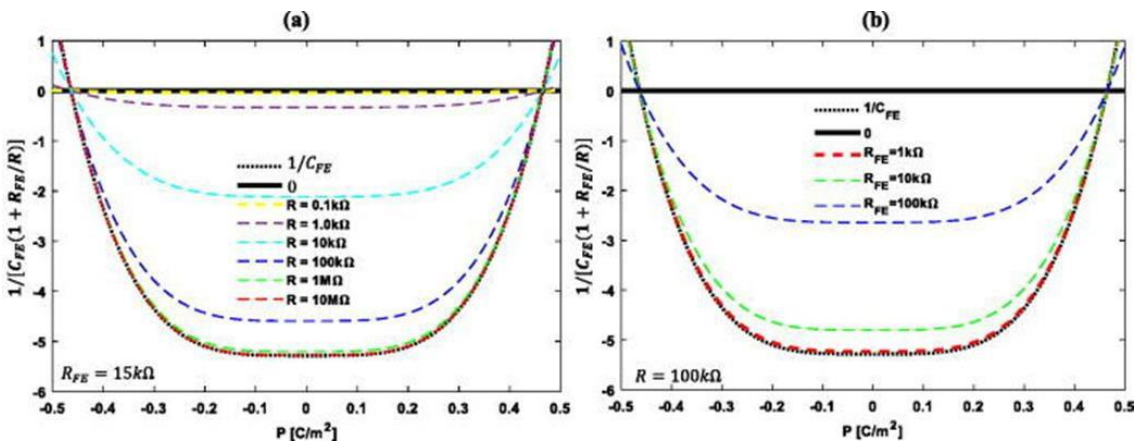

Figure 4.7. Graphical representation of Eq. (13) for (a) different values of R and (b) different values of R_{FE}.

Now let us outline the key dissimilarities between Miller and L-K models with respect to the NC effect in the R-FE network considering step-input that we discussed so far:

(i) Effects of R: With an increase in R, the polarization range of NC effect decreases according to Millermodel and remains unchanged according to the L-K model. However, the voltage window of NC effect (ΔV_{NC}) shows a non-monotonic trend with respect to R accordingto Miller model. In contrary, the L-K model predicts a strictly increasing trend. To visualize this difference, ΔV_{NC} for different values of R is shown in Fig. 3-8 consideringboth of the models. From Fig. 4.8, we can see that ΔV_{NC} increases with the increase inR for both models, if R is very low (R < ~10 kΩ). On the other hand, for a higher rangeof R (R > ~10 kΩ), ΔV_{NC} decreases according to the Miller model and increases according to the L-K model. In fact, according to our simulation for R = 10 MΩ, ΔV_{NC}vanishes for Miller model, whereas ΔV_{NC} is maximum for L-K model.

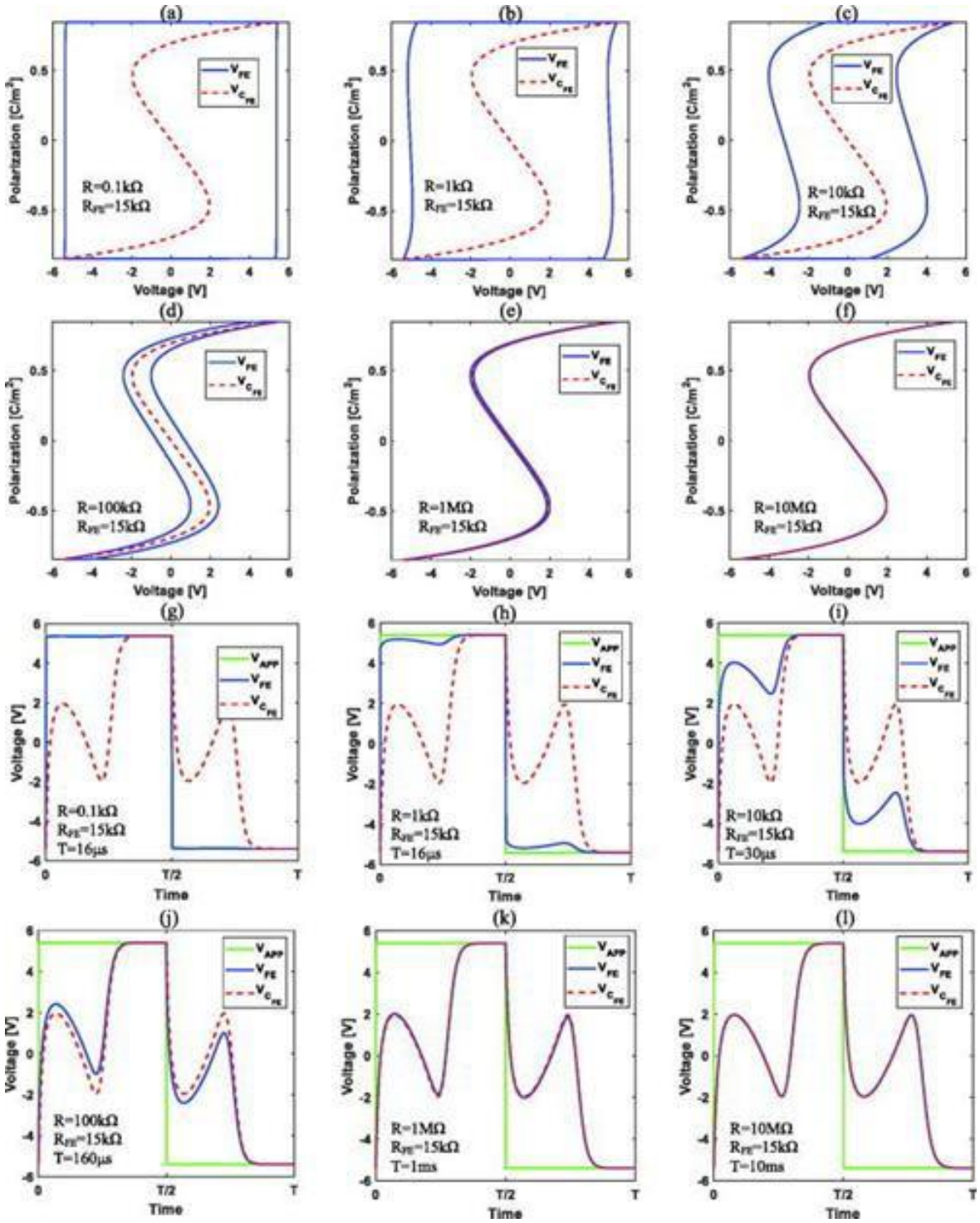

Figure 4.8. Considering L-K model (a)–(f) $P–V_{FE}$ and $P-V_{CFE}$ loop of FE in a R-FE network under step input for R = 0.1 kΩ, 1 kΩ, 10 kΩ, 100 kΩ, 1 MΩ, 10 MΩ. (g)–(l) V_{FE} and V_{CFE} transients of FE in a R-FE network under step input for R = 0.1 kΩ, 1 kΩ, 10 kΩ, 100 kΩ, 1 MΩ,10 MΩ.

(ii) Increase in τ or ρ: According to Miller model, the voltage window and polarization range of NC effect increase with the increase in τ. However, according to L-K model, the voltage window of NC effect decreases with the increase in ρ, while the polarization range ofNC effect remains unchanged.

(iii) After the application of positive step input in the R-FE network, V_{FE} (within the voltagewindow of NC effect) can decrease beyond 0 V and even go to negative voltage for a high value of R in case of L-K model [Figs. 4.7(d)–5.7(f)]. However, for a low value of R, V_{RFE} may remain in positive voltage [Figs. 4.7(a)–5.7(c)]. In contrast, accordingto the Miller model, V_{FE} can decrease up to V_{CFE} but can never be negative [Figs. 4.5(a)–5.5(f)]. Interestingly, in experimental results reported so far, V_{FE} is alwayspositive within the NC window for positive step input in an R-FE network.

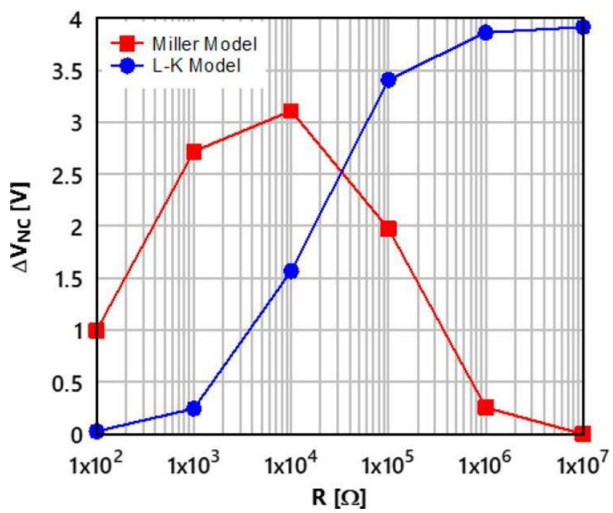

Figure 4.9. Voltage window of NC effect (ΔV_{NC}) for different values of R considering Miller and L-K models.

The above discussion assumed constant τ and ρ. However, it is important to note that even if τ andρ are not constant, the trends we described earlier for changing external resistance (R), τ and ρ, donot change. We briefly discuss the cases here.

4.3.3 Step input with variable τ and ρ

(A) Miller model of FE

(i) $\tau \neq$ constant: Let us recall Eq. (3.3), which gives the generic condition of NC effect. It can be observed that if τ decreases with increasing polarization (or V_{CFE}), i.e., $d\tau/dV_{CFE}$ is negative, then NC effect will be more prominent compared to τ = constant. Similarly, the NC effect decreases if $d\tau/dV_{CFE}$ is positive. It may be noted that according to Merz'slaw [25] τ decreases with an increase in V_{CFE} (or V_{FE}). This dependence has an impact on the trends of NC effect with respect to R. It is easy to understand that the transient voltage across FE decreases with the increase in R. That implies an increase in τ within the NC regime. Therefore, voltage-dependent τ, as per Merz's law, tends to increase the voltage window of NC effect with the increase in R. Recall our earlier discussion (assuming constant τ) that the voltage window of NC effect changes non-monotonically with the increase in R due to multiple factors. Now, with the insight of this discussion on variable τ, we can expect an increase in the range of R within which the NC effect shows increasing trend with the increase in R compared to the case when τ is constant.

(ii) $\tau \propto C_{FE}$: Let us assume $\tau = R_0C_{FE}$, where R_0 is a proportionality constant, which is similar to say that $R_{FE} = R_0$ = constant. Putting $\tau = R_0C_{FE}$ in Eq. (3.2), we can derive the condition of NC effect as follows:

$$\frac{1}{C_{FE}}\left[\frac{R_0}{R + R_0}\right] < 0 \tag{4.14}$$

Interestingly, from Eq. (3.10) we can say that NC effect can only occur if $C_{FE} < 0$, which is not possible for Miller model as $C_{FE} > 0$. Thus, according to Miller model, NC effect does not take place, if $\tau \propto C_{FE}$ or R_{FE} = constant. Now, let us recall one of our earlier discussions regarding Ref.[13]. In Ref. [13], the NC effect has been demonstrated in an R-FE network, where FE has been modeled as a series connected time variant capacitor and a constant resistor. Here, we argue that, if we consider the capacitor as voltage variant (as in Miller model) rather than time variant, then NC effect cannot be observed for constant R_{FE}. Since voltage dependence of C_{FE} is more fundamental, our analysis accounts for the time dependence of C_{FE} through voltage,

i.e., $dC_{FE}/dt = dC_{FE}/dV_{FE} \times dV_{FE}/dt$. Since Ref. [13] considers a generic time dependence of C_{FE}, our conclusions are different than Ref. [13]. It may be reiterated that if R_{FE} is not constant, the NC effect can be observed as discussed before.

(B) L-K model of FE

Considering positive step input, let us recall Eq. (3.5), which indicates that NC effect takes place due to negative C_{FE}. That means, when polarization increases V_{CFE} decreases. So, from Eq. (3.5), it is evident that, if ρ decreases with increasing polarization (or decrease in V_{CFE}), $d\rho/dV_{CFE}$ is positive. That means the left hand side of Eq. (3.5) will be more negative, which implies an increase in the NC effect. Similarly, we can say that NC effect decreases if ρ shows an increasingbehavior with decreasing polarization.

4.3.4 Ramp input

The discussion in the previous sub-section is focused on the step response of the R-FE network. We now discuss response to a ramp input voltage (V_{APP}) and describe the impact on NC effect forboth models.

(A) Miller model of FE

Let us recall Eq. (3.3) for the Miller model, which is the generic condition of NC effect in the R- FE network. Now for simplicity, considering constant τ we can rewrite Eq. (3.3) as follows

$$\left|\frac{dC_{FE}}{dV_{C_{FE}}}\right| > \frac{\frac{dV_{APP}}{dV_{C_{FE}}} + \frac{RC_{FE}}{\tau}}{R\left|dV_{C_{FE}}/dt\right|} \tag{4.15}$$

As V_{CFE} is driven by V_{APP}, it is intuitive that an increase in ramp rate ($|dV_{APP}/dt|$) causes an increase in $|dV_{CFE}/dt|$. Now, from Eq. (3.11), we can observe that right hand side of the equation decreases with increase in $|dV_{CFE}/dt|$. (Note, the change in $|dV_{APP}/dV_{CFE}|$ in Eq. (3.11) is negligible, because both numerator and denominator of $|dV_{APP}/dV_{CFE}|$(=$|dV_{APP}/dt|/|dV_{CFE}/dt|$) increase with $|dV_{APP}/dt|$.) Since the right hand side of Eq. (3.11) decreases with the increase in $|dV_{APP}/dt|$, it becomes easier to meet the condition of NC effect due to increase in the ramp rate. In other words, considering the Miller model, NC effect in the R-FE network increases with the increase in the ramp rate of input

voltage. Simulated $P–V_{FE}$ and $P-V_{CFE}$ in the R-FE network for alternating ramp input with different ramp rates are shown in Fig. 4.9(a), which show the increase in the voltage window of NC effect with the increase in the ramp-rate of V_{APP}. To get the physical picture of this phenomena, we can think that an increase in dV_{APP}/dt yields a larger displacement current (I). This, in turn, causes the voltage drop across R_{FE} ($V_{RFE}=IR_{FE}$) to increase leading to a larger voltageovershoot. In other words, with the increase in dV_{APP}/dt, effects of P lag increase. Such increased voltage overshoot followed by snap back (due to sudden increase in C_{FE}) causes an increased voltage window of NC effect. From Fig. 4.9(a) we can see such increased overshoot (difference between a black dashed line and colored solid line) due to increase in ramp rate. This results in a larger voltage window of NC effect.

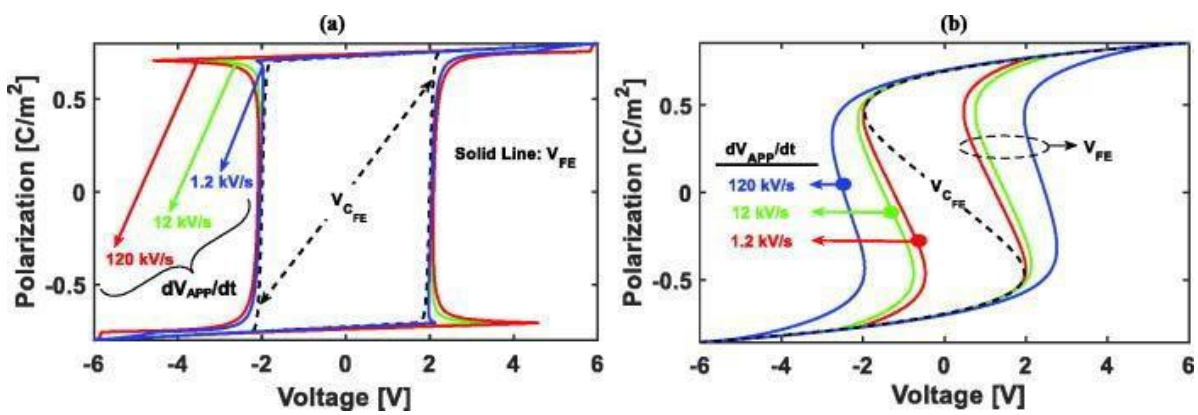

Figure 4.10. $P–V_{FE}$ and $P-V_{CFE}$ loop of FE in a R-FE network under ramp input for different dV_{APP}/dt considering (a) Miller model and (b) L-K model. (Here, the external resistance R = 10 kΩ.).

(B) L-K model of FE

Now, considering L-K model, let us recall Eq. (3.5). The equation represents the generic condition of NC effect in the R-FE network. Assuming $d\rho/dV_{CFE}=0$ (for simplicity), we can rewrite Eq. (3.5) as follows:

$$\frac{C_{FE}}{|I|(R+\rho(T_{FE}/A_{FE}))}\left[1+\frac{\rho T_{FE}}{A_{FE}R}\left(\frac{dV_{APP}}{dV_{C_{FE}}}\right)\right]<0 \tag{4.16}$$

Let us recall our earlier discussion that with the increase in $|d_{VAPP}/dt|$, $|dV_{CFE}/dt|$ also increases. So,current ($I=C_{FE}\times(dV_{CFE}/dt)$) increases with the increase in ramp rate. Now from Eq. (3.12), we cansay that the left hand side of the equation becomes less negative with the increase in |I|. (Like ourdiscussion for Miller model, here also the change in $|dV_{APP}/dV_{CFE}|$ is negligible compared to the change in $|dV_{CFE}/dt|$ due to increase in ramp rate.) That means, the NC effect decreases with the increase in ramp-rate of the input voltage. Simulated $P–V_{FE}$ and $P-V_{CFE}$ curves of FE in the R-FE network for alternating ramp input with different ramp rates are shown in Fig. 4.9(b). These resultsvalidate the trend discussed above. The figure shows that $P–V_{FE}$ curves of FE move away from the$P-V_{CFE}$ curve with an increase in ramp-rate of V_{APP}. The reason for this behavior can be attributedto the increase in $|I|$ with the increase in $|dV_{APP}/dt|$. That causes increase in voltage drop across $R_{FE}$and V_{FE} to be higher V_{CFE} (because $V_{FE}=V_{CFE}+V_{RFE}$). That is why FE is less likely to follow the Landau path ($P-V_{CFE}$), which implies a decrease in NC effect with increase in ramp rate. Thus, the trends for NC effect with respect to the ramp rate are opposite for L-K and Miller models (i.e.,NC effect increases with increasing ramp rate for Miller model while it decreases for the L-K model).

From the analysis in this section, we can draw two important conclusions that can guide future experiments. First, for step input, NC effect shows a non-monotonic trend with respect to R for the Miller model, but an increasing behavior for the L-K model. Second, for ramp input, with the increases in ramp rate ($|dV_{APP}/dt|$), NC effect increases according to Miller model but decreases according to L-K model.

So far, our discussion was based on the assumption that the peak value of V_{APP} and therefore V_{FE} issufficiently large for the FE to be fully polarized, i.e., to follow the major loop across all the rangesof the parameters considered. However, if the peak value of V_{APP} is not sufficiently large in the experimental setup, V_{FE} may not able to reach the coercive voltage of major loop, which implies that FE will traverse through minor loop. Hence dC_{FE}/dV_{CFE} near the coercive voltage of FE will decrease. According to our analysis on Miller model,if dC_{FE}/dV_{CFE} decreases, NC effect will also decrease in an R-FE network. Lower the peak V_{APP}, smaller the minor loops will be, which will reduce or even eliminate the NC effect. Hence, in addition to the trends

discussed in this section with respect to R, τ, and ramp rate, the impact of peak value of V_{APP} may also need to be considered for the NC effect, especially when traversal through minor loops becomes likely. It is important to note that whether or not the minor loops aretraversed, increase in R yields a non-monotonic trend in NC effect considering the Miller model and therefore, the conclusions and differences between the two models presented above hold true.

4.4 Summary

In this chapter, we have explained and analyzed the experimentally observed NC effect of FE in the R-FE network through the Miller model, where the intrinsic capacitance of FE is strictly positive. From this analysis, we have developed an argument that the experimentallyobserved NC effect may not be necessarily because of the intrinsic negative capacitance path of Landau theory. Rather, such an NC effect can be caused by an increase in the slope of *P-V* characteristics of FE near the coercive voltage and the polarization lag with respect to an applied electric field associated with nucleation and domain-wall propagation. We have also pointed out several key differences or opposite trends in NC effect between our explanation (Miller model: FEcapacitor is intrinsically positive) and the previous explanation (L-K model: FE capacitor can be intrinsically negative). Some of them are as follows: (i) with the increase in external resistance (R)in R-FE network, NC effect shows a non-monotonic trend (increases for lower range of R and decreases for higher range of R) according to Miller model, while NC effect monotonically increases according to L-K model. Keeping these trends in mind, it may be possible to experimentally investigate the NC effect further which will be important for the advancement of FE based devices.

4.5 References

[1] A. M. Ionescu and H. Riel, “Tunnel field-effect transistors as energy-efficient electronic switches,” Nature 479, 329–337 (2011).

[2] N. Shukla, A. V. Thathachary, A. Agrawal, H. Paik, A. Aziz, D. G. Schlom, S. K. Gupta, R. Engel-Herbert, and S. Datta, “A steep-slope transistor based on abrupt electronic phase transition,” Nat. Commun. 6, 7812 (2015).

[3] T. N. Theis and P. M. Solomon, “It's time to reinvent the transistor!,” Science 327(5973),

1600–1601 (2010).

[4] T. N. Theis and P. M. Solomon, “In quest of the “Next Switch”: Prospects for greatly reduced power dissipation in a successor to the silicon field-effect transistor,” Proc. IEEE 98(12), 2005–2014 (2010).

[5] S. Salahuddin and S. Datta, “Use of negative capacitance to provide voltage amplification for low power nanoscale devices,” Nano Lett. 8(2), 405–410 (2008).

[6] L. D. Landau and I. M. Khalatnikov, “On the anomalous absorption of sound near a second order phase transition point,” Dokl. Akad. Nauk SSSR 96, 469–472 (1954).

[7] W. J. Hu, D. Juo, L. You, J. Wang, Y. Chen, Y. Chu, and T. Wu, “Universal ferroelectric switching dynamics of vinylidene fluoride-trifluoroethylene copolymer films,” Sci. Rep. 4, 4772 (2014).

[8] E. B. Araujo and J. A. Eiras, “Effect of temperature and frequency on dielectric and ferroelectric properties of PZT thin films,” Mater. Lett. 46, 265–269 (2000).

[9] C. Wang, K. Laub, and Q. Wanga, “Dynamic hysteresis and scaling behaviours of lead-free $0.94Bi_{0.5}Na_{0.5}TiO_{3-0.06}BaTiO_3$ bulk ceramics,” RSC Adv. 6, 30148–30153 (2016).

[10] A. I. Khan, K. Chatterjee, B. Wang, S. Drapcho, L. You, C. Serrao, S. R. Bakaul, R. Ramesh, and S. Salahuddin, “Negative capacitance in a ferroelectric capacitor,” Nat. Mater. 14, 182–186 (2015).

[11] A. I. Khan, D. Bhowmik, P. Yu, S. J. Kim, X. Pan, R. Ramesh, and S. Salahuddin, “Experimental evidence of ferroelectric negative capacitance in nanoscale heterostructures,” Appl. Phys. Lett. 99, 113501 (2011).

[12] W. Gao, A. Khan, X. Marti, C. Nelson, C. Serrao, J. Ravichandran, R. Ramesh, and S. Salahuddin, “Room-temperature negative capacitance in a ferroelectric-dielectric superlattice heterostructure,” Nano Lett. 14(10), 5814–5819 (2014).

[13] S. J. Song, Y. J. Kim, M. H. Park, Y. H. Lee, H. J. Kim, T. Moon, K. D. Kim, J. Choi, Z. Chen, A. Jiang, and C. S. Hwang, “Alternative interpretations for decreasing voltage with increasing charge in ferroelectric capacitors,” Sci. Rep. 6, 20825 (2016).

[14] A. T. Bartic, D. J. Wouters, H. E. Maes, J. T. Rickes, and R. M. Waser, “ Miller model for the simulation of ferroelectric capacitors,” J. Appl. Phys. 89, 3420 (2001).

[15] L. D. Landau, “Theory of phase transformations. I,” Zh. Eksp. Teor. Fiz. 7, 19 (1937).

[16] L. D. Landau, “Theory of phase transformations. II,” Zh. Eksp. Teor. Fiz. 7, 627 (1937).

[17] S. L. Miller, J. R. Schwank, R. D. Nasby, and M. S. Rodgers, “Modeling ferroelectric capacitor switching with asymmetric nonperiodic input signals and arbitrary initial conditions,” J. Appl. Phys. 70, 2849 (1991).

[18] A. F. Devonshire, “Theory of barium titanate: Part I,” Philos. Mag. 40, 1040 (1949).

[19] A. F. Devonshire, “Theory of barium titanate: Part II,” Philos. Mag. 42, 1065 (1951).

[20] A. F. Devonshire, “Theory of ferroelectrics,” Adv. Phys. 3, 85 (1954).

[21] A. Sutor, S. J. Rupitsch, and R. Lerch, “A Miller-based hysteresis model for magnetic and ferroelectric hysteresis,” Appl. Phys. A 100, 425–430 (2010).

[22] K. Dragosits, R. Hagenbeck, and S. Selberherr, “Transient simulation of ferroelectric hysteresis,” in Proceedings of the International Conference on Modeling and Simulation of Microsystems (2000), pp. 433–436.

[23] S. Chang, U. E. Avci, D. E. Nikonov, S. Manipatruni, and I. A. Young, “Physical origin of transient negative capacitance in a ferroelectric capacitor,” Phys. Rev. Applied 9, 014010 (2018).

[24] M. Hoffmann, M. Pešić, K. Chatterjee, A. I. Khan, S. Salahuddin, S. Slesazeck, U. Schroeder, and T. Mikolajick, “Direct observation of negative capacitance in polycrystalline ferroelectric HfO2,” Adv. Funct. Mater. 26, 8643–8649 (2016).

[25] W. J. Merz, “Domain formation and domain wall motions in ferroelectric $BaTiO_3$ single crystals,” Phys. Rev. 95, 690–698 (1954).

[26] P. Sharma, J. Zhang, A. K. Saha, S. Gupta, and S. Datta, “Negative capacitance transients in metal-ferroelectric $Hf_{0.5}Zr_{0.5}O_2$-insulator-semiconductor (MFIS) capacitors,” in 2017 75th Annual Device Research Conference (DRC) (2017), Vol. 75, pp. 1–2.

[27] P. Sharma, K. Tapily, A. K. Saha, J. Zhang, A. Shaughnessy, A. Aziz, G. L. Snider, S. Gupta, R. D. Clark, and S. Datta, “Impact of total and partial dipole switching on the switching slope of gate-last negative capacitance FETs with ferroelectric hafnium zirconium oxide gate stack,” in Symposium on VLSI Technology (2017).

[28] M. Si, C. Su, C. Jiang, N. J. Conrad, H. Zhou, K. D. Maize, G. Qiu, C. Wu, A. Shakouri, M. A. Alam, and P. D. Ye, “Steep slope MoS_2 2D transistors: Negative capacitance and negative differential resistance,” Nature Nanotechnology 13, 24–28 (2018).

5. PHASE-FIELD MODELING OF POLARIZATION SWITCHING IN FERROELECTRIC HZO

5.1 Introduction

In this chapter, we analyze the accumulative polarization (*P*) switching characteristics of ferroelectric (FE) thin films under the influence of sequential electric-field pulses. By developing a dynamic phase-field simulation framework based on time-dependent Landau-Ginzburg model, we analyze *P* excitation and relaxation characteristics in FE. In particular, we show that the domain-wall instability can cause different spontaneous *P*-excitation/relaxation behaviors that, in turn, can influence *P*-switching dynamics for different pulse sequences. By assuming a local and global distribution of coercive field among the grains of an FE sample, we model the *P*-accumulation process in $Hf_{0.4}Zr_{0.6}O_2$ (HZO) and its dependency on applied electric field and excitation/relaxation time. According to our analysis, domain-wall motion along with its instability under certain conditions leads to spontaneous *P*-excitation and *P*-relaxation, which play a pivotal role in accumulative *P*-switching. Such phenomena depend on the extent of accumulated-*P* and are more prominent in scaled FE samples.

Ferroelectric (FE) materials, particularly Zr doped HfO2 (Hf1-xZrxO2:HZO [1]) have drawn significant research interest in recent times due to CMOS process compatibility [2], thickness scalability [3,4] as well as many promising attributes of ferroelectric field effect transistors [2,5] (FEFETs) for low-power logic [5-8] and non-volatile memories [9-10] applications. In addition, FEFETs can provide multiple non-volatile resistive states that harness the multi-domain FE characteristics, leading to the possibilities for multi-bit synapses [11,12] in a neuromorphic hardware [13]. Further, newly reported accumulative polarization (P)-switching process [14] in ultra-thin FE leads to many appealing opportunities for novel applications like correlation detection [15] and other non-Boolean computing paradigms [16]. For such emerging applications of FEFETs, the P-switching dynamics in response to sub/super-coercive voltage pulse trains play an important role and are, therefore, critical to understand.

To that effect, we analyze the spatially local P-switching dynamics and its participation in globally observable P-accumulation characteristics in response to a pulse train. Our analysis is based on a dynamic phase field model [17, 18] coupled with measured accumulation characteristics of HZO. By providing the spatial distribution of P (P-map) in different electric field (E-field) excitation and relaxation steps, we discuss different types of P excitation and relaxation processes and their corresponding dependency on E-field (E) amplitude (E^{app}_{max}), ON time (or excitation time T_{on}) and OFF time of the pulse (or relaxation time T_{off}). Finally, considering a coercive-field distribution among different FE grains, we analyze the experimental P-accumulation characteristics by utilizing our simulation framework.

5.2 Experimentally Observed Accumulative Polarization Switching in HZO

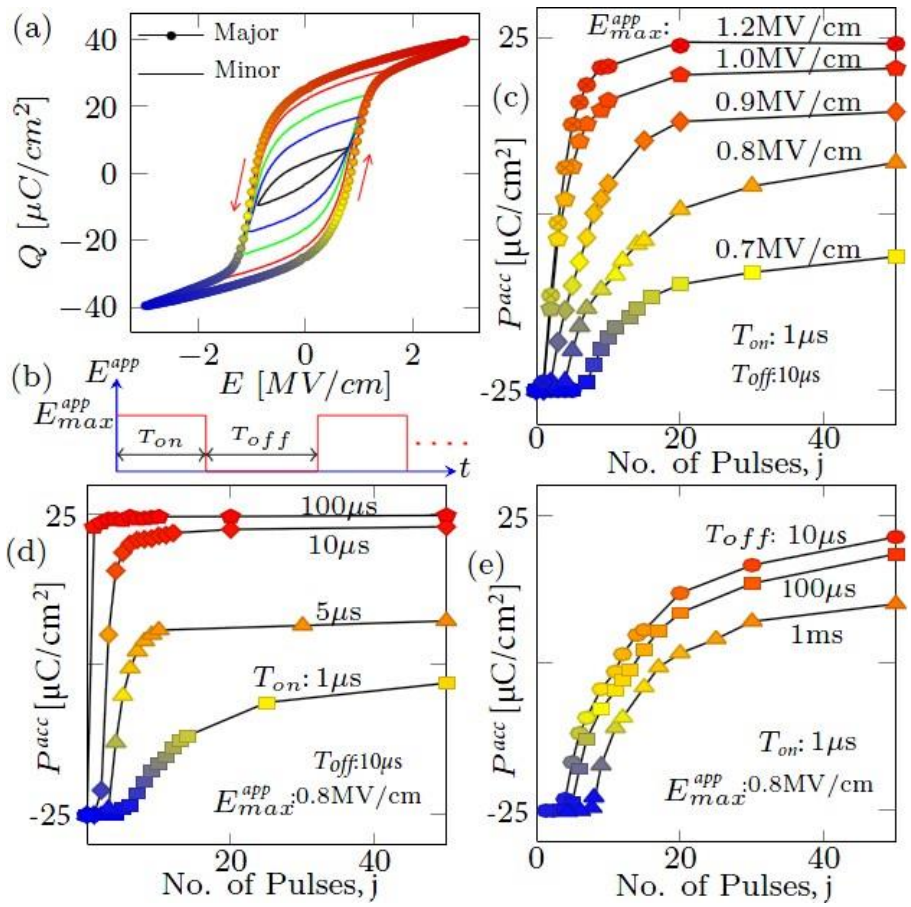

Figure 5.1. (a) Q-E curves of a 10nm HZO film. (b) Applied E-field pulses showing pulse-amplitude (E^{app}_{max}), excitation time (Ton) and relaxation time (Toff). Accumulated polarization, P^{acc} vs. number of E-field pulses (j) for different (c) E^{app}_{max}, (d) Ton and (e) Toff.

Let us start by describing the experimentally observed P-switching characteristics in HZO. Fig. 5.1(a) shows the measured charge vs. E-field (Q-E) characteristics of a 10nm HZO film (x=0.6, grown by ALD with W capping layer as top and bottom contact). Here, Q=P+ϵ_0E, where ϵ_0 is the vacuum permittivity. We observe excellent accumulative P-switching in HZO as the response of successive E-field stimulation (Fig. 5.1(b)), where the P-accumulation (P^{acc}) characteristics exhibit a strong dependence on the E-pulse properties. For example, we observe faster P^{acc} with the increase in E_{max}^{app} (Fig. 5.1(c)), increase in Ton (Fig. 5.1(d)) and/or decrease in Toff (Fig. 5.1(e)). Also, P^{acc} saturates after a certain number of pulses. Such saturation occurs at higher P with the increase in E_{max}^{app} , increase in Ton and decrease in Toff. It is noteworthy that such accumulated-P observed in the experiments is the average of locally accumulated-P in different grains. Hence, to explain the experimental results described above, it is critical to understand the spatially local P-switching dynamics in an individual grain. We analyze such processes in detail based on our phase-field model, calibrated to the experiment.

5.3 Phase-field Simulation of metal-ferroelectric-metal

Considering a thin (~10nm) FE film, we assume that the P direction is only along the thickness (z-axis). Hence, Px=0, Py=0, Pz≠0 and Pz can have a spatial distribution in x-y plane. However, we assume uniform Pz along the z-axis (dPz/dz=0) owing to the ultra-thin nature of the film. The temporal and spatial evolution of P can be described by the time (t)-dependent Landau-Ginzburg (TDLG) equation [18, 19]: $\delta F/\delta Pz = -\rho(\partial Pz/\partial t)$. Here, ρ is the kinetic coefficient and F is the total energy [19] of the system composed of free energy, domain-wall energy, electrostatic and electroelastic energy. Considering up to the 6th order terms in Landau's free energy expansion [20], the normalized representation of TDLG equation within the FE is given by the following equation.

$$-\rho_n \frac{dP_n}{dt} = -E_n^{app} - K_P^n \nabla^2 P_n + \hat{\alpha} P_n + \hat{\beta} {P_n}^3 + \hat{\gamma} {P_n}^5 \tag{5.1}$$

Here, Pn (=P_Z/P_C) and E_n^{app} (=E^{app}/E_C) are polarization and E-field normalized with respect to E_C (coercive field) and P_C (P at E=E_C), respectively. $\hat{\alpha}$, $\hat{\beta}$ and $\hat{\gamma}$ are the normalized Landau coefficients, ρ_n is the normalized kinetic coefficient and k_p^n is the normalized domain-interaction parameter. Eqn. 7.1, is similar to the Euler-Lagrange equation of motion [21], incorporates

interactions among neighboring domains (via $K^n\nabla^2 P_n$) giving rise to Klein-Gordon type field equation [22]. In our simulations, we self-consistently solve eqn. 5.1 in a real space grid by considering Neumann boundary at the edges [23]. It is noteworthy that Pn denotes normalized microscopic P in each grid point, while the analogous quantity of experimentally measured P is spatial average of P_n, denoted as $\bar{Pn}$. Also, $K^n\nabla^2 P_n$ can be thought of as the local effective interaction E-field, E^{int}. Therefore, the P switching depends on $E_{napp}+E_{nint}$. For instance, P-switching will occur for $|E_{napp}+E_{nint}|>1$ (since the normalized coercive field=1).

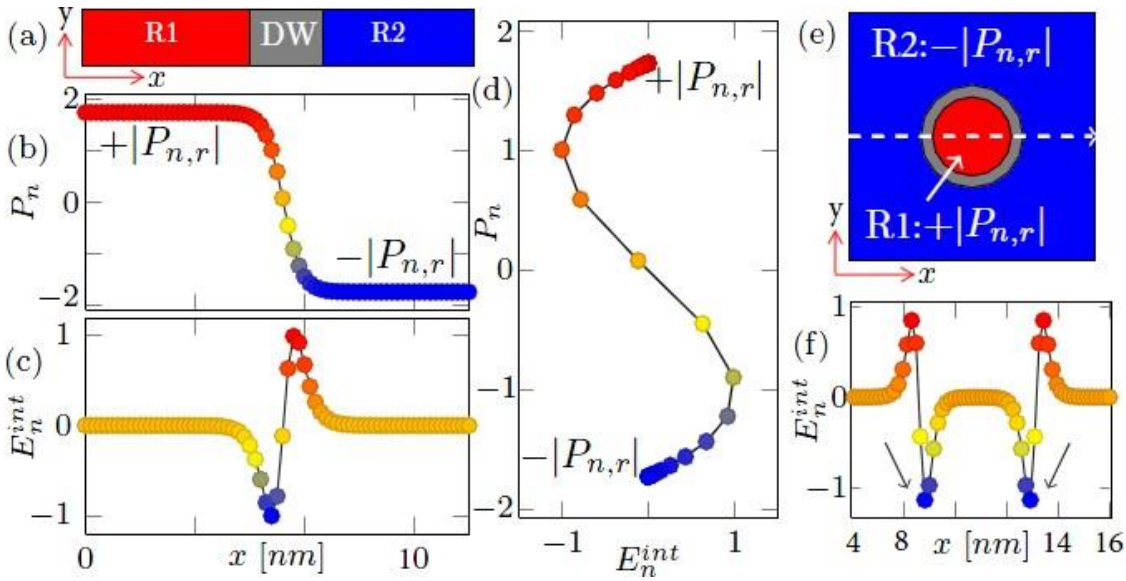

Figure 5.2. (a) FE structure showing 1D domain-wall (DW) and spatial distribution of (b) polarization, P_n and (c) interaction E-field, E_n^{int}. (d) Static P_n-E_n^{int} relation. (e) FE structure showing 2D DW and spatial distribution of (f) E_n^{int} along the x-axis.

In general, P-switching can take place in two different ways, namely (i) direct nucleation and (ii) Domain-wall (DW) assisted nucleation. To understand such P-switching processes, let us start by considering the FE sample in Fig. 5.2(a), where region R1 exhibits Pn=+|Pn,r| and R2 exhibits Pn=-|Pn,r| and they are separated by a DW within which Pn varies gradually along the x-axis (Fig. 5.2(b)). Here, Pn,r is the remnant polarization. In this case, the domain structure is effectively 1D as $d^2P_n/dy^2=0$. Direct nucleation occurs for super-coercive applied fields ($|E_n^{app}|>1$), wherein region R2 will switch to +P at once if E-field is applied for a sufficient time. On the other hand, DW assisted nucleation (which is the main focus of this work) is observed for sub-coercive applied fields ($|E_n^{app}|<1$), in which E_{nint}

plays a key role. To explain this, let us consider E_n^{app}=0 and static condition (dPn/dt=0). Hence, eqn. (7.1) can be written as, E_n^{app}=$K_{Pn}\nabla^2 P_n=\hat{\alpha}_n P_n+\hat{\beta}_n P_n^3+\hat{\gamma}_n P_n^5$. Note, E_n^{int} is localized and non-zero only within DW (Fig. 5.2(c)). Fig. 5.2(d) shows the relation between E_n^{int} and Pn, signifying that the symmetric spatial distribution of Pn provides a symmetric E_n^{int} in the 1D case. Here, the symmetric E_n^{int} plays a critical role by balancing the forces due to E_n^{int} ($\propto PE_n^{int}$) on the two sides of the DW, yielding stable and static DW for E_n^{app}=0. This can also be understood by noting that $|E_n^{int}|\leq 1$, which leads to stable DW due to no P-switching. However, by applying a sub-coercive E-field, $0<|E_n^{app}|<1$, we can get a total local E-field, $|E_n^{app}+E_n^{int}|>1$ and that can eventually initiate P-switching. Such P-switching is a spatially local and temporally gradual process, which is referred to DW motion or DW assisted nucleation.

5.4 Polarization Switching Dynamics in 2D FE Grain

With the understanding of the 1D DW, let us now consider 2D DW and the corresponding P-switching for which, we analyze two cases by considering homogeneous E_C (case-1) and a distribution of E_C (case-2) in an FE grain.

5.4.1 Case-1: Homogeneous Coercive-field

Let us start with case-1 and consider a square FE sample (Fig. 5.2(e)) where a circular region R1 exhibits Pn=+|Pn,r|, which is surrounded by R2 with Pn=-|Pn,r|. Here, the DW is 2D and the corresponding $\nabla^2 P_n$ in the polar coordinate can be written as $[(\partial^2 P_n/\partial r^2)+(1/r)(\partial P_n/\partial r)]$. Note that, the $(1/r)(\partial P/\partial r)$ term exhibits a radial (r) dependency and hence, $\nabla^2 P_n$ becomes radially asymmetric, even for a symmetric radial distribution of P_n (symmetric $\partial^2 P_n/\partial r^2$ and $\partial P_n/\partial r$). Therefore, E_{nint} becomes spatially asymmetric (Fig. 5.2(f)), where $|E_{nint}|>1$ at the inner interface and $|E_{nint}|<1$ at the outer interface of DW. Such asymmetry in the E_{nint} causes the DW to undergo an effective inward force. Consequently, the DW becomes unstable and R1 region shrinks spontaneously with time (as $|E_{nint}|>1$ at the interior end of the DW). Such spontaneous phenomena play an important role in the P-switching dynamics that we discuss subsequently. (Note, such a DW instability is in contrast with the 1D case that we discussed above where symmetric E_{nint} leads to stable DW).

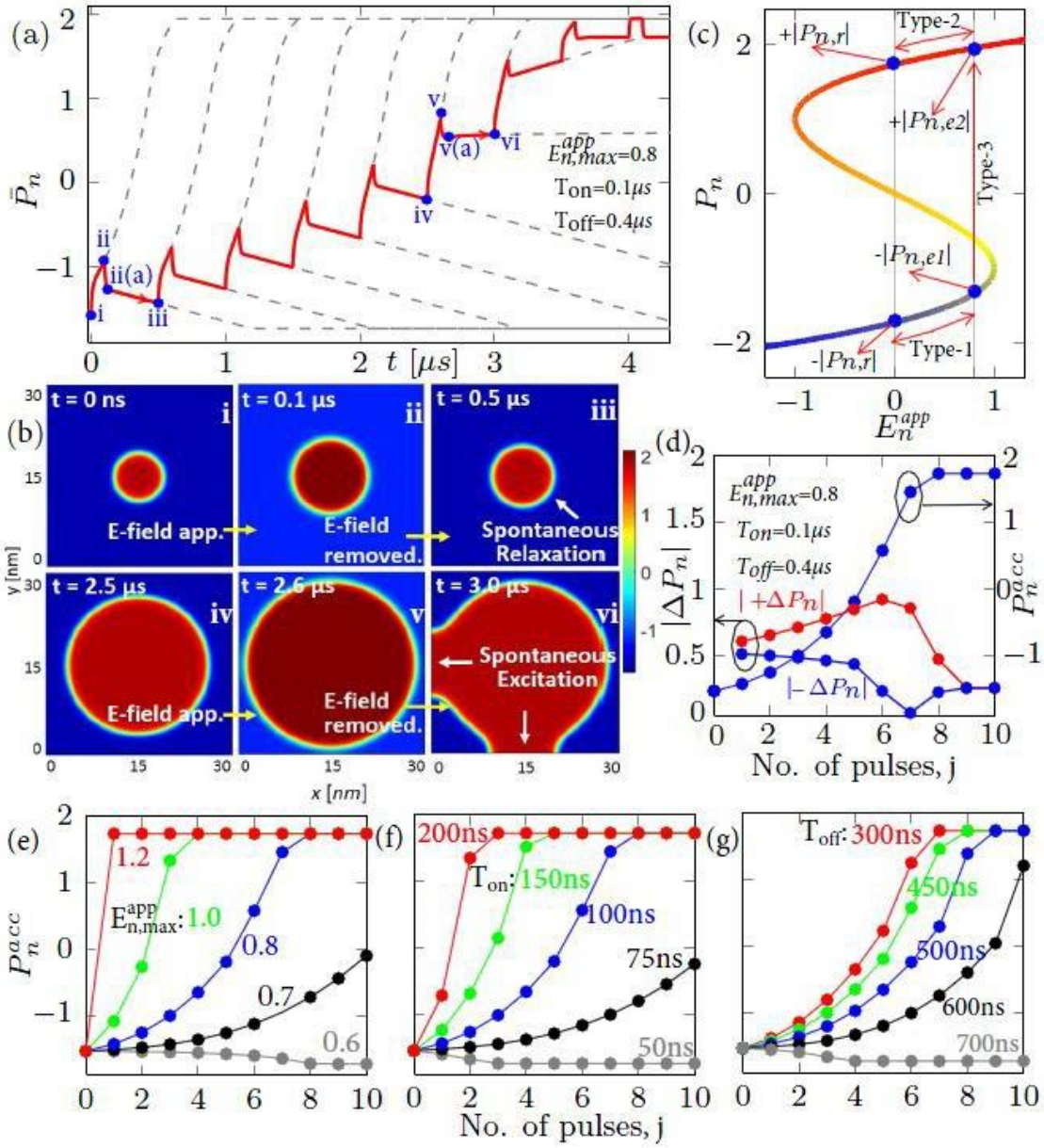

Figure 5.3. (a) Simulated transient $\bar{P}_n$ considering case-1 for a sequence of E-field pulses. Corresponding (b) P-map at point i-vi. (c) Static P_n vs. E_n^{app} showing different stimulated excitation/relaxation components. (d) Increase and decrease in P_n (respectively $|\Delta^+P_n|$ and $|\Delta^-P_n|$) and accumulated P (P_n^{acc}) in each excitation/relaxation sequence w.r.t. pulse number (j). P_{nacc} vs. j for different (e) $E^{app}_{n,max}$, (f) T_{on} and (g) T_{off} .

Let us now consider a sequence of sub-coercive E-field pulses ($E_{n,maxapp}$=0.8) applied to this sample of FE. Simulated transient P_n is shown in Fig. 5.3(a) and the initial P-map at t=0ns is shown in Fig.

5.3(b)-i, where the initially switched region (red) can be assumed as a pinned-type domain. After the arrival of first E-field pulse, R1 domain grows circularly, nucleating new lattices sequentially at the outer edge of the DW (Fig. 5.3(b)-ii). That implies an increase in R1 area and decrease in R2 area by an amount ΔA_{j+} (j= E-field pulse number). The corresponding P-excitation characteristics (Fig. 5.3(a):(i-ii)) comprise of three different components (Fig. 5.3(c)), *i.e.* type-1: -|Pn,r| to -|Pn,e1| (in R2), type-2: +|Pn,r| to +|Pn,e2| (in R1) and type-3: -|Pn,r| to +|Pn,e2| (in ΔA_{j+}).

After the end of first E-field pulse, the DW propagation stops and the P changes due to type 1 and 2 components get immediately relaxed to -|Pn,r| and +|Pn,r|, respectively. We call these type-1 and 2 relaxations, respectively (Fig. 5.3(c)). Similarly, the newly nucleated part (ΔA_{j+}) also rapidly get relaxed to +|Pn,r| by following type-2 relaxation. Corresponding transient relaxation in P_n can be seen in Fig. 5.3(a) (from point ii to ii(a)). Interestingly, followed by such rapid relaxation, there is another relaxation component that gradually reduces P_n until the arrival of next E-field pulse (Fig. 5.3(a): ii(a)-iii). Such spontaneous P-relaxation is the outcome of DW instability (due to E_{nint} asymmetry) that causes spontaneous shrinking of R1 domain (Fig. 5.3(b): ii-iii). We define the spontaneous decrease in R1 area in the absence of E-field as ΔA_{j-}.

Now, due to sequential E-field pulses, rather than completely collapsing, DW moves further towards the grain boundary by following P-excitation and relaxation sequences. Once DW reaches sufficiently close to the grain boundary, spontaneous relaxation is not observed in the absence of E-field (during T_{off}). Instead, spontaneous P-excitation (Fig. 5.3(a): v(a)-vi) takes place. This is because, as the DW reaches near the edges, R2 domain becomes very narrow and hence, $\nabla^2 P_n$ increases. Therefore, at the outer interface of the DW (alongside R2), $|E_{nint}|>1$ and that causes an effective outward force in R2. As a result, R2 domain spontaneously switches to +P (Fig. 3(b): iv-vi). After all the lattices switch to +|Pn,r|, transient P_n exhibits only type-2 excitation and relaxation.

Note that the P-maps at the beginning of different E-field pulses are different and play an important role in each P-excitation/relaxation behavior. Let us define the increase in P_n during each excitation period ($|\Delta_+ P_n|_j$). Recall that each $|\Delta_+ P_n|_j$ consists of three excitation components. It can be shown mathematically from eqn. 1 that P change due to type-1 excitation is higher in magnitude than type-2 (Fig. 5.3(c)). Now, with the increase in pulse number (j), R1 area increases and R2 area decreases.

Therefore, the contribution from type-2 excitation (in R1) increases and type-1 excitation (in R2) decreases. Hence, we expect an overall decrease in total excitation (type-1+2) with respect to (w.r.t.) j. Now, type-3 excitation (corresponding to R1 area increase during j-th excitation) can be written as, $\Delta A_{j+}=\pi[(r_j+dr_j)^2-r_j^2]=\pi[dr_j^2+2r_j dr_j]$. Here r_j is the domain radius before j-th excitation and dr_j is the increase in radius during j-th excitation. Note that a linear increase in dr_j w.r.t. time gives rise to quadratic increase in R1 area. That implies that if we keep the E-pulse ON for a long time, the P_n dynamics will be quadratic w.r.t. time (gray lines in Fig. 5.3(a)). Similarly, assuming dr_j as constant irrespective of the value of j, we can see that $\pi\times 2r_j dr_j$ increases with j as r_j increases. That implies an incremental change in ΔA_{j+} and hence, type-3 excitation component increases with j. Note that the type-3 contribution is dominant over type-1+2 and therefore $|\Delta_+ P_n|_j$ increase with the increase with j up to j=6 (Fig. 5.3(d)). For, j>6, R1 domain reaches the grain boundary and the quadratic growth of R1 no longer holds true. Hence, type-3 contribution decreases significantly, leading to the domination of type-1+2 excitation and decrease in $|\Delta_+ P_n|_j$ with j. After R2 domain vanishes (or switched to +P at j=9), $|\Delta_+ P_n|_j$ only exhibits type-2 excitation.

Similarly, the decrease in P_n during each relaxation period ($|\Delta_- P_n|_j$) consists of type-1+2 relaxation and a spontaneous part. Like type-1+2 excitation, type-1+2 relaxation decreases as j increases. However, the spontaneous component (ΔA_{j-}) behaves non-monotonically w.r.t. j. ΔA_{j-} (decrease in R1 area) changes sign from positive (+) to negative (-) at j=6 as the spontaneous component changes from relaxation to excitation characteristics. Therefore, till the spontaneous contribution is relaxation (j≤6), $|\Delta_- P_n|_j$ decreases with the increase in j. Once the spontaneous contribution leads to excitation (j>7), $|\Delta_- P_n|_j$ increases with j and becomes constant at j=9 (with only type-2 relaxation in R1).

P_n at the end of each excitation-relaxation sequence, called accumulated polarization (P_{nacc}) is shown in Fig. 5.3(a). Note that the change in P_{nacc} at each pulse is basically proportional to ΔA_{j+}- ΔA_{j-}. We discussed earlier that ΔA_{j+} shows incremental increase with the increase in j, whereas, ΔA_{j-} exhibits non-monotonic change along with a sign change from `+' to `-'. Therefore, P_{nacc} initially increases slowly when ΔA_{j-} is `+' and once $\Delta A_{j-}$ becomes `-', then increases rapidly. On the other hand, the flat region (Fig. 5.3(a), j≥9) in P_{nacc} signifies an absence in P-accumulation once the whole sample (or grain) completely switches to +P.

The trends in P accumulation w.r.t the pulse attributes are illustrated in Fig. 5.3(e-g). With the increase in pulse amplitude ($E_{n,maxapp}$), R1 domain grows more rapidly (increase in dA_+/dt) leading to faster accumulation (Fig. 5.3(e)). Similarly, with the increase in T_{on}, ΔA_{j+} increases during each pulse and therefore, P_{nacc}saturates at a lower j (Fig. 5.3(f)). Also, an increase in T_{off} leads to an increase in spontaneous relaxation (increase in ΔA_{j-}). Consequently, larger number of pulses is required for $P_{nacc}$to get saturated (Fig. 5.3(g)). Note that, if $E_{n,maxapp}$ or/and T_{on} is/are very low, so that (ΔA_{j+}-ΔA_{j-})<0, then, rather than accumulation, R1 can get completely relaxed to -P. The same is true for a high Toff. Such scenarios can be seen in Fig. 5.3(e-g) (gray lines). Note that here, we assume the pinned (or initially nucleated) domain at the center of the grain. However, depending on the position of the pinned domain, the pulse number (j) corresponds to the spontaneous relaxation/excitation may vary, while retaining the overall accumulative nature in P-switching dynamics.

5.4.2 Case-2: Non-homogeneous Coercive-field

Now, we consider case-2, where we assume a Gaussian distribution of Ec in an FE grain (Fig. 5. 4(a)) by considering a spatial distribution of $\hat{\alpha}$, $\hat{\beta}$ and $\hat{\gamma}$. Note that Ec is assumed to be less near the grain boundary (Fig. 5.4(b)), which can be understood as the cause of strain relaxation near the edges [24, 25]. Like the previous discussion, considering a sequence of E-field pulses (E^{app} =0.92), simulated $\bar{Pn}$ is shown in Fig. 5.4(c). Note that the FE grain was initially switched to -|Pn,r| (Fig. 5.4(d): i). Therefore, P-switching occurs as a two-step process: (1) E-field induced nucleation and (2) E-field assisted domain growth. Once the first E-field pulse arrives, direct nucleation starts from the grain edges (with lower Ec) and propagates inward (Fig. 5.4(d): ii). After the end of E-field pulse, further nucleation stops and type-1-2 relaxation takes place (Fig. 5.4(c):ii-ii(a)) followed by a spontaneous relaxation (Fig. 5.4(c):ii(a)-iii and Fig. 5.4(d): iii) due to DW instability. However, after the 3rd pulse (j>3), spontaneous excitation occurs in the absence of E-field (Fig. 5.4(c): v(a)-vi), rather than spontaneous relaxation.

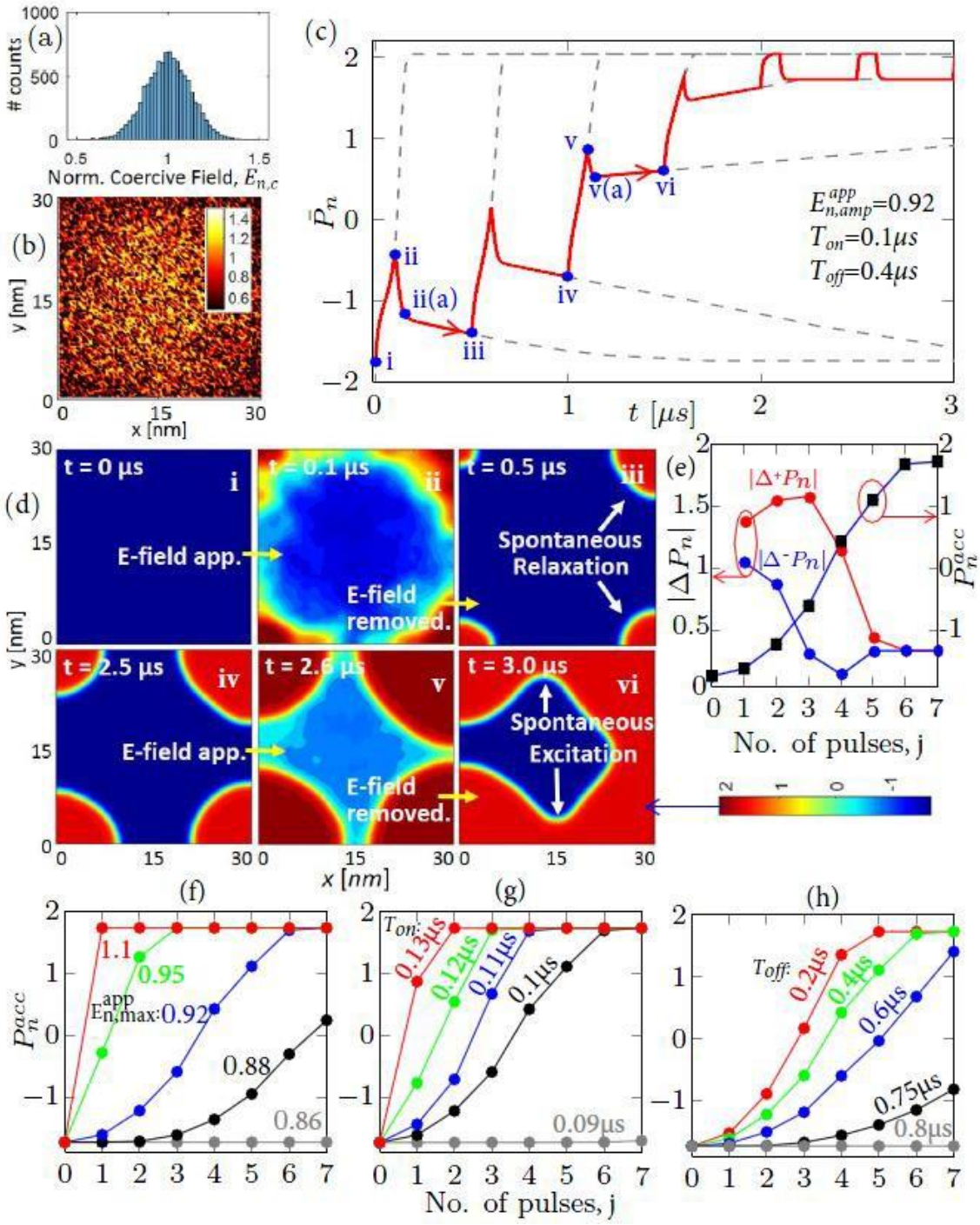

Figure 5.4. Distribution of $E_{n,c}$, (a) as area fraction and (b) as spatial, in an FE grain. (c) Simulated transient P_n. Corresponding (d) P-map at point i-vi, (e) $|\Delta^+ P_n|$, $|\Delta^- P_n|$) and P^{acc} in w.r.t. pulse number (j). P_n^{acc} vs. j for different (f) $E^{app}_{n,max}$, (g) T_{on} and (h) T_{off}.

Note that, the origin of spontaneous excitation in this case is not the instability of DW near the grain boundary. In contrast, when two DWs are sufficiently close, then the intermediate domain experiences a non-zero E^{int} governed by both the DWs. Therefore, total E^{int}>1 at DW interfaces alongside the intermediate domain. Consequently, the intermediate domain becomes unstable and spontaneously switches to +P (Fig. 5.4(d): v-vi). Such spontaneous excitation continues up to j=4, till all the lattices have switched to +P. Corresponding $|\Delta^{+}\bar{P}n|$, $|\Delta^{-}\bar{P}n|$ and P^{acc} are shown in Fig. 5.4(e-h) that present similar trends like case-1. However, an important difference between these two cases is stronger spontaneous excitation and relaxation in case-2 compared to case-1, which yields relatively abrupt P-switching in case-2.

5.5 Simulated Polarization Switching Dynamics in HZO

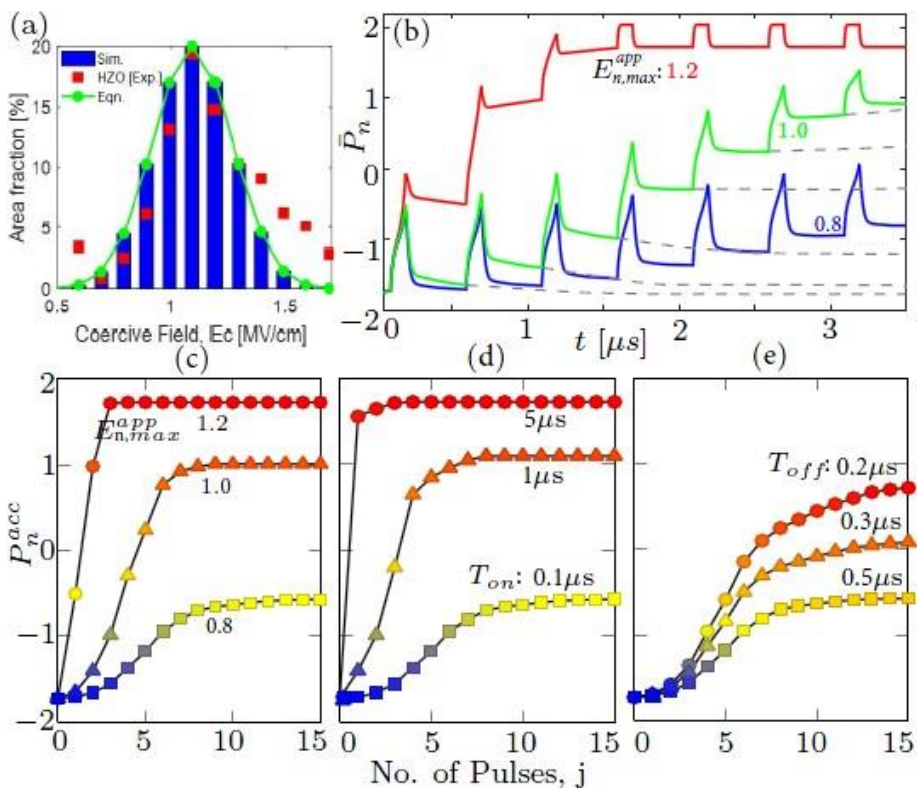

Figure 5.5. (a) E_C distribution in HZO: (red) experiment; (blue/green) used for simulation. (b) Simulated transient $\bar{P}_n$ for different $E^{app}_{n,max}$. P^{acc}_n vs. j for different (c) $E^{app}_{n,max}$, (d) T_{on} and (e) T_{off}.

With the understating of P-excitation/relaxation processes in an FE grain, we now analyze the P-accumulation in HZO by considering an ensemble of grains. The global Ec distribution for HZO (80μmx80μm) is shown in Fig. 5.5(a), which we extract from the measured P-E curves. Then, we use each sampled Ec as the mean value of a local Gaussian distribution of Ec in a grain (like case-2). Considering a large number of grains and multiplying each local Ec distribution with the corresponding area fraction, the resultant global distribution of Ec is shown in Fig. 5.5(a).

By considering a sequence of E-field pulses (for $E_{n,maxapp}$=0.8,1.0,1.2), simulated P_n and corresponding P_{nacc} are shown in Fig. 5.5(b-c). While, the signatures of the dynamics of single grain (discussed above) are manifested in HZO (ensemble of grains), two important differences can be observed in HZO: (1) saturation of accumulated P occurs at an intermediate value which increases for higher $E_{n,maxapp}$, higher T_{on} and or lower T_{off} (Fig. 5.5(c-e)) and (2) for a long relaxation time, the overall P does not relax completely (Fig. 5.5(b): gray dashed lines). The former observation is attributed to two processes. First, grains with low mean Ec switch completely after sufficient number of pulses and therefore, do not contribute to P accumulation further, leading to intermediate saturation. Second, grains with sufficiently high mean Ec exhibit low initial nucleation for a given $E_{n,maxapp}$ and T_{on}. Therefore, given a relaxation time, the grains with higher Ec are more likely to relax completely and hence, do not participate in P-accumulation. Now, with the increase in $E_{n,maxapp}$ and T_{on}, initial nucleation is enhanced, reducing the probability of complete relaxation in high Ec grains. A decrease in T_{off} also has a similar effect on relaxation. This results in the contribution of larger number of grains to P-accumulation leading to P saturation at a higher value (Fig. 5.5(c-e)). For the second observation (incomplete relaxation for large T_{off}), the reason is attributed to low mean Ec grains that completely switch during the excitation and hence, do not participate in spontaneous relaxation. Note that the large distribution of Ec corresponds to the large area of our fabricated HZO sample. However, by scaling the area of HZO, less number of grains along with a compact global distribution of Ec can be achieved. Therefore, the P-accumulation of a scaled HZO should exhibit less number of saturation levels as well as more prominent spontaneous P-excitation/relaxation which leads to more abrupt P-switching.

5.6 Summary

In summary, we experimentally demonstrated the accumulative P-switching in HZO. Then, developing a phase-field model, we discuss the P-switching dynamics by analyzing different stimulated and spontaneous P-excitation/relaxation mechanisms governed by domain-domain interaction and DW instability. We attribute the strength and directional change in DW instability as one of the key factors for accumulative P-switching. Finally, considering an inter/intra-grain coercive-field distribution in our simulations, we describe the experimentally observed accumulative P-switching in HZO.

5.7 References

[1] J. Muller, T. S. Boscke, U. Schroder, S. Mueller, D. Brauhaus, U. Bottger, L. Frey, and T. Mikolajick, Nano Lett. 12, 4318 (2012).

[2] 2P. Sharma, K. Tapily, A. K. Saha, J. Zhang, A. Shaughnessy, A. Aziz, G. L. Snider, S. Gupta, R. D. Clark, and S. Datta, in 2017 Symposium on VLSI Technology (2017) pp. T154–T155.

[3] Y. Wei, P. Nukala, M. Salverda, S. Matzen, H. J. Zhao, J. Momand, A. S. Everhardt, G. Agnus, G. R. Blake, P. Lecoeur, B. J. Kooi, J. iguez, B. Dkhil, and B. Noheda, Nature Materials 17, 1095 (2014).

[4] A. I. Khan, D. Bhowmik, P. Yu, S. J. Kim, X. Pan, R. Ramesh, and S. Salahuddin, Appl. Phys. Lett. 113, 182903 (2018).

[5] S. Salahuddin and S. Datta, Nano Lett. 8, 405 (2008).

[6] A. I. Khan, K. Chatterjee, B. Wang, S. Drapcho, L. You, C. Serrao, S. R. Bakaul, R. Ramesh, and S. Salahuddin, Nature Materials 14, 182 (2014).

[7] A. I. Khan, D. Bhowmik, P. Yu, S. J. Kim, X. Pan, R. Ramesh, and S. Salahuddin, Appl. Phys. Lett. 99, 113501 (2011).

[8] A. K. Saha, P. Sharma, I. Dabo, S. Datta, and S. K. Gupta, in 2017 IEEE International Electron Devices Meeting (IEDM) (2017) pp. 13.5.1–13.5.4.

[9] M. Trentzsch, S. Flachowsky, R. Richter, J. Paul, B. Reimer, D. Utess, S. Jansen, H. Mulaosmanovic, S. Mller, S. Slesazeck, J. Ocker, M. Noack, J. Mller, P. Polakowski, J.

Schreiter, S. Beyer, T. Mikolajick, and B. Rice, in 2016 IEEE International Electron Devices Meeting (IEDM) (2016) pp. 11.5.1–11.5.4.

[10] K. Chatterjee, S. Kim, G. Karbasian, A. J. Tan, A. K. Yadav, A. I. Khan, C. Hu, and S. Salahuddin, IEEE Electron Device Letters 38, 1379 (2017).

[11] H. Mulaosmanovic, J. Ocker, S. Mller, M. Noack, J. Mller, P. Polakowski, T. Mikolajick, and S. Slesazeck, in 2017 Symposium on VLSI Technology (2017) pp. T176–T177.

[12] M. Jerry, P. Chen, J. Zhang, P. Sharma, K. Ni, S. Yu, and S. Datta, in 2017 IEEE International Electron Devices Meeting (IEDM) (2017) pp. 6.2.1–6.2.4.

[13] G. Indiveri and S. Liu, Proceedings of the IEEE 103, 1379 (2015).

[14] H. Mulaosmanovic, T. Mikolajick, , and S. Slesazeck, ACS Appl. Mater. Interfaces 10, 1944 (2018).

[15] K. Ni, B. Grisafe, W. Chakraborty, A. K. Saha, S. Dutta, M. Jerry, J. A. Smith, S. Gupta, and S. Datta, in 2018 IEEE International Electron Devices Meeting (IEDM) (2018) pp. 16.1.1–16.1.4.

[16] H. Mulaosmanovic, E. Chicca, M. Bertele, T. Mikolajickac, and S. Slesazecka, Nanoscale 10, 21755 (2018).

[17] Y. L. Li, S. Y. Hu, Z. K. Liu, , and L. Q. Chen, Appl. Phys. Lett. 78, 3878 (2001).

[18] K. M. Rabe, C. H. Ahn, and J.-M. Triscone, Physics of Ferroelectrics – A Modern Perspective (Springer, 2007).

[19] S. Nambu and D. A. Sagala, Phys. Rev. B 50, 5838 (1994).

[20] R. Lynden-Bell, Molecular Physics 86, 1353 (1995).

[21] K. Elder, H. Gould, and J. Tobochnik, Computers in Physics 7, 27 (1993).

[22] A. K. Bandyopadhyay, P. C. Ray, and V. Gopalan, Journal of Physics: Condensed Matter 18, 4093 (2006).

[23] A. Cano and D. Jimnez, Appl. Phys. Lett. 97, 133509 (2010).

[24] A. Emelyanov, N. Pertsev, S. Hoffmann-Eifert, U. B¨ottger, and R. Waser, Journal of Electroceramics 9, 5 (2002).

[25] J.-S. Lee, E.-C. Park, J.-H. Park, B.-I. Lee, and S.-K. Joo, MRS Proceedings 596, 315 (1999).

6. PHASE-FIELD MODELING OF FERROELECTRIC HETEROSTRUCTURES

6.1 Introduction

In this chapter, we investigate the multi-domain polarization switching mechanism in metal-ferroelectric-dielectric/insulator-metal (MFIM) stacks and its dependence on the dielectric thickness (T_{DE}) and ferroelectric thickness (T_{FE}). We fabricate HZO-Al_2O_3 (FE-DE) stack and experimentally demonstrate a decrease in remnant polarization and an increase in coercive voltage of the FE-DE stack with an increase in T_{DE}. Similarly, we show a decrease in remnant polarization and a non-significant decrease in coercive voltage of the MFIM stack with the decrease in T_{FE}. Using phase-field simulations, we show that an increase in T_{DE} results in a larger number of reverse domains in the FE layer to suppress the depolarization field and that leads to a decrease in remanent polarization and an increase in coercive voltage. Further, the applied voltage-driven polarization switching suggests domain-nucleation dominant characteristics for low T_{DE}, and domain-wall motion-induced behavior for higher T_{DE}. The similar multi-domain effects are also observed with the reduction in the FE thickness. In addition, we show that the hysteretic charge-voltage characteristics of the FE layer in the MFIM stack exhibit a negative slope region due to the multi-domain polarization switching in the FE layer. Based on our analysis, the trends in charge-voltage characteristics of the FE-DE stack with respect to different T_{DE} can be described well with multi-domain polarization switching mechanisms and are out of the scope of single-domain models. In addition to the hysteretic multi-domain polarization switching in MFIM stack, we also analyze the non-hysteretic polarization switching featuring negative capacitance effects in the MFIM and metal-ferroelectric-insulator-semiconductor (MFIS) stack under soft-DW displacement. Such soft-DW appears at low T_{FE} and/or FE materials with high gradient energy coefficients. We systematically analyze these multi-domain negative capacitance effects by considering a range of physical and material parameters.

6.2 Effects of dielectric thickness in MFIM stack

In the FEFET gate stack, a dielectric (DE) layer exists between the FE and the semiconductor channel [1]-[10], which can significantly impact the FEFET characteristics [11]. According to the

single-domain Landau-Khalatnikov (LK) model of FE, an increase in DE thickness (T_{DE}) should increase the depolarization field and reduce the coercive voltage (V_C) of the FE-DE stack [12]-[13]. However, the FE-DE stack with Zr-doped HfO_2 (HZO) as the FE and Al_2O_3/HfO_2 as the DE have been demonstrated [14]-[15] to exhibit an increasing coercive voltage (V_C) with the increase in T_{DE}. Therefore, it is important to bridge the gap between the theoretical understanding and experimental observations regarding the role of T_{DE} in FEFET and for that, a common approach is to analyze the FE-DE stack [12]-[13]. To that end, in this letter, we experimentally and theoretically analyze the *P*-switching in FE-DE stack with HZO as the FE and Al_2O_3 as the DE layer. Our results signify an increase in V_C, a decrease in remanent-*P* (P_R) and a decrease in *P*-switching slope with the increase in T_{DE}. By employing phase-field simulations, we show that such dependencies can be attributed to the multi-domain phenomena in FE [16] which cannot be captured in the single-domain *P*-switching model. To further study the role of the dielectric, we analyze the dependence of V_C, P_R and the switching slope of the FE-DE stack on the dielectric permittivity through phase-field simulations.

6.3 Multi-Domain Phase-Field Simulation Framework for MFIM stack

In our 2D phase-field simulation, we self-consistently solve the time-dependent Ginzburg-Landau (TDGL) equation (eqn. 6.1) and Poisson's equation (eqn. 6.2) as shown below [18]-[19].

$$-\frac{1}{\Gamma}\frac{\partial P}{\partial t} = \alpha P + \beta P^3 + \gamma P^5 - g_{11}\frac{d^2P}{dz^2} - g_{44}\frac{d^2P}{dx^2} + \frac{d\phi}{dz} \quad (6.1)$$

$$-\epsilon_0\left[\frac{\partial}{\partial x}\left(\epsilon_x\frac{\partial\phi}{\partial x}\right) + \frac{\partial}{\partial z}\left(\epsilon_z\frac{\partial\phi}{\partial z}\right)\right] = -\frac{dP}{dz} \quad (6.2)$$

Here, α, β, and γ are Landau coefficients; $g_{11(44)}$ is the gradient coefficient; $\epsilon_{z(x)}$ is relative background permittivity; Γ is viscosity coefficient; ϕ is potential; *P* is the polarization of FE unit cell. We assume that the *P*-direction (c-axis of the orthorhombic HZO crystal) is parallel to the film thickness (z-axis) [18]-[19]. Note that the *dP/dz* induces charges in the FE layer and thus enters in eqn. 2. At the FE-DE interface, $\lambda(dP/dz)$-*P*=0 is used for the surface energy contribution, where λ is the extrapolation length [20]-[21]. All simulation parameters are given in Fig. 6.1(d).

Due to the noncentrosymmetric crystal and lower elastic interactions in the out-of-plane direction compared to the in-plane direction in HZO [22], we use $g_{11}<g_{44}$. Similarly, as the P-direction is along the z-axis, therefore, a lower number of atoms per unit cell take part in ϵ_z compared to ϵ_x and hence, $\epsilon_z<\epsilon_x$ (which is similar to other FE like PZT [23]). We consider the length (l, along the x-direction) of the system to be 30nm which is analogous to the average grain size of HZO [24]. To be consistent with the experimental measurements, the simulations are performed based on the quasi-static criteria (negligible dP/dt). Therefore, our simulation results are independent of the value of Γ. Further, we use a smaller FE region (equivalent to the size of a grain ~30nm) in simulation compared to the area of our experimental sample because of the scale-free nature of the FE HZO [22]. In the multi-domain scenario, P_{avg} is computed by integrating the displacement field at the metal-DE (or metal-FE) interface ($P_{avg}= (\int \epsilon_0\epsilon_{z,DE}E_{z,DE}dx)/l = (\int (P + \epsilon_0\epsilon_{z,FE}E_{z,FE})dx)/l$). Here, the $E_{z,FE(DE)}$ is the out-of-plane (z) component of the electric field in the FE (DE) layer. The simulated P_{avg}-V_{app} characteristics of the FE-DE stack is shown in Fig. 6.1(b) illustrating good agreement with the experimental results (Fig. 6.1(c)).

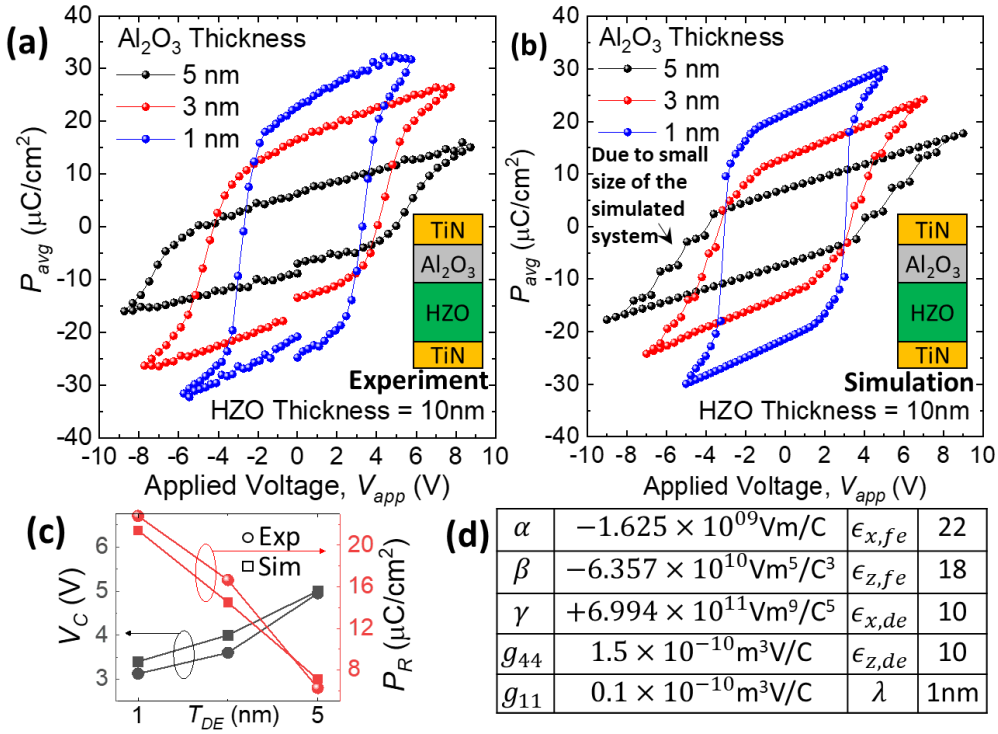

(d)

α	-1.625×10^{09}Vm/C	$\epsilon_{x,fe}$	22
β	-6.357×10^{10}Vm^5/C^3	$\epsilon_{z,fe}$	18
γ	$+6.994\times10^{11}$Vm^9/C^5	$\epsilon_{x,de}$	10
g_{44}	1.5×10^{-10}m^{3}V/C	$\epsilon_{z,de}$	10
g_{11}	0.1×10^{-10}m^{3}V/C	λ	1nm

Figure 6.1. (a) Measured and (b) simulated P_{avg}-V_{app} characteristics of FE-DE stack for different T_{DE}. (c) average V_C (V_{app} at P_{avg}=0) and P_R (P_{avg} at V_{app}=0) for different T_{DE}. (d) Table showing the simulation parameters.

For the fabrication of the FE-DE stacks (in collaboration with Prof. Peide Ye, Purdue University), we start with the standard solvent cleaning of heavily p-doped Si substrates. Then, 30nm TiN layer is deposited by atomic layer deposition (ALD) at 250 °C, using $[(CH_3)_2N]_4Ti$ and NH_3 as the Ti and N precursors, respectively. After this, an HZO film is deposited by ALD at 200 °C, using $[(CH_3)_2N]_4Hf$, $[(CH_3)_2N]_4Zr$, and H_2O as the Hf, Zr, and O precursors, respectively. HfO_2:ZrO_2 cycle ratio of 1:1 is used to form the 10nm $Hf_{0.5}Zr_{0.5}O_2$ film. Similarly, on top of HZO, an Al_2O_3 layer is deposited followed by a 30nm TiN layer deposition. After that, the samples are annealed at 500 °C in N_2 environment for 1 minute by rapid thermal annealing. Then, Ti/Au top electrodes are fabricated using photolithography, e-beam evaporation, and lift-off process (area=5024μm^2). The average polarization (P_{avg}) versus applied voltage (V_{app}) measurement is carried out using a Radiant RT66C FE tester at room temperature at a very low frequency (50Hz). Considering the polarization switching time in HZO (<1μs) [17], such low-frequency measurements can be considered as quasi-static. Fig. 6.1(a) shows the P_{avg}-V_{app} characteristics of FE-DE stack for 10nm HZO and 1/3/5nm Al_2O_3. Our results show a decrease in P_R (P_{avg} at V_{app}=0V), an increase in V_C (V_{app} at P_{avg}=0) and a decrease in P-switching slope with the increases in T_{DE}. To explain such dependencies, we now analyze the P-switching in the FE-DE stack based on multi-domain phase-field simulation.

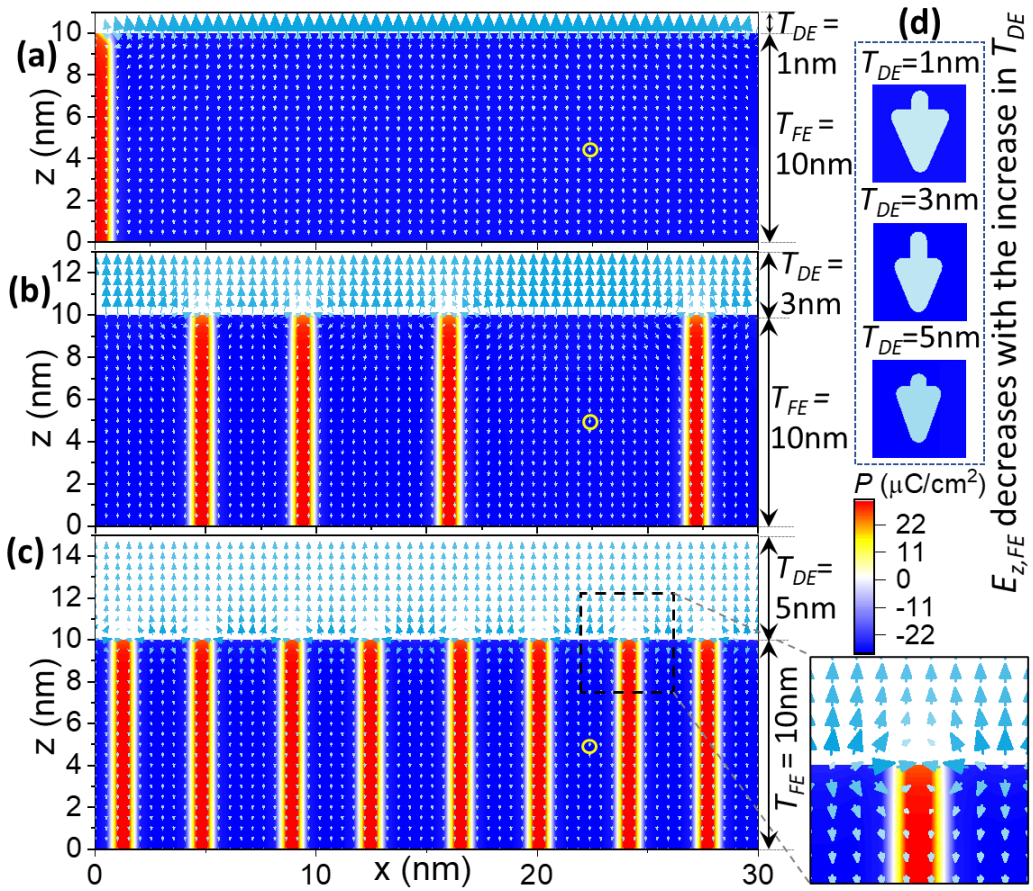

Figure 6.2. Simulated P (color map) and E-field (arrow) profile in FE-DE for T_{DE} = (a) 1nm (b) 3nm, and (c) 5nm. The blue (red) regions signifying -P (+P) domains. (d) $E_{z,FE}$ in FE at the yellow circle shown in (a-c).

(A) Multi-domain state at V_{app}=0V: To explain these characteristics, let us start with V_{app}=0V and P_R <0. In an FE-DE stack, the P-induced bound charges appear near the FE-DE interface leading to a non-zero $E_{z,DE}$ and $E_{z,FE}$. If P is homogeneous (e.g. in single-domain (SD) state), then $E_{z,FE}$ will be directed opposite to the P-direction yielding depolarization energy f_{dep} (= $-PE_{z,FE}$). At the same time, $E_{z,FE}$ will reduce the P magnitude (|P|) leading to an increase in the free energy (f_{free}). In order to suppress f_{dep} and f_{free} (to minimize the overall energy), FE breaks into multiple domains with opposite P-directions. In this multi-domain (MD) state, the P-induced bound charges at the FE-DE interface not only give rise to $E_{z,FE(DE)}$ (as before), but also form in-plane E-field ($E_{x,FE(DE)}$) called stray field [18], [25]. As a portion of the bound charge gets compensated by the stray-field, $E_{z,FE(DE)}$ is reduced in the MD state (compared to the SD state) leading to a reduction in f_{dep} and

f_{free}. However, this suppression of f_{dep} and f_{free} occurs at the cost of (i) gradient energy, f_{grad} ($=g_{44}(dP/dx)^2$) due to the spatial variation of P in the domain-walls (DW) and (ii) electrostatic energy f_{elec} ($=\epsilon_0\epsilon_{x,FE}E_{x,FE}^2$) due to the stray fields. Hence, the formation of the MD state occurs as an interplay among competing energy components to obtain the minimum energy. With this understanding, let us now discuss the impact of T_{DE} on P_R.

(B) Effects of T_{DE} on P_R: In the FE-DE stack (at V_{app}=0 and P_R<0), an increase in T_{DE} tends to increase $E_{z,FE}$ due to the higher voltage drop across DE and an equal and opposite voltage drop across the FE layer. This increase in $E_{z,FE}$ tends to increase f_{dep} and f_{free}. To counter this, a larger number of oppositely polarized domains (+P in Fig. 6.2) appear that create more stray fields to suppress $E_{z,FE}$. The simulated P and E-field profiles in Fig. 6.2(a-c) validate the increase in the number of +P domains (red domains) and suppression of $E_{z,FE}$ (Fig. 6.2(d)) with the increase in T_{DE}. The appearance of a larger number of +P domains leads to a smaller size of -P domains (blue) and hence, reduced $|P_R|$ with the increase in T_{DE} (Fig. 6.1(a-c)).

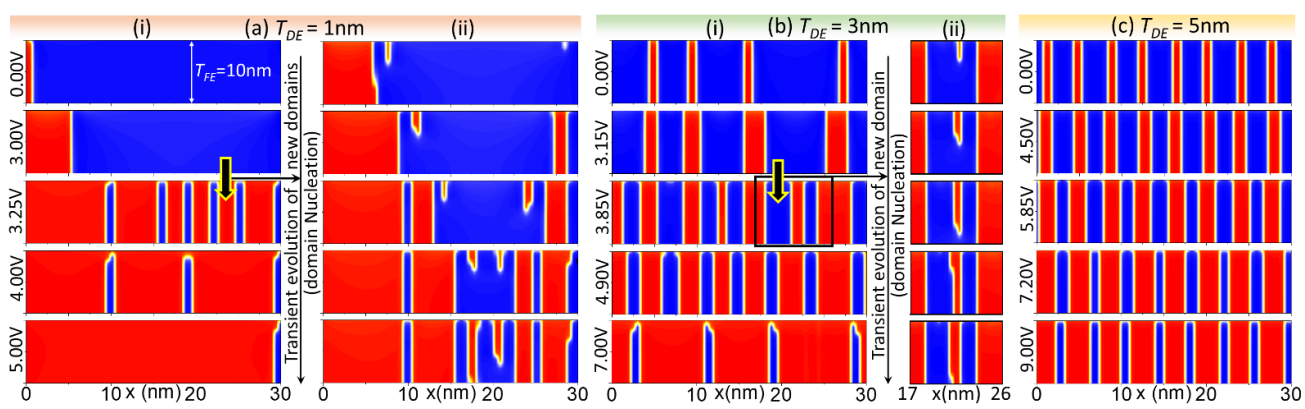

Figure 6.3. Simulated polarization profile in FE at a different applied voltage (V_{app}) in FE-DE stack for different T_{DE} = (a) 1nm, (b) 3nm and (c) 5nm showing domain nucleation and domain-wall motion based polarization switching. In all the cases, the FE thickness is 10nm.

(C) Nucleation and DW motion based P-switching: Now, let us discuss V_{app}-induced P-switching. P-switching can take place if $f_{grad}+f_{dep}+f_{elec}+f_{\text{free}} > \max(f_{free})$. In the MD state, $E_{z,FE}$ is maximum away from DW near the FE-DE interface, which leads to maximum f_{dep}. In contrast, f_{grad} is maximum near the DW due to the largest variation in P. Now, with an increase in V_{app}, $E_{z,FE}$

increases leading to a change in P magnitude ($|P|$ increases in $+P$ domains and decreases in $-P$ domains). Thus, $f=f_{grad}+f_{dep}+f_{elec}+f_{\text{free}}$ increases [16]. If the increase in f is dominant near the DW, then P-switching occurs through DW motion. However, if the increase in f is dominant away from the DW, then P-switching occurs through the nucleation of new domains. P profiles at different V_{app} are shown in Fig. 6.3(a)-i for T_{DE}=1nm. With the increase in V_{app}, P-switching starts through DW motion (at V_{app}=1.5V) and at V_{app}>3V several new domains nucleate causing a denser domain pattern. The transient nature of domain nucleation is shown in Fig. 6.3(a)-ii signifying their formation starting from the FE-DE interface. Once, the domain pattern becomes denser, a significant portion of $E_{z,FE}$ is suppressed by the stray fields at the expense of an increased f_{grad}. Hence, with further increase in V_{app}, P-switching takes place through DW motion leading to complete switching of several domains. Similarly, for T_{DE}=3nm (Fig. 6.3(b)-i-ii), P-switching initiates through DW motion (at V_{app}=1.85V) followed by domain nucleation (at V_{app}>3.15V) and then DW motion. However, for T_{DE}=5nm (Fig. 6.3(c)), the initial domain pattern is much denser, which suppresses $E_{z,FE}$ at the cost of f_{grad}. Hence, nucleation of new domains is not observed, and P-switching takes place only through DW motion (at V_{app}>3.6V).

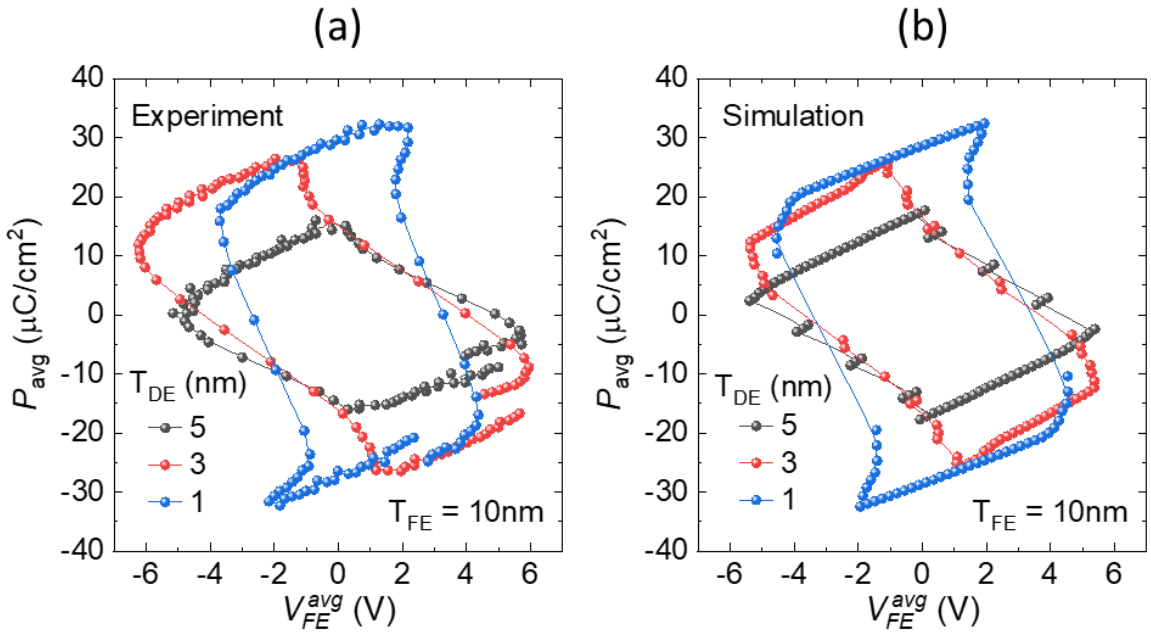

Figure 6.4. Extracted P_{avg}-V_{FE} characteristics of FE in the FE-DE stack from the (a) experimental and (b) simulated P_{avg}-V_{app} characteristics.

(D) Effects of T_{DE} on Negative switching slope of the P-V_{FE} characteristics: The extracted P_{avg}-V_{FE} characteristics from experimental and simulated P_{avg}-V_{app} characteristics are shown in Fig. 6.4 (a-b) signifying the negative dP_{avg}/dV_{FE} region. Such negative dP_{avg}/dV_{FE} exists during the P-switching in the FE layer via domain nucleation and/or DW motion. Recall that the local $E_{z,FE}$ in the FE layer is depolarizing i.e. opposite to the direction of P. Now, let us consider the FE-DE stack is in the P_R<0 states (average $E_{z,FE}>0$). When V_{app} is increased and leads to MD P-switching, the P_{avg} increases either through the formation of new +P domains (nucleation) or through the size increase of +P domains (DW displacement). Both of these phenomena lead to a decrease in average $E_{z,FE}$ (i.e. the average $E_{z,FE}$ becomes less positive). As the increase in P_{avg} accompanies the decrease in average V_{FE} (=$T_{FE}E_{z,FE}$), thus the dP_{avg}/dV_{FE} becomes negative. It is important to note that the appearance of negative dP_{avg}/dV_{FE} is an electrostatic effect rather than a transient artifact. However, the actual slope of dP_{avg}/dV_{FE} can certainly be impacted by the frequency of the applied V_{app} due to the time-dependency of domain-nucleation and DW-motion.

(E) Effects of T_{DE} on P-switching slope of the FE-DE stack: The DW motion occurs via lattice-by-lattice propagation yielding a gradual increase in P_{avg}. However, the nucleation of a new domain involves simultaneous P-switching in several lattices leading to a sharper change in P_{avg}. Since, with an increase in T_{DE}, the dominant P-switching mechanism changes from nucleation to DW-motion-based, P-switching becomes more gradual - Fig. 6.1(a-b)). Further, our simulations show a step-wise P-switching behavior for T_{DE}=5nm (Fig. 6.1(b)), where each step jump signifies the DW displacement, and the flatter region corresponds to no DW displacement. The non-zero slope of the flat region is due to the response of P magnitudes and $\epsilon_{z,FE}$ to $E_{z,FE}$. In this flat region, with an increase in V_{app}, $E_{z,FE}$ first increases. If the increase in $E_{z,FE}$ is beyond a critical value so that f>max(f_{free}), then the P-switching takes place via DW displacement. Recall that the P-switching leads to an increase in P_{avg} and a simultaneous reduction in $E_{z,FE}$ yielding a negative slope in the P_{avg}-V_{FE} characteristics (dP_{avg}/dV_{FE}<0) and a step jump in the P_{avg}-V_{app} characteristics. Therefore, this process can be described as the sequential increase and decrease in $E_{z,FE}$ where the former is the cause and later is the effect of partial P-switching. Now, after each P-switching step, to induce further DW motion, V_{app} needs to be increased to increase $E_{z,FE}$ beyond a (new) critical value. Consequently, we observe a step-wise P-switching behavior in Fig. 1(b) and Fig 4(b).

However, such step-jumps are absent in the measured characteristics because of the larger area (lots of grains) of the fabricated sample compared to our simulation (~one grain). Thus, even though the DW motion may absent in some of the grains of the experimental sample, it may be present in other grains (due to the variation in grain size and/or crystallographic angle) leading to a continuous increase in P_{avg}. Hence, we expect that simulation of a larger system considering multiple grains may reduce this mismatch between the simulation and experimental results.

(F) Effects of T_{DE} on V_C: Let us now explain the effect of T_{DE} on V_C (defined as the V_{app} where P_{avg} = 0). For that, we consider the voltage drop across FE averaged along the length (referred as $V_{FE}=(\iint E_{z,FE}dxdz)/l$). As an increase in T_{DE} suppresses $E_{z,FE}$ (discussed before), it leads to a decrease in V_{FE} at V_{app}=0V. With the decrease in initial V_{FE}, a higher V_{app} is required to achieve a critical V_{FE} to trigger P-switching. Therefore, the DW motion initiates at V_{app}=1.5V for T_{DE}=1nm and at 1.85V for T_{DE}=3nm. Similarly, the domain nucleation takes place at V_{app}>3V for T_{DE}=1nm and V_{app}>3.15V for T_{DE}=3nm. Further, dP_{avg}/dV_{app} decreases with the decrease in T_{DE} (discussed before) leading to an increase in required V_{app} to achieve P_{avg}=0. Due to the decrease in initial V_{FE} (at V_{app}=0V) and lower dP_{avg}/dV_{app}, V_C of the FE-DE stack increases with an increase in T_{DE}. Note that the increase in V_C for larger T_{DE} cannot be captured by the SD mode, but can be described well considering the MD effects (as explained above).

So far, we have discussed different attributes of P_{avg}-V_{app} characteristics of FE-DE stack with respect to different T_{DE}. Which can also be regarded as the equivalent of different DE capacitance, $C_{DE}=\epsilon_0\epsilon_{DE}/T_{DE}$. Therefore, one can argue that the same P_{avg}-V_{app} characteristics can be obtained with a different DE material (different ϵ_{DE} and T_{DE}) by keeping the same C_{DE}. However, we show that the P_{avg}-V_{app} characteristics are not unique to C_{DE}, rather depends on the choice of ϵ_{DE}.

6.4 Effects of ferroelectric thickness in MFIM stack

The experimentally measured and simulated Q-V_{app} characteristics of MFIM stack with different FE thickness (T_{FE}) is shown in Fig. 6.5 suggesting a decrease in remanent polarization with the decrease in T_{FE}. This is because, with decrease in T_{FE}, similar remanent polarization would induce a higher depolarization filed (and higher depolarization energy) in FE layer. To compensate such

energy, the FE layer breaks into a greater number of domains (Fig. 6.6). Due to the appearance of a greater number of reverse domains with the decrease in T_{FE}, the remanent polarization decreases with the scaling of FE thickness.

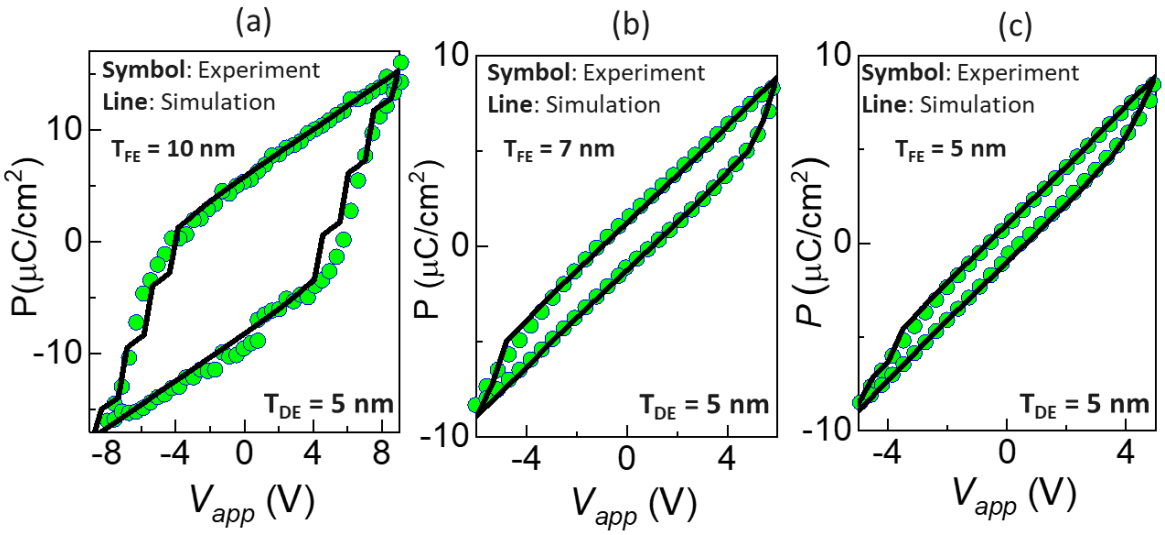

Figure 6.5. Experimental (symbol) and simulated (solid-line) Q-V_{app} characteristics of MFIM stack for different FE thickness (T_{FE}).

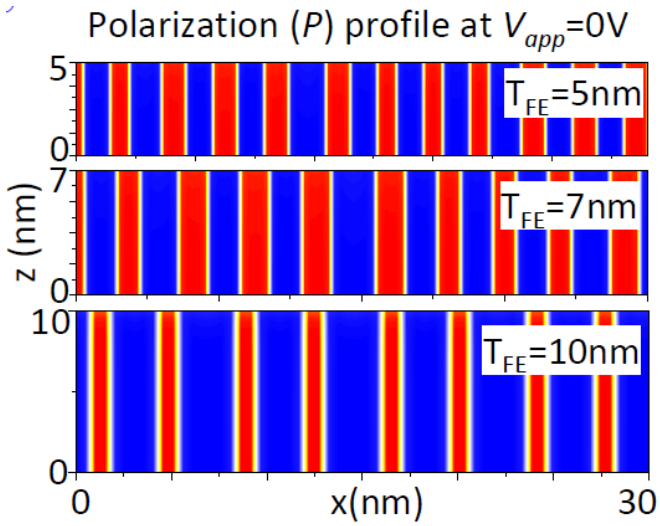

Figure 6.6. Domain pattern of FE layer in the MFIM stack for different T_{FE} at the negative remanent polarization. The average remanent polarization decreases with the decrease in TFE due the appearance of a greater number of reverse domains.

Similar to the MFIM stack with different T_{DE}, the Q-V_{FE}^{avg} characteristics of the FE layer is shown in Fig. 6.7 for different T_{FE} signifying the appearance of negative switching slope during the P-switching. It is important to note that the negative slope does not significantly change with T_{FE}.

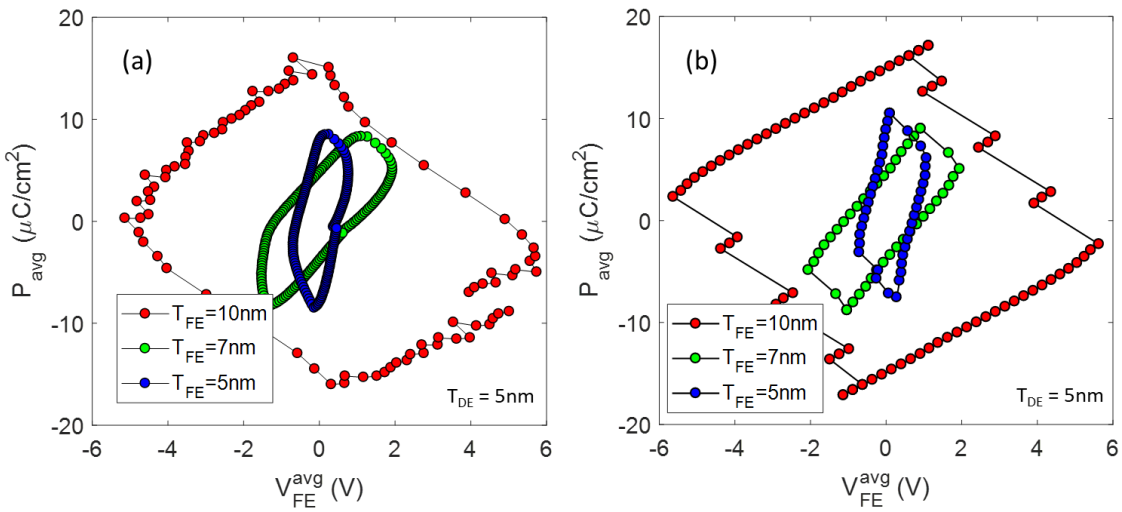

Figure 6.7. Average charge (Q) versus average voltage across the FE layer (V_{FE}^{avg}) in MFIM stack extracted from (a) experiment and (b) simulated P-V_{app} characteristics.

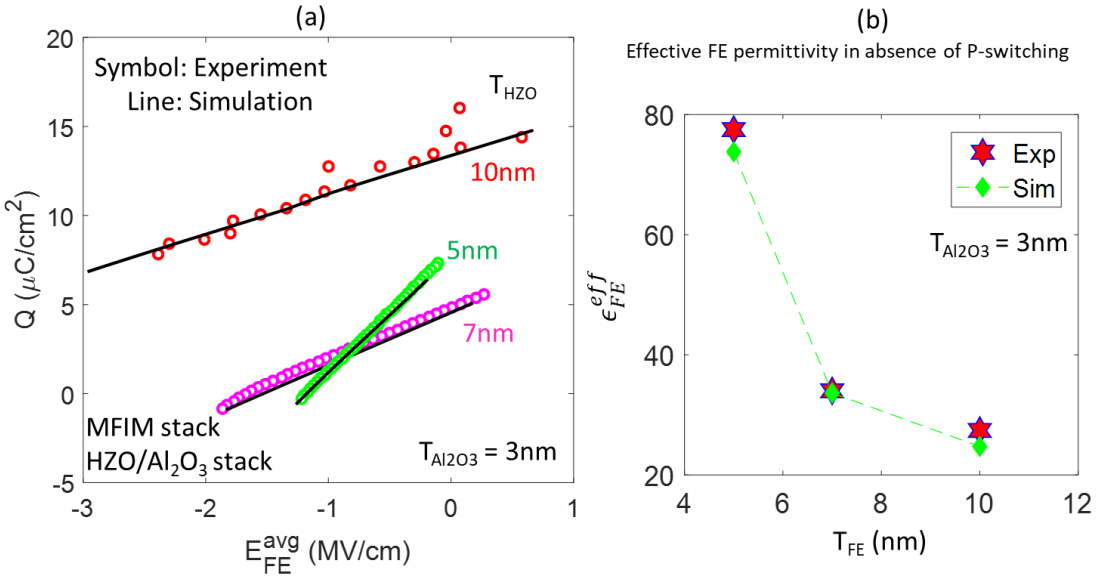

Figure 6.8. Average charge (Q) versus average electric field in the FE layer (E_{FE}^{avg}) in MFIM stack in absence of polarization switching. (b) Effective permittivity of the FE layer (in MFIM stack) with respect to FE thickness.

The Q-E_{FE}^{avg} characteristics of the FE layer (in MFIM stack) in absence of polarization switching are shown in Fig. 6.8 that signifies an increase in slope (dQ/dE_{FE}^{avg}) with the decrease in T_{FE}. That implies, the effective FE permittivity enhances (but remain positive) with the decrease in T_{FE} even in absence of P-switching in the FE layer (Fig. 6.8(b)). This is because of the electrostatic interactions among the multi-domain polarization and their applied voltage dependent magnitude response that we have discussed earlier.

6.5 Effects of gradient energy coefficients in MFIM stack

Let us start by considering an MFIM stack with an applied voltage (V_{app}) of 0 V. It is well known that in MFIM stack, spontaneous polarization (P) appears at the FE-DE interface, which leads to a voltage drop across the DE layer. As a result, an E-field appears in FE opposite to the P direction, called depolarization field, which leads to an increase in the depolarization energy density. Let us define the E-field along the thickness of the FE film (z-axis) as $E_{z,FE}$ and the depolarization energy density as f_{dep}=−$E_{z,FE}$×P. However, f_{dep} can be suppressed with the formation of periodic 180° domains of alternating P-directions (P↓ and P↑).

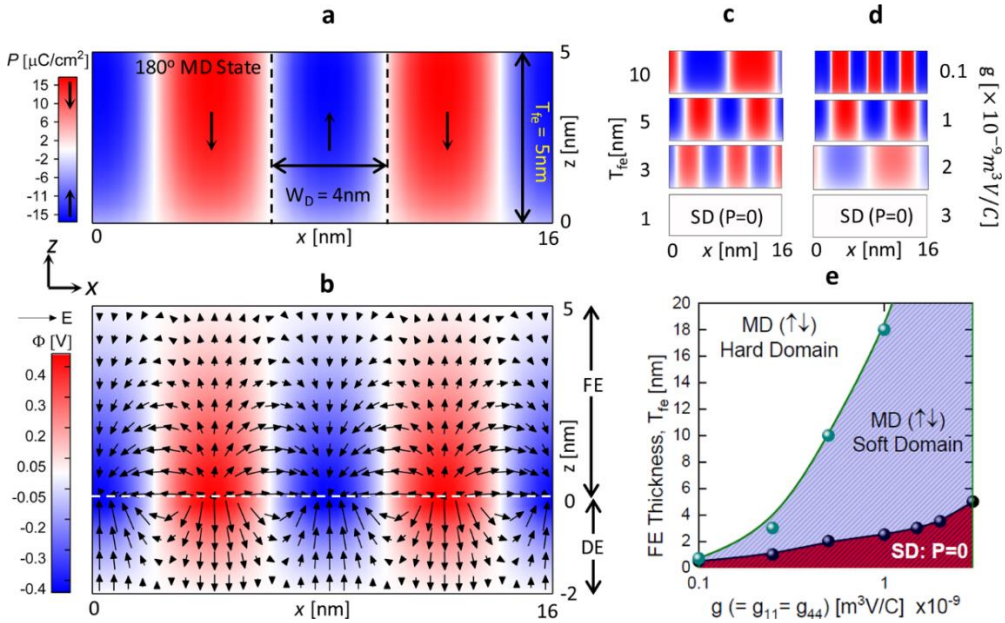

Figure 6.9. (**a**) Polarization profile of FE (P(x,z)P(x,z)) and (**b**) potential profile ($\Phi(x, z)$) of MFIM stack at $V_{app} = 0$ V showing 180° domain formation in FE. Here, $T_{fe} = 5$ nm, $T_{de} = 2$ nm, $\varepsilon_{de} = 10$ (Al_2O_3). Polarization profiles of FE in MFIM for (**c**) different T_{fe} and (**d**) different g at $V_{app} = 0$ V. (**e**) g vs critical T_{fe} for MD (P↑↓) state with soft-DW, hard-DW and SD (P = 0) state for $\varepsilon_{de} = 10$. The lateral dimension (along the x-axis) of 100 nm is used for all simulations.

Simulation result considering such a scenario is shown in Fig. 7.9(a) for T_{fe} = 5 nm, T_{de} = 2 nm (Al_2O_3), g=1×10^{-9}m^{3}V/C. Here, ↑ (↓) sign denotes the +z (−z) direction. In this multi-domain (MD) state, the magnitude of the local $E_{z,FE}$ (at a particular point in the FE) is greatly reduced due to stray fields (in-plane E-field, $E_{x,FE}$) between P↑ and P↓ domains, as shown in Fig. 7.9(b). While this decrease in local $E_{z,FE}$ is larger near the domain walls (DWs) compared to inside of the domains, the suppression of average $E_{z,FE}$ is significant across the entire length of the stack (along the xx-direction). The resultant decrease in f_{dep}, however, comes at the cost of DW energy density (F_{dw}), which is comprised of (a) the electrostatic energy density ($f_{x,elec}=\varepsilon_0\varepsilon_{x,FE}\times E^2_{x,fe}$) due to stray fields, where $\varepsilon_{x,FE}$ is the in-plane background permittivity of FE and (b) x-component of gradient energy density ($f_{x,grad}=g\times(dP/dx)^2$) due to the spatial variation in P along the x-axis. Subsequently, we will refer to the sum of $f_{x,grad}$ and $f_{x,elec}$ over the FE region as the DW energy ($F_{dw}=\iint f_{dw}dxdz$, where, $f_{dw}=f_{x,grad}+f_{x,elec}$). Note that the magnitude of P inside of a domain also varies along the z-axis exhibiting a minima at the DE interface and gradually increases in the bulk FE (away from the DE interface). This induces a bound charge density $\rho_b=-dP/dz$ and further suppresses the $E_{z,FE}$ (and hence, f_{dep}) inside of the domain. However, this additional suppression of $E_{z,FE}$ occurs at the cost of an increase in the z-component of gradient energy density ($f_{z,grad}=g\times(dP/dz)^2$). Our simulations show that $f_{z,grad}$ occurs in FE both in the MD (co-existing P↑ and P↓) and poled (either P↑ or P↓) states. In the MD state, achieved by suppressing f_{dep} at the cost of f_{dw} and $f_{z,grad}$ while minimizing the overall system energy, the intricate interactions of these energy components with each other as well as the free energy (f_{free}) play a key role in determining the charge response of FE in the MFIM stack and its dependence on the device/material parameters, as discussed subsequently [26]-[36].

Now, let us first consider the implication of FE thickness, T_{FE} on the formation of MD state. The P configurations of FE in MFIM stacks shown in Fig. 7.9(c), suggest that the number of domains and DWs (within a certain length) increases with the decrease in T_{FE}. As T_{FE} decreases, $f_{z,grad}$ increases as a similar P variation along z-axis (i.e. similar P maxima in the bulk and minima in the interface) occurs within a lower T_{FE}. One of the possible ways to reduce $f_{z,grad}$ could be decreasing P variation by increasing P magnitude in the interface, but this would increase f_{dep}. As an alternative, an increase in the number of DWs leads to reduced domain width and thus, reduces the P magnitude in the bulk region. Therefore, an increase in $f_{z,grad}$ due

to T_{FE} scaling is mitigated by increasing the number of DWs. In this case, suppression of f_{dep} becomes more significant inside of a domain (as P decreases in magnitude) and also on an average (as the number of DWs increases). At the same time, with decreasing T_{FE}, as the number of DWs increases, the nature of DW changes from hard to soft type (Fig. 7.9(c)). Here, the term hard-DW implies that the spatial variation in P is localized and abrupt (dP/dx is high) only near the DWs. Thus, $f_{x,grad}$ is non-zero in the DW and zero (or very small) within the domains. In contrast, in a soft-DW, the P variation is more gradual (dP/dx is low) and the effects of DW diffuses along the length-scale of a domain. That implies $f_{x,grad}$ becomes non-zero inside of a domain.

Similar to the effect of T_{FE}, the gradient energy coefficient (g) also determines the number of DWs in FE. As $f_{x,grad}$ is one of the components of f_{dw}, a decrease in g leads to lower DW energy cost and, thus, leads to larger number of domains and DWs. Such an increase in the number of DWs density with the decrease in g is shown in Fig. 7.9(d). Further, the nature of DW changes from hard to soft type as gg increases. This is because, for higher g, dP/dx decreases to compensate for the $f_{x,grad}$ and thus the P-variation becomes more gradual and diffuses within the domain. The nature of DW (i.e. soft or hard) in MFIM for different g and T_{FE} is illustrated in Fig. 7.9(e) showing that the critical T_{FE} for hard to soft DW transition decreases with a decrease in g. Further, if T_{FE} is scaled below a critical value, a single domain (SD) state with homogenous $P = 0$ stabilizes (Fig. 7.9(c): $T_{FE} = 1$ nm), where the suppression of f_{dep} occurs at the cost of f_{free} rather than f_{dw}. For suppressing f_{dep}, if f_{dw} is higher than f_{free} then the SD state is preferred over the MD state. In addition, the critical T_{FE}, for MD to SD transition, decreases with a decrease in g as shown in Fig. 7.9(e). As f_{dw} decreases with g, a lower T_{FE} is needed to go beyond f_{free}. Note that if g is very small, the critical T_{FE} can potentially become so small that the SD state or soft MD state may not be physically realizable. For example, if $g<0.1\times10^{-9}\mathrm{m}^3\mathrm{V/C}$, the critical T_{FE} for SD state (0.25 nm) and soft MD state (0.5 nm) is lower than or comparable to a unit cell height of HZO.

In the above discussion, the stability of SD state with $P = 0$ may or may not imply that the ferroelectricity of the FE layer will be retained, and the same Landau coefficients can be used to calculate the polarization switching characteristics. Rather, one needs to calculate the f_{free} of the ferroelectric phase at $P = 0$ along with the paraelectric and anti-ferroelectric phases (i.e.,

orthorhombic, monoclinic and tetragonal phase for HZO). In such a case, the state with lowest f_{free} will be stabilized and if the stable phase is either paraelectric or anti-ferroelectric, then the Landau coefficients for ferroelectric phase cannot be used to simulate the polarization switching characteristics. However, such calculation requires first-principal simulation, which is out of the scope of our current study. Hence, we limit our analysis to the MD states.

Further, in the MD state, the nature of DW plays an important role in E-field driven DW motion. To displace the hard-DW, the applied E-field needs to be higher than a critical value called coercive field of DW motion, $E_{c,DW}$. Therefore, the hard-DW motion based P-switching is hysteretic, because, the applied E-field needs to be higher than the positive $E_{c,DW}$ for forward DW motion and lower than the negative $E_{c,DW}$ for reverse DW motion. In contrast, $|E_{c,DW}|$ is infinitesimally small (~0) for soft-DW and hence, non-hysteretic DW motion is possible. As in this work, our focus is on analyzing the non-hysteretic NC effect, we restrict our discussion only for soft-DW motion based P-switching.

6.6 Multi-domain Negative capacitance effects in MFIM Stack

Let us begin by discussing *P*-switching in the MFIM stack with soft-DW. The simulated average charge density (Q) vs applied voltage (V_{app}) characteristics is shown in Fig. 7.10(a) for $T_{FE} = 5$ nm, $T_{DE} = 4$ nm (Al_2O_3), $g=1\times10^{-9} m^3V/C$. Here, Q is calculated as the average displacement field at the Metal-DE interface based on following equation.

$$Q = \frac{1}{l}[\int_0^l \varepsilon_0 \varepsilon_{de} \times E_{z,de}(x)dx] \tag{6.1}$$

where, $E_{z,DE}$ is the z-component of E-field at Metal-DE interface and *l* is the length of the stack. For $|V_{app}|<2V$, a continuous Q-V_{app} path exists when the FE is in the MD state and P-switching takes place through DW motion (see Fig. 7.10(b)). If $|V_{app}|$ is increased above 2V, MD state (*P*) switches to the poled state (either P↑ or P↓). Now, with decreasing $|V_{app}|$, MD state forms from the poled state at a lower $|V_{app}|$ (0.9 V) and that induces a hysteresis in the Q-V_{app} characteristics. Therefore, for non-hysteretic operation, the MD state needs to be retained by limiting V_{app}. Interestingly, in the MD state, Q is higher in the MFIM stack compared to the MIM (Metal-Insulator-Metal) at the same V_{app} as shown in Fig. 7.10(a). This implies that the effective

capacitance of the MFIM stack is higher than MIM. In a static scenario, such a phenomenon is only possible if the FE layer acts as an effective negative capacitor. The Q–V_{fe}^{avg} characteristics are shown in Fig. 7.10(a). In the MD state, as the potential drop across the FE layer is non-homogeneous along the x-axis (Fig. 7.9(b)), the average potential drop across the FE layer (V_{fe}^{avg}) is calculated using the following equation.

$$V_{fe}^{avg} = V_{app} - \frac{1}{l}[\int_0^l V_{int}(x)dx] \tag{6.2}$$

Here, $V_{int}(x)$ is the FE-DE interface potential, Q is calculated by taking the average displacement field at the FE-DE interface. Figure 7.10(a) shows that the effective FE capacitance, $C_{fe}^{eff-avg}$=dQ/dV_{fe}^{avg} is indeed negative while FE is in MD state which implies that the effective average permittivity of the FE layer in the out-of-plane direction, $\epsilon_{z,fe}^{eff-avg}$ is negative.

The DW-motion induced negative effective permittivity can be described as follows. When V_{app} = 0V, the P↓ and P↑ domains in FE are equal in size and the local $E_{z,FE}$ (depolarizing field) is directed opposite to the local P (i.e. P↓ domains exhibit E↑ and P↑ domains exhibit E↓). Note that $f_{x,grad}$ is non-zero inside of the domain (due to DW diffusion in soft-DW) and that causes the P to decrease in magnitude. Now, with the increase in V_{app}, P↓ domains grow and P↑ domains shrink in size, due to positive stiffness of DW motion. As the DW moves away from P↓ domain and towards the P↑ domain, $f_{x,grad}$ in P↓ domain decreases and in P↑ domain increases. Due to this effect as well as increase in V_{app}, the magnitude of local P in P↓ domain increases and in P↑ domain decreases. Our simulation shows that as a result of this, the depolarizing field ($E_{z,fe}$) in P↓ domain increases and in P↑ domain decreases in magnitude. This implies f_{dep} increases (decreases) in P↓ (P↑) domain. The increase (decreases) in f_{dep} in P↓ (P↑) domains is possible as it is accompanied by a decrease (increase) in $f_{x,grad}$. As the oppositely directed local E-field in FE increases (decreases) with the increase (decrease) in local P in both P↓ and P↑ domains, the effective local permittivity of the domains ($\varepsilon_{z,fe}^{eff}$) become negative.

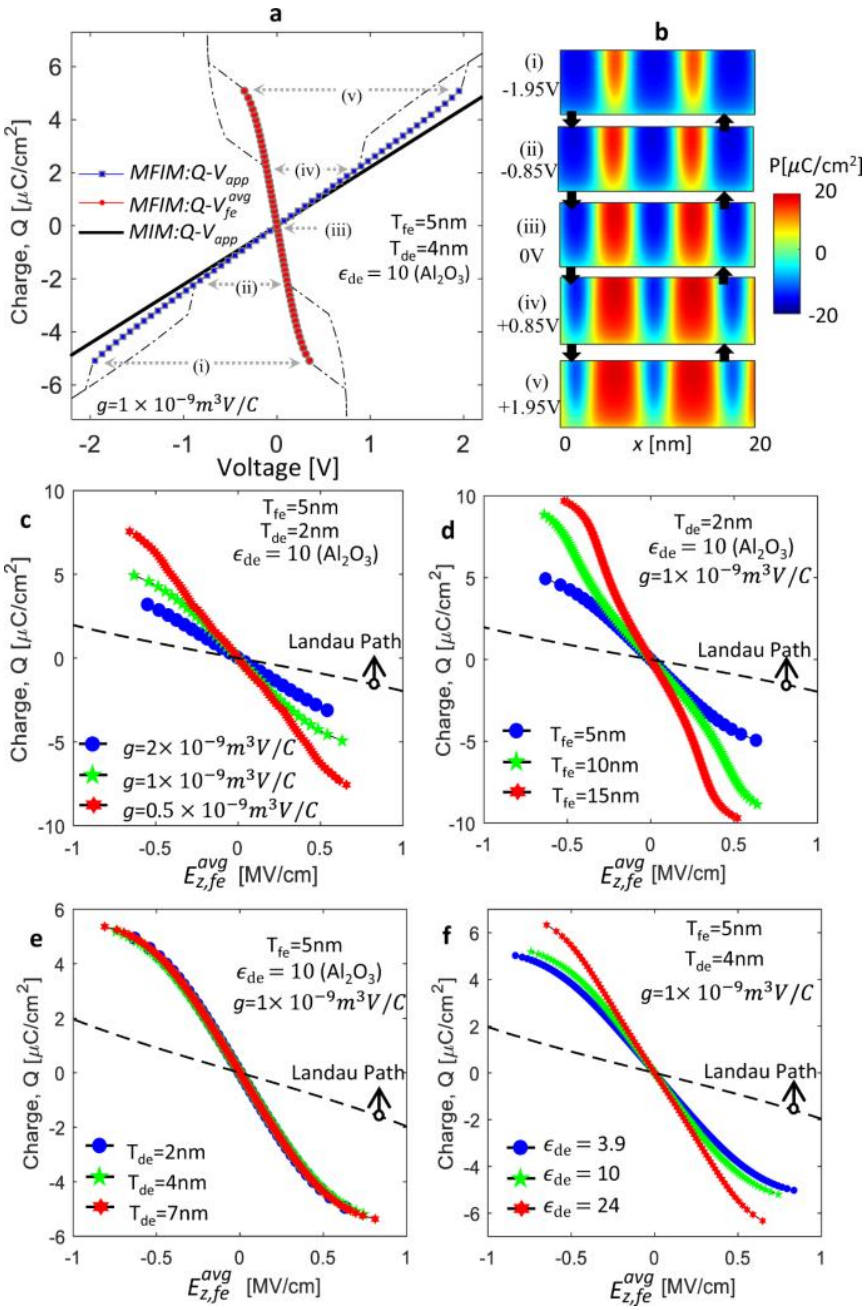

Figure 6.10. Q-V_{app} characteristics of MFIM stack when FE is in MD state (blue) showing enhanced charge response of MFIM stack compared to MIM (Metal-DE-Metal black-solid) stack. The black-dashed line represents the poled state (if $V_{app} > 2$ V). Q-VavgfeVfeavg response (red-circle). (b) P(x,z) of FE at different Vapp (as marked in Fig. 7.10(a)). Q-Eavgz,feEz,feavg characteristics of FE in MFIM stack considering (c) different g, (d) different T_{fe}, (e) different T_{de} and (f) different ε_{de}. black-dashed line in (c–f) is the single domain Landau path. The lateral dimension (along the x-axis) of 100 nm is used for all simulations.

At the same time, in the DW, the asymmetry in P distribution (due to unequal P↑ and P↓ domain sizes and P magnitudes) causes F_{dw} (comprised of $f_{x,grad}$ and $f_{x,elec}$) to decrease compared to the symmetric P distribution (at $V_{app} = 0$ V). Such a decrease in F_{dw} allows a further increase in average $E_{z,fe}^{avg}$ (an increase in depolarization energy) in the DW, while the average-P (directed opposite to $E_{z,fe}^{avg}$) in the DW increases (due to unequal P magnitudes in P↑ and P↓ domain). As a consequence, the permittivity of the DW region also becomes negative. These effective local (and non-homogeneous) negative permittivity ($\epsilon_{z,fe}^{eff-avg}$) of the domain and DW regions give rise to an average effective negative permittivity in the FE layer, i.e. $\epsilon_{z,fe}^{eff-avg}$<0.

Here, it is important to note that the appearance of negative effective permittivity is essentially an apparent phenomenon of change in long range interaction of P, its gradient and/or DW energy under DW motion. In particular, the change in P in MFIM is not directly driven by the local E-field, rather, the change in P is driven by the applied E-field induced domain-wall motion. Therefore, the change in local E-field is the effect of change in P and not the opposite. In other words, the depolarizing E-field appears depending on the change in P induced by DW motion. Even though, such phenomena lead to a negative effective permittivity of the FE layer, the susceptibility of the FE layer and the whole system (MFIM stack) is positive with respect to the applied E-field. That implies, the change in polarization is always in the direction of the change in applied E-field.

As we have identified that the F_{dw} plays a crucial role in providing negative $\epsilon_{z,fe}^{eff-avg}$, therefore, it is intuitive that the NC effect is dependent on its components, i.e. $f_{x,grad}$ and $f_{x,elec}$. To investigate such dependency, the average effective NC path in the Q-$E_{z,fe}^{avg}$ responses of MFIM stack for different g are shown in Fig. 7.10(c). Here, $E_{z,fe}^{avg}$ is the z-component of E-field in FE averaged along the length (x-axis), which we calculate as $E_{z,fe}^{avg} = V_{z,fe}^{avg}/T_{FE}$. Figure 7.10(c) shows an increase in the NC effect with an increase in gg. Here, similar to the earlier works , an increase in the NC effect implies an increase in $1/|\epsilon_{z,fe}^{eff-avg}| = \epsilon_0 |dE_{z,fe}^{avg}/dQ|$. As the $f_{x,grad}$ increases with the increase in g, a higher energy modulation is achieved by displacing the DW, which further provides a higher increase (or decrease) in f_{dep} in P↓ (or P↑) domains, leading to larger NC effect.

Similarly, dP/dx increases as the number of domains and the DWs increase with the decrease in T_{FE}. Therefore, $f_{x,grad}$ increases and provides an increased NC effect with decreasing T_{FE} (Fig. 7.10(d)). However, the soft-DW induced NC path does not depend on T_{DE} (Fig. 7.10(e)). This is because, in the MD state, the average depolarization field (which is zero at $V_{app} = 0$) as well as $f_{x,grad}$ and $f_{x,elec}$ are independent of T_{DE} within the limit of soft-DW. Interestingly, the MD-NC path does depend on the relative DE permittivity (ε_{DE}) as shown in Fig. 7.10(f). This is because the in-plane E-field, $E_{x,FE}$ in the DW needs to satisfy the in-plane boundary condition at the FE-DE interface, which is $E_{x,FE}$=$E_{x,DE}$, where $E_{x,FE}$ and $E_{x,DE}$ are the in-plane E-field in DE and FE, respectively. As the $E_{x,DE}$ increases with the decrease in ε_{DE} (considering similar P difference between two consecutive domains), therefore, $E_{x,FE}$ also increases in FE, which further increases the $f_{x,elec}$ stored in the DW. Therefore, the F_{dw} increases and hence, NC effect increases with the decrease in ε_{DE} as shown in Fig. 7.10(f). From this analysis, we can summarize that, (i) an FE material with higher g, (ii) T_{FE} scaling and/or (iii) using DE materials with low ε_{DE} are key design knobs to enhance DW-induced NC effect in MFIM stack. Note that in all of the cases discussed above, the MD NC path does not coincide with the Landau path (Fig. 7.10(c–f)) and the MD NC effect is less ($1/|\epsilon_{z,fe}^{eff-avg}|$ is less) compared to the NC effect that corresponds to Landau path. As the MD NC path is dependent on T_{FE}, g and ε_{DE}, therefore, the charge enhancement characteristics also depend on them.

6.7 Multi-domain negative capacitance effects in MFIS stack

So far, we discussed how the DW-induced effective NC in FE can enhance the overall charge response of MFIM stack. Next, we turn our attention to the MFIS stack with an undoped silicon as the semiconductor layer. To compare the MFIS results with conventional MOS capacitor, we also simulate MIIS (Metal-HfO_2-SiO_2-Si) and MIS (Metal-SiO_2-Si) stacks. The silicon layer thickness of 10 nm is considered for all the simulations of MFIS, MIIS, and MIS stacks. The simulated Q-V_{app} and C-V_{app} (capacitance, C=dQ/dV_{app}) responses are shown in Fig. 7.11(a,b), which illustrate an enhanced charge and capacitance response of MFIS compared to the MIIS and MIS stacks. We attribute this enhanced charge/capacitance response to the negative $\epsilon_{z,fe}^{eff-avg}$ of FE that we discussed earlier for MFIM. Now, to analyze the effects of T_{FE}, Q-V_{app} characteristics for different T_{FE} are illustrated in Fig. 7.11(d) showing minor enhancement in the charge response

with an increase in T_{FE}. To understand this, a relation can be derived between the charge response in MFIS (Q_{MFIS}) and in MIS (Q_{MIS}) when $\epsilon_{z,fe}^{eff-avg}$ is negative as follows.

$$\frac{dQ_{MFIS}}{dQ_{MIS}} = \frac{dQ_{MFIS}/dV_{app}}{dQ_{MIS}/dV_{app}} = \left(1 - \frac{C_{MIS} \times T_{fe}}{|\varepsilon_{z,fe}^{eff-avg}|}\right)^{-1} \tag{6.4}$$

Here, C_{MIS} is the capacitance per unit area of MIS stack. Recall that, $1/|\epsilon_{z,fe}^{eff-avg}|$ decreases with the increase in T_{FE} (discussed for MFIM). However, the increase in T_{FE} dominates over decrease in $1/|\epsilon_{z,fe}^{eff-avg}|$ in the expression of Q_{MFIS} above. Consequently, the charge responses show a mild boost (1.01x) with the increase in T_{FE} (due to two counteracting factors). Similarly, to analyze the effect of $f_{x,grad}$, we simulate MFIS stack for different values of g. The Q-V_{app} characteristics (Fig. 7.11(c)) show that the MFIS charge response enhances with the increase in g and are higher than the corresponding MIIS and MIS stacks. This is because the NC effect enhances ($1/|\epsilon_{z,fe}^{eff-avg}|$ increases) with the increase in g, as we discussed earlier in the context of MFIM.

The overall enhancement in charge/capacitance response of MFIS stack (compared to MIS and MIIS) can be easily understood from the effective negative $\epsilon_{z,fe}^{eff-avg}$ of FE. However, for FE-FET operation, it is also important to analyze the semiconductor surface potential (Ψ) in MFIS, especially, when FE is in MD state (Fig. 7.12(a)). In fact, Ψ(x) in MFIS is non-homogeneous as shown in Fig. 7.12(b) at $V_{app} = 0$ V. To understand this, let us consider the potential at the FE-DE interface, Vint(x). Note that in the MD state, E-field in FE, $E_{z,fe}$ (=(V_{app}–V_{int}(x))/T_{FE}) is directed opposite to the local P and exhibits a non-homogeneous profile along the x-direction due to periodic P↑ and P↓ domains.

Therefore, V_{int}(x) becomes non-homogenous and exhibits a maximum (max-V_{int}), and minima (min-V_{int}) corresponding to the center of P↓ and P↑ domains, respectively. This non-homogeneity in V_{int}(x) induces a spatially varying Ψ(x) as shown in Fig. 7.12(b), which, in turn exhibits a maxima (max-Ψ) and minima (min-Ψ). This further leads to local accumulation and co-existence of electrons or holes in the undoped Si layer (Fig. 7.12). Now, with the increase in V_{app} (~1.2 V), P↓ domains grow and P↑ domains shrink in size leading to an overall increase in average P (Fig. 6(d)). Simultaneously, min/max-V_{int} increases (Fig. 7.13(a)) and at the same time

exhibits a differential amplification ($dV_{int}/dV_{app}>1$) as shown in Fig. 7.13(b). Here the local differential amplification in min/max-V_{int} can be attributed to the effective local negative permittivity of FE in the P↓ and P↑ domains (discussed for MFIM). Now, as V_{int} increases, Ψ everywhere at the Si interface increases and becomes positive (but still remains non-homogeneous, see Fig. 7.12(e)). Therefore, electron density (n) dominates over hole density (p) locally and globally (Fig. 7.12(f)). Note that the increase in nn causes the non-homogeneity in Ψ to decrease (Fig. 7.12(e,f)) compared to $V_{app} = 0$ V (Fig. 7.12(b,c)).

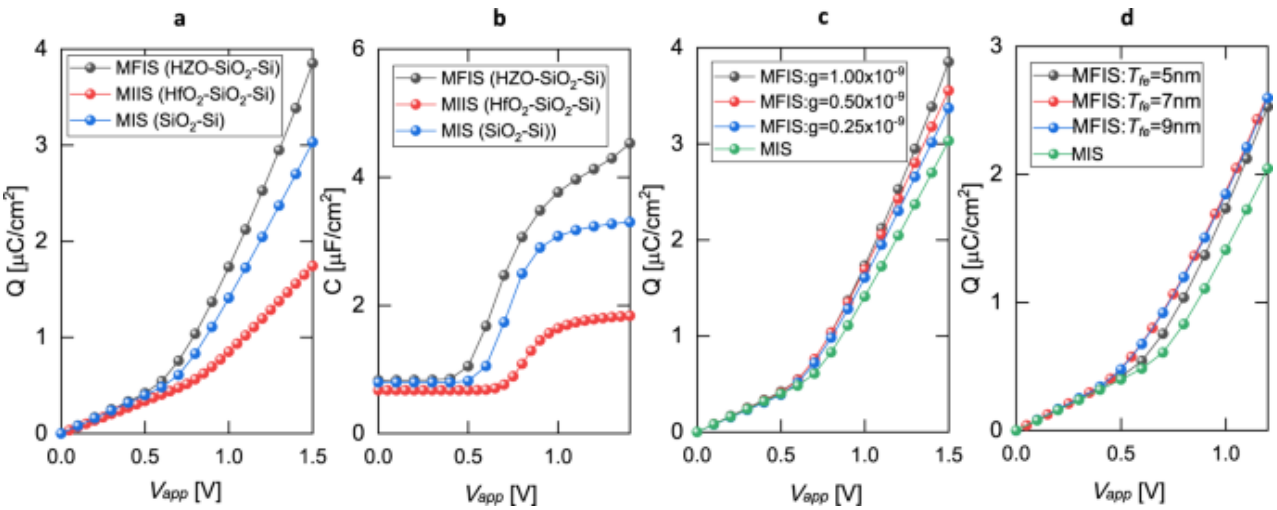

Figure 6.11. (a) Q-V_{app} and (b) C-V_{app} of MFIS (HZO(5 nm)-SiO_2(1 nm)-Si(10 nm)), MIS (SiO_2(1 nm)-Si(10 nm)), MIIS (HfO_2(5 nm)-SiO_2(1 nm)-Si(10 nm)) stacks.Here, g=1×10^{-9}m^{3}V/C. Q-V_{app} of MFIS stack for different (c) g and (d) T_{fe} and their comparison with MIS stack. The lateral dimension (along the x-axis) of 100 nm is used for all simulations.

The Ψ for MFIS, MIIS and MIS stacks for $V_{app} = 0$ V and 1.2 V are shown in Fig. 7.12(b,e). At Vapp=0V, the max(min)-Ψ in MFIS is higher(lower) than the MIIS and MIS stacks. At Vapp = 1.2 V, the max-Ψ in the MFIS is higher than the MIIS and MIS and the min-Ψ in MFIS is higher than MIIS but lower than the MIS. This can be understood from the following discussion. As in the MD state, Ez,fe is directed opposite to the local P, therefore, the max-Vint is larger than Vapp (for P↓ domains with E↑ i.e. Ez,fe<0) and the min-Vint remains less than Vapp (for P↑ with E↓ i.e. Ez,fe>0).

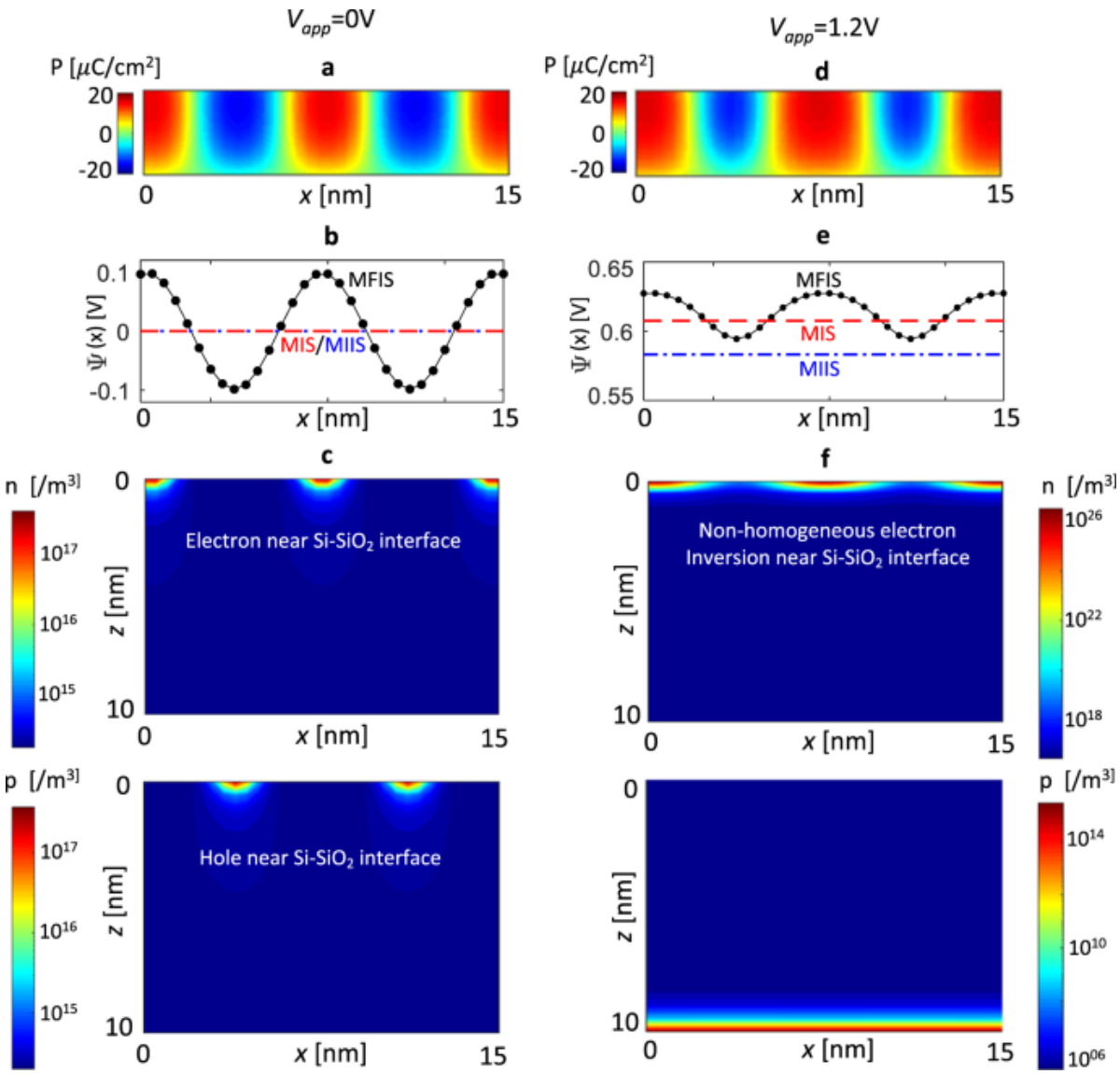

Figure 6.12. (**a**) P(x,z) of FE, (**b**) surface potential (Ψ(x)), and (**c**) electron concentration (*n*) and hole concentration (*p*) in Si layer of MFIS stack at $V_{app} = 0$ V. (**d**) P(x,z) of FE, (**e**) Ψ(*x*), and (**f**) n and p in Si layer of MFIS stack at $V_{app} = 1.2$ V. Here, $T_{fe} = 5$ nm, $T_{de} = 1$ nm (SiO_2), $T_{si} = 10$ nm and g=1×10^{-9}m^{3}V/C. The lateral dimension (along the *x*-axis) of 100 nm is used for all simulations.

This holds true when the FE is in 180° MD state and an only exception to this (where min-Vint>Vapp can occur) is for a very small voltage window just before the MD state switches to the poled state. Hence, as long as FE remains in the 180° MD state (i.e. does not switch to the poled state), the min(max)-Vint is always lower(higher) than Vapp in MFIS (see Fig. 7.13(a)). Note that, this statement is also true for MFIM. Now, in the MIS stack, DE potential is directly driven

by Vapp and hence Vint=Vapp. Therefore, min-Vint of MFIS is always less than Vint (=Vapp) of MIS as shown in Fig. 7.13(a). In addition, $d\Psi/dV_{int}$ is <1 and equal for both MFIS and MIS due to the same positive capacitance of the DE layer. As a consequence, the min-Ψ of MFIS is inevitably lower than the Ψ of MIS, when the FE is in 180° MD state (Fig. 7.13(c)). However, in MIIS, the Vint (HfO_2-SiO_2 interface potential) is not directly driven by Vapp and due to the positive capacitance of the HfO_2 layer, dVint/dVapp<1 and Vint<Vapp (Fig. 7.13(b,c)). Now, considering the differential amplification of min-Vint in MFIS (d(min−Vint)/dVapp>1) as shown in Fig. 7.13(b), the min-Vint of MFIS becomes higher than the Vint of MIIS beyond a certain Vapp (Fig. 7.13(c)). As a result, min-Ψ of MFIS becomes higher than the Ψ of MIIS at Vapp>1V) as shown in Fig. 7.13(c). Briefly, in MFIS, the min-Ψ can exceed the Ψ in MIIS but remains lower than the MIS, while the max-Ψ is always higher than the Ψ in MIIS and MIS.

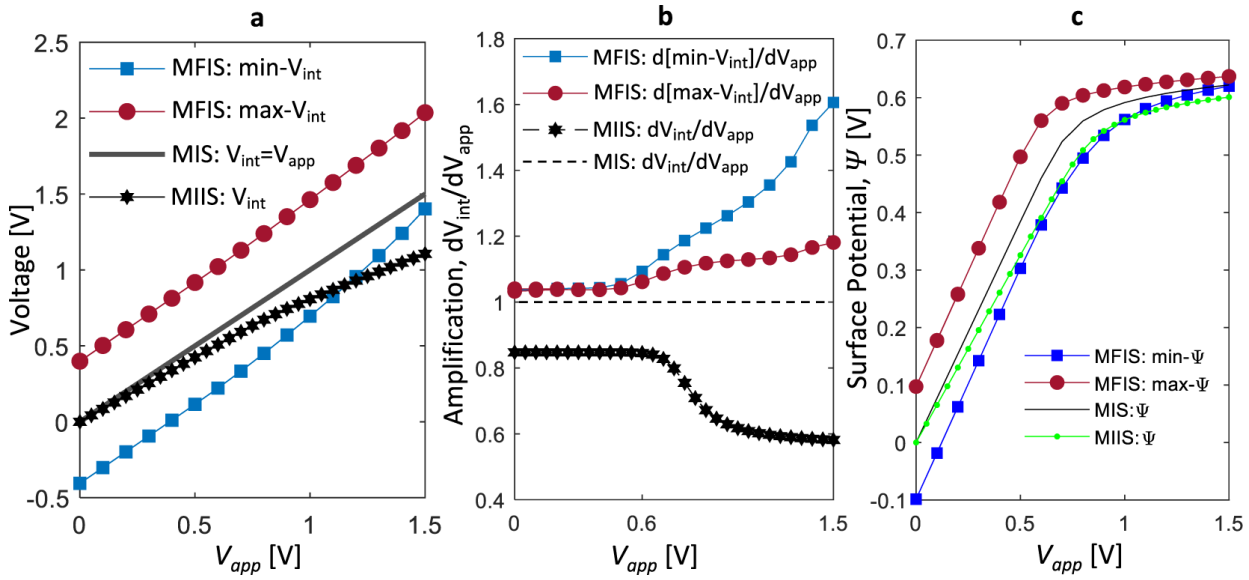

Figure 6.13. (**a**) FE-DE interface potential, V_{int} of MFIS, MIS and MIIS stacks. (**b**) dV_{int}/dV_{app} of MFIS, MIS and MIIS stacks showing differential amplification of min/max-V_{int} in MFIS stack. (**c**) Surface potential, Ψ of MFIS, MIS and MIIS stacks. Here, $T_{fe} = 5$ nm, $T_{de} = 1$ nm (SiO_2), $T_{Si} = 10$ nm and g=1×10^{-9}m^{3}V/C. The lateral dimension (along the *x*-axis) of 100 nm is used for all simulations.

Now, let us make a rough assumption that the channel current in FEFET will be mostly dependent on the min-Ψ as that determines the highest potential barrier seen by the source electrons. Then, based on the above discussion, we can expect that the OFF current (at $V_{app} = 0$ V) of FEFET will

be significantly less compared to the MIS/MIIS-FET, and the ON current ($V_{app} \sim 1.2$ V) will be higher than the MIIS-FET but comparable to MIS-FET. As the Ψ is highly non-homogeneous in MFIS stack in the low voltage regime, calculation of SS of FEFETs needs further exploration by considering source/drain regions along with the DW-induced non-homogeneous semiconductor potential and solving the transport equations to obtain the impact of the MD FE on the FEFET characteristics.

6.8 Summary

In summary, we show that the FE layer forms a denser domain pattern with increasing T_{DE} by suppressing the depolarization field and leading to a higher hysteresis in the FE-DE stack. Simultaneously, the mechanism of *P*-switching can be modulated from nucleation to DW-motion dominant by increasing T_{DE}. In addition, we show that the DW energy and thus the coercive voltage and remanent P can further be modulated by ϵ_{DE} while keeping the same C_{DE}. Such T_{DE} and ϵ_{DE} dependency can serve as the potential knobs to deploy the application-driven optimization of the FEFET gate stack. For instance, FEFETs with low T_{DE} (high switching slope) can be used for the design of binary NVMs and neurons, while high T_{DE} can be utilized for multi-bit memories and synapse designs. In addition, by performing phase-field simulation, we show that the energy stored in FE DW can be harnessed to enhance the capacitance of the MFIM and MFIS stack, where the soft-DW displacement leads to a static and hysteresis-free negative capacitance in the MD FE. Our analysis indicates that the effective negative permittivity of the FE layer is dependent on the FE thickness, gradient energy coefficient, in-plane permittivity of the DE and is independent of DE thickness within the limit of soft-DW. Further, the DW-induced NC effect can lead to an enhanced charge/capacitance response in MFIS stack compared to MIS/MIIS stack. However, such a charge/capacitance enhancement in MFIS does not guarantee an enhanced local Ψ in Si compared to MIS. In fact, Ψ becomes spatially varying due to the MD nature of FE and the variation is higher at low applied voltages. In addition, we discuss that the minimum Ψ in MFIS can exceed the Ψ in MIIS but remains smaller than the MIS. Nevertheless, considering the local differential amplification of Vint, the on/off current ratio of FEFET can potentially exceed the MIS/MIIS-FET. Since the non-homogeneity in Ψ is absent in conventional MOS capacitor (and MOSFET),

therefore, as future work, it will be important to investigate the impact of such potential profile on the low voltage conduction of FEFETs.

6.9 References

[1] J. Müller, T. S. Böscke, S. Müller, E. Yurchuk, P. Polakowski, J. Paul, D. Martin, T. Schenk, K. Khullar, A. Kersch, W. Weinreich, S. Riedel, K. Seidel, A. Kumar, T. M. Arruda, S. V. Kalinin, T. Schlösser, R. Boschke, R. van Bentum, U. Schröder, and T. Mikolajick, "Ferroelectric hafnium oxide: A CMOS-compatible and highly scalable approach to future ferroelectric memories," *IEDM*, 2013.

[2] A. K. Saha, B. Grisafe, S. Datta, and S. K. Gupta, "Microscopic Crystal Phase Inspired Modeling of Zr Concentration Effects in $Hf_{1-x}Zr_xO_2$ Thin Films," *IEEE VLSI Technology*, 2017.

[3] K. Ni, B. Grisafe, W. Chakraborty, A. K. Saha, S. Dutta, M. Jerry, J. A. Smith, S. Gupta, and S. Datta, "In-Memory Computing Primitive for Sensor Data Fusion in 28 nm HKMG FeFET Technology," *IEDM*, 2018.

[4] A. K. Saha, K. Ni, S. Dutta, S. Datta, and S. Gupta, "Phase field modeling of domain dynamics and polarization accumulation in ferroelectric HZO," *Appl. Phys. Lett.*, 2019.

[5] K. Chatterjee, S. Kim, G. Karbasian, A. J. Tan, A. K. Yadav, A. I. Khan, C. Hu, and S. Salahuddin, "Self-Aligned, Gate Last, FDSOI, Ferroelectric Gate Memory Device With 5.5-nm $Hf_{0.8}Zr_{0.2}O_2$, High Endurance and Breakdown Recovery," *IEEE Electron Device Lett.*, 2017.

[6] S. Dünkel, M. Trentzsch, R. Richter, P. Moll, C. Fuchs, O. Gehring, M. Majer, S. Wittek, B. Müller, T. Melde, H. Mulaosmanovic, Stefan Slesazeck, S. Müller, J. Ocker, M. Noack, D-A Löhr, P. Polakowski, J. Müller, T. Mikolajick, J. Höntschel, B. Rice, J. Pellerin, S. Beyer, "A FeFET based super-low-power ultra-fast embedded NVM technology for 22nm FDSOI and beyond", *IEDM*, 2017.

[7] H. Mulaosmanovic, E. Chicca, M. Bertele, T. Mikolajickac, and S. Slesazecka, "Mimicking biological neurons with a nanoscale ferroelectric transistor," *Nanoscale*, 2018.

[8] H. Mulaosmanovic, J. Ocker, S. Müller, M. Noack, J. Müller, P. Polakowski, T. Mikolajick, and S. Slesazeck, "Novel ferroelectric FET based synapse for neuromorphic systems," *IEEE VLSI Technol.*, 2017.

[9] M. Jerry, P. Chen, J. Zhang, P. Sharma, K. Ni, S. Yu, and S. Datta, "Ferroelectric FET analog synapse for acceleration of deep neural network training," *IEDM*, 2017.

[10] P. Sharma, K. Tapily, A. K. Saha, J. Zhang, A. Shaughnessy, A. Aziz, G. L. Snider, S. Gupta, R. D. Clark, and S. Datta, "Impact of total and partial dipole switching on the switching slope of gate-last negative capacitance FETs with ferroelectric hafnium zirconium oxide gate stack," in *Proc. IEEE VLSI Technol.*, 2017.

[11] V. Gaddam, D. Das, and S. Jeon, "Insertion of HfO_2 Seed/Dielectric Layer to the Ferroelectric HZO Films for Heightened Remanent Polarization in MFM Capacitors," *IEEE Trans. on Electron Devices*, 2020.

[12] S. Salahuddin, and S. Datta, "Use of negative capacitance to provide voltage amplification for low power nanoscale devices," *Nano Lett.*, 2007

[13] A. K. Saha, S. Datta, and S. Gupta, "'Negative capacitance' in resistor-ferroelectric and ferroelectric-dielectric networks: Apparent or intrinsic?," *J. Appl. Phys.*, 2018.

[14] W. Xiao , C. Liu, Y. Peng, S. Zheng , Q. Feng , C. Zhang ,J. Zhang , Y. Hao, M. Liao, and Y. Zhou, "Performance Improvement of $Hf_{0.5}Zr_{0.5}O_2$-Based Ferroelectric-Field-Effect Transistors With ZrO_2 Seed Layers," *IEEE Electron Device Lett.*, 2019.

[15] M. Si, X. Lyu, and P. D. Ye, "Ferroelectric Polarization Switching of Hafnium Zirconium Oxide in Ferroelectric/Dielectric Stack," *ACS Appl. Electron. Mater.*, 2019.

[16] A. M. Bratkovsky and A. P. Levanyuk, "Abrupt appearance of the domain pattern and fatigue of thin ferroelectric films," *AIP Conference Proceedings*, 2000.

[17] M. Si, X. Lyu, P. R. Shrestha, X. Sun, H. Wang, K. P. Cheung, and P. D. Ye, "Ultrafast measurements of polarization switching dynamics on ferroelectric and anti-ferroelectric hafnium zirconium oxide," *Appl. Phys. Lett.*, 2019.

[18] A. K. Saha, and S. K. Gupta, "Multi-Domain Negative Capacitance Effects in Metal-Ferroelectric-Insulator-Semiconductor/Metal Stacks: A Phase-field Simulation Based Study," *Scientific Reports*, 2020.

[19] H.W. Park, J. Roh, Y. B. Lee, and C. S. Hwang, "Modeling of negative capacitance in ferroelectric thin films," *Adv. Mater.*, 2019.

[20] M. D. Glinchuk and E. A. Eliseev, “Ferroelectric thin film properties-Depolarization field and renormalization of a “bulk” free energy coefficients,” *J. Appl. Phys.*, 2003.

[21] P. Chandra and P. B. Littlewood, “A Landau Primer for Ferroelectrics” in *Physics of Ferroelectrics: A Modern Perspective, Topics Appl. Physics*, vol. 105, K. Rabe, C. H. Ahn, J.-M. Triscone, Eds., Berlin: Springer-Verlag, 2007.

[22] H.-J. Lee, M. Lee, K. Lee, J. Jo, H. Yang, Y. Kim, S. C. Chae, U. Waghmare, J. H. Lee, “Scale-free ferroelectricity induced by flat phonon bands in HfO_2,” *Science*, 2020.

[23] A. I. Kurchak, E. A. Eliseev, S. V. Kalinin, M. V. Strikha, and A. N. Morozovska, “p−n Junction Dynamics Induced in a Graphene Channel by Ferroelectric-Domain Motion in the Substrate,” *Phys. Rev. Applied*, 2017.

[24] H. J. Kim, M. H. Park, Y. J. Kim, Y. H. Lee, W. Jeon, T. Gwon, T. Moon, K. D. Kim, and C. S. Hwanga, “Grain size engineering for ferroelectric $Hf_{0.5}Zr_{0.5}O_2$ films by an insertion of Al_2O_3 interlayer,” *Appl. Phys. Lett.*, 2014.

[25] J. Íñiguez, P. Zubko, I. Luk’yanchuk, and A. Cano, “Ferroelectric negative capacitance,” *Nat. Rev. Mater.*, 2019.

[26] Íñiguez, J., Zubko, P., Luk’yanchuk, I. & Cano, A. Ferroelectric negative capacitance. Nat. Rev. Mater., 2019.

[27] Zubko, P. et al. Negative capacitance in multidomain ferroelectric superlattices. Nature, 2016.

[28] Yadav, A. K. et al. Spatially resolved steady-state negative capacitance. Nature, 2019.

[29] Luk’yanchuk, I., Sené, A. & Vinokur, V. M. Electrodynamics of ferroelectric flms with negative capacitance. Phys. Rev. B, 2018.

[30] Kopal, A., Mokrý, P., Fousek, J. & Bahník, T. Displacements of 180 domain walls in electroded ferroelectric single crystals: The effect of surface layers on restoring force. Ferroelectrics, 1999.

[31] Bratkovsky, A. M. & Levanyuk, A. P. Abrupt appearance of the domain pattern and fatigue of thin ferroelectric flms. Phys. Rev. Lett., 2000.

[32] Bratkovsky, A. M. & Levanyuk, A. P. Very large dielectric response of thin ferroelectric flms with the dead layers. Phys. Rev. B, 2001.

[33] Luk’yanchuk, I., Tikhonov, Y., Sené, A., Razumnaya, A. & Vinokur, V. M. Harnessing ferroelectric domains for negative capacitance. Commun. Phys., 2019.

[34] Cano, A. & Jiménez, D. Multidomain ferroelectricity as a limiting factor for voltage amplifcation in ferroelectric feld-efect transistors. Appl. Phys. Lett., 2010.

[35] Choudhury, S. et al. The influence of 180 ferroelectric domain wall width on the threshold feld for wall motion. J. Appl. Phys., 2008.

[36] Wang, J., Shi, S.-Q., Chen, L.-Q., Li, Y. & Zhang, T.-Y. Phase-feld simulations of ferroelectric/ferroelastic polarization switching. Acta Materialia, 2004.

7. PHASE-FIELD MODELING OF FERROELECTRIC FIELD EFFECT TRANSISTOR (FEFET)

7.1 Introduction

FEFET have been demonstrated to offer multi-level memory/synaptic functionalities for high FE thickness (T_{FE}~10nm) [1-2] and non-hysteretic switch behavior with enhanced gate control for low T_{FE} (<3nm) [3-4]. However, the multi-domain effects in FE and its correlation with T_{FE}, as well as the enhanced permittivity (ϵ_r) behavior is yet to be understood. In this chapter, we analyze multi-domain polarization (P) switching and the origin of enhanced-ϵ_r in FEFETs and their dependence on T_{FE}. Our analysis is based on self-consistent phase-field model of FEFET, validated with our experimental characteristics of metal-ferroelectric-insulator-metal (MFIM) and metal-ferroelectric-insulator-semiconductor (MFIS) stack for different T_{FE}. Unlike previous FEFET models [5-8], which assume a certain number of FE domains [5], in our model, the multi-domain formation in the FE is self-consistently determined by electrostatics, which allows us to comprehensively analyze the microscopic domain interactions in FE and its influence on the underlying transistor channel.

In this chapter, we present a phase-field simulation framework for ferroelectric field effect transistor (FeFET) which captures multi-domain effects by self-consistently solving 2D time-dependent Ginzburg-Landau (TDGL), Poisson's, and semiconductor charge/transport equations. Using our phase-field model and experiments, we analyze electrostatics-driven multi-domain formation and voltage-induced polarization (P) switching for different FE thickness (T_{FE}). Considering HZO as the FE material, we show that for T_{FE} = 5nm – 10 nm, FEFETs exhibit multi-level memory functionality; while for T_{FE} = 1.5nm – 3 nm, FEFETs can serve as non-hysteretic switches with enhanced gate control. Our results signify that as T_{FE} is reduced from 10nm to 5nm, denser domain patterns emerge in FE, and the dominant P-switching mechanism changes from nucleation to domain-wall motion based leading to a decreased memory window with T_{FE} scaling. Moreover, as T_{FE} is scaled further from 3nm to 1.5nm, effective permittivity of the gate stack increases due to multi-domain electrostatic interactions. Interestingly, for HZO thickness below 1.5nm, the DW becomes soft and our simulation suggest the appearance of multi-domain negative

capacitance effect in FeFET characteristics. In addition, we also analyze the gate length scaling behavior in FeFET and that signifies a better short-channel behavior compared to conventional high-k based transistors (HKFET).

7.2 Phase-Field Simulation Framework for FeFET

In our phase-field simulation, we self-consistently solve the time-dependent Ginzburg Landau (TDGL) equation [9-10] for polarization (P), Poisson's equation for potential (ϕ) and semiconductor charge equations for charge density (ρ). The considered FEFET structure and simulation flow are shown in Fig. 7.1. We consider HZO ($Hf_{0.5}Zr_{0.5}O_2$) as FE, where the P direction is assumed to be along the film thickness, which is analogous to the c-axis of its orthorhombic crystal phase. In addition, the Landau coefficients used in simulation are assumed to be strain normalized based on the assumption of a stress free interface. All the physics modules are solved in finite-difference approach by assuming a grid size of 0.5nm in all the physical directions. Under the above mentioned assumptions, the TDGL equations and the Poisson's equations can be written as the following equations.

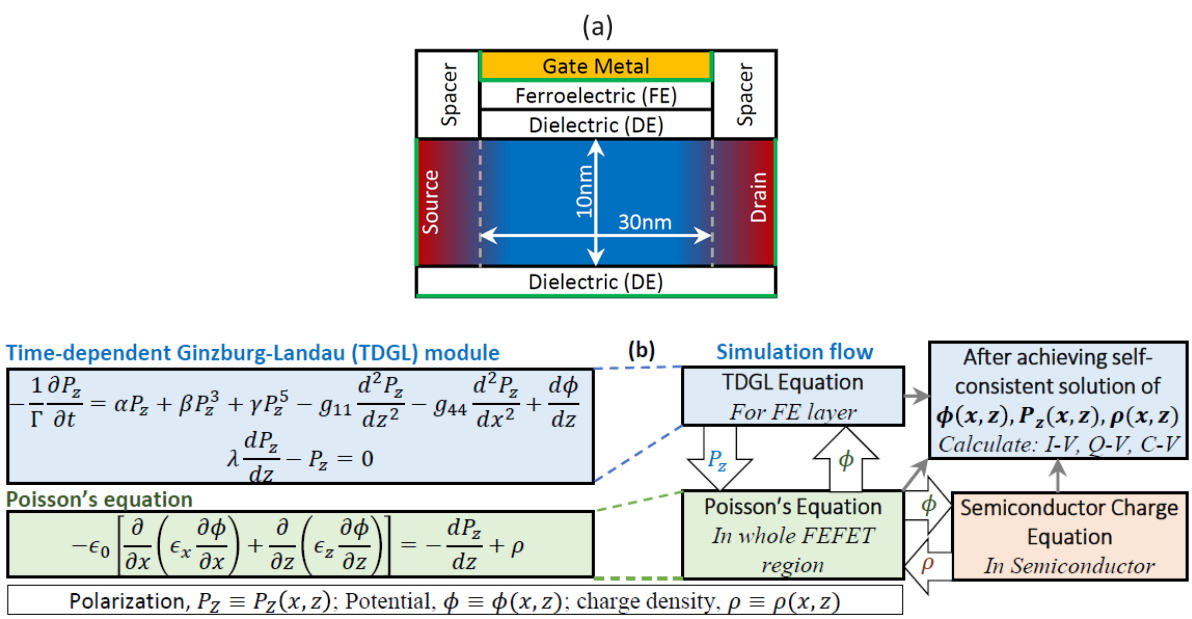

Figure 7.1. (a) Simulated FeFET structure, (b) self-consistent simulation flow among TDGL, Poisson's and semiconductor (silicon) charge equations (c) FE parameters used in FEFET simulation. For the simulation of metal-FE-insulator-metal (MFIM) stack only Poisson's and TDGL equations are used.

7.3 FEFET Characteristic with high FE thickness (5nm – 10nm)

We first analyze the FEFETs for T_{FE} scaled from 10nm to 5nm. The simulated gate charge (Q) versus gate voltage (V_{GS}) for T_{FE}=10nm (Fig. 7.2(a)) shows hysteretic characteristics with a two-step increase (decrease) in Q during the forward (reverse) sweep. The P profile of FE layer (Fig. 7.2(b)) suggests that, with the increase in V_G, P-switching first happens through nucleation of new +P domain at the source (S) and drain (D) side of FE giving rise to a sharp increase in Q-V_G characteristics. With the further increase in V_G, the -P domain between the newly nucleated +P and the previous +P domains completely switches to +P through DW motion. This gives rise to second step in the Q-V_G characteristics. Note that the reason for dominant P-switching at the S/D side is the higher E-field (originating from the depletion regions in S/D) compared to the center of the FE. Considering the SET and RESET condition (after applying V_G=+5V and V_G=-5V, respectively), the potential profile of the FEFET is shown in Fig. 7.9 (a) for V_G=0V, illustrating highly non-uniform potential distribution in the channel due to MD state of FE. For RESET state, domains near the S/D side are in -P state which induce a large negative potential across the channel- S/D junction. In contrast, for SET state, due to the dominant +P domain near the S/D side, the potential across the channel-S/D junction becomes positive. As a result of P-induced change in channel potential, we observe a large V_T (=V_{GS} at I_D=1μA/μm) shift in the I_D-V_{GS} characteristics of FEFET between RESET and SET states (Fig. 7.3(b)). Moreover, due to the step wise P-switching in the FE layer, different V_T shift in the I_D-V_{GS} characteristics of FEFET are obtained for different V_{SET} value as shown in Fig. 7.3(b), leading to multi-level memory behavior.

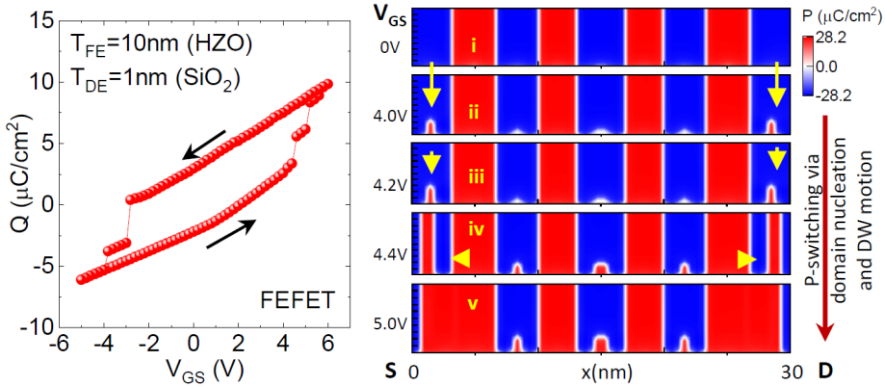

Figure 7.2. (a) Simulated gate charge (Q) vs V_{GS} at V_{DS}=0V of FEFET showing hysteretic characteristics demonstrating the P-switching in the FE layer. (b) P-profile in FE for different V_{GS} in FEFET showing domain nucleation (i-iv) followed by DW motion (iv-v) based P-switching. Note: P-switching is dominant near the source (S) and drain (D) region.

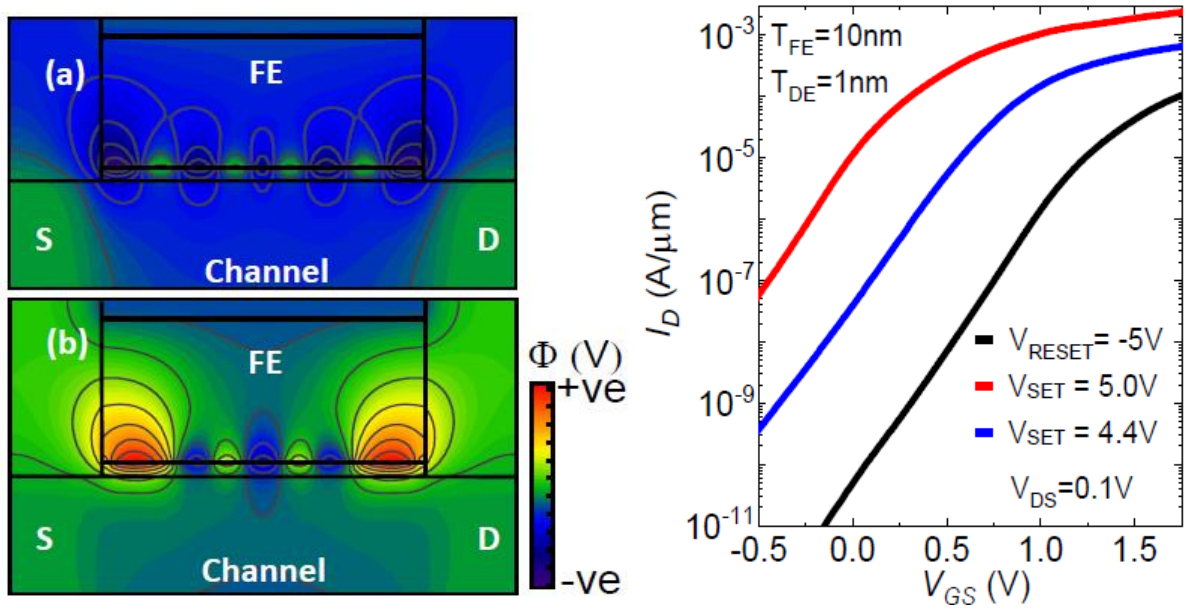

Figure 7.3. FEFET potential profile at V_{GS}=0V after (a) V_{RESET}=V_{GS}=-5V and (b) V_{SET}=V_{GS}=6V showing *P*-switching induced change in channel potential as well as non-uniform potential in channel. (c) I_D-V_{GS} characteristics of FEFET for different V_{SET} showing the *P*-switching induced V_T shift and memory behavior.

Similar to T_{FE}=10nm, Q-V_G characteristics for T_{FE}=5nm (Fig. 7.4(a)) signifies hysteretic characteristics with smaller step-wise change in Q. This is because for lower T_{FE} (5nm), the domain density is more (compared to T_{FE}=10nm). Hence, V_G-induced *P*-switching takes place via DW motion (Fig. 7.4(b)) leading to a smaller step-wise change in Q-V_G characteristics. Similar to T_{FE}=10nm, the *P*-switching for T_{FE}=5nm is more dominant near S/D (Fig. 7.4(b)). The FEFET potential profile for RESET and SET states at V_G=0V (Fig. 7.5(a)) show a larger channel potential and smaller source barrier for the SET state due to the *P*-switching in FE. Due to *P*-switching with smaller steps, a smaller change in V_T is observed in the I_D-V_{GS} characteristics (Fig. 7.5(b)) at lower T_{FE} (~5nm). Note that the V_T shift between V_{SET}=3.4V and 3.6V is insignificant as *P*-switching takes away from the S/D side and thus has less impact on source barrier. Moreover, we observe an increased memory window (MW=ΔV_G at I_D=1μA/μm) (Fig. 7.6) for higher T_{FE} (=10nm) due to nucleation dominated *P*-switching. The MW decreases, and V_T shift becomes smaller for lower T_{FE} (=5nm) due to denser domain pattern and DW motion based *P*-switching, however, leads to multi-level memory operation.

I_D-V_{DS} characteristics for FEFET (T_{FE}=5nm) with SET state illustrates hysteretic characteristics (Fig. 7.7(a)) similar to experimental results in [11]. In the forward path, I_D increases with the increase in V_{DS} and exhibits a sharp decrease at some critical V_{DS}. This is because, the increase in V_{DS} leads to *P*-switching via domain wall motion near the drain side (Fig. 7.7(b)) due to negative V_{GD}. This results in an increase in drain-to-channel barrier which reduces I_D. In the reverse V_{DS} sweep, the reduced I_D state is retained due to *P*-retention and follows a different path from the forward sweep. The critical V_{DS} (which triggers *P*-switching) increases with the increasing T_{FE} and increasing V_{GS} (Fig. 7.7(c)).

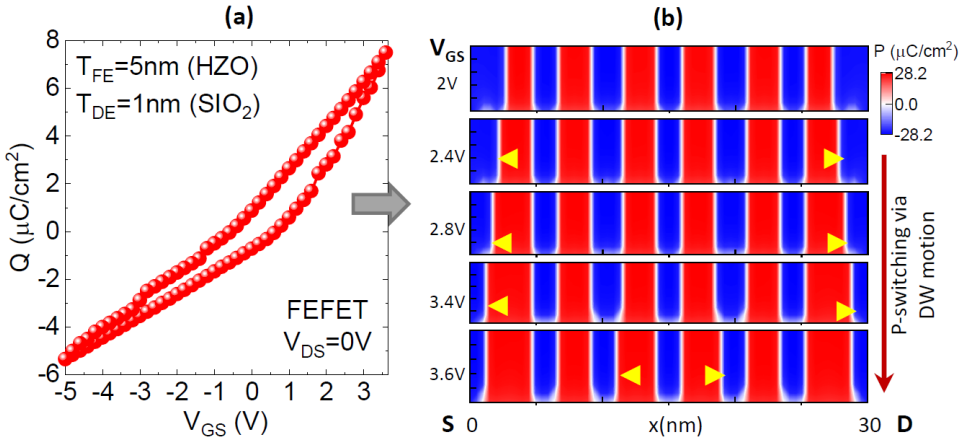

Figure 7.4. Simulated Q-V_{GS} of FEFET showing hysteretic characteristics for T_{FE} = 5nm due to DW motion. *P* profile in FE for different V_{GS} in FEFET showing DW motion-based *P*-switching. Here, the yellow arrows point towards the direction of DW displacements.

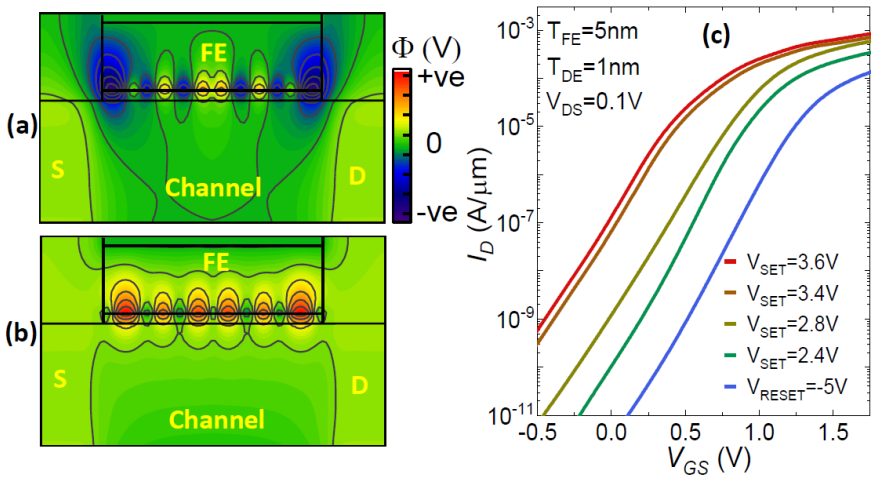

Figure 7.5. FEFET Potential profile at V_{GS}= 0V after (a)V_{RESET}= -3.6V and (b)V_{SET} = 3.6V showing *P*-switching induced change in channel potential. (c) I_D-V_{GS} characteristics of FEFET with T_{FE}=5nm showing multi-level memory operation.

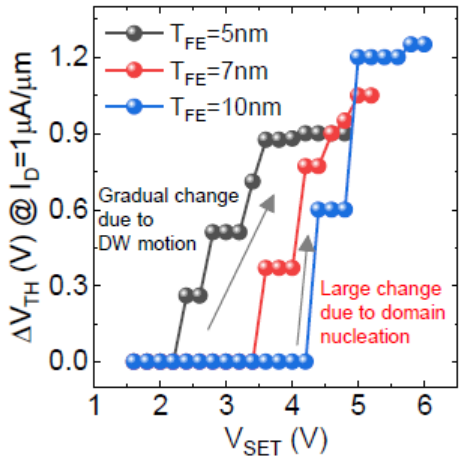

Figure 7.6. (a) Memory window (ΔV_{TH}) for different T_{FE} and V_{SET} showing that MW increases with the increase in T_{FE}.

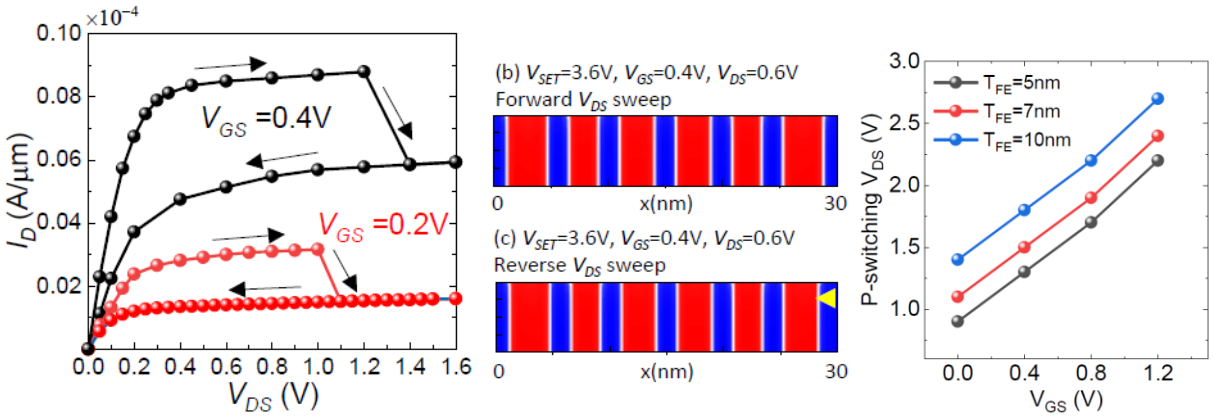

Figure 7.7. I_D-V_{DS} characteristics showing hysteretic behavior. The *P*-profile of the FE layer is shown for V_{DS}=0.6V considering (b) forward V_{DS} sweep and (c) reverse V_{DS} sweep. Due to the *P*-switching near drain side the drain barrier height increases leading to a lower current in reverse sweep compared to forward sweep. V_{DS} to induce *P*-switching in drain-side for different V_{GS} showing *P*-switching occur at higher V_{DS} for increasing T_{FE}.

Note that, due to the 2D nature of our simulation, the MD state formation occurs only along the channel length. However, due to the polycrystalline nature of HZO, MD state can form along the width direction also. Consideration of MD state along the width can potentially lead to a gradual V_T shift, as well as a gradual V_{DS} induced decrease in I_D as shown in experiments [2,11].

7.4 FeFET Characteristic with low FE thickness (2nm – 3nm)

Let us now turn our attention to T_{FE} scaling below 5nm. The measured capacitance-voltage (*C-V*) characteristics of MFIS stack (Fig. 7.8(a)) with 2.5nm HZO/0.8nm SiO_2/p-Si as is shown in Fig. 7.8(b) suggesting a higher capacitance compared to a physically equivalent MOS capacitor (2.5nm HfO2/0.8nm SiO_2/p-Si). This suggests enhanced-ϵ_r behavior of HZO. The simulated *C-V* characteristics show good agreement with the experimental results (Fig. 7.8(b)). The *P* and *E*-field profile of FE-DE layer of the MFIS stack (Fig. 7.8(c-d)) show that the FE layer is in the MD state with a dense domain pattern and no *P*-switching occurs within the operational voltage range (0-1V). Instead, the charge response is due to the background permittivity of FE and change in polarization magnitude (|*P*|) and not due to the change in P-direction through domain nucleation or DW motion. Enhanced-ϵ_r stems from the fact that some stray *E*-field lines between the domains with opposite *P* at 0V (Fig. 7.8(c)) transforms into out-of-plane component at -0.5V (Fig. 7.8(d)).

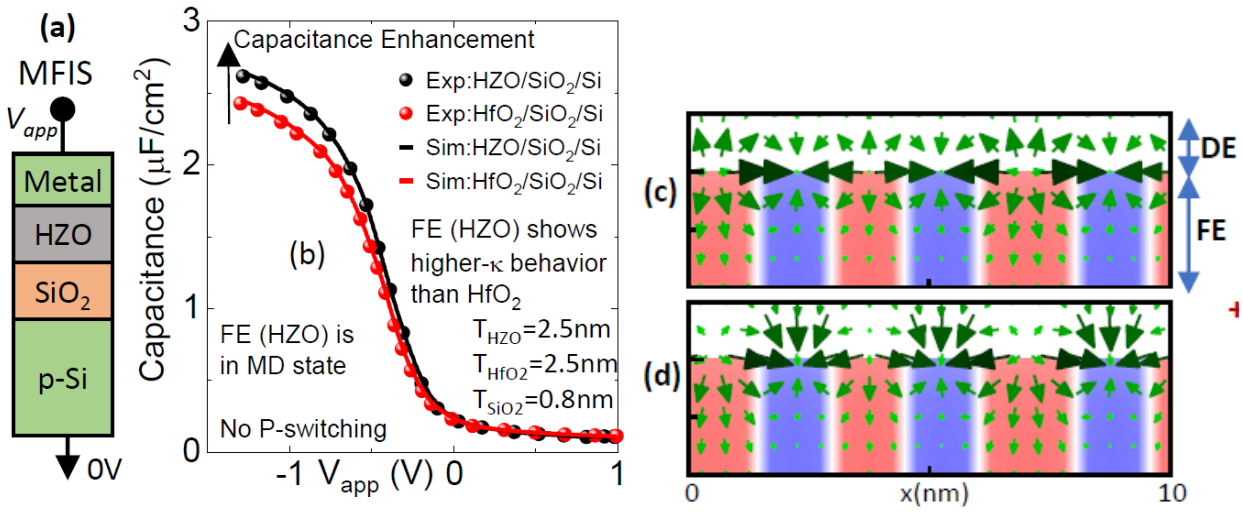

Figure 7.8. (a) MFIS stack; (b) C-V characteristics of MFIS stack compared to MOS capacitor showing high-k behavior of the FE layer (c) P and E-field profile in the FE and DE layer of MFIS stack at (c) 0V and (d) -0.5V showing the transformation of stray/in-plane E-field to out-of-plane E-field due the change in local P magnitude. This phenomenon leads to extra charge in the FE-DE interface yielding an enhanced effective permittivity of the FE layer.

To understand this phenomenon, a two dipole (with opposite dipole moment) model has been discussed in chapter 4, where the dipoles are analogous to the domains with opposite *P* direction in FE. First, note that at 0V, there are stray E-fields lines between the dipoles. Now, with the increase in voltage, |*P*| in +*P* domain increase and -*P* domain decreases. That leads to a decrease in the stray E-field between the dipoles. Instead, an out-of-plane E-field by compensating more charges at the FE-DE interface. The additional charges on the FE interface from this transformation of stray *E*-field to out-of-plane *E*-field leads to an enhanced effective ϵ_r behavior of the FE layer. The simulated FEFET characteristics with 2nm HZO is shown in Fig. 7.9(a) showing an improved I_D and subthreshold swing (SS) compared to a FET with 2nm HfO_2. Note that the stray E-fields exist near the DW. As the domain and DW density increases with the decrease in T_{FE}, the stray *E*-field in the FE layer increases. Thus, stray E-field can be transformed into out-of-plane E-field to a larger extent leading to an increase in effective-ϵ_r of FE with the decrease in T_{FE} (Fig. 7.9(b)). Therefore, the SS improvement in FEFET is more significant compared to HfO_2-FET with the decrease in oxide thickness (Fig. 7.9(c)).

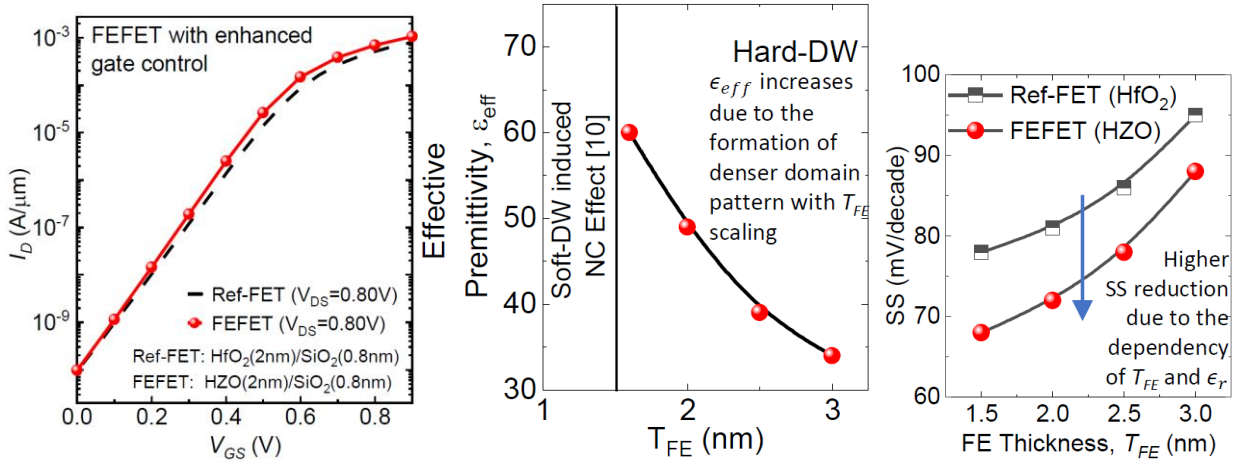

Figure 7.9. I_D-V_{GS} characteristics of FEFET showing higher-k behavior with enhanced gate control compared to Ref-FET (with HfO_2/SiO_2 gate stack). Effective permittivity of the FE layer for different T_{FE} showing that the permittivity increases with the decrease in FE thickness. Subthreshold swing (SS) for different $T_{FE}=T_{HfO2}$ showing more SS reduction in FEFET.

7.5 FeFET Characteristic with ultra-low FE thickness (<1.5nm)

According to our simulation, the FE layer in FEFET exhibits soft-DW for T_{FE}=1.2nm that undergoes soft-DW displacement under the influence of applied V_{GS} (Fig. 7.10(a)). Interestingly, the presence of MD state in the FE layer leads to a significantly non-homogeneous potential profile in the underlying Si channel. Therefore, the FE-DE interface potential (V_{INT}) and the surface potential (ψ_s) also becomes non-homogeneous. Similarly, the conduction-band (CB) profile of NCFET in Si at SiO_2 interface shows rippled type features (Fig. 7.10(b-c)). At the OFF state (V_{GS}=0V), the CB maxima in NCFET is higher compared to the HKFET and thus the OFF-state current of NCFET is lower compared to the HKFET (Fig. 7.11(a)). Similarly, at the ON state (V_{GS}=0.6V), the CB maxima in NCFET is lower compared to the HKFET and hence, the ON state current of NCFET is higher compared to the HKFET (Fig. 7.11(a)). Further, due to the MD NC effect of the FE layer, the NCFET exhibits enhanced capacitance (C) versus V_{GS} characteristics compared to the conventional HKFET. It is noteworthy that the MD NC effect of FE leads to an amplification in average V_{INT} (dV_{INT}^{avg}/dV_{GS}>1 in Fig. 7.11(c)) in NCFET, which further leads to a decrease in SS compared to HKFET (for which dV_{INT}^{avg}/dV_{GS}<1).

Now, let us analyze the effects of drain voltage (V_{DS}) in MD NCFET. The CB profiles of NCFET and HKFET at different V_{DS} are shown in Fig. 7.12 (a) and (b), respectively. Note that the CB profile of HKFET exhibits only one maximum. Therefore, the surface potential increases (or the CB maxima decreases) with the increase in V_{DS}. This leads to a finite output conductance (g_{ds}) in the I_D-V_{DS} characteristics of HKFET. However, in NCFET, due to the presence of MD state in FE, the CB profile exhibits several local maxima along the gate length direction. In such a scenario, an increase in V_{DS} mostly reduces the CB peaks near the drain side but causes a negligible change near the source side. This is because the V_{DS}-induced electric-field can be compensated by the (i) local change in P magnitude in the FE layer near the drain side and (ii) higher local charge in the Si in the valley of rippled CB profile near the drain side. Therefore, the penetration of drain induced field towards the source side is somewhat shielded. As in the NCFET, the CB peaks near the source side do not significantly depend on V_{DS} in the saturation region, therefore, NCFET exhibits significantly lower g_{ds} compared to the HKFET (Fig. 7.12(c-d)). Due to a similar rationale, the drain-induced barrier lowering (DIBL) in MD NCFET is expected to be significantly reduced

compared to the HKFET. Such unique attribution of MD state in FE further leads to an interesting feature from the prospect of gate length scaling which we discuss in the next sub-section.

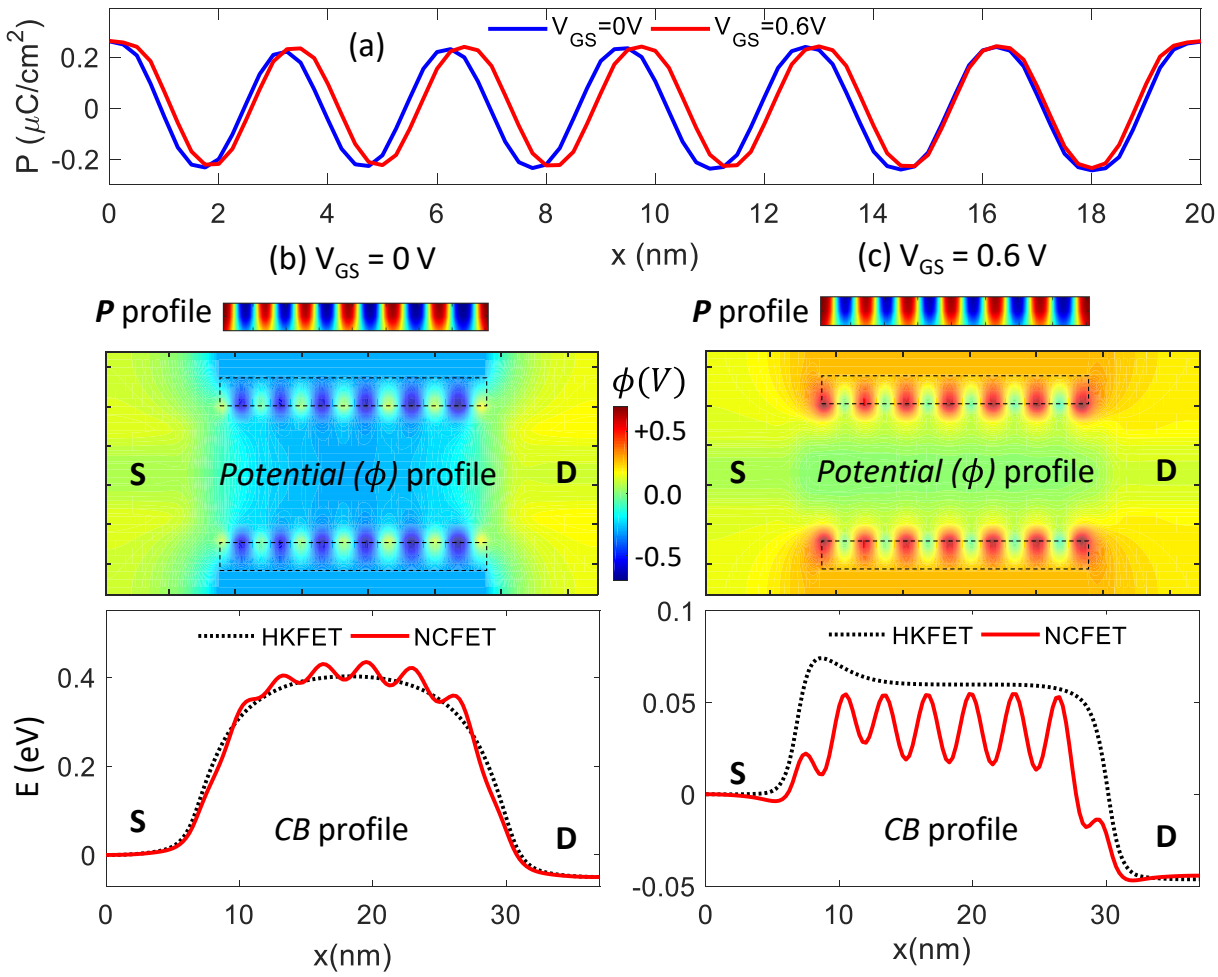

Figure 7.10. Polarization (*P*) profile of FE layer at the FE-DE interface of NCFET showing gate voltage (V_{GS}) driven soft-DW displacement. P map in FE, potential (***ϕ***) profile of NCFET and conduction band (CB) profile of NCFET and HKFET at (b) V_{GS} = 0V and (c) V_{GS} = 0.6V. Here, V_{DS} = 0.05V.

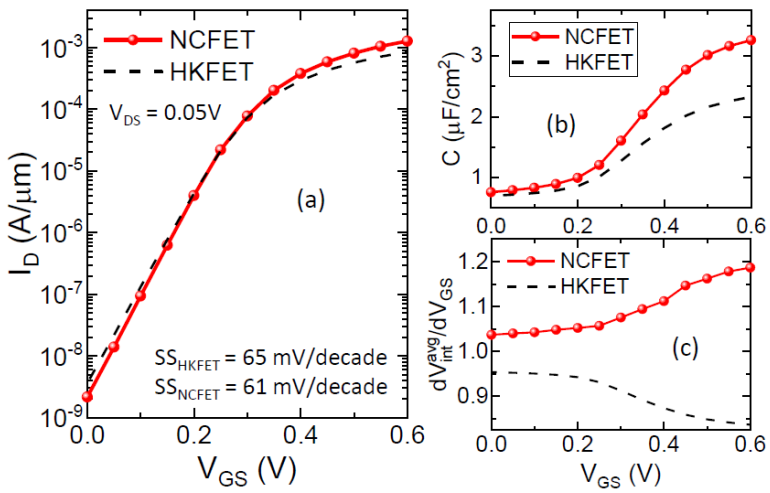

Figure 7.11: (a) I_D-V_{GS} and (b) C-V_{GS} characteristics of NCFET and HKFET signifying improved gate control and reduced SS in NCFET. (c) Differential change in average HZO-SiO_2 (HfO_2-SiO_2) interface potential in NCFET (HKFET) with respect to V_{GS}.

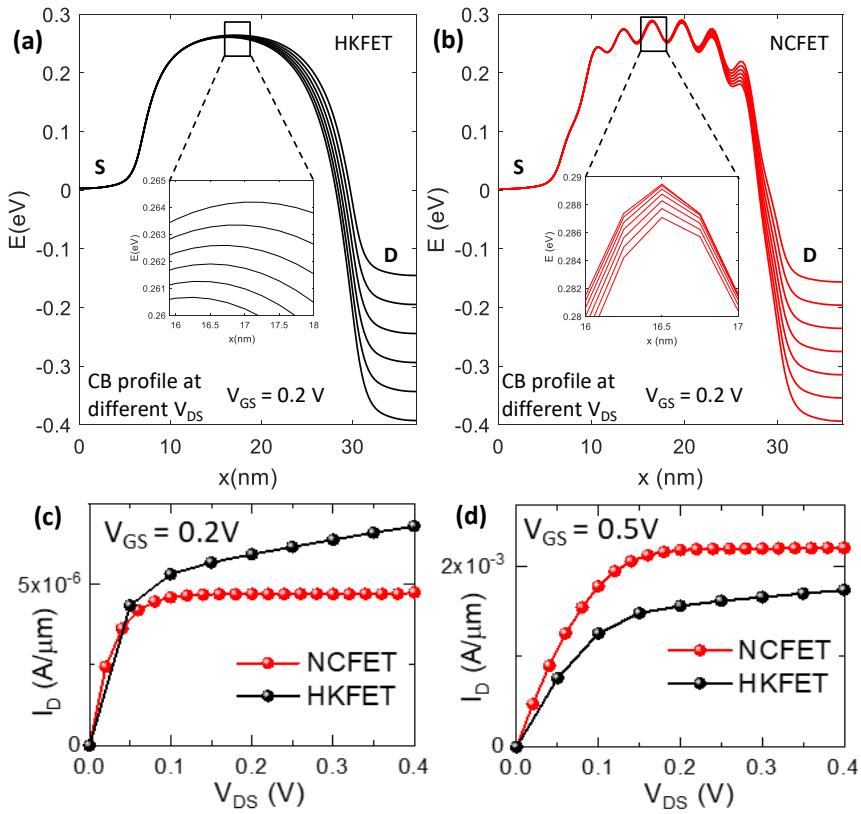

Figure 7.12. Conduction band (CB) profile of (a) HKFET and (b) NCFET at different V_{DS} and V_{GS} = 0.2V. I_D-V_{DS} characteristics of NCFET and HKFET at (c) V_{GS} = 0.2V and (d) V_{GS} = 0.5V signifying a decreased output conductance (g_{ds}) in NCFET compared to HKFET.

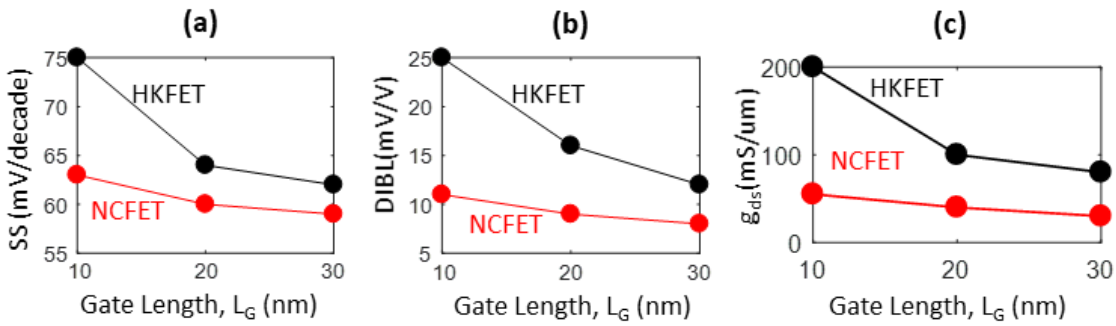

Figure 7.13. (a) Subthreshold-swing (SS), (b) drain-induced barrier lowering (DIBL) and (c) output conductance (g_{ds}) of FeFET/NCFET and HKFET signifying the robust gate length (L_G) scaling behavior of multi-domain NCFET compared to HKFET.

Subthreshold-swing (SS), drain-induced barrier lowering (DIBL) and output conductance (g_{ds}) of FeFET/NCFET and HKFET are shown in Fig. 7.13. and that signifies a robust gate length (L_G) scaling behavior of multi-domain NCFET compared to HKFET. This is because of the presence of DW in the FE layer as well as the higher local charge density in the Si channel (at the valley of the rippled conduction band) that shields the penetration of the drain field toward the source side of the Si conduction bands. Therefore, the short-channel effects in the multi-domain NCFETs are significantly suppressed even in a very short gate length NCFET.

So far, we have discussed the characteristics of multi-domain FeFET considering a value of gradient coefficient (g) that is calibrated with experiments. In the next section, we will analyze the FEFET characteristics for a range of very high gradient energy coefficient value.

7.6 FeFET characteristic with ultra-low FE thickness and high gradient energy coefficients

Negative capacitance of the ferroelectric (FE) integrated in the gate stack of an FEFET interacts with the capacitance of the underlying transistor to yield steep switching. However, if the FE is fabricated directly on a dielectric layer (i.e. without an inter-layer metal (Fig.8.14(b)) [1, 2]), the non-uniform electric field (E) in the channel makes the polarization (P) in FE variable along the gate length. Many models of FEFETs [3-5] assume uniform P and therefore, can potentially be valid for FEFETs with an inter-layer metal (Fig. 7.14(a)) which screens the effect of non-uniform

channel potential from FE. However, for FEFETs without the metal, it is essential to capture the interactions of FE polarization with the non-uniform *E*-field in the underlying channel. To analyze this, we assume a very high gradient energy coefficient ($g=K_P$) that does not allow the electrostatic driven multi-domain formation, however, can reflect the spatial variation in *P* along the gate length direction. In addition, we assume that the *P* variation in the FE layer along the thickness direction (*dP/dy*) is negligible (~0) due to very high *g* and ultra-thin nature of the FE film. This modified simulation framework captures the variation of ferroelectric (FE) polarization (P) along the gate length due to non-uniform electricfield (E) along the channel. Unlike our previous analysis in this chapter, the Landau parameters are calibrated with a different 10nm HZO films. Based on the calibrated model, we analyze the gate/drain voltage dependence of P distribution in the FE and its effect on the channel potential and current-voltage characteristics. Our results highlight the importance of larger domain interaction to boost the benefits of FEFETswith subthreshold swing (SS) as small as ~50mV/decade achieved at room temperature. As domaininteraction increases, the characteristics of FEFETs without inter-layer metal (SS, negative drain induced barrier lowering (DIBL), negative output conductance) approach those of an ideal single-domain FEFETs with inter-layer metal.

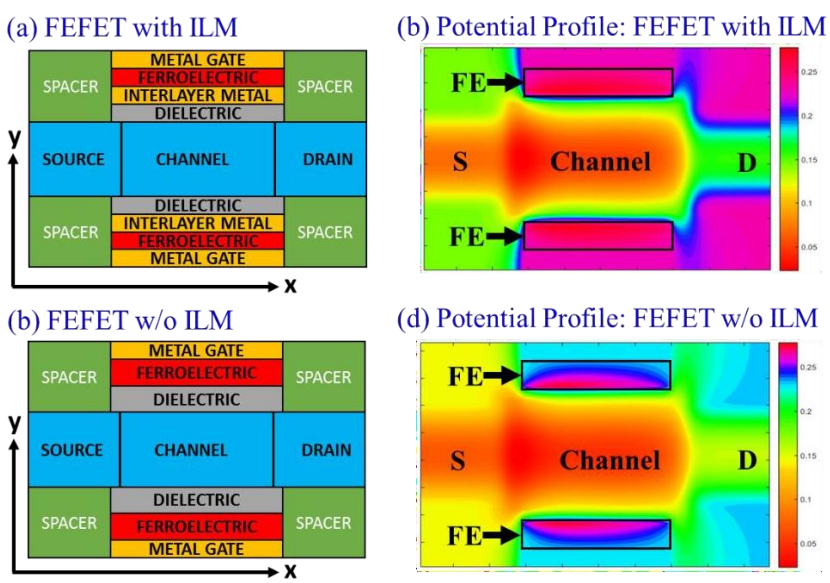

Figure 7.14. (a) FEFET Structure with an interlayer metal (ILM) and (b) corresponding potential profile showing uniform potential distribution in FE along the gate length. (c) FEFET Structure without an ILM and (d) corresponding potential profile showing non-uniform potential distribution in FE along the gate length.

7.6.1 Experimental Characterization of HZO and Model Calibration

To extract the Landau coefficient (α, β and γ) of HZO we consider metal-ferroelectric-insulator (SiO_2)-Si (MFIS) capacitor, where Si is highly doped. The MFIS capacitors are fabricated on highly doped p-type Si substrate (~10^{20} cm^{-3}). First, a 10 nm $Hf_{0.5}Zr_{0.5}O_2$ (HZO) film is grown by atomic layer deposition (ALD). A capping layer of 5 nm TiN is subsequently deposited by ALD. Next, the crystallization of HZO film is performed with rapid thermal process (RTP) in N_2 ambient at 500^0C for 30s. Finally, the top electrode is patterned using lithography and subsequent etch. The TEM image of MFIS capacitor is shown in Fig. 7.15(a-b) and the measured P-E curve and corresponding Landau coefficients are shown in Fig. 7.15(c-d). This experimental results were provided by Prof. Suman datta (University of Notre Dame).

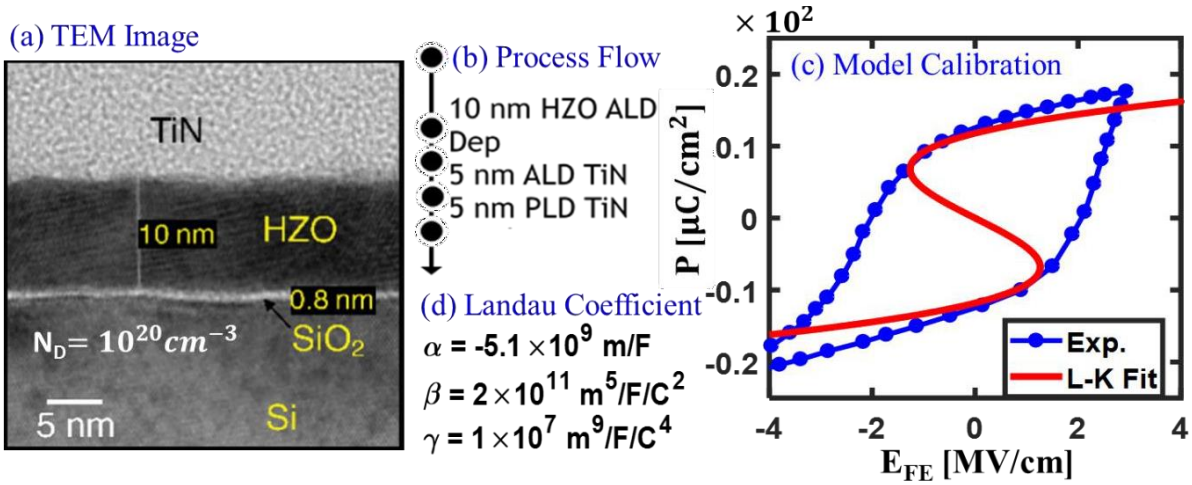

Figure 7.15. (a) The TEM image of MFIS capacitor, (b) the measured and fitted P-E curve, (c) process flow and (d) the calibrated Landau coefficients.

7.6.2 Effects of FE polarization variation along the gate length

To analyze the effect of multi-domain FE behavior on FEFET characteristics, we show the variation of P_y along the gate length for different gate/drain biases (V_{GS} and V_{DS} - Fig. 7.16) At V_{GS}=0, all FE domains exhibit negative P_y due to the negative E emanating from the source/drain (S/D) depletion regions. At V_{DS}=0.6V, P_y is more negative at the drain-end due to larger drain E-fields. As V_{GS} is increased, FE domains start to flip (negative-P to positive-P) from source-end of FE and create a domain wall. With further increase in V_{GS}, the domain wall shifts towards drain

(Fig. 7.16(a)). If V_{DS} is decreased (Fig. 7.16(b)), the drain E-fields decrease and P_y on the drain end becomes less negative. At low V_{DS} (0-0.25V) and V_{GS} = 0.6V, all domains flip to positive P_y. In Fig. 7.17, we show the variation in P_y-E_y of FE with respect to the S-shaped L-K path (K_P=0). Increase in V_{GS} tends to pull the FE polarization towards more positive values. On the other hand, an increase in V_{DS} tends to increase the variability of P_y and E_y along the gate length. It is important to note that the difference between simulated P-E and the LK path is due to the domain interaction term ($0.5\times K_P\times d^2P_y/dx^2$). It is also interesting to observe that at V_{GS} = 0.6V and V_{DS} = 0.1V, the distribution of P_y significantly reduces (under the influence of high gate E-field). This reduces the contribution of $0.5\times K_P\times d^2P_y/dx^2$ and the simulated P-E points lie on the L-K path.

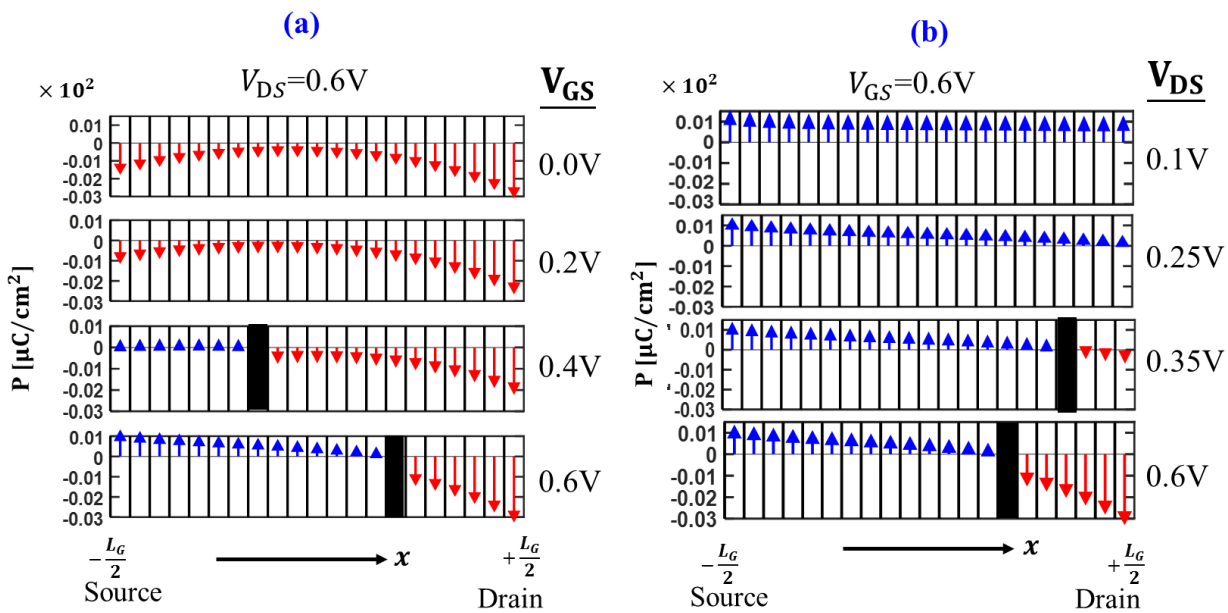

Figure 7.16. Polarization of FE along the gate (from source to drain) for (a) V_{DS} = 0.6V and different V_{GS}, (b) V_{GS} = 0.6V and different V_{DS}. The variation is caused by non-uniform electric field along the channel due to built-in potential and high V_{DS}.

Next, we analyze the conduction band (CB) along the S/D (Fig. 7.18(a)). As discuss previously, at low V_{GS}, P_y is negative (Fig. 5-5(a)), which pulls up the CB compared to the standard FET. At high V_{DS}, P_y is larger than at low V_{DS}. Thus, CB is pulled further up as V_{DS} increases, leading to negative DIBL (Fig. 7.17(a)). At high V_{GS}, and low V_{DS} (=0.1V), all the FE domains have P_y>0 (Fig. 7.17(b)). This leads to negative E_y in the FE layer, which lowers the CB compared to standard. With small increase in V_{DS} (<0.2V), P_y still remains positive, and the top of the source barrier is lowered as in a standard FET. However, further increase in V_{DS} (>0.2V), P_y at the drain end becomes negative.

Due to domain interaction, P_y on the source end becomes less positive, which pulls up the CB (Fig. 7.17). This non-monotonic behavior of CB with respect to V_{DS} leads to interesting FEFET characteristics, as discussed subsequently.

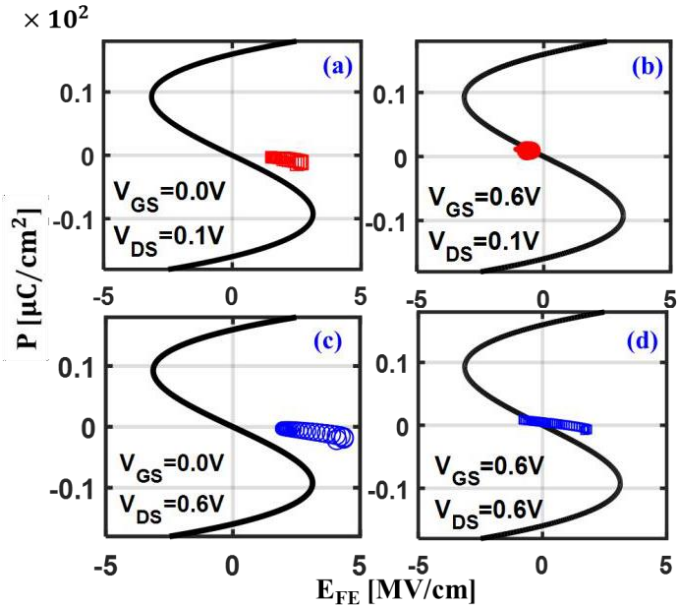

Figure 7.17. Polarization of FE for different biases showing that high V_{GS} pulls the polarization in positive direction and high V_{DS} increases its variability along the gate length.

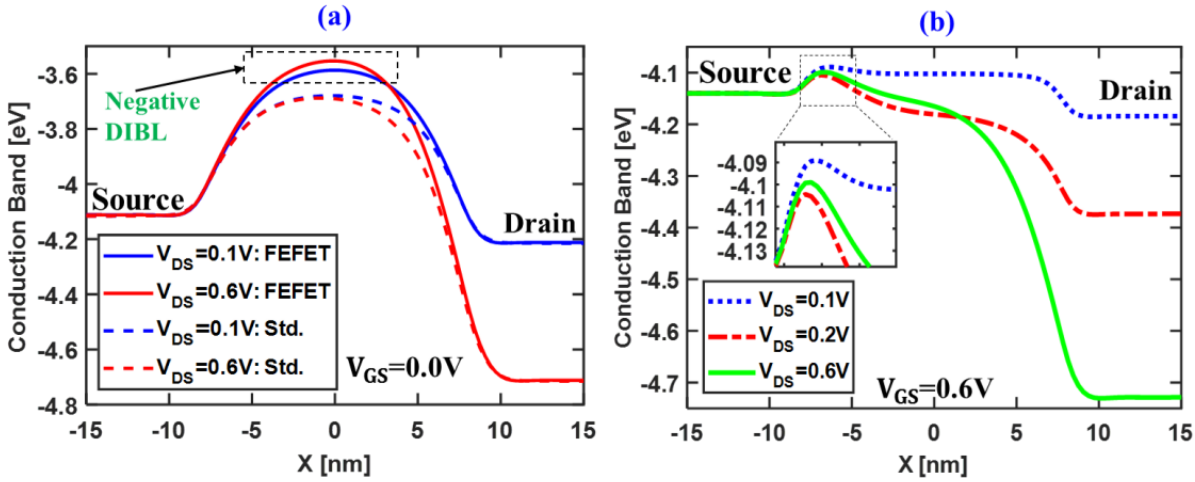

Figure 7.18. Conduction band at (a) V_{GS} = 0V showing negative DIBL due to decrease in polarization caused by drain electric fields, and (b) V_{GS} = 0.6V showing non-monotonic effect on V_{DS} on the top of the source barrier, which is caused by the impact of drain electric fields on the channel potential which tends to lower the barrier and polarization reduction in FE with increasing V_{DS} which tends to increase the barrier.

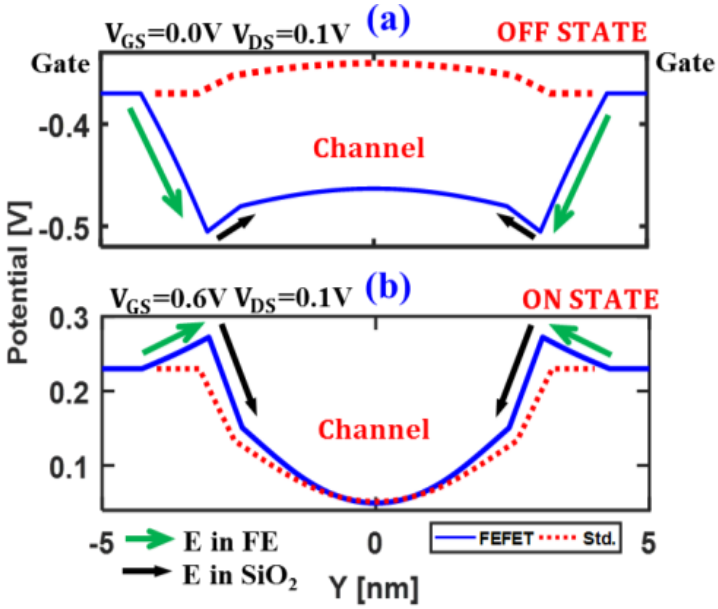

Figure 7.19. Potential (ϕ) along the gate-to-gate direction at (a) V_{GS} = 0V and (b) V_{GS} = 0.6V showing opposite electric fields in FE and SiO_2 due to negative dP/dV of FE.

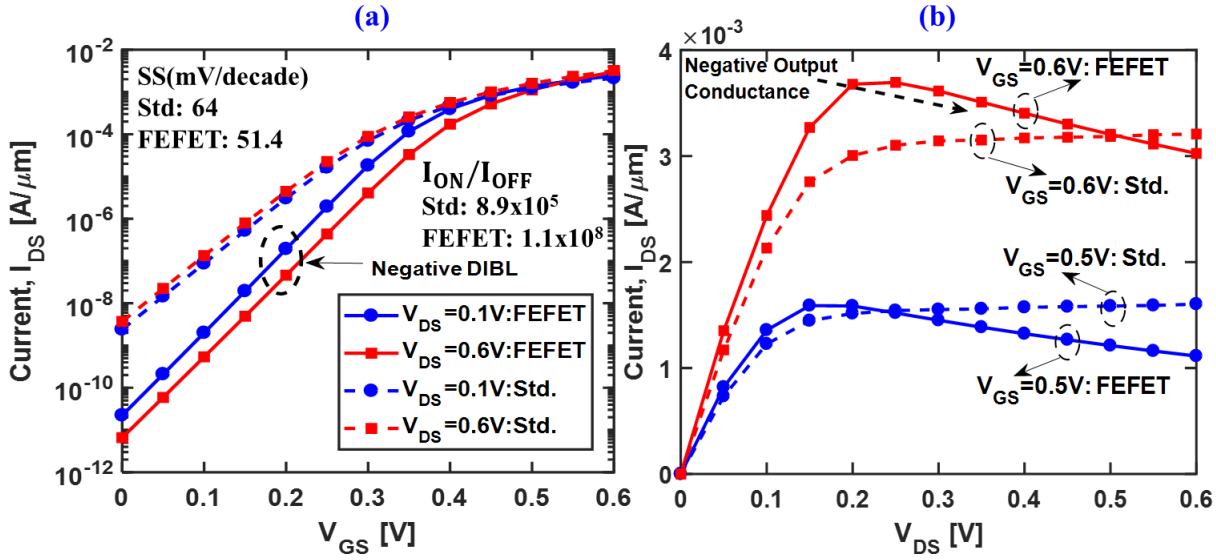

Figure 7.20. (a) I_D-V_{GS} characteristics of FEFET showing negative DIBL and steep-slope characteristics. (b) I_D-V_{DS} characteristics of FEFET showing negative output conductance (NOC).

The gate to gate potential profile of the FEFET and baseline FET are shown in Fig. 7.19. At V_{GS}=0V, the voltage drop across FE is positive due to negative P_y, which lowers the channel potentialcompared to the baseline. On the other hand, at V_{GS} =0.6V, the voltage drop across FE is negative (due to positive P_y), which increases the channel potential, showing voltage step-up due to the negative capacitance (NC) effect. These effects are manifested in the transfer and output characteristics of FEFET (Fig. 7.20). Decrease in OFF current (I_{OFF}) due to lowering of channel potential at V_{GS} = 0 can be observed. Lower SS (due to NC effect) as well negative DIBL (due to the impact of drain E-fields on P_y) can also be seen. The non-monotonic behavior of CB with respect to V_{DS} (Fig. 7.17(b)) yields non-monotonic trends of I_{DS} with respect to V_{DS} (Fig. 7.20(b)), which results in negative output conductance (NOC).

7.6.3 Effect of domain coupling (K_P) in FEFET characteristics

Next, we analyze the effect of domain interaction on FEFET characteristics. Decreasing K_P lowers the interactions between FE domains, allowing more variation along the gate length (Fig. 7.21(a)). As a result, the effect of drain-side P_y on the source-side P_y decreases. Thus, the increase in the source barrier caused by drain E-fields (see Fig. 7.17(a)) is lower for lower K_P. This translates to an increase in I_{OFF} as K_P is decreased (Fig. 7.21(c)). For the same reason, negative output conductanceeffect also decreases for low K_P (Fig. 7.21(d)). To explain the increase in SS with decrease in K_P, let us consider Fig. 5-9(b), which shows lower |E| in the FE as K_P is lowered. This can be easily understood from the LK equation, which shows that the domain interaction term adds an additional component to E, since $d^2Py/dx^2 < 0$ (Fig. 7.16). Thus, as K_P decreases, E in FE also decreases leading to lower NC effect. To further analyze the effect of P_y variation along x-axis, we simulate an FEFET with a metal layer between FE and SiO_2. This inter-layer metal maximizesthe effect of drain E-fields by distributing the potential uniformly along the gate. Further, the NCeffect uniformly affects the potential along the channel. Thus, reduction in SS is larger for FEFETwith inter-layer metal compared to FEFET without the metal (Fig. 7.21(b)). Fig. 7.22 compares SS,ON-OFF current ratio, DIBL and output conductance of FEFETs with and without metal. It can be observed that as K_P increases, the behavior of FEFET without metal approaches the one with the inter-layer metal.

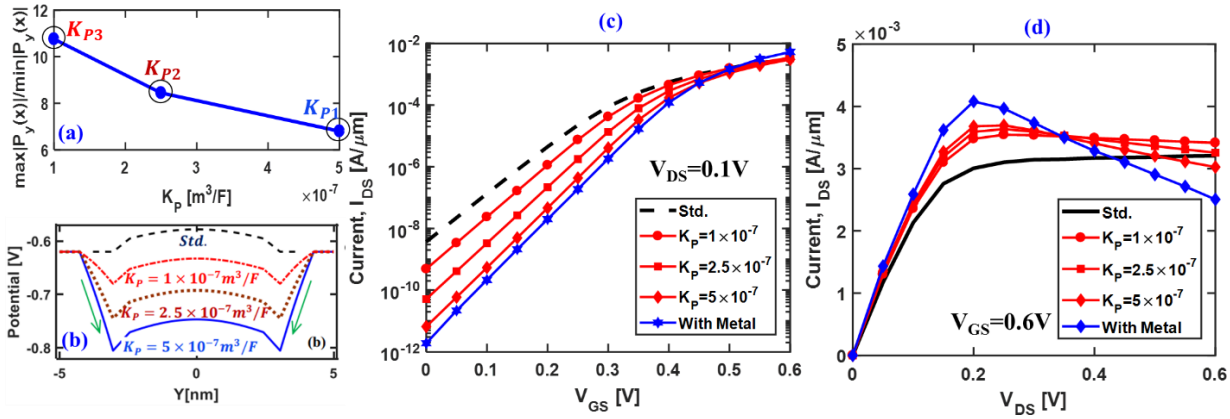

Figure 7.21. (a) Ratio of maximum to minimum $|P_y|$ of FE along the gate for different K_P showing decrease in P_y variation with higher K_P, (b) gate to gate potential profile for different K_P showing larger $|E_y|$ in FE for larger K_P. (c) I_{DS}-V_{GS} characteristics of FEFET for different K_P showing that increase in K_P reduces subthreshold-swing (SS) and increase the ration of ON and OFF current. (d) I_{DS}-V_{DS} characteristics of FEFET for different K_P showing that increase in K_P boosts NOC.

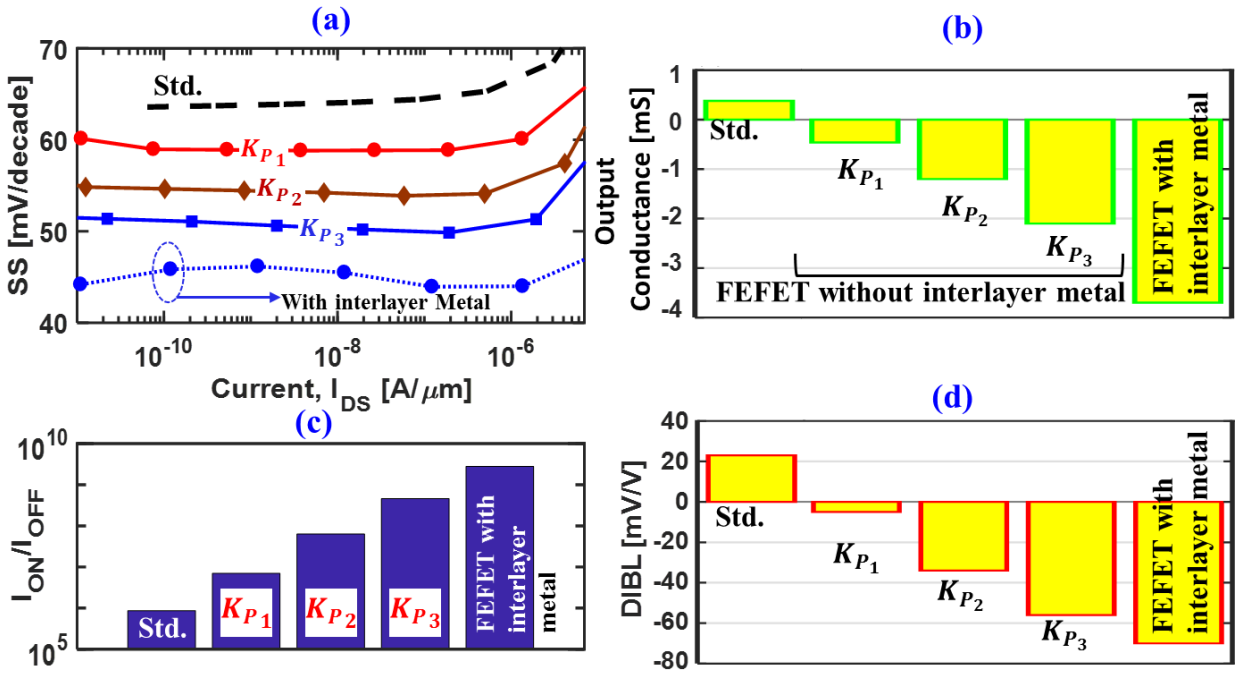

Figure 7.22. Comparison of (a) SS, (b) I_{ON}/I_{OFF}, (c) DIBL and (d) output conductance of FEFETs without interlayer metal (different K_P), with interlayer metal and baseline (std.) FET. Results show that the metrics of FEFET without metal approach those of FEFET with metal as K_P increases.

7.7 Summary

In summary, we analyze the FEFET characteristics with T_{FE}=5nm-10nm for memory operation where the number of memory state can be increased in scaled FEFET by reducing the T_{FE} so that the DW motion becomes preferable P-switching mechanism over domain nucleation. In addition, we investigate the origin of enhanced-ϵ_r behavior of thin (1.5nm-3nm) FE layer as an outcome of electrostatic multi-domain interaction in dense MD state and analyze its influence in FEFET for logic operation. The trends obtained from our model for different T_{FE} in terms memory and improved-SS logic operation. In addition, we analyze the NCFET device characteristics consisting of MD FE with soft-DW and compared its performances with conventional HKFET. Our analysis suggests MD NC effect leads to improved SS in NCFET compared to HKFET where the FE MD state induced rippled potential profile in the channel plays a vital role in improving the short-channel effects in NCFET. Besides, we discussed the effect of polarization variation in FE along the gate length and showed that with increase in the domain interaction, the signatures of NC effect (negative DIBL, negative output conductance andlower SS) become more prominent.

7.8 References

[1] A. K. Saha, B. Grisafe, S. Datta, and S. K. Gupta, "Microscopic Crystal Phase Inspired Modeling of Zr Concentration Effects in $Hf_{1-x}Zr_xO_2$ Thin Films," *IEEE VLSI Technology*, 2017.

[2] K. Ni, B. Grisafe, W. Chakraborty, A. K. Saha, S. Dutta, M. Jerry, J. A. Smith, S. Gupta, and S. Datta, "In-Memory Computing Primitive for Sensor Data Fusion in 28 nm HKMG FeFET Technology," *IEDM*, 2018.

[3] A. K. Saha, K. Ni, S. Dutta, S. Datta, and S. Gupta, "Phase field modeling of domain dynamics and polarization accumulation in ferroelectric HZO," *Appl. Phys. Lett.*, 2019.

[4] K. Chatterjee, S. Kim, G. Karbasian, A. J. Tan, A. K. Yadav, A. I. Khan, C. Hu, and S. Salahuddin, "Self-Aligned, Gate Last, FDSOI, Ferroelectric Gate Memory Device With 5.5-nm $Hf_{0.8}Zr_{0.2}O_2$, High Endurance and Breakdown Recovery," *IEEE Electron Device Lett.*, 2017.

[5] S. Dünkel, M. Trentzsch, R. Richter, P. Moll, C. Fuchs, O. Gehring, M. Majer, S. Wittek, B. Müller, T. Melde, H. Mulaosmanovic, Stefan Slesazeck, S. Müller, J. Ocker, M. Noack, D-A Löhr, P. Polakowski, J. Müller, T. Mikolajick, J. Höntschel, B. Rice, J. Pellerin, S. Beyer, "A FeFET based super-low-power ultra-fast embedded NVM technology for 22nm FDSOI and beyond", *IEDM*, 2017.

[6] H. Mulaosmanovic, E. Chicca, M. Bertele, T. Mikolajickac, and S. Slesazecka, "Mimicking biological neurons with a nanoscale ferroelectric transistor," *Nanoscale*, 2018.

[7] H. Mulaosmanovic, J. Ocker, S. Müller, M. Noack, J. Müller, P. Polakowski, T. Mikolajick, and S. Slesazeck, "Novel ferroelectric FET based synapse for neuromorphic systems," *IEEE VLSI Technol.*, 2017.

[8] M. Jerry, P. Chen, J. Zhang, P. Sharma, K. Ni, S. Yu, and S. Datta, "Ferroelectric FET analog synapse for acceleration of deep neural network training," *IEDM*, 2017.

[9] P. Sharma, K. Tapily, A. K. Saha, J. Zhang, A. Shaughnessy, A. Aziz, G. L. Snider, S. Gupta, R. D. Clark, and S. Datta, "Impact of total and partial dipole switching on the switching slope of gate-last negative capacitance FETs with ferroelectric hafnium zirconium oxide gate stack," in *Proc. IEEE VLSI Technol.*, 2017.

[10] V. Gaddam, D. Das, and S. Jeon, "Insertion of HfO_2 Seed/Dielectric Layer to the Ferroelectric HZO Films for Heightened Remanent Polarization in MFM Capacitors," *IEEE Trans. on Electron Devices*, 2020.

[11] S. Salahuddin, and S. Datta, "Use of negative capacitance to provide voltage amplification for low power nanoscale devices," *Nano Lett.*, 2007

[12] A. K. Saha, S. Datta, and S. Gupta, "'Negative capacitance' in resistor-ferroelectric and ferroelectric-dielectric networks: Apparent or intrinsic?," *J. Appl. Phys.*, 2018.

[13] W. Xiao , C. Liu, Y. Peng, S. Zheng , Q. Feng , C. Zhang ,J. Zhang , Y. Hao, M. Liao, and Y. Zhou, "Performance Improvement of $Hf_{0.5}Zr_{0.5}O_2$-Based Ferroelectric-Field-Effect Transistors With ZrO_2 Seed Layers," *IEEE Electron Device Lett.*, 2019.

[14] M. Si, X. Lyu, and P. D. Ye, "Ferroelectric Polarization Switching of Hafnium Zirconium Oxide in Ferroelectric/Dielectric Stack," *ACS Appl. Electron. Mater.*, 2019.

[15] A. M. Bratkovsky and A. P. Levanyuk, "Abrupt appearance of the domain pattern and fatigue of thin ferroelectric films," *AIP Conference Proceedings*, 2000.

[16] M. Si, X. Lyu, P. R. Shrestha, X. Sun, H. Wang, K. P. Cheung, and P. D. Ye, "Ultrafast measurements of polarization switching dynamics on ferroelectric and anti-ferroelectric hafnium zirconium oxide," *Appl. Phys. Lett.*, 2019.

[17] A. K. Saha, and S. K. Gupta, "Multi-Domain Negative Capacitance Effects in Metal-Ferroelectric-Insulator-Semiconductor/Metal Stacks: A Phase-field Simulation Based Study," *Scientific Reports*, 2020.

[18] H.W. Park, J. Roh, Y. B. Lee, and C. S. Hwang, "Modeling of negative capacitance in ferroelectric thin films," *Adv. Mater.*, 2019.

8. CIRCUIT COMPATIBLE COMPACT MODELING OF FERROELECTRIC AND ANTIFERROELECTRIC FETS

8.1 Introduction

In this chapter, we analyze ferroelectric (FE) and anti-ferroelectric (AFE) field effect transistors (FETs) (shown in Fig. 8.1(a)) and compare their subthreshold characteristics and hysteretic behavior. To facilitate this analysis, we develop a Preisach based [1] circuit compatible model for FE/AFE. Whereas in FE capacitor the two stable polarization (P) states are $-P_R$ and $+P_R$, in case of AFE capacitor, non-volatility can be achieved within 0↔+PR by imposing a built-in potential through work-function engineering (Fig, 9.1(b)). However, in FE/AFEFETs, FE/AFE can be partially polarized (forming minor P-V loop), which we analyze in this chapter. Finally, correlating the negative capacitance (NC) effect in FE/AFE with domain-wall propagation [2], we explore the steep subthreshold swing (SS) characteristics of FE/AFE-FET and analyze their transient nature and dependence on flat-band voltage (V_{FB}) and maximum applied gate voltage (V_{GS}).

8.2 PREISACH BASED MODEL OF FE/AFE-FET

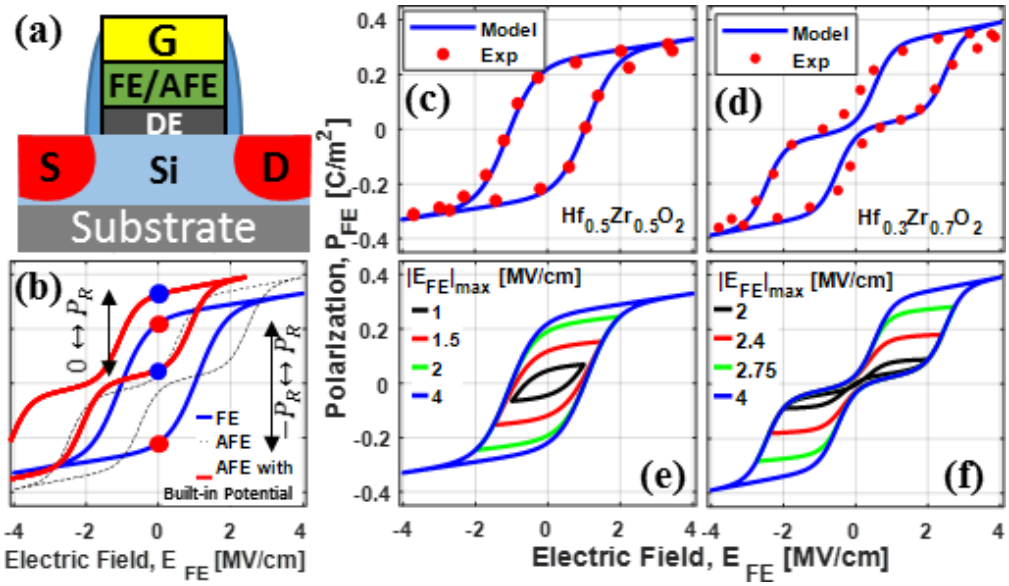

Figure 8.1. (a) FE/AFE-FET. (b) Stable P-state of FE/AFE. (c) FE and (d) AFE P-E loop (model calibration). (e) FE and (f) AFE major/minor loop formation.

FE: Major Loop $P_S = 0.25C/m^2, P_R = .19C/m^2, E_C = 1.1MV/cm$

$$P_M^{\pm} = Ps\left[\tanh\left(\frac{E_{C_{FE}} \mp E_C}{2\delta}\right)\right] + C_0 E_{C_{FE}}; \quad \delta = \alpha \times \left[ln\left[\frac{P_S + P_R}{P_S + P_R}\right]\right]^{-1}$$

AFE: Major Loop $P_S = 0.29C/m^2, P_R = .22C/m^2, E_C^{1,2} = 2.5, 0.5MV/cm$

$$P_M^{\pm} = \frac{Ps}{2}\left[\tanh\left(\frac{E_{C_{AFE}} - E_c^{2,1}}{2\delta}\right) - \tanh\left(\frac{-E_{C_{AFE}} - E_c^{1,2}}{2\delta}\right)\right] + C_0 E_{C_{AFE}}$$

FE/AFE Minor Loop: $\alpha = 0.5, \beta = 2, \eta = 2, C_0 = .01F/m^2, \tau = 1ns$

$$\frac{dP_m}{dE_{C_{FE/AFE}}} = \frac{\Gamma \times dP_M}{dE_{C_{FE/AFE}}}; \quad \Sigma = \left[\sqrt{\frac{P_m - P_M}{\pm\eta P_S - P_m}}\right]; \quad \Gamma = 1 - \tanh[\beta \times \Sigma]$$

Transient characteristics:

$$\frac{dE_{C_{FE/AFE}}}{dt} = \frac{1}{\tau}\left[E_{FE/AFE} - E_{C_{FE/AFE}}\right]$$

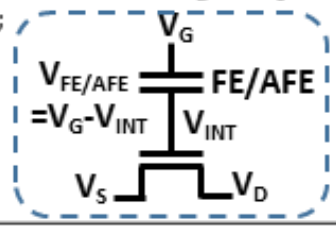

Figure 8.2. FE/AFE Model Equations for major/minor P-E loop formation. Calibrated FE andAFE parameters are shown. The schematic model of FE/AFE-FET is shown in inset.

To perform FE/AFE-FET simulations, we have developed a model for FE/AFE based on Miller's analytical equations (Fig. 8.2) [1]-[3]. We calibrated (Fig. 1(c-f)) the model parameters with experimental results [4] obtained for HZO (FE:$Hf_{0.5}Zr_{0.5}O_2$ & AFE:$Hf_{0.3}Zr_{0.7}O_2$). Considering the lag between P and applied voltage (V_{FE}) through τ parameter (which can be attributed as the delay associated with domain wall propagation in FE/AFE), the model can capture the NC effect in FE/AFE [2]. Furthermore, the model can capture major/minor loop formation of FE/AFE (Fig. 8.1(e-f)) depending on the peak applied voltage through dynamic capacitance calculation (Fig. 8.2). In this work, we have used 45nm high-k planar FET as the baseline transistor and FE/AFE with a thickness ($T_{FE/AFE}$) = 3nm.

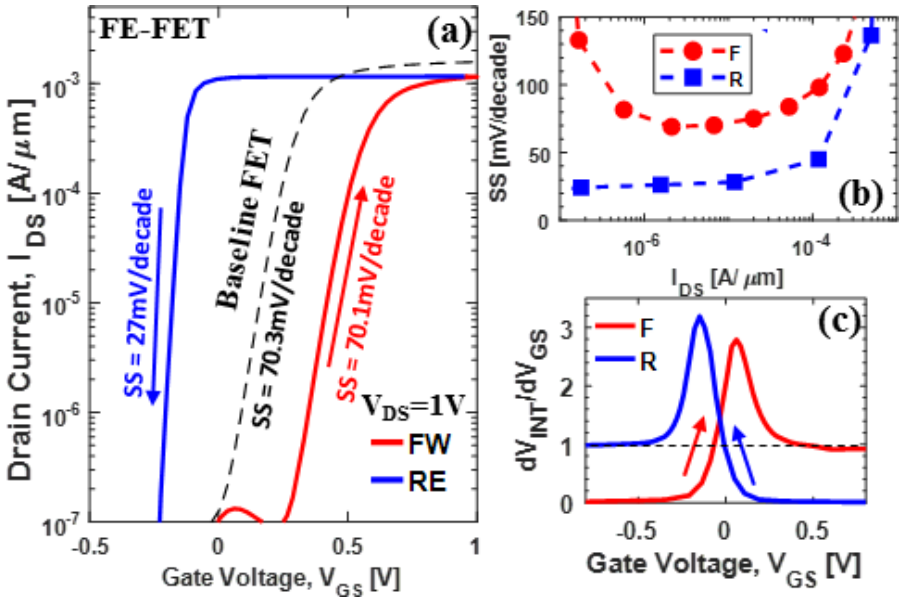

Figure 8.3. (a) I_{DS}-V_{GS} (b) subthreshold swing (SS) and (c) internal voltage amplification characteristics for FE-FET showing stepper SS in forward (F) sweep. [T_{FE}=3nm].

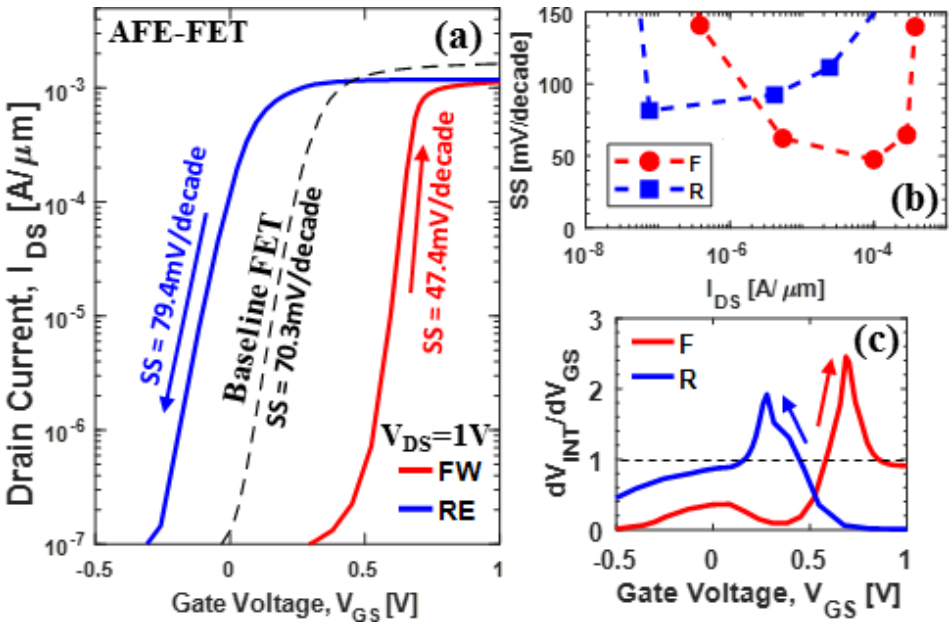

Figure 8.4. (a) I_{DS}-V_{GS} (b) subthreshold swing (SS) and (c) internal voltage amplification characteristics for AFE-FET showing stepper SS in reverse (R) sweep. [T_{AFE}=3nm].

8.3 Analysis and Discussion

The I_{DS}-V_{GS} characteristics of FEFET (Fig. 7-3(a)) shows non-volatile hysteretic behavior with ~0.6V hysteresis. At the same time, SS in the reverse (R) sweep direction of V_{GS} shows steeper than 60mv/decade at 300K (Fig. 8.3(b)), whereas in the forward (F) sweep, SS is similar to the baseline FET (min SS=70.16 mV/decade). Fig. 8.3(c) shows the internal voltage amplification (dV_{INT}/dV_{GS}, where V_{INT} is the voltage at the interface of FE/AFE and the gate of the underlying FET). This amplification, which is due to NC effect, is higher in R-sweep compared to F-sweep in FEFETs. Similar to FEFET, I_{DS}-V_{GS} characteristics of AFEFET (Fig. 8.4(a)) shows non-volatile hysteretic behavior, but now, steeper SS and higher dV_{INT}/dV_{GS} occurs in F-sweep direction compared to R-sweep (Fig. 8.4(b-c)). To understand the asymmetry in dV_{INT}/dV_{GS} and SS of FE/AFE-FET, let us first discuss the physical origin of NC effect. According to our FE/AFE model, NC effect is the outcome of two-step process: (i) overshoot of FE/AFE voltage ($V_{FE/AFE}$= $E_{FE/AFE}\times T_{FE/AFE}$, solid line in Fig. 8.5(a)) beyond the steady-state P-$VC_{FE/AFE}$ (where $V_{CFE/AFE}$ = $E_{CFE/AFE}\times T_{FE/AFE}$, dashed line in Fig. 8.5(a)) and (ii) snap-back towards the steady state P-$V_{CFE/AFE}$. Thesetwo phenomena are directly related with the delay parameter τ and large change in FE/AFE capacitance ($C_{FE/AFE}$) i.e. large $dC_{FE/AFE}/d|V_{CFE/AFE}|$ near the coercive voltage. According to [2], $V_{FE/AFE}$ overshoot increases with the increase in ramp rate of the applied V_{GS} (dV_{GS}/dt) and increase in τ, whereas the snap-back increases as $dC_{FE/AFE}/d|V_{CFE/AFE}|$ increases. That means for a constant τ, NC effect can be increased by (i) increase in $dC_{FE/AFE}/d|V_{CFE/AFE}|$ or (ii) increase in dV_{GS}/dt. Now, in general, $dC_{FE/AFE}/d|V_{CFE/AFE}|$ is comparatively lower in minor P-$V_{CFE/AFE}$ path than major path. Therefore, in FEFET, as FE traverses a path closer to the major loop in R-sweep than F-sweep (Fig. 8.5(a)), NC effect and hence, dV_{INT}/dV_{GS} is higher in R-sweep. Similarly, in AFEFET, AFE traverses major path in F-sweep and minor path in R-sweep resulting higher dV_{INT}/dV_{GS} in F-sweep.

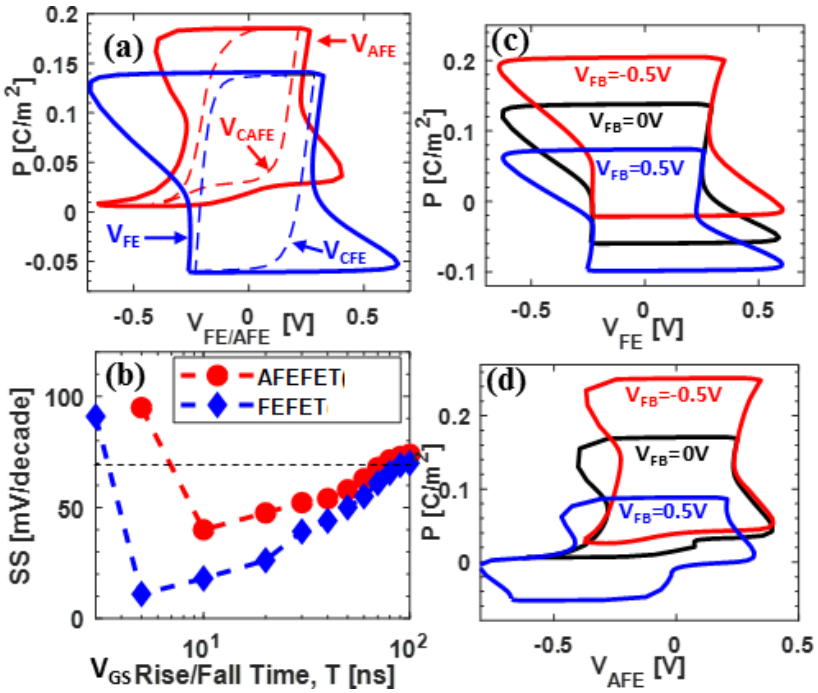

Figure 8.5. (a) P-$V_{FE/AFE}$ loop of FE/AFE in FE/AFE-FET showing NC effect (b) min. SS for different rise/fall time of V_{GS} showing non-monotonic dependence on T. (c-d) P-$V_{FE/AFE}$ loop of FE/AFE in FE/AFE-FET for different flat band voltage (V_{FB}) showing the P-$V_{FE/AFE}$ loop moves towards +ve P with the decrease in V_{FB}.

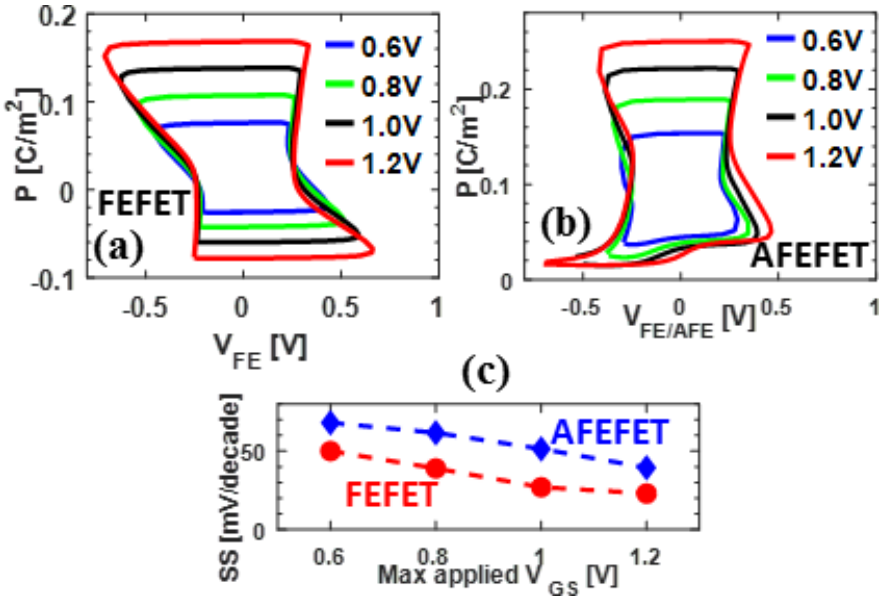

Figure 8.6. (a-b) P-$V_{FE/AFE}$ loop and (b) min. SS of FE/AFE-FET for different applied V_{GS}showing increase in NC effect and hence decrease in SS with the increase in V_{GS}. [dV_{GS}/dt=constant, V_{FB}=0V].

However, NC effect or dV_{INT}/dV_{GS} >1 may not guarantee the observation of SS<60mV/decade, rather it depends on the region of operation of the FET or the range of P where NC occurs. In a FET, minimum (min.) SS occurs in sub-threshold or weak-inversion region, whereas SS is quite high in near accumulation and strong inversion region. For FEFET (Fig. 8.5(a)), we observe that NC effect occurs in moderate positive (+ve) P region (R-sweep) and low negative (-ve) P region (F-sweep) of the FE. This, respectively, corresponds to the weak-inversion and near-accumulation region of the FEFET. Therefore, steeper SS is visible only in R-sweep, even though dV_{INT}/dV_{GS}>1 occurs in both R and F-sweeps (Fig. 8.3(c)). In contrast, for AFEFET, NC effect occurs in moderate +ve P region (F-sweep) and high +ve P region (R-sweep) of the AFE. This respectivelycorresponds to the strong-inversion and weak-inversion region of the AFEFET. Hence steeper SSis visible only in F-sweep direction. In addition, as NC effect is a transient phenomenon, SS also depends on the rise/fall time (T) of the applied V_{GS}. For very fast ramp input ($T \approx \tau$), FE/AFE polarization does not switch completely, and therefore, NC effect vanishes. On the other hand, forvery slow ramp input ($T >> \tau$), voltage overshoot becomes negligible and so does the NC effect. Min. SS of FE/AFE-FET for different T have been plotted in Fig. 8.5(b). SS<60mV/decade is observed only for certain value of T (4ns ~ 0.1us), which is in agreement with our discussion that the NC effect occurs within a range of T ($\tau<T<100\tau$).

Now, we will analyze the impact of flat-band voltage (V_{FB}) and maximum (max.) applied V_{GS} on SS characteristics of FE/AFEFET. By tuning V_{FB}, it is possible to change the polarization range of NC effect and by changing V_{GS} swing, it is possible to control major/minor loop traversal of FE/AFE. First, to analyze the impact of V_{FB}, P-$V_{FE/AFE}$ loop of FE/AFE-FET for different V_{FB} have been plotted in Fig. 8.6(a-b) showing that the range of P where NC occurs, shifts towards +ve P with the decrease in V_{FB}. Therefore, in FEFET, the min. SS for F-sweep decreases while for R-sweep, it increases with a decrease in V_{FB}. Min SS for F- and R- sweeps become equal at $V_{FB}\approx$-0.4V. However, for AFEFET, min. SS in both sweep directions decrease with a decrease in V_{FB} and cross each other at $V_{FB}\approx$-0.3V. Now, we will analyze the impact of V_{GS}. From Fig. 8.6(a-b), we can observe that with an increase in V_{GS} swing, P-$V_{FE/AFE}$ becomes closer to the major loop and therefore $dC_{FE/AFE}/dV_{CFE/AFE}$ increases. Therefore, NC effect increases both in FE/AFE-FET with the increase in V_{GS} and hence, min SS also decreases with the increase in applied V_{GS} swing(Fig. 8.6(c)).

8.4 Summary:

In summary, We develop a multi-domain FE/AFE-FET model based on Preisach based Miller's equation. Utilizing the model discussed the SS characteristics of hysteretic FE/AFE-FETs and analyzed their dependence on flat-band and applied gate voltage. Our analysis suggests that with V_{FB} reduction, symmetric SS characteristics can be achieved in FE/AFE-FETs.

8.5 References

[1] S. L. Miller, J. R. Schwank, R. D. Nasby, and M. S. Rodgers, "Modeling ferroelectric capacitor switching with asymmetric nonperiodic input signals and arbitrary initial conditions," *Journal of Applied Physics*, 1991.

[2] A. K. Saha, S. Datta, S. K. Gupta, ""Negative capacitance" in resistor-ferroelectric and ferroelectric-dielectric networks: Apparent or intrinsic?," *Journal of Applied Physics*, 2018.

[3] A. K. Saha, and S. K. Gupta, "Modeling and Comparative Analysis of Hysteretic Ferroelectric and Anti-ferroelectric FETs," *Device Research Conference*, 2018.

[4] J. Muller, et al., "Ferroelectricity in Simple Binary ZrO_2 and HfO_2," *Nano Letter*, 2012.

9. MODELING OF FERROELECTRIC SEMICONDUCTOR-BASED DEVICES

9.1 Introduction

Unlike semiconductor insulators (PZT, HZO, etc.), there are ferroelectric materials that exhibit low bandgap (< 2eV) and hence, display semiconducting properties. Most perovskite-based (ABO_3 group: PZT, BTO, BFO, etc.) conventional ferroelectric materials exhibit a bandgap higher than 2eV and thus fall into the broad category of ferroelectric insulators. On contrary, the recent discovery of ferroelectricity in non-perovskite-based 2D material (i.e., α-In_2Se_3) signifies a bandgap of ~1.4eV and that signifies a combined ferroelectric and semiconductivity in the same material system. Very recently, several novel device concepts utilizing such ferroelectric semiconducting (FeS) materials have been explored for a versatile set of applications ranging from solar cell to non-volatile memory. In this chapter, we discuss the modeling and operational principle of two different FeS based devices, namely ferroelectric semiconductor metal junction (FeSMJ) and ferroelectric semiconductor field-effect transistors (FeSFET) by employing first-principle density functional theory (DFT) based simulation and self-consistent device simulation.

9.2 Ferroelectric-semiconductor-metal-junction (FeSMJ) for non-volatile memory application

Ferroelectric (Fe) materials have gained an immense research interest for their applications in electronic [1-4] devices due to their electrically switchable spontaneous polarization and hysteretic characteristics. Fe materials with high bandgap, called Fe-insulators, have been extensively investigated for versatile non-volatile memory (NVM) devices, such as Fe-random-access-memory (Fe-RAM) [5], Fe-field-effect-transistor (Fe-FET) [6-7], Fe-tunnel-Junction (FTJ) [8-10], etc. Unlike Fe-RAM and Fe-FET, where the Fe layer acts as a capacitive element, the FTJ functionality depends on the tunneling current through the Fe layer. In the FTJ, the Fe layer is sandwiched by two different metal electrodes. Due to the different properties (e.g. the screening length) of the electrodes, the tunneling barrier height at the metal-Fe interface of FTJ depends on the polarization (P) direction. Thus, FTJ can exhibit P-dependent tunneling resistance that facilitates the sensing of its P-state, leading to the design of a two-terminal NVM element [8]. However, as the dominant transport mechanism of FTJ is direct tunneling, to obtain a desired

current density for sufficient operational speed, the Fe-insulator thickness needs to be significantly low (<3nm for HZO [9]). Unfortunately, with thickness scaling, the Fe-insulator *P* decreases [9], which reduces the ratio of the tunneling-resistance[9], and therefore, the distinguishability of the FTJ memory states decreases. In addition, most of the Fe-insulators (i.e. doped-HfO_2) comprise oxygen atoms and the dynamic change in oxygen vacancies can play a major role in its Fe characteristics [11]. Therefore, a decrease in ferroelectricity with scaling and issues related to oxygen vacancies lead to significant challenges in the design and implementation of FTJ-based NVMs.

Similar to Fe-insulator, Fe material with low bandgap called Fe-semiconductor (FeS) also exhibit spontaneous *P* which is switchable via applied electric-field [12-16]. The van-der-Waals (vdW) stack of α-In_2Se_3 has recently been discovered as a 2D FeS material that can retain the Fe and semiconducting properties even for a monolayer thickness [12-16]. This suggests a remarkable possibility for thickness scaling. In addition, as α-In_2Se_3 is not an oxide, the issues related to oxygen vacancies are expected to be non-existent in this FeS material. Recently, similar to FTJ, a metal-FeS-metal junction device (called FeSMJ) has been demonstrated to exhibit *P*-dependent resistance states [17]. Unlike FTJ, FeSMJ can provide significant current density even with a high FeS thickness and it does not require different metal electrodes for NVM functionalities [17]. To understand such unique working-principle of FeSMJ and to enable their device-level optimization, a detailed analysis of the material properties α-In_2Se_3 as well as the device characteristics is needed. To address this need, in this work, we experimentally and theoretically analyze α-In_2Se_3 based FeSMJ devices and examine their thickness scalability. Our analysis is based on experimental characterization, first-principle simulations and self-consistent device simulation. Moreover, we investigate the FeSMJ thickness scalability and compare it with FTJ at the device and array levels to analyze its potential for NVM applications.

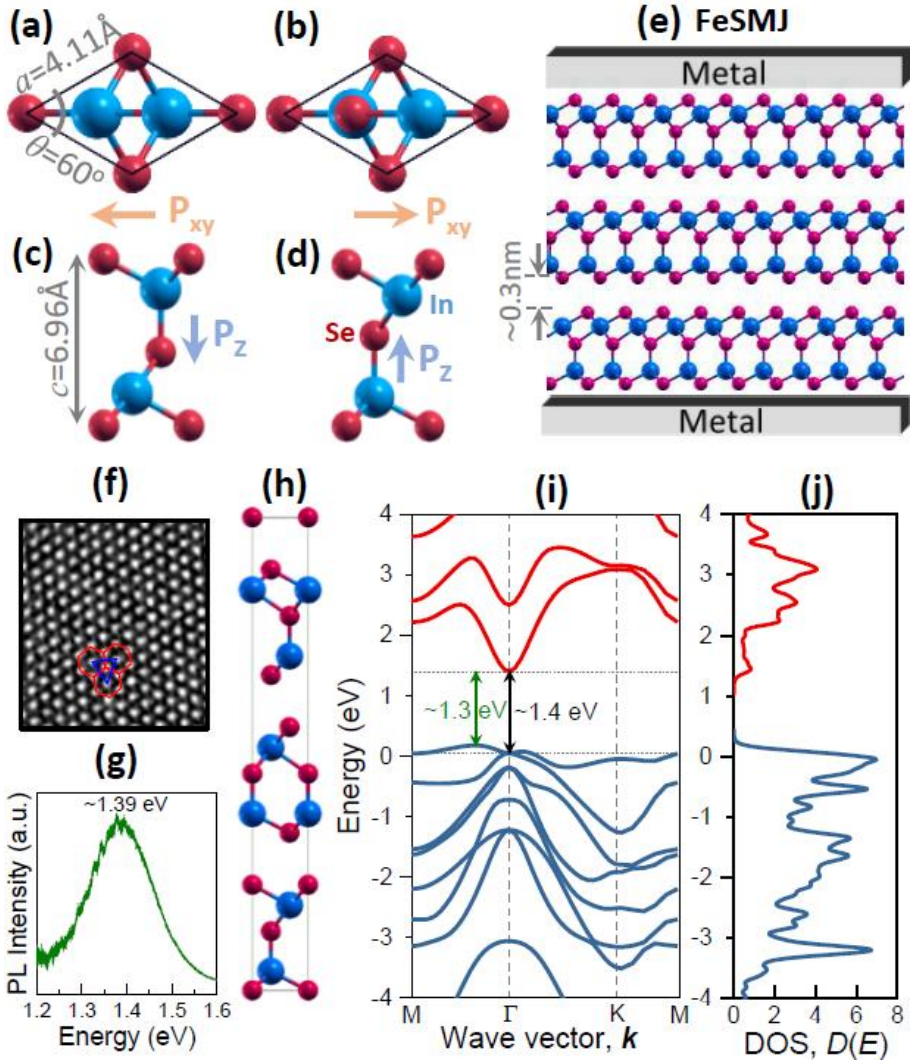

Figure 9.1. Unit cell of α-In_2Se_3 (a-b) top view and (c-d) side view. (e) FeSMJ device structure with vdW stack of α-In_2Se_3. (f) STEM image of the fabricated α-In_2Se_3 surface. (g) Measured photoluminescence (PL) spectrum. (h) Supercell of bulk α-In_2Se_3 vdW stack. (i) Energy-dispersion relation and (j) density of states of α-In_2Se_3 vdW stack from DFT simulation.

9.3 First-principle and device simulation framework of α-In_2Se_3 based FeSMJ

To begin with, we first discuss the material properties of α-In_2Se_3. Unit cells of the α-In_2Se_3 monolayer are shown in Fig. 9.1(a-d) indicating non-centrosymmetric crystal structure, where the central Selenium (Se) atom is displaced from the centrosymmetric position. As a result, α-In_2Se_3 exhibits both in-plane (Fig. 9.1(a-b)) and out-of-plane polarization (Fig. 9.1(c-d)). The arrangement of α-In_2Se_3 layers in a vdW stack is shown in Fig. 9.1(e) where each layer is separated by a vdW gap [12-14]. Employing this α-In_2Se_3 as the FeS layer in a metal-FeS-metal

configuration, the FeSMJ structure is shown in Fig. 9.1(e). Now, to characterize its properties, α-In_2Se_3 vdW stack was grown by the melt method with a layered non-centrosymmetric rhombohedral R3m structure. The details of the fabrication process can be found in our previous work [16]. The high-angle-annular-dark-field STEM image of thin α-In_2Se_3 flake is shown in Fig. 9.1(f) that signifies a high-quality single-crystalline hexagonal structure. The photoluminescence measurement (Fig. 9.1(g)) of α-In_2Se_3 suggests a direct optical/direct bandgap of ~1.39eV. To analyze the semiconducting properties further, we conduct first-principle simulations (based on density function theory (DFT)) in Quantum Espresso (QE) [18-19] with hybrid orbital HSE correction [20]. Unlike previous simulation-based studies of a few numbers of layers [12], we consider bulk α-In_2Se_3 vdW stack by taking a super-cell of three In_2Se_3 layers (Fig. 9.1(h)) periodically repeated in all three directions (*x*, *y* and *z*-axis). Note that the thickness of our experimental sample is 120nm (~120 In_2Se_3 layers), therefore, we investigate the bulk properties, rather than a few-layer system. The simulated energy-dispersion relation is shown in Fig. 9.1(i) that illustrates a direct optical gap of ~1.4eV (consistent with experiments) and an indirect bandgap of ~1.3eV. Similarly, the density of states (DOS) is shown in Fig. 9.1(j) that suggests a lower conduction DOS compared to the valence DOS. Hence, the equilibrium Fermi level (E_F) is closer to the conduction band minima (E_C) compared to the valence band maxima (E_V). We utilize this DOS characteristics in our device simulation for the calculation of carrier concentration in the FeS layers, as discussed subsequently.

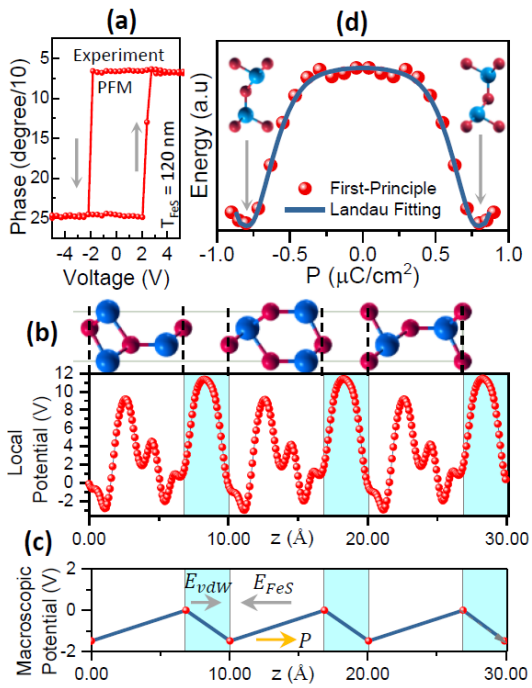

Figure 9.2. (a) Measured PFM phase response of FeS with T_{FeS}=120nm. (b) Local electrostatic potential and (c) macroscopic potential profile in α-In_2Se_3 vdW stack (along the z-axis). (d) Polarization vs energy of α-In_2Se_3.

Next, we analyze the Fe properties of the α-In_2Se_3 vdW stack. Fig. 9.2(a) shows the piezoresponse force microscopy (PFM) phase versus applied-voltage hysteresis loop of a 120nm thick α-In_2Se_3 stack that suggests a Fe *P*-switching with a coercive voltage of ~2V. However, due to the semiconducting properties of α-In_2Se_3, a direct measurement of *P* through conventional methods is not possible [16]. Hence, we perform the Berry phase analysis [21] on the DFT wave-functions of α-In_2Se_3 in QE. Our analysis suggests an out-of-plane remanent *P* of ~7.68μC/cm^2. Note that, unlike previously calculated *P* (by dipole correction method) for a few-layer system[12], our calculated *P* is for bulk α-In_2Se_3. To further understand the Fe properties of α-In_2Se_3, the microscopic potential energy (averaged across the *x*-*y* plane) along the FeS thickness (z-axis) obtained from the DFT simulation is shown in Fig. 9.2(b). The extracted macroscopic potential (Fig. 9.2(c)) suggests an opposite electric-field in FeS layers and vdW gaps. Now, the electrostatic condition at the interface of FeS and vdW gap can be written as,

$$\epsilon_0 E_{vdW} = \epsilon_0 \epsilon_r E_{FeS} + P \qquad (9.1)$$

Here, E_{vdW} and E_{FeS} are the electric-fields in the vdW gap and FeS layer, respectively; ϵ_r is the relative background permittivity of the FeS layer, ϵ_0 is the vacuum permittivity and P is the spontaneous polarization. The above equation suggests that, E_{vdW} and E_{FeS} can be non-zero and hold the opposite sign if and only if the P is non-zero and that further confirms the existence of spontaneous P in the FeS layer. Using the calculated value of P, E_{vdW} and E_{FeS}, we obtain ϵ_r=~7 from Eqn. (1). Further, we calculate the total energy (u) with respect to the change in P based on the nudge-elastic-band (NEB) [22] method in QE. The change in P is captured by moving the central Se atoms between two stable positions as shown in Fig. 9.2(d) followed by Berry phase calculation for P. To capture the temperature effect in u, we have considered phonon-energy correction [23] for 300K temperature. The resultant u-P characteristics are shown in Fig. 9.2(d) signifying a double-well energy landscape. We fit the simulated u-P characteristics with Landau's free energy polynomial [24] as shown in Fig. 9.2(d) based on the following equation.

$$u = \frac{1}{2}\alpha P^2 + \frac{1}{4}\beta P^4 + \frac{1}{6}\gamma P^6 + \frac{1}{8}\delta P^8 \qquad (9.2)$$

The obtained Landau coefficients (α, β, γ and δ) are shown in the inset of Fig. 9.3(a). Based on the extracted parameters of α-In_2Se_3, we self-consistently solve Landau-Ginzburg-Devonshire equation[3], Poisson's equation and semiconductor charge equations for the FeSMJ structure. Then, we use the potential profile in a NEGF framework to calculate the current in the FeSMJ. The simulation flow and parameters are shown in Fig. 9.3(a). In our simulation, we consider the vdW gap of 3Å between the subsequent FeS layers (obtained from DFT simulation with structural relaxation) along with a vdW gap of 1.5Å between the metal and FeS layer as shown in Fig. 9.3(b). We utilize this simulation framework along with the experimental results to investigate the FeSMJ device characteristics.

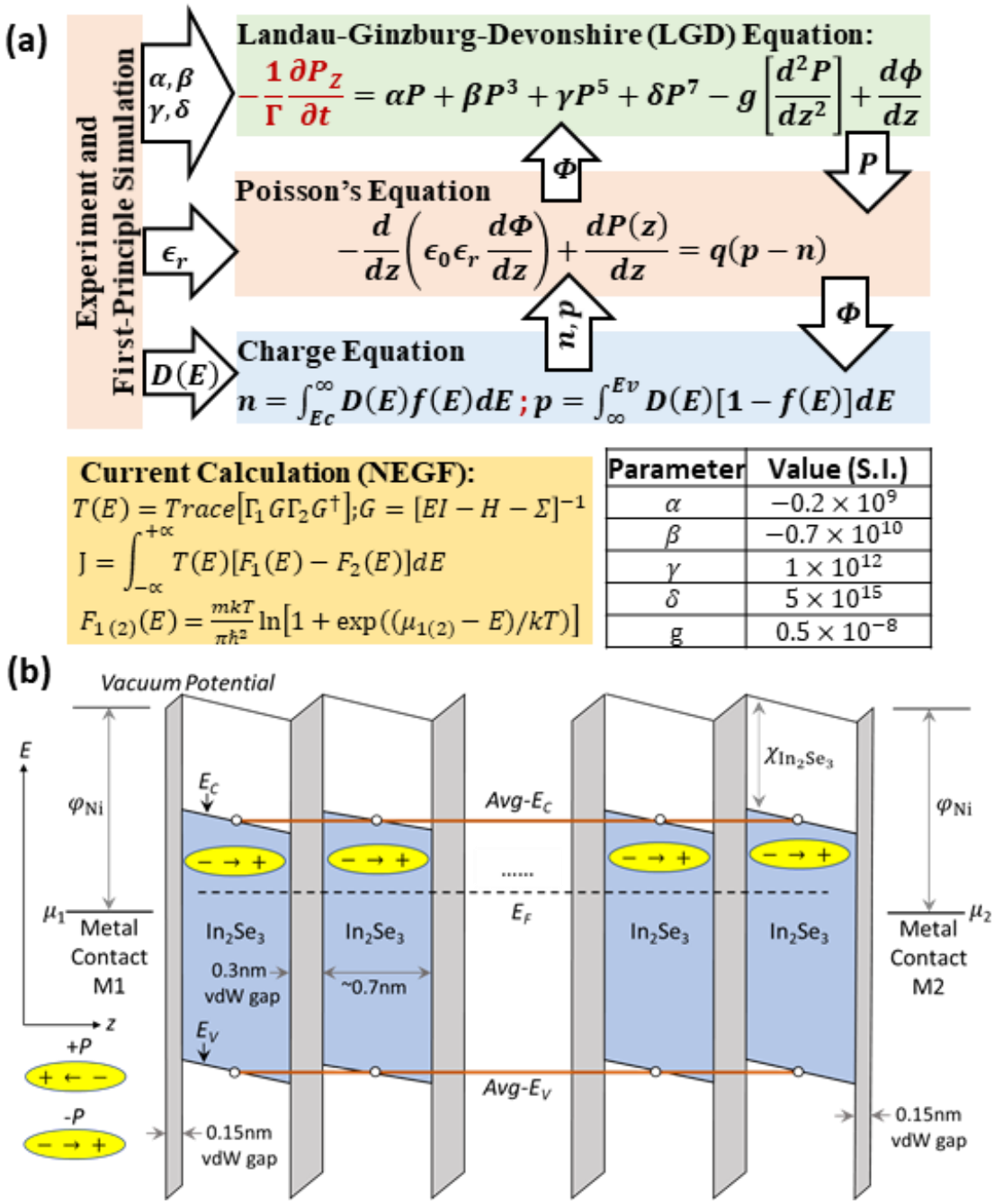

Parameter	Value (S.I.)
α	-0.2×10^9
β	-0.7×10^{10}
γ	1×10^{12}
δ	5×10^{15}
g	0.5×10^{-8}

Figure 9.3. (a) Self-consistent simulation flow, equations and parameters used for FeSMJ device simulation. (b) Band alignment of M-FeS-M structure before equilibrium.

9.4 FeSMJ Simulation Results

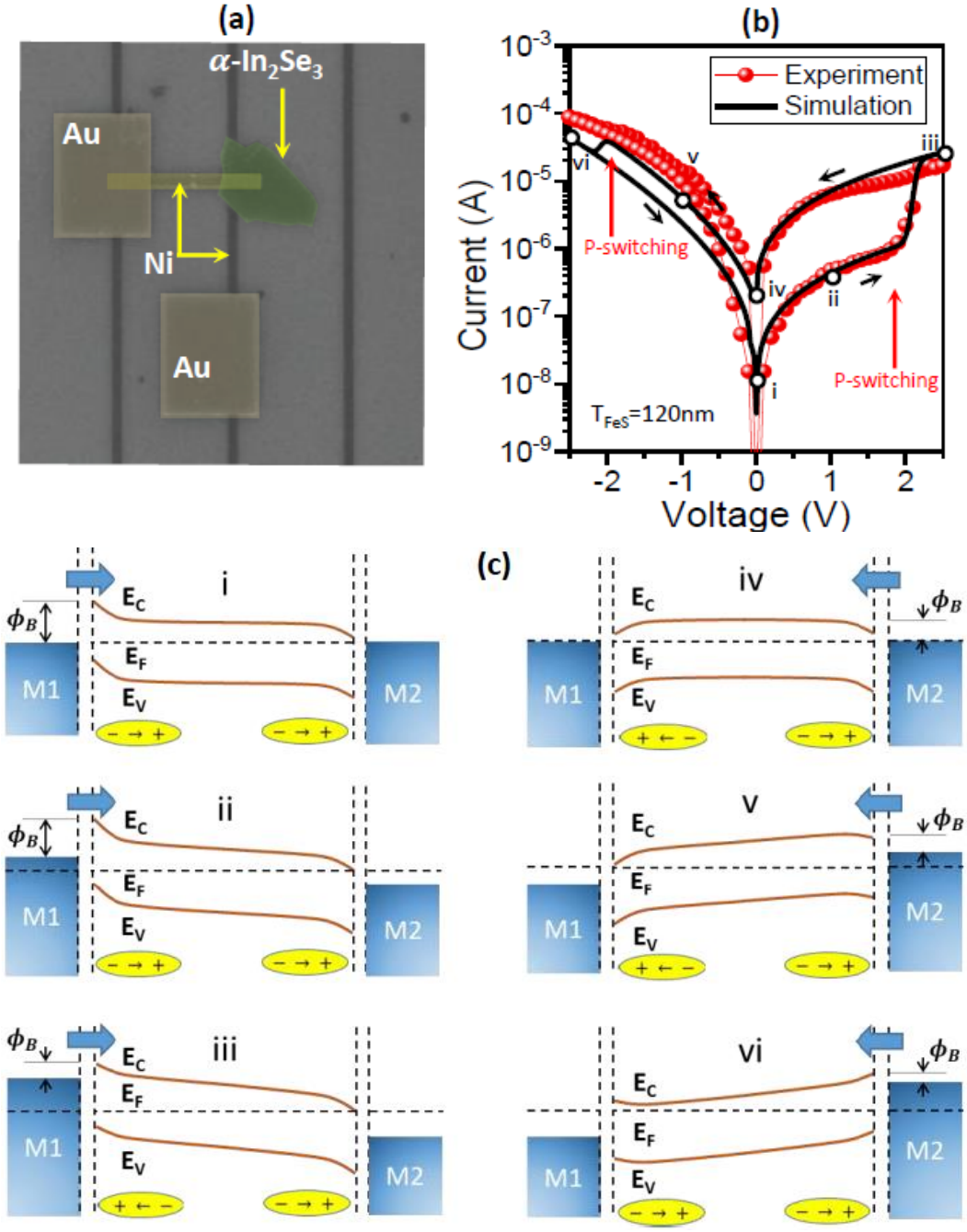

Figure 9.4. (a) SEM image of the fabricated FeSMJ. (b) Measured and simulated *I-V* characteristics of FeSMJ with T_{FeS}=120nm. (c) Band diagram of FeSMJ for different points marked in (b). Here, E_C and E_V are taken at the center of each FeS layers and the vdW regions within the FeS layers are not shown for the clarity.

The top-view of the fabricated FeSMJ is shown in Fig. 9.4(a). Here, the FeS thickness (T_{FeS}) is 120nm and the same metal (Ni) is used as the top and bottom contacts. The measured current (I) vs voltage (V) characteristics (Fig. 9.4(b)) exhibit a counter-clockwise hysteresis due to which the FeSMJ shows two different resistive states. Let us define the current at low-resistance state (LRS) and high-resistance state (HRS) as I_{LRS} and I_{HRS}, respectively. Note that the I_{HRS} to I_{LRS} switching occurs near ~2V which is similar to the coercieve voltage of P-switching (see PFM phase in Fig. 9.2(a)) indicating the change in current is due to the P-switching in the FeS layer. Here, one noticeable thing is that the characteristics are asymmetric with respect to the voltage polarity. For example, the hysteresis window, currents (I_{LRS} and I_{HRS}), and their ratio (I_{LRS}/I_{HRS}) are unequal for positive and negative V. To understand the possible origin of asymmetry and the FeSMJ operation, we perform device-level simulation. The simulated I-V curve considering T_{FeS}=120nm and Nickel as metal contacts is shown in Fig. 9.4(b) indicating a good agreement with the experimental results. Due to a Schottky barrier at the metal-FeS interface (Fig. 9.3(b)), the observed current is due to the electron injection from the metal to FeS via Schottky tunneling along with direct tunneling through the vdW gaps.

Now, to understand the working principle, the equilibrium band diagram of FeSMJ (along the FeS thickness) is shown in Fig. 9.4(c)-i. Note, the band diagram is for an undoped α-In_2Se_3, in which the E_F is closer to the E_C, as discussed before. Without any loss of generality, let us assume that initially, all the FeS layers are in -z directed polarization state (-P). Let us call the left electrode M1 and right electrode M2. Now, the P-induced negative (positive) bound charges appear in the FeS near the M1 (M2) interface. The bound charges and the work-function difference between the metal and FeS induce an E-field within the vdW gap and the FeS layers. As a result, holes (electrons) appear at FeS-M1 (M2) interface to partially compensate the negative (positive) bound charges. Simultaneously, a built-in potential with opposite polarity appears across the two FeS-M junctions, yielding different Schottky barrier height (ϕ_B) for the mobile-carriers. For example, in Fig. 9.4(c)-i, ϕ_B at the FeS-M1 interface is higher than the FeS-M2 interface due to the negative and positive voltage across the respective vdW gaps. Depending on whether the electron-injecting barrier exhibits low or high ϕ_B, FeSMJ operates in LRS or HRS. Moreover, voltage-driven P-switching can enable transitioning between LRS and HRS, and vice versa. To understand this, let us consider a positive bias at M2. Hence, the electron injection takes place from M1 to FeS. As

the corresponding ϕ_B is high, FeSMJ operates in HRS. Concurrently, hole (electron) concentration at the FeS-M1 (M2) interface increases. As the hole DOS is higher compared to the electron DOS, the increase in hole concentration is higher compared to the electron concentration (Fig. 9.4(c)-ii). This leads to a higher electric-field near the FeS-M1 interface compared to the FeS-M2 interface. At sufficiently high positive voltages (~2V in Fig. 9.5d-ii), the electric-field near the FeS-M1 increases beyond the coercive field. Hence, a few layers near the M1 interface switch to +*P* (+*z* directed) as shown in Fig. 9.4(c)-iii. Consequently, ϕ_B at the FeS-M1 interface significantly decreases, leading to an abrupt increase in the current (LRS). The LRS operation continues even when the voltage is reduced to 0 due to *P*-retention. Now, when a negative voltage is applied at M2, electron injects from M2 to FeS (Fig. 9.4(c)-iv). As the corresponding ϕ_B is low, the FeSMJ continues to operate in LRS. With a further increase in the negative polarity voltage, the electric-field near the M1-FeS interface switches the polarization back to –*P* (Fig. 9.4(c)-vi). This significantly reduces the E-field near the M1-FeS interface, the effect of which penetrates throughout the FeS including near the electron injecting electrode (FeS-M2 interface) and that reduces the current. However, unlike V>0V, where switching from HRS to LRS is abrupt, here the change in current is gradual. This is because for V>0V, the change in ϕ_B of the electron injecting junction (FeS-M1) is large due to *P*-switching near that interface. On the other hand, for V<0V, the electron injecting ϕ_B does not change significantly as *P*-switching occurs on the other electrode. Therefore, the voltage hysteresis, I_{LRS}, I_{HRS}, and I_{LRS}/I_{HRS} are asymmetric with respect to the voltage polarity (i.e. lower for V<0 than for V >0). To complete the discussion, if the initial *P* is opposite (+*P* for all the FeS layers), the *I-V* characteristics would be the opposite of what we discussed so far, i.e. a gradual HRS-to-LRS switching for V>0V (for *P*-switching near the FeS-M2 interface causing a non-significant change in the electron injecting ϕ_B) and an abrupt LRS-to-HRS switching for V<0V (due to *P*-switching near the FeS-M2 interface causing a change in the electron injecting ϕ_B). This can be understood from the symmetry of the device structure and by considering the relative nature of the *P* direction and the polarity of the applied voltage. That implies the *I-V* characteristics for -*P* and V>0 should be a mirrored (with respect to the *y*-axis) version of the *I-V* characteristics for +*P* and V<0.

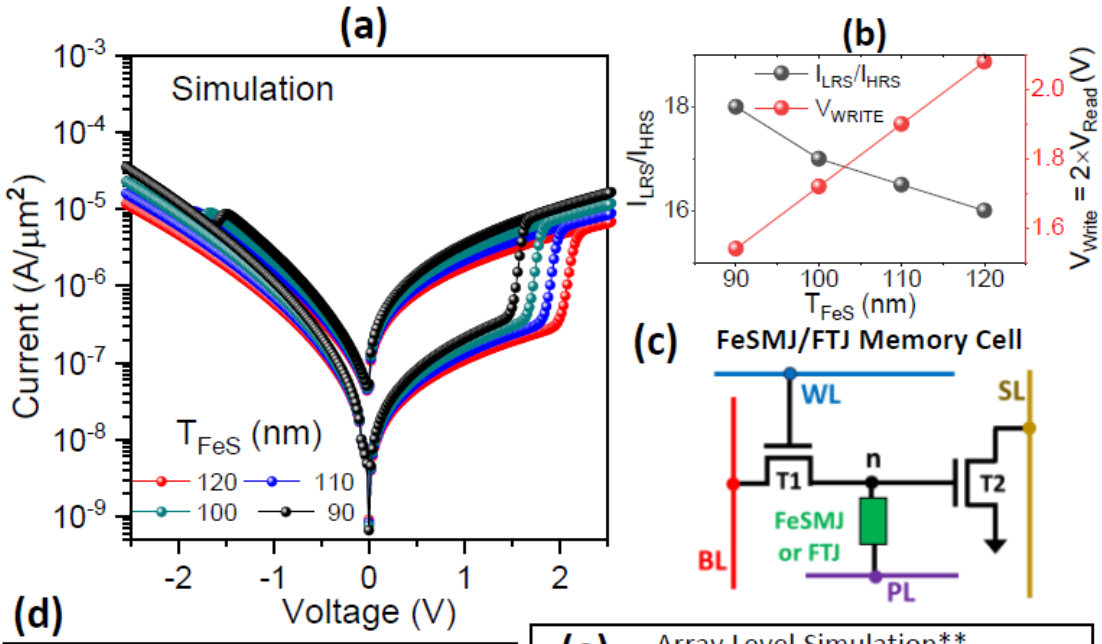

(d)

	FeSTJ	FTJ
Transport mechanism	Schottky tunneling	Direct tunneling
Current density	~10^{-5} A/μm^2	>10^{-8} A/μm^2
I_{LRS}/I_{HRS}	<10^3	<10^3

(e) Array Level Simulation**
Array Size = 1MB (1024x1024)

	FeSMJ	FTJ[25]	FTJ[26]	FTJ[27]	FTJ[28]
T_{READ}	0.6us	27us	94us	157us	292us
E_{READ}	1	16	73	125	221
E_{WRITE}	1	1.3	1.6	0.92	1.8

** In table-(e) the values are normalized with resect to the FeSMJ values.
Comparison is performed for iso-area and iso-sense-margin (SM = 15uA)

Figure 9.5. (a) *I-V* characteristics, (b) write voltage, read voltage and I_{LRS}/I_{HRS} of FeSMJ for different FeS thickness. (c) FeSMJ/FTJ memory cell. (d) device and (e) array level comparison between FeSMJ and FTJ (T_{READ}: Read time, E_{READ}: Read energy per, E_{WRITE}=Write energy).

Now, let us discuss the influence of FeS thickness on FeSMJ device characteristics. The simulated *I-V* characteristics of FeSMJ with different T_{FeS} are shown in Fig. 9.5(a). With thickness scaling, the coercive-field can be achieved at a lower applied voltage, therefore, the required voltage to switch the resistance state (called write voltage, V_{write}) decreases as shown in Fig. 5(b). Also, a decrease in T_{FeS} leads to an increase in electric-field (for the same applied voltage) yielding an increase in both I_{LRS} and I_{HRS} as shown in Fig. 9.5(a). Note that the *P* induced bound charges in the FeS-M interfaces lead to an E-field in the FeS layers (even in absence of an applied voltage). Such E-field further leads to a built-in potential across the FeS layers, where the built-in potential increases with the increase in FeS thickness. Moreover, this built-in potential leads to mobile

carrier density near the M-FeS interface (as the local potential determines the difference between fermi-level and conduction/valence-band). However, with the decrease in T_{FeS}, the built-in potential decreases and that leads to lower mobile carrier concentration near the M-FeS interface. Now, recall that the mobile-carrier concentration in FeS partially compensates the effect of *P*-induced bound charge. As the mobile-carrier concentration decreases with the decrease in T_{FeS}, therefore, the effect of *P*-induced bound charge becomes more prominent. Hence, the *P*-dependent modulation in ϕ_B increases with the decreases in T_{FeS}, which leads to an increase in I_{LRS}/I_{HRS} (Fig. 9.5(b)). Consequently, improved distinguishability (I_{LRS}/I_{HRS}) along with low voltage NVM operation can be achieved by scaling down the T_{FeS}.

9.5 Non-volatile-memory (NVM) performance of FeSMJ

Next, we evaluate the FeSMJ NVM performance in comparison with FTJ. In an array, each NVM cell (Fig. 9.5(c)) is comprised of a FeSMJ/FTJ connected in series with an access-transistor (T1) and their internal node (n) is connected to the gate of another transistor (T2) that senses the FeSMJ/FTJ resistive state-dependent discharging of the internal node potential. The read and write methodologies of this 2T-1R memory cell are described in [33]. In this analysis, we compare the different flavors of HfO_2 based FTJs [25-28] with our FeSMJ devices for an array size of 1Mb by considering iso-area and iso-sense-margin (SM). The area of 40nmx40nm is obtained based on the layout design for each memory cell. The device-level comparison (Fig. 9.5(d)) suggests that the FeSMJ has a key advantage of higher current density than HfO_2 based FTJ (due to Schottky transport in the former as opposed to direct tunneling in the latter). Therefore, for the same area, FeSMJ provides lower resistance (~10^{-3} times) compared to the FTJs. As the discharging of the internal node (n) depends on the FeSMJ/FTJ resistance, FeSMJ provides faster discharge and hence, smaller read-time compared to FTJs (Fig. 9.5(e)). Further, due to the slow discharge of the internal node, the T2 transistor remains turned ON for a longer period of time for FTJ. As a result, we observe significantly higher read energy for FTJ compared to FeSMJ. Moreover, we observe a little higher write energy for FTJ [25,26,28] due to their higher write voltage (>3V) compared to FeSMJ (2.5V). Due to such notable benefit of FeSMJ over HfO_2 based FTJs for NVM application, further exploration of FeSMJ is required to investigate its retention characteristics in addition to its correlation with scaling. Note that, in this comparison, we only consider HfO_2 based FTJs

because of their aggressive scalability [29]. However, there are different perovskite-based FTJs (with significantly high current and high I_{LRS}/I_{HRS}) where the memory operation not only depends on the *P*-switching but also depends on the migration of oxygen vacancies [30], ions [31], and formation of the conductive paths [32]. The scalability and variability of such devices are yet to be investigated and therefore, not included in this comparison.

9.6 Summary

In summary, the FeS polarization induces a built-in potential across the vdW gap between FeS and metal contact leading to a *P*-dependent Schottky barrier for electron injection. By invoking voltage-driven *P*-switching, the barrier height can be modulated, which leads to transitions between HRS and LRS in FeSMJ. Further, in FeSMJ with high T_{FeS}, the appearance of mobile-carriers can lead to a partial *P*-switching yielding asymmetric FeSMJ *I*-*V* characteristics. However, with T_{FeS} scaling, I_{LRS}/I_{HRS} increases and the asymmetry reduces due to complete *P*-switching. Most importantly, FeSMJ exhibits a significantly high current density due to Schottky tunneling. Due to such appealing characteristics and fundamental differences in the transport mechanisms, FeSMJ-NVM exhibits significantly improved performances compared to FTJ-NVM.

9.7 References

[1] H. Mulaosmanovic, E. Chicca, M. Bertele, T. Mikolajickac, and S. Slesazecka, Nanoscale 10, 21755 (2018)

[2] H. Mulaosmanovic, J. Ocker, S. Müller, M. Noack, J. Müller, P. Polakowski, T. Mikolajick, and S. Slesazeck, in 2017 Symposium on VLSI Technology (2017), pp. T176-T177.

[3] A. K. Saha, and S. K. Gupta, Scientific Reports 10 (10207), 2020.

[4] Z. Tan, L. Hong, Z. Fan, J. Tian, L. Zhang, Y. Jiang, Z. Hou, D. Chen, M. Qin, M. Zeng, J. Gao, X. Lu, G. Zhou, X. Gao, and J.-M. Liu, NPG Asia Materials 11, 20 (2019).

[5] M. Park, Y. Lee, T. Mikolajick, U. Schroeder, and C. Hwang, MRS Communications, 8(3), 795 (2018).

[6] K. Chatterjee, S. Kim, G. Karbasian, A. J. Tan, A. K. Yadav, A. I. Khan, C. Hu, and S. Salahuddin, IEEE Electron Device Lett. 38, 1379 (2017).

[7] P. Sharma, K. Tapily, A. K. Saha, J. Zhang, A. Shaughnessy, A. Aziz, G. L. Snider, S. Gupta, R. D. Clark, and S. Datta, in 2017 Symposium on VLSI Technology (2017), pp. T154–T155.

[8] V. Garcia, and M. Bibes, Nature Communications 5, 4289 (2014).

[9] F. Mo, Y. Tagawa, T. Saraya, T. Hiramoto and M. Kobayashi, in IEEE International Electron Device Meeting (IEDM) (2018), pp. 16.3.1-16.3.4.

[10] H. Ryu, H. Wu, F. Rao, and W. Zhu, Scientific Reports 9, 20383 (2019).

[11] D. Z. Gao, J. Strand, M. S. Munde, and A. L. Shluger, Front. Phys. 7, 43 (2019).

[12] W. Ding, J. Jhu, Z. Wang, Y. Gao, D. Xiao, Y. Gu, Z. Zhang, and W. Zhu, Nature Communications, 8 14956 (2017)

[13] C. Zheng, L. Yu, L. Zhu, J. L. Collins, D. Kim, Y. Lou, C. Xu, M. Li, Z. Wei, Y. Zhang, M. T. Edmonds, S. Li, J. Seidel, Y. Zhu, J. Z. Liu, W. Tang, and M. S. Fuhrer, Science Advances 4, 7 (2018).

[14] C. Cui, W. Hu, X. Yan, C. Addiego, W. Gao, Y. Wang, Z. Wang, L. Li, Y. Cheng, P. Li, X. Zhang, H. N. Alshareef, T. Wu, W. Zhu, X. Pan, and L. Li, Nano Letters 18, 1253 (2018).

[15] S. Wan, Y. Li, W. Li, X. Mao, W. Zhu, and H. Zeng, Nanoscale 10, 14885 (2018).

[16] M. Si, A. K. Saha, S. Gao, G. Qiu, J. Qin, Y. Duan, J. Jian, C. Niu, H. Wang, W. Wu, S. K. Gupta, and P. D. Ye, Nature Electronics 2, 580 (2019).

[17] M. Si, Y. Luo, W. Chung, H. Bae, D. Zheng, J. Li, J. Qin, G. Qiu, S. Yu, and P. D. Ye, in IEEE International Electron Device Meeting (IEDM), 2019.

[18] P. Giannozzi, et al., J.Phys.:Condens.Matter 21, 395502 (2009).

[19] P Giannozzi, et al., J.Phys.:Condens.Matter 29, 465901 (2017).

[20] A. V. Krukau, O. A. Vydrov, A. F. Izmaylov, and G. E. Scuseria, J. Chem. Phys. 125, 224106 (2006).

[21] R. D. King-Smith, and D. Vanderbilt, Phys. Rev. B 47, 1651 (1993).

[22] G. Henkelman, B. P. Uberuaga, and H. A. Jónsson, J. Chem. Phys. 113, 9901 (2000).

[23] D. S. Sholl, and J. A. Steckel, Density Functional Theory: A Practical Introduction, Wiley (2009), pp 113-130.

[24] Lev D. Landau, Zh. Eksp. Teor. Fiz. 7, 19 (1937).

[25] S. Slesazeck, T. Ravsher, V. Havel, E. T. Breyer, H. Mulaosmanovic, T. Mikolajick, in IEEE International Electron Device Meeting (IEDM) (2019), pp. 38.6.1-38.6.4.

[26] B. Max, M. Hoffmann, S. Slesazeck, and T. Mikolajick, in 2018 48th European Solid-State Device Research Conference (ESSDERC), (2018).

[27] M. Kobayashi, Y. Tagawa, F. Mo, T. Saraya, and T. Hiramoto, IEEE Journal of the Electron Devices Society, vol. 7, pp. 134-139 (2019).

[28] S. Fujii, Y. Kamimuta, T. Ino, Y. Nakasaki, R. Takaishi, and M. Saitoh, in 2016 Symposium on VLSI Technology, pp. 1-2 (2016).

[29] H.-J. Lee, M. Lee, K. Lee, J. Jo, H. Yang, Y. Kim, S. Chul Chae, U. Waghmare, J. H. Lee, Science 369, 6509, pp. 1343-1347 (2020).

[30] P. Hou, J. Wang, X. Zhong, and Y. Wu, RSC Advances, 6(59), 54113–54118 (2016).

[31] R. Guo, Y. Zhou, L. Wu, Z.-R. Wang, Z. Lim, X. Yan, W. Lin, H. Wang, H. Yoong, S. Chen, T. Venkatesan, J. Wang, G. M. Chow, A. Gruverman, X. Miao, Y. Zhu, and J. Chen, ACS Applied Materials & Interfaces, 10(15), 12862–12869 (2018).

[32] H. Yamada, V. Garcia, S. Fusil, S. Boyn, M. Marinova, A. Gloter, S. Xavier, J. Grollier, E. Jacquet, C. Carrétéro, C. Deranlot, M.Bibes, and A. Barthélémy, ACS Nano 7, 6, 5385–5390 (2013).

[33] A. K. Saha, M. Si, P. D. Ye, and S. Gupta, ‘α-In2Se3 based Ferroelectric-Semiconductor Metal Junction for Non-Volatile Memories,’ Applied Physics Letter, 117 (18), 2020.

10. CONCLUSION

10.1 Summary

Ferroelectric materials, by virtue of multi-domain polarization switching dynamics, have been identified as one of the promising candidates for emerging electronic devices. This dissertation explored several ferroelectric-based device concepts for a range of applications spanning from steep-slope logic to non-volatile memory. For this exploration, we developed several self-consistent device simulation frameworks and compact models extensively calibrated with experiments. In addition, we offered insights into different physical phenomena in ferroelectric materials and heterostructures, and analyzed their implications in application-driven device optimization.

As a ferroelectric insulator, Zr doped HfO_2 (HZO) is one of the most promising materials for electronic devices due to its seamless compatibility with CMOS process flow. In this work, we investigated the Zr concentration-dependent transition in HZO crystals and the corresponding evolution of dielectric, ferroelectric, and anti-ferroelectric characteristics due to stability of monoclinic, orthorhombic and tetragonal phases, respectively. Providing the microscopic insights of strain-induced crystal phase transformations, we proposed a novel physics-based model that shows good agreement with experimental results for HZO with different Zr concentrations. Further, considering the HZO as the gate-insulator of an FEFET with interlayer metal (FEMFET), we analyzed the optimal Zr concentration (~60%) for non-volatile memory operation.

One of the intriguing features of ferroelectric material is negative capacitance effects. In a heterogeneous system (MFIM and MFIS), ferroelectric materials can exhibit negative capacitance (NC) effects leading to differential amplification in local potential and can provide an enhanced charge and capacitance response for the whole system compared to their constituents. In this thesis, we systematically investigated the underlying physical mechanism of the NC effect in the ferroelectric material. Based upon the fundamental physics of ferroelectric material, we analyzed different assumptions, conditions, and distinct features of the quasi-static NC effect in the single-domain and multi-domain scenarios. While the quasi-static and hysteresis-free NC effect was

initially propounded in the context of a single-domain scenario, we highlighted that the similar effects can be observed in multi-domain (MD) FEs. To compensate for the depolarization effects in MFIM and MFIS stack, the FE layer breaks in multiple domains and the nature of the domain wall (DW: hard and soft) depends on the ferroelectric and underlying dielectric layer thickness. Further, we have indicated that the polarization switching via soft-DW displacements is non-hysteretic and for hard-DW the characteristics are hysteretic. While both the soft and hard-DW displacement yields quasi-static NC effects, the non-hysteretic NC can only be obtained for soft-DW displacement. In addition, we emphasized that, under certain scenarios, the effective capacitance of the FE layer may not be negative but can exhibit an enhanced positive capacitance compared to its intrinsic value. Such a phenomenon occurs in the absence of DW displacement in MD FE with hard-DW due to the electrostatic interaction between domains. Further, we analyze different physical and material properties of ferroelectric materials from the context of optimizing the multi-domain negative capacitance and enhanced positive capacitance effect in the MFIM and MFIS stack. In addition to that, we also investigated the hysteretic polarization switching characteristics in MFIM stack and identified the infulence of the dielectric (DE) layer thickness on different macroscopic properties (i.e., coercive voltage and remanent polarization). Our analysis unveiled that the increase in DE layer thickness causes an increase in domain density and thus leads to a decrease in remanent polarization, an increase in coercive voltage and an increase in polarization switching slope as well.

Next, we analyzed the multi-domain FEFET characteristics by developing a phase-field based self-consistent device simulation framework. Considering HZO as the FE layer, we first analyzed the dependence of the multi-domain patterns on the HZO thickness and their critical role in dictating the steep-switching (both in the negative and positive capacitance regimes) and non-volatile characteristics of FEFETs. We showed that the FE thickness scaling first leads to an increase in the domain density in the hard-DW regime, followed by soft DW formation and finally polarization collapse. For the hard-DW regimes with high FE thickness, the polarization switching is dominated by nucleation and that leads to a large change in the threshold voltage. However, with the decrease in FE thickness, the domain density increases leading to a transition towards DW-motion based P-switching, which leads to a smaller change in the FEFET threshold voltage. Furthermore, we analyzed the correlation between the memory window and the number of memory

states in the context of FE thickness scaling. In addition to that we analyze the FEFET performance from the perspective of negative capacitance effects and enhanced positive capacitance effects signifying a reduced subthreshold-swing, reduced short channel effects and superior scalability of FEFETs compared to the conventional high-k FET. Moreover, our analysis suggested that an improved NCFET performance can be obtained for an increased gradient energy coefficient.

Further, we developed a Preisach based circuit compatible model for FEFET (and antiferroelectric-FET) with interlayer metal (FEMFET) that captures the multi-domain polarization switching effects in the FE layer. Utilizing this model, we have explored the hysteretic characteristics of FEMFETs and analyzed the impact of transient negative capacitance effects in the subthreshold-swing behavior.

Next, we analyzed the polarization switching mechanism in metal-FE-metal devices by considering the intra-grain and inter-grain variation in HZO properties due to its polycrystalline nature. According to our analysis, the applied voltage modulated multi-domain polarization switching in HZO exhibits unique accumulative features where the variation and coupling among the grains play the key role. In addition, our analysis suggests a unique spontaneous polarization switching process in FE and signifies the possibilities for the realization of quasi-leaky-integration and fire (QLIF) type bio-plausible neuronal functionalities in FE based devices.

One of the key aspects of this dissertation is the development of significantly advanced models for ferroelectric devices (compared to the existing models). For instance, most of the previous FEFET models assumed single-domain polarization switching, homogeneous polarization in FE layer [xx], abtirary domain formation and/or analytical approximations. In contrary, the phase-field simulation framework of FEFET developed in this work can capture electrostatic driven multi-domain formation, microscopic polarization switching via both the domain-nucleation and domain-wall motion, multi-domain negative chapacitance effects, enhanced positive capacitance effects and multi-domain polarization driven non-gomognity in the semiconductor channel as well – a set of features those have never been captured in previous existing models.

Unlike semiconductor insulators (e.g., HZO), there are ferroelectric materials that exhibit a considerably low bandgap (< 2eV) and hence, display semiconducting properties. In this regard, non-perovskite-based 2D ferroelectric α-In_2Se_3 shows a bandgap of ~1.4eV, which suggests a combined ferroelectricity and semiconducting attributes in the same material system. As part of this work, we explored the modeling and operational principle of ferroelectric semiconductor metal junction (FESMJ) based devices in the context of non-volatile memory (NVM) application. Based on the first-principal simulation, we identified an asymmetric density-of-states in α-In_2Se_3 and that causes a higher hole density compared to the electron density. Such asymmetry in carrier concentration further triggers non-homogeneous electric-field and thus asymmetric polarization in the FES layers. Our device-level simulation of FESMJ indicated that the FES polarization-dependent modulation of Schottky barrier heights plays a key role in providing the NVM functionality. In addition, we demonstrated that the thickness scaling of FeS leads to a reduction in read/write voltage and an increase in distinguishability. Our array-level analysis of FESMJ NVM recommended a lower read-time and read-write energy with respect to the HfO_2-based ferroelectric insulator tunnel junction (FTJ) signifying its potential for energy-efficient and high-density NVM applications.

10.2 Outlook and Future Work:

In this dissertation, we have extensively investigated different flavors of ferroelectric-based devices with a vision to develop the physical understandings of device functionalities and evaluate their performance for different applications. For that, we have undertaken a comprehensive exploration starting from the first-principal study, 1D/2D device simulation and circuit-compatible compact modeling as well. However, beyond the topics explored in this work, there can be other important effects and interactions in this material system, which will require further investigation. The following topics are some of the extensions of the research work presented in this dissertation:

10.2.1 3D phase-field simulation considering polycrystallinity and other effects:

The ferroelectric HZO is well known to exhibit polycrystalline properties that incorporate different grains with different crystal phases and different crystal angles. While the effects of such polycrystallinity have been partially explored in the context of metal-HZO-metal capacitors, the

development of a more advanced simulation framework is required for the investigation of polycrystalline effects in HZO based devices (i.e., FEFETs, FTJs etc.). For example, the integration of 3D grain-growth models with the 3D extension of a phase-field simulation framework will be essential to capture the effects of inter-grain interactions in the multi-domain formation and the polarization switching dynamics in ferroelectric devices. Such a framework will also allow a more accurate prediction of device performances, analysis of variation and scaling effects. Further, the consideration of the other effects, i.e., (i) inhomogeneous strain, (ii) flexoelectric effects and (iii) electrocaloric effects in ferroelectric-based devices can possibly lead to new device implications.

10.2.2 3D phase-field simulation of Ferroelectric-semiconductor based devices

Unlike the ferroelectric HZO, which exhibits uniaxial polarization, the ferroelectric-semiconductor α-In_2Se_3 has polarization components both along the in-plane and out-of-plane directions. In the context of FESMJ, in this work, we only consider the out-of-plane polarization components. However, consideration of both of these polarization components and the development of a 3D phase-field framework will be important to analyze the multi-domain aspect of these devices. Moreover, one of the intriguing properties of the FES materials is their utility as the semiconductor channel of FETs. While the non-volatile memory functionality of FESFETs has been explored under the 1D assumption (considering only the out-of-plane polarization component), it will be crucial to analyze the effect of in-plane polarization in FESFETs as well. In particular, the in-plane polarization in FES is in parallel to the carrier transport direction, which can potentially lead to different source/drain contact resistance based on the polarity of the in-plane polarization. Hence, consideration of both the polarization components will be crucial for analyzing the implications for FES-based devices (FESMJ and FESFET). Such an investigation can lead to new operational principles and possibilities for a better device design or novel device functionalities.

10.2.3 Ferroelectric-based stochastic neuromimetic devices.

In the case of hard-DW, we discussed that the multi-domain pattern in FE is not unique (in chapter 2). This leads to the possibilities for multi-domain formation with different domain patterns with

different average polarization and coercive voltage for DW motion. Therefore, cycle-to-cycle stochasticity is expected during the multi-domain polarization switching in scaled ferroelectric devices. Exploration of such electrostatic driven stochasticity will be crucial to analyze from the perspective of FEFET operation. While this intrinsic stochasticity can be detrimental for conventional FEFET operation (i.e., memory), the same can be constructively utilized for several unconventional computing platforms (i.e., stochastic/neural computation). Such a stochastic behavior of scaled FEFETs can be utilized for the compact realization of stochastic neurons and synaptic devices and therefore demands further exploration.

10.3 Electrostriction augmented steep-slope FEFETs

Electrostriction is a property of all ferroelectric materials, that causes them to change their shape under the application of an electric field. Therefore, considering the FEFET operation, an applied gate voltage should not only change the polarization of the ferroelectric layer but should also alter the ferroelectric thickness leading to an increase in strain in the underlying semiconductor. Interestingly, the bandgap and the mobility of the semiconducting material change under the induced strain, and thus the electrostriction of the ferroelectric insulator can lead to a secondary modulation in the semiconductor channel in combination with the primary electrostatic modulation. In addition to the negative capacitance or enhanced positive capacitance effects of the ferroelectric layer, this secondary modulation of the semiconductor channel can be utilized for harnessing a sub-60mV/decade subthreshold swing in FEFETs. A comprehensive analysis of such interactions is yet to be done and can be beneficial for the design of electrostriction augmented steep-slope functionalities in FEFETs.

VITA

Atanu Kumar Saha is a Ph.D. candidate at Purdue University. He earned his BSc and MSc degree in Electrical Engineering from Bangladesh University of Engineering & Technology (BUET) in 2013 and 2015, respectively. Prior to joining Dr. Gupta's research group, he worked as a lecturer in BRAC University, Bangladesh from 2013-2016. His research interest includes ferroelectricity based devices, 2D semiconductor and device modeling.

PUBLICATIONS

Book Chapter:

[B1] M. A. Alam, N. Zagni, **A. K. Saha**, N Thakuria, S. Thirumala, S. K. Gupta, "Negative Capacitors and Applications" Springer, (accepted).

Journal Papers:

[J1] **A. K. Saha**, M. Si, P. D. Ye, and S. Gupta, 'Multi-domain Polarization Switching in HZO-Dielectric Stack: The Role of Dielectric Thickness,' **Applied Physics Letter**. (*Under review*)

[J2] **A. K. Saha**, and S. Gupta, 'Negative Capacitance in Ferroelectric Heterostructures: A Theoretical Perspective,' **Journal of Applied Physics**, 129 (8), 2021. (**Featured article**)

[J3] **A. K. Saha**, M. Si, P. D. Ye, and S. Gupta, 'α-In2Se3 based Ferroelectric-Semiconductor Metal Junction for Non-Volatile Memories,' **Applied Physics Letter**, 117 (18), 2020.

[J4] **A. K. Saha**, and S. Gupta, "Multi-domain Negative Capacitance Effect in Ferroelectric Heterostructures," **Scientific Reports**, 10 (1), 2020.

[J5] I. Chakraborty, A. Jaiswal, **A. K. Saha**, S. Gupta, and K. Roy, "Pathways to Efficient Neuromorphic Computing with Non-Volatile Technologies," **Applied Physics Reviews**, 7 (2), 2020. (**Featured article**)

[J6] **A. K. Saha**, K. Ni, S. Dutta, S. Datta and S. Gupta, "Phase Field Modeling of Domain Dynamics and Polarization Accumulation in Ferroelectric HZO," **Applied Physics Letters**, 114 (20), 2019.

[J7] M. Si, **A. K. Saha**, …, W. Wu, S. Gupta, P. D. Ye, "Room Temperature Electrocaloric Effect in 2D Ferroelectric $CuInP_2S_6$ for Solid State Refrigeration", **ACS Nano**, 13 (8), 2019.

[J8] M. Si, **A. K. Saha**, S. Gao, G. Qiu, J. Qin, Y. Duan, J. Jian, C. Niu, H. Wang, W. Wu, S. Gupta, and P. D. Ye, "A Ferroelectric Semiconductor Field-Effect Transistor", **Nature Electronics**, 2 (12) 2019.

[J9] N. Thakuria, **A. K. Saha**, S. K. Thirumala, B. Jung, S. Gupta, "Oscillators Utilizing Ferroelectric-Based Transistors and Their Coupled Dynamics", **IEEE Transactions on Electron Devices**, 66 (5), 2019.

[J10] **A. K. Saha**, S. Datta and S. Gupta, "Negative Capacitance Effect in Resistor-Ferroelectric and Ferroelectric-Dielectric Networks: Apparent or Intrinsic?" **Journal of Applied Physics**, 123 (10), 2018. (**Featured article** and **one of the highest read articles in 2019 published by JAP**).

[J11] **A. K. Saha**, G. Saha, and ABM Rashid, "Graphene Nanoribbon Quantum-Well Interband and Intersubband Photodetector," **IEEE Transaction on Electron Devices**, 62 (12), 2015.

Conference Papers:

[C1] **A. K. Saha**, and S. Gupta, "Effective Ferroelectric Permittivity in Metal-Ferroelectric-Insulator-Semiconductor (MFIS) Heterostructures: The Implications of Hard and Soft Domain Walls," MRS Spring Meeting & Exhibit, 2021.

[C2] W. Chakraborty, M. S. Jose, J. Gomez, **A. K. Saha**, K. A. Aabrar, P. Fay, S. Gupta and S. Datta, "Higher-k HZO Trigate Transistors with Higher DC and RF Performance and Improved Reliability," Symposia on VLSI Technology (VLSI Tech), 2021. (To be presented)

[C3] **A. K. Saha**, M. Si, K. Ni, P. D. Ye, S. Datta, S. Gupta, "Ferroelectric Thickness Dependent Domain Interactions in FEFETs for Memory and Logic: A Phase-field Model based Analysis," IEEE Intl. Electron Devices Meeting (IEDM), 2020.

[C4] N. Thakuria, **A. K. Saha**, S. K. Thirumala, D. Schulman, S. Das, S. K. Gupta, "Polarization-induced Strain-coupled TMD FETs (PS-FETs) for Non-Volatile Memory Applications," Device Research Conf. (DRC), 2020.

[C5] **A. K. Saha**, B. Grisafe, S. Datta, and S. K. Gupta, "Microscopic Crystal Phase Inspired Modeling of Zr Concentration Effects in Hf1-xZrxO2Thin Films," Symposia on VLSI Technology (VLSI Tech.), 2019.

[C6] S. Dutta, **A. K. Saha**, P. Panda, W. Chakraborty, J. Gomez, A. Khanna, S. K. Gupta, K. Roy, and S. Datta, "Biologically Plausible Ferroelectric Quasi-Leaky Integrate and Fire Neuron," Symposia on VLSI Technology (VLSI Tech), 2019.

[C7] K. Ni, **A. K. Saha**, W. Chakraborty, … , J. Smith, G. Rayner, S. Gupta, S. Datta, "Equivalent Oxide Thickness Scaling With HZO High-κ Dielectric Near Morphotropic Phase Boundary," IEEE Intl. Electron Devices Meeting (IEDM), 2019.

[C8] **A. K. Saha**, S. Datta, and S. K. Gupta, 'Modeling Approaches of Ferroelectric Transistors,' Semiconductor Research Corporation (SRC) TECHCON, Austin, TX, US, 2018 (Internal conference of SRC).

[C9] **A. K. Saha**, and S. K. Gupta, "Modeling and Comparative Analysis of Hysteretic Ferroelectric and Anti-ferroelectric FETs," Device Research Conf. (DRC), 2018.

[C10] K. Ni, B. Grisafe, W. Chakraborty, **A. K. Saha**, S. Dutta, M. Jerry, J. Smith, S. K. Gupta, and S. Datta, "In-Memory Computing Primitive for Sensor Data Fusion in 28 nm HKMG FeFET Technology", IEEE Intl. Electron Devices Meeting (IEDM), 2018.

[C11] M. Jerry, J. Smith, K. Ni, **A. K. Saha**, S. Gupta, S. Datta, "Insights on the DC Characterization of Ferroelectric Field-Effect-Transistors," Device Research Conf. (DRC), 2018.

[C12] A. Aziz, E. T. Breyer, A. Chen, X. Chen, S. Datta, S. K. Gupta, M. Hoffmann, X. S. Hu, A. Ionescu, M. Jerry, T. Mikolajick, H. Mulaosmanovic, K. Ni, M. Niemier, I. O'Connor, **A. K. Saha**, S. Slesazeck, S. K. Thirumala, X. Yin, "Computing with Fe-FETs: Devices, models, systems, and applications," Design, Automation & Test in Europe Conf. & Exhibition (DATE), 2018.

[C13] **A. K. Saha**, P. Sharma, I. Dabo, S. Datta, and S. K. Gupta, "Ferroelectric Transistor Model based on Self-Consistent Solution of 2D Poisson's, NEGF and Multi-Domain Landau Equations", IEEE Intl. Electron Devices Meeting (IEDM), 2017.

[C14] P. Sharma, K. Tapily, **A. K. Saha**, … , S. K. Gupta, R. D. Clark, and S. Datta, "Impact of Total and Partial Dipole Switching on the Switching Slope of NC-FETs with Ferroelectric HZO Gate Stack," Symposia on VLSI Technology (VLSI Tech), 2017.

[C15] P. Sharma, J. Zhang, **A. K. Saha**, S. Gupta, and S. Datta, "Negative capacitance transients in metal-ferroelectric HZO-Insulator-Semiconductor (MFIS) capacitors," Device Research Conf. (DRC), 2017.